# 2015 Capstone Aircraft Design: Project Big Bird

University of Washington

Seattle, Washington, 98195-2400

June 13, 2015

**This report provides the comprehensive record of the professional work done for AA 410/411 Aircraft Design course. Concept design, preliminary design, final design of the airplane, project management, and analysis of the various testings are included. Future students could use this report as a guide for their project to improve the quality of the project.**

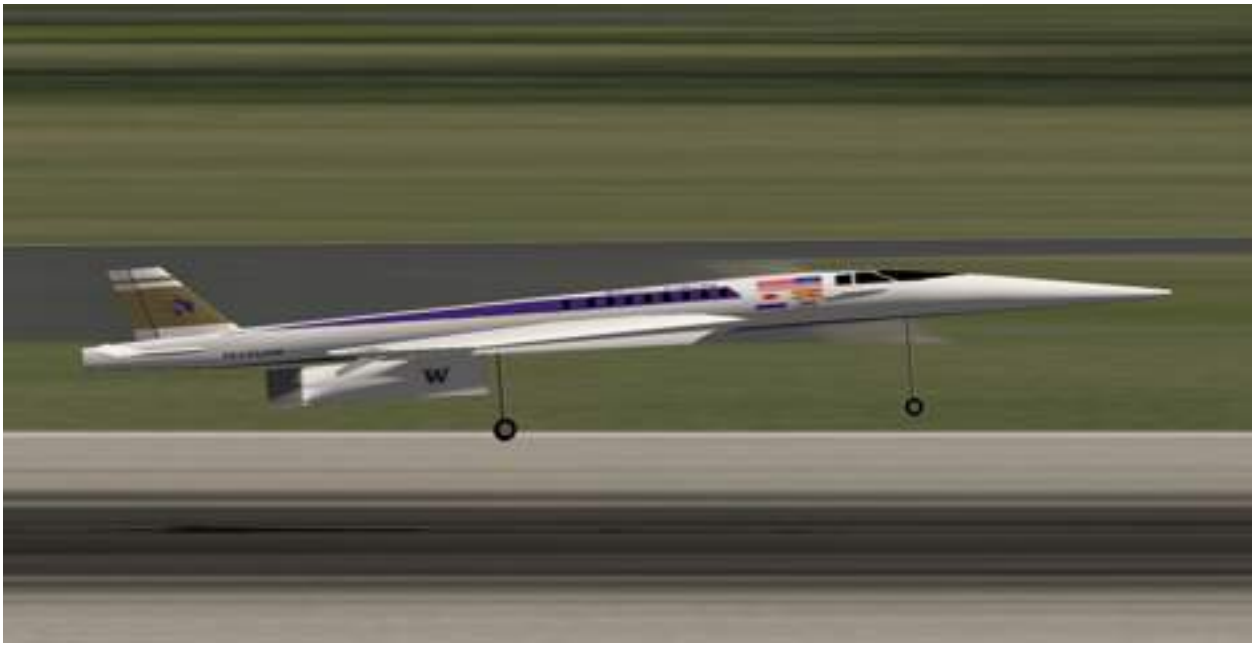

# Table of Contents

# List of Figures

# List of Tables

# 1. Acknowledegment

**Special Thanks to:**

- **United States Air Force**
  Generous Monetary Contributions
- **Chuck Bower**
  AMA Certified/ FAA approved turbine model aircraft Instructor-Pilot CBRC, Whidbey Island RC Society, Academy of Model Aeronautics
- **Kirsten Wind Tunnel**
  Jack Ross- Business Manager
  Nathan Precup- Operations Manager
  UWAL Crew
- **Dr. Eii Livne**
  Professor, William E. Boeing Department of Aeronautics & Astronautics
  University of Washington
- **Dr. Marat Mor**
  University of Washington Associate Professor(Industry Affiliate)
  Stirling Dynamics Inc.
  Finite Element Consultant
- **Chester(Chet) Nelson**
  University of Washington Associate Professor(Industry Affiliate)
  Technical Fellow, Boeing Commercial Airplanes
- AeroTEC
  Robert Dick - Vehicle Integration Adviso
  Todd Leighton - Vehicle Integration Advisor
  Wind Tunnel Model and Molds Suppliers
- **University of Washington** William E. Boeing Department of Aeronautics and Astronautics
  College of Engineering

# 2. Project Overview

This program was the senior capstone project for the undergraduates of the William E. Boeing Department of Aeronautics and Astronautics at the University of Washington. 36 undergraduate students were involved in this two-quarter project. Two project leads managed the project, and the students were divided into 8 different disciplinary teams which had an elected team lead. The aim of the project was to design and build a modern airplane to satisfy a given set of requirements including weight, stability, control, performance, and

handling qualities. The students were exposed to a industry level software and hardware through designing and constructing while obtaining experiences from using facilities such as University of Washington Kirsten Wind Tunnel, 3×3 wind tunnel, machine shops, and testing equipment for the duration of the project. The development of the project was overseen by Professor Eli Livne and experienced professionals from industry as listed in acknowledgement section.

## 2.1. General 2015 UW Capstone Airplane Design Challenge

Design a research UAV that would contribute to the research of a tailless long range supersonic design. The objective is to reduce any non-lifting surface to save on weight and maintain the stability and dynamic performance of the R-UAV. By incrementally adding vector thrust the vertical tail can also potentially be decreased in size.

## 2.2. Technical Requirements

Several technical requirements were presented for this year's project.

### *2.2.1. R-UAV Performance*

- Stability in all axes
- $V_{appr} = 1.23 \times V_{stall}$
- $V_{takeoff} = 1.15 \times V_{stall}$
- Landing distance $< 400$ ft.
- Endurance of 7 minutes
- Worst-case-scenario endurance of 4.5 minutes
- Climb gradient of $18° - 20°$
- Static $\frac{T}{W} = 1.1 \times SSBJstatic\frac{T}{S}$ at MTOGW(0.55)
- Glide slope of 5° or steeper at $V_{appr}$

### *2.2.2. UAV Stability and Control*

- Limited adverse roll due to yaw control
- Minimum CG range of 6%
- Lateral-directional control authority must be sufficient to trim out imbalanced yaw forces
- Nose-down pitch control at high $\alpha$ must produce an angular acceleration of $8deg/s$
- Static yaw stability of $C_{n_\beta} = 0.002deg^{-1}, yaw$

### 2.3. Technical Challenges

Based on the technical requirements, technical challenges are listed below.

- Tradeoffs of Vertical Tail vs. alternative control options
- Innovation in control effectors
- Versatility of the configuration (options for testing at different variations)
- Controllability/maneuverability
- Meeting the weight upper limit
- Meeting the performance challenge
- Meeting the S& C challenge
- Airframe / Propulsion integration (Nacelle design and location, etc.)
- Meeting the schedule challenge (with a team of committed but inexperienced students)
- Exploratory "simple" active control for stability augmentation Safety and Reliability

## 3. Project Management

The project management team was in charge enforcing the schedule, assessing risk probability and mitigation, overseeing the budget, time allocation, and documentation of the project. Out of the project management team there are two lead project managers overseeing the technical aspect, and two project managers for all generic aspects of the project.

### 3.1. Team Structure

The team structure was composed of several individual. Two project lead were voted for at the start of the project by the class. Upon the choosing of the project leads each individual member chose what teams they would like to participate in. For each of the technical disciplines team leads are voted for by there respected team members. To further help with the project two documentation managers where elected. There were eight different teams performing special tasks. The teams and their main responsibilities are listed below.

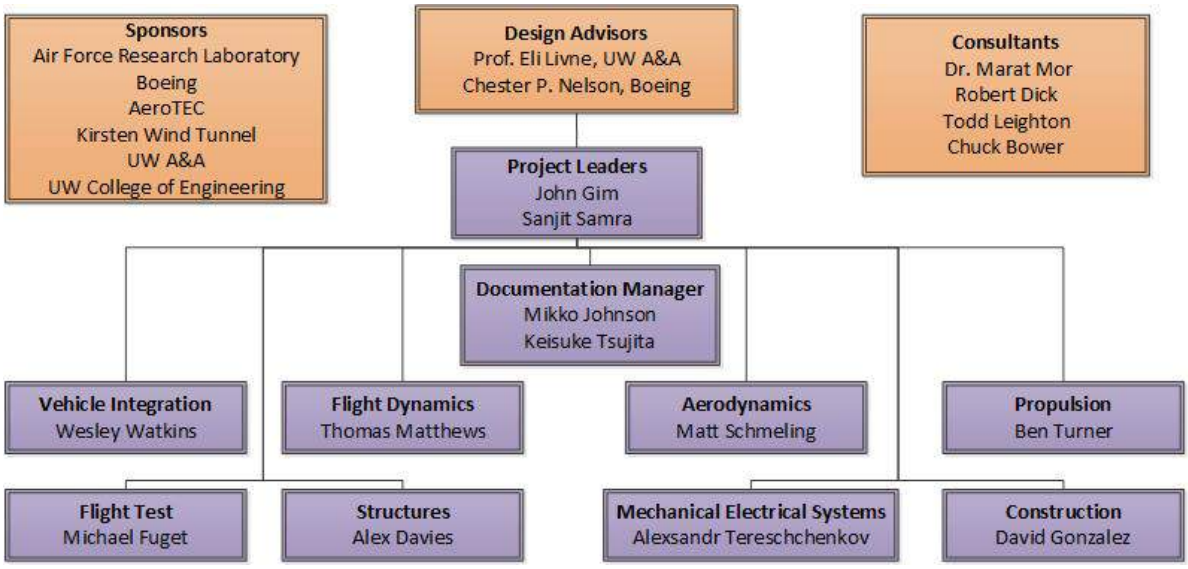


**Figure 3.1.1:** Team structure

- Construction
  - Training of the students for specialized skills such as molding, lay ups, 3D printing, laser cutting, hot wire-cutting, integration and actuation of avionics instruments.
  - Manufacturing of several wind tunnel model parts
  - Manufacturing and integration of R-UAV parts.
  - Construction of R-UAV
- Flight Dynamics
  - Sizing of control surfaces
  - Analysis of wind tunnel test, specifically for control surfaces effectiveness
  - Performance analysis
  - Flight dynamic modeling and design of controllers for stabilization of the airplane
  - Development of the flight simulator using X-Plane
- Flight Test
  - Developing the procedure for flight test
  - Preparation for flight test
- Mechanical Electrical Systems
  - Design of the mechanical and electrical systems that is on the R-UAV
  - Selection of components of the systems
  - Detailed programming and setting of the controlling devises including controllers and ground stations

- Propulsion
  - Selection of propulsion system
  - Design of super sonic nacelle
  - Design of R-UAV design and determination of the location
  - 3'×3' wind tunnel test for thrust vectoring
  - Static testing of nacelle and EDF
  - Wind tunnel testing and the analysis of the results for thrust vectoring
- Structure
  - Initial structural design
  - Material testing
  - Prototyping and component testing
  - Structural layout and analysis
- Vehicle Integration
  - Design of the wind tunnel model and molds for fuselage and wing.
  - Design of the construction tools
  - Weight sizing, including analysis on balance, weights, and moments of inertia

The whole structure of the teams and their members are shown in Fig. 3.1.2.

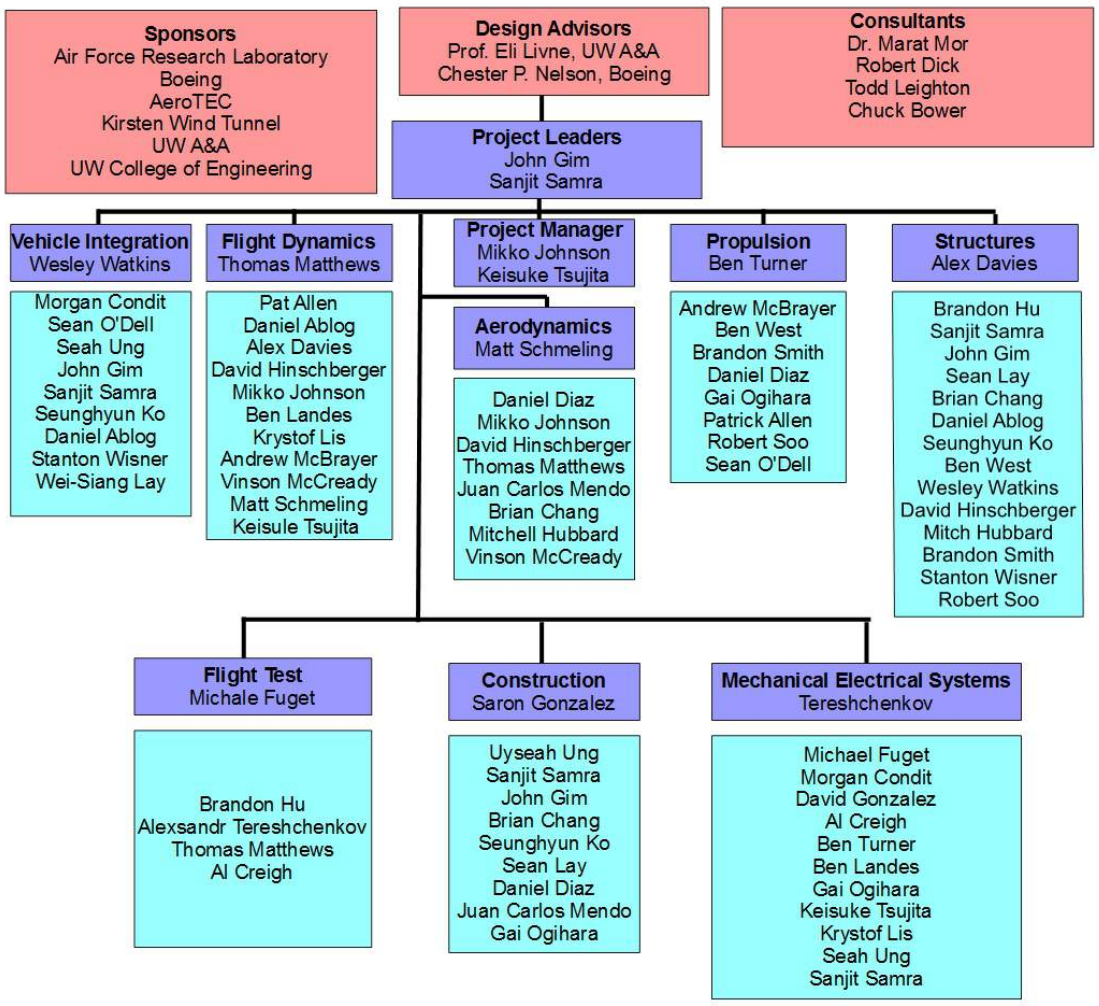


**Figure 3.1.2:** Structure of team

## 3.2. Budget

For 2015 project, total of $134,302.49 were spent. The Aircraft Design budget was composed of support from the University, Boeing, and the Air Force. In addition to this there was full and partial material/supply donation from various companies such as the Airtech, AeroTEC, Fiber Lay, Fisheries. Each purchase made was categorized into different groupings: Software licensing, M-E systems, material/coupon testing and supplies, Wind Tunnel model/molds, R-UAV, wind tunnel testing, and shop tools and supplies. The breakdown of the total budget spent are shown in Fig. 3.2.1.

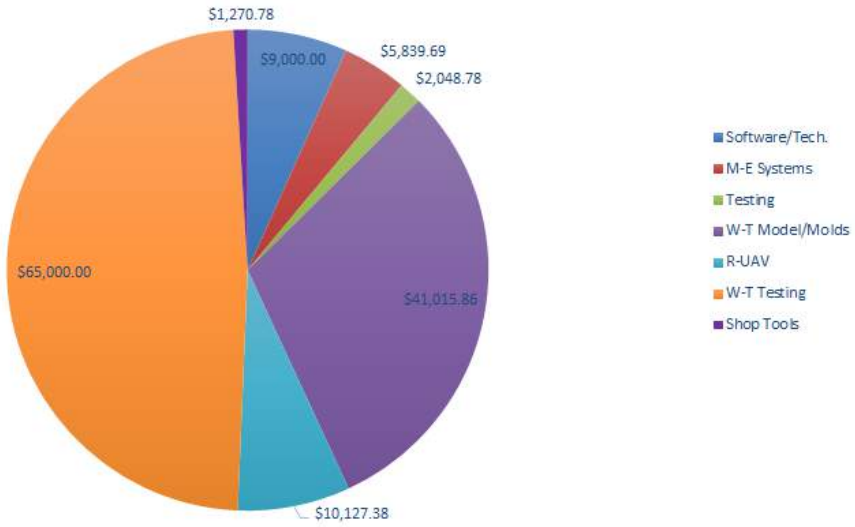


**Figure 3.2.1:** Breakdown of the budget spent

It should be noted that the University of Washington Kirsten wind tunnel supplied complimentary time worth approximately $65,0000 at there rate for commercial use, and AeroTEC supplied the wind tunnel model and part molds at cost for approximately $41,000. Wind tunnel hours are free however they were added to the budget to provide a real world understanding of the finances of the budget. All technical advisors and adjunct instructors also supplied their time at no cost to the project.

To broaden the budget three technical teams applied for the Engineering Capstone Award individually. The teams that applied for the award are propulsion, mechanical-electrical, and flight dynamics. Each team received $1000 resulting in a total of $3000 that was added to the budget allocation. With the additional fund the teams were allowed to stretch their design capability. Future teams should consider applying for this award such as the structure in addition to what we applied for.

## 3.3. Schedule

The project schedule was defined by the management and team leads. In addition to this a Ghant chart was created for the subsections of each team tasks. Leads where to adhere to this schedule or make changes as needed under certain provisions set by management. Below in Fig. 3.3.1 the final summarized schedule as of June.

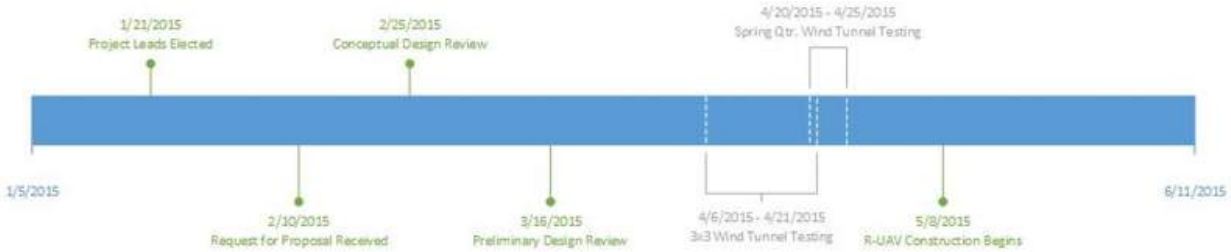


**Figure 3.3.1:** Project schedule timeline

### 3.4. Time Allocation

Due to the high intensity of the challenges presented, a lot of hours were spent for the entire project. The allocation of the time spent is shown in Fig. 3.4.1. As the figure shows, the project spent time to construction the most while structures team also spend significant amount of time.

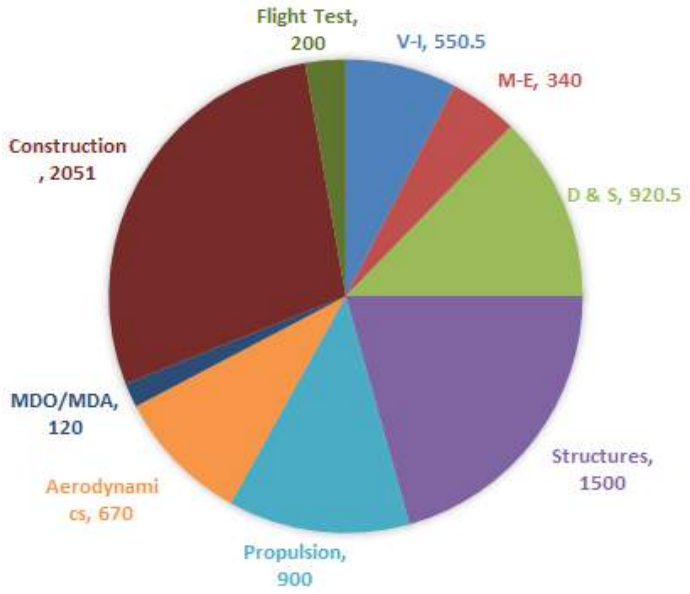


**Figure 3.4.1:** Breakdown of the budget spent

### 3.5. Risks and Risk Mitigation

One of the most important works of the project management is to assess all the risks concerned with the project. If the major risks are identified and mollification process is embedded in the schedule, then major problems can be avoided. Risks analysis with the industry standards, major risks were managed. Fig. 3.5.1 shows the risk analysis matrix.

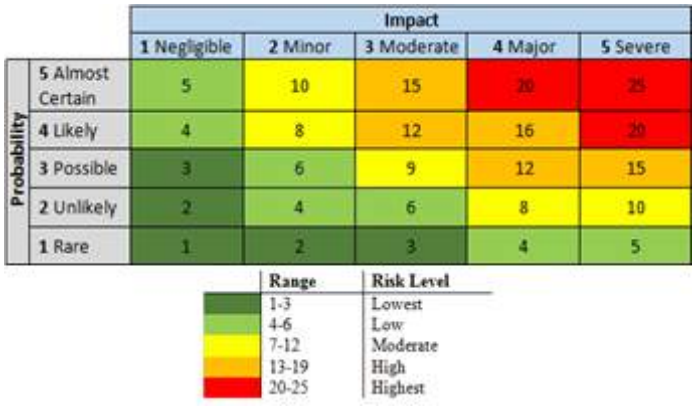


**Figure 3.5.1:** Risk Management Chart

There were several major risks identified. The first one was the delay of wind-tunnel

model and mold delivery. In order to avoid critical consequences due to this risk, work delegation to OML finalization were restructured. Also, usage of parts from past wind-tunnel models and machining of necessary molds in house were planned. Another risk identified was exceeding maximum take-off weight. In order to avoid this, very conservative baseline weight sizing, revisions to weight as project progresses through design and manufacturing, privatization of components and payload, and increase of thrust to compensate for weight were planned. Also, delay in R-UAV construction was one of the major risks. For this risk, machining of necessary molds in house, usage of the previous year's model for the flight test, and considering different companies for outsourcing workload were considered. Below is the structure of how the risk mitigation chart was composed using Fig. 3.5.1.

| | | Impact | Probability | Risk Level |
|---|---|---|---|---|
| Risk 1 | Delay in wind tunnel model delivery | Severe | Possible | High |
| Mitigation 1.1 | Re-structure all work delegation to OML finalization | Major | Likely | High |
| Mitigation 1.2 | Recycle parts from 2013 wind tunnel model | Minor | Possible | Low |
| Mitigation 1.3 | Send OML on time (one week before PDR) | Negligible | Likely | Low |

| | | Impact | Probability | Risk Level |
|---|---|---|---|---|
| Risk 2 | Exceeding R-UAV MTOW | Severe | Possible | High |
| Mitigation 2.1 | Conservative baseline weight sizing | Major | Rare | Low |
| Mitigation 2.2 | Each team updates weights during progress | Negligible | Likely | Low |
| Mitigation 2.3 | Change propulsive systems to provide more thrust-to-weight | Major | Rare | Low |
| Mitigation 2.4 | Prioritize components and payloads | Negligible | Possible | Lowest |

| | | Impact | Probability | Risk Level |
|---|---|---|---|---|
| Risk 3 | Significant delays in R-UAV molds | Severe | Possible | High |
| Mitigation 3.1 | Machine molds in-house | Major | Possible | High |
| Mitigation 3.2 | Use previous years models for flight tests | Major | Unlikely | Moderate |
| Mitigation 3.3 | Outsource to a different company at highest cost | Minor | Unlikely | Low |

| | | Impact | Probability | Risk Level |
|---|---|---|---|---|
| Risk 4 | Failure of vectored thrust system during Kirsten wind tunnel testing | Moderate | Possible | Moderate |
| Mitigation 4.1 | Use 3x3 wind tunnel to test standalone vectored thrust system | Minor | Likely | Moderate |
| Mitigation 4.2 | Convert wind tunnel test using flow-through nacelles | Minor | Possible | Low |

| | | Impact | Probability | Risk Level |
|---|---|---|---|---|
| Risk 5 | Non-operational vectored thrust system by scheduled flight test | Severe | Possible | High |
| Mitigation 5.1 | Prioritize all relevant team members to vectored thrust system | Major | Possible | High |
| Mitigation 5.2 | Retrofit off-the-shelf systems | Moderate | Possible | Moderate |

# 4. Conceptual Design

The class analyzed the project overviews, motivations, goals, and technical requirements. Following this process, the class "brainstormed" possible design solutions. As discussion evolved, it was decided to combine the best characteristics of recent years. Those characteristics are listed below

- Three-surface planform
- Closely side mounted propulsion systems
- Cranked wing
- Fuselage similar to 2014
- "Fishtail"

Upon the discussions held in class, the final choice for 2015 contributions to the development of tailless supersonic long range technology were decided to be

- Thrust vectoring for yaw control
- Wing tip rudders/ winglet for yaw stability and directional control

On a configuration that is representative of long-range supersonic configurations but low-risk in other areas:

- Use tails (horizontal and vertical plus canards)
- Use lessons from long-range supersonic development – High Speed Civil Transport (HSCT) key features.

In addition to those stated above, the class decided to implement technologies such as

- Engines / nacelles – below wing and fuselage.
- For the R-UAV – Electric propulsion
- An array of wing and tail control surfaces, but not as comprehensive as in 2014.
- Focus on low-speed characteristics
- Reduce weight and lengthen endurance with a larger payload capacity than in 2014
- Vectored thrust proof-of-concept
- Wingtip devices proof of concept (for lateral-directional control)

### 4.1. Comparison of the 2013 and 2014 Models

The comparison the several elements of 2013 and 2014 models are shown in Table 4.1.1.

**Table 4.1.1:** Comparison of 2013 and 2014 model

| | **2013** | **2014** |
|---|---|---|
| Inboard Sweep Angle, deg | 68 | 62.03 |
| Outer Sweep Angle, deg | 43 | 50.04 |
| Nominal Wingspan, in | 55 | 51.33 |
| Inboard Wingspan, in | 21.3 | 25.5 |
| Inboard Length, in | 49 | 46 |
| Fuselage-Wing-Tail Integration | One piece wing planform<br>Detachable nose<br>Nose-fuselage-tail connected by a square bar | One piece wing planform<br>Separate Nose<br>Separate tail |
| Availability of modular pieces | Ghost room in Kirsten Wind Tunnel | Box on 1st floor of Kirsten Wind Tunnel<br>Extra long 70" nose piece ready for testing |
| Constraints | Geometric IB sweep | Geometric IB sweep |
| Ease of notch area changes | Easier | Harder |
| Inboard/Outboard crank position | On the outer wind tunnel piece | At the conjoining transition between inboard and outboard wing pieces. |
| Disadvantages | Must construct entirely new fuselage | For our horizontal tail, must modify existing fuselage (probably constructing a new piece is best) |
| Yaw Control | Better due to higher sweep | |

# 5. Preliminary Design

## 5.1. Weight Analysis

### *5.1.1. Initial Weight Sizing*

Unlike previous years, there was no full-scale design to model the weight after. However, the weight of the R-UAV was limited based on requirements set forth by industry professionals.

The two immediate airworthiness requirements that set weight limitations were:

1. Minimum installed R-UAV static thrust to weight = 1.1x static T/W of a full scale MTOGW, assuming for a full-scale, the max static T/W = 0.55

2. The approximate full-scale aircraft wing loading between 50 - 80 psf

The most stringent weight restrictions were ultimately the performance characteristics of the aircraft. Specifics can be found in the performance section of this paper, however, in order to meet all requirements, such as take-off speed, take-off distance, and rate-of-climb gradient, the weight of the overall R-UAV was limited to a maximum of 36 lbf.

### *5.1.2. Initial Weights Analysis*

An initial weight estimate for the R-UAV was based on approximations on data from 2006 and 2014, as well as fixed weight data. The structural weight of the R-UAV was approximated using a weight breakdown from 2006. Each portion of the aircraft was separated based on percentage of weight per part compared to the overall weight. These percentages were then applied to the 2014 total weight. The extra step to apply the weight percentages to 2014 was taken due to the similarities between the 2014 and 2015 designs, as well as material choices. Information regarding the 2006 and 2014 weight breakdowns used in this analysis can be found in Appendix **??**. This methodology produced area weights of each part to represent the skin, internal structure, and other factors such as epoxy and paint. The calculated weight densities are listed in Table 5.1.1.

**Table 5.1.1:** Area densities for various components

| Part | Area Density (lbf/$ft^2$) |
|---|---|
| Fuselage | 0.559 |
| Wing | 0.465 |
| Canard | 0.808 |
| Vertical Tail | 0.483 |
| Horizontal Stabilator | 0.483 |
| Winglet | 0.0517 |

The size of the wind tunnel model was restricted based on the size of available parts from previous models, specifically the inboard wing of the 2013 design. It was desirable to keep the R-UAV as close to this scale as possible for continuity. A figure of scaling factors, where a scaling factor of 1 is equivalent to the size of the wind tunnel model, versus overall R-UAV weight is shown in Fig. 5.1.1. The plot shows two lines, one for the estimated weight based on the methodology described above and another with a correction factor of 15% to account for any unforeseen weight additions, such as primer or fasteners.

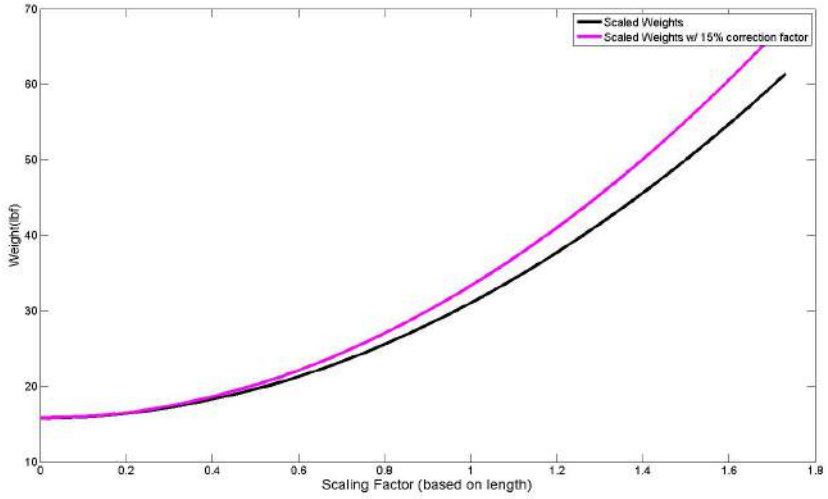


**Figure 5.1.1:** Comparison of potential weights for various scaling factors.

Four specific scales were analyzed: 77.5% of the length, 87.2% of the length, length of the wind tunnel model, and 112% the length of the wind tunnel model. The low and high scale values were analyzed as approximate lower and upper bounds based on the weight restrictions outlined previously. The length scale of 87.2% corresponds to a wing area identical to the wing area of the 2014 design, which could be used as an additional weight comparison. A list of the weights per scale is shown in Table 5.1.2.

**Table 5.1.2:** Initial Estimated Total Weight

| **Scale** | **Total Weight ,lbf** | **15 % Added Weight ,lbf** |
|---|---|---|
| Wind Tunnel | 31.1 | 33.4 |
| 77.5% | 22.5 | 23.4 |
| 87.2% | 27.4 | 29.2 |
| 112% | 35.0 | 37.8 |

It was determined based on this analysis that it was possible to build the R-UAV to the same size as the wind tunnel model.

### *5.1.3. Vertical Tail Sizing*

A handbook method from Raymer (REF) was used to size the vertical tail. This is shown in Eq. 5.1.1, which approximates the necessary area of the vertical tail using the main wing span, wing, and the distance from the tail quarter-chord to the wing quarter-chord $l_{VT}$.

$$S^{VT} = \frac{c_{VT} b_W W_{SW}}{l_{VT}} \tag{5.1.1}$$

$c_{VT}$ values chosen conservatively to be .08 and .07 since long-fuselage aircraft with higher wing loading require larger values. Using VLAERO+, an initial (non-ESDU) MAC value was found to be 30.44in. Similarly, the wing span was found to be $b_W = 56$in, the separation distance $l =_{VT}= 120$in. Wing Area was 1184.38 $in^2$. The vertical tail geometry values calculated are shown in Table 5.1.3.

**Table 5.1.3:** Initial usable vertical tails for wind tunnel testing

| Tail Volume Coefficient | Area of Tail, $in^2$ |
|---|---|
| .07 | 79 |
| .08 | 105 |

### *5.1.4. Horizontal Tail & Canard Sizing*

The horizontal tail was initially sized conservatively based on requirements to trim the aircraft over an acceptable flight envelope and to rotate the aircraft upward upon takeoff. The aircraft was defined in VLAERO+ and the horizontal tail was sized up until the aircraft could be trimmed; this capability was defined within the constraints of low deflection angles (less than 10°) and a static margin of at least 6

It was decided early-on in the preliminary design process to use a three-surface configuration (canard, horizontal stabilizer and flaps) for longitudinal stability and control. Canards and an all-moving horizontal tail (referred to henceforth as the "stabilator") would need to sized so that they could be used in conjunction and provide the longitudinal control necessary to pitch the aircraft up at takeoff conditions and to efficiently provide control at cruise conditions. To completely specify control deflections necessary for a given trim condition, the ratio of canard to stabilator deflection ('gear ratio') was defined. The trimmability of the design at cruise conditions was assessed by plotting trimmed control deflections versus gear ratio $R$ at various airspeeds and confirming that reasonable control deflections were sufficient for trim over some range of small gear ratios. This was a particularly stringent requirement at low trimmed airspeeds with higher angles of attack. Such a plot is shown in Fig. 5.1.2, which shows viable deflections at a gear ratios between -1 and -2 (with the stabilator deflected negatively) for a worst-case scenario C.G. location at a low trimmed airspeed.

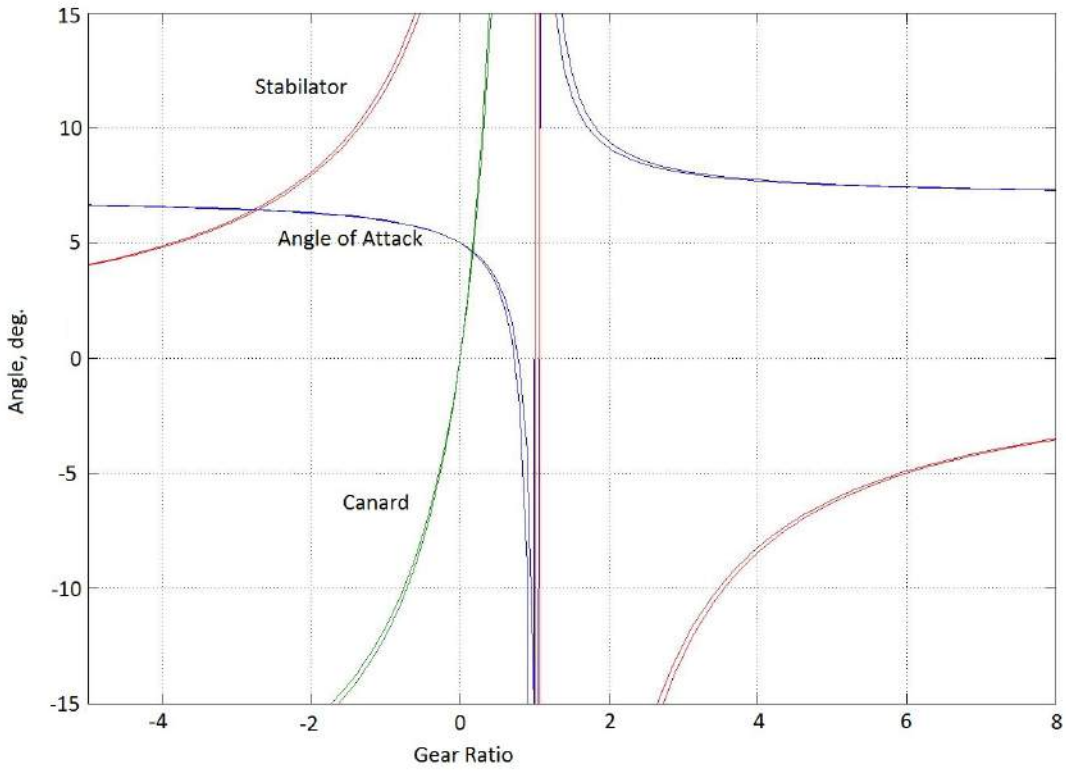


**Figure 5.1.2:** Trimmed control deflections and angle of attack as functions of canard-stabilator gear ratio at 55mph.

The sizes and locations of all lifting surfaces also had to be selected to produce a favorable neutral point which would allow a feasible C.G. location given the required 6% static margin. The gear ratio was deliberately kept small such that both control surfaces were used; it was desired that the canard not stall too readily nor be responsible for providing a disproportionately large amount of the aircraft's pitching control authority.

VLAERO+ was used extensively to select the size and location of the canard and stabilator. The control effectiveness ($\partial c_M/\partial \delta$ was taken from VLAERO and used in a Matlab script to calculate the necessary deflections of the stabilator and canard to meet certain trim and rotation requirements. The resulting control surface sizes for wind tunnel testing are given in Table 5.1.4

**Table 5.1.4:** Initial usable all-flying surface sizes for wind tunnel testing.

| Configuration | Canard Area, $in^2$ | Stabilator Area, $in^2$ |
|---|---|---|
| Smaller Canard | 36 | 95 |
| Larger Canard | 47 | 62 |

### *5.1.5. Winglet Sizing*

A strategy for reducing the area of non-lifting surfaces on the R-UAV was to use all-flying winglets to achieve both directional stability and control. The winglets were chosen to be all-flying in order to reduce the number of complicated parts that would need to be designed, tested, and constructed. Designing all-flying winglets would prove to be a significant technical challenge, but was deemed to be worth the effort if they could be proven to be effective. The winglets were designed vertically instead of with dihedral to further reduce the structural and control complications, even though they would not help in reducing induced drag.

The winglets were sized as shown in Table 5.1.5 in VLAERO+ to fulfull the requirements that the airplane be able to trim while maintaining a 10° crab-angle and counter the yaw imbalance from a single-engine-out scenario.

**Table 5.1.5:** Winglet sizes for wind tunnel testing.

| Winglet Area, $in^2$ | $C_{n\delta}$ |
|---|---|
| 12 | 0.000236 |
| 16 | 0.000351 |
| 20 | .000486 |

### *5.1.6. Aileron Sizing*

The ailerons were initially sized using a combination of historical plots from Raymer (REFERENCE) and from the performance of past years' models. Typically, according to Raymer, ailerons should span 50% to 90% of the wingspan. Using the conservative percentage of 50% of the span and the following Fig. 5.1.3, aileron sizes were calculated.

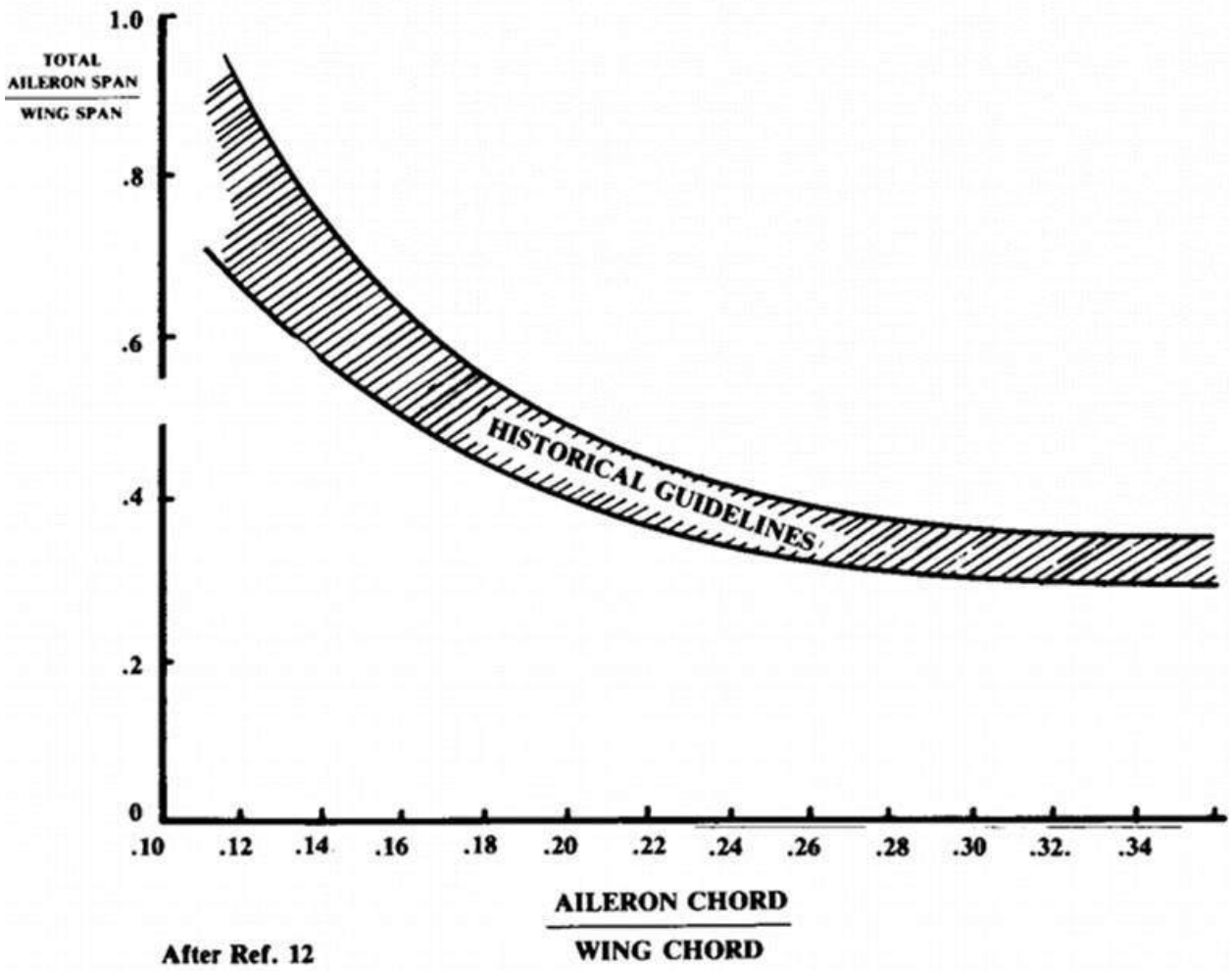


**Figure 5.1.3:** Historical aileron guidelines found from Raymer used to size RUAV ailerons.

The total aileron area necessary was projected to be 75 inches using Fig. 5.1.3. In order to provide versatility for wind tunnel testing, the ailerons were split into two equally-wide sections. This resulted in a total of three separate testable control surfaces on each main-wing trailing edge including the inboard flaps.

## 5.2. Propulsion

### *5.2.1. Initial Design*

The first task of the propulsion team was to select the propulsion system which would be used on the final R-UAV. The two main choices for the propulsion system were an electric ducted fan (EDF) and a turbine. After considering the advantages and disadvantages of each, the electric ducted fan was selected. A table of the pros and cons of each system is shown below in Table 5.2.1. The electric ducted fan would be more reliable, simple, and safe. A turbine would be more complex and also come with more rules and regulations which

would cause more delays during testing. Perhaps most importantly, three electric ducted fans were already available from the 2013 project as well as test data from the previous years. The 2015 aircraft would be of comparable size and have similar mission requirements to the 2013 and 2014 aircraft, which led the propulsion team to believe that these electric ducted fans would provide sufficient thrust.

**Table 5.2.1:** Propulsion System Pros and Cons

| **Type of Propulsion System** | **Pros** | **Cons** |
|---|---|---|
| Electric Ducted Fan | • Easy to operate<br>• Less noise<br>• Less emissions<br>• Safe and reliable<br>• Data available from 2013/2014<br>• 2013 EDFs were available to use | • Less thrust generated<br>• Batteries are heavy and will not reduce their mass as fuel would in flight |
| Turbine | • More thrust generated<br>• More similar to a full-scale design | • More complex<br>• Increased risk and fire hazards<br>• Difficult to use and test |

The EDFs were manufactured by Stumax Aircraft. They are model SM100-45DF 100 mm diameter EDFs. They are the same model of EDF used during the 2013 and 2014 projects. The specifications for these fans are shown below in Table 5.2.2. It can be seen that the static thrust available from one of these EDFs is 11-14.3 lb. If each EDF produced 11 lb of thrust, the R-UAV would generate 22 lb of thrust total. If the R-UAV weighed 36 lb, as was the goal for the aircraft, it would have a thrust to weight ratio of 0.611. This would be sufficient for our aircraft, especially because this would be our minimum value.

**Table 5.2.2:** Electric Ducted Fan Specifications

| | |
|---|---|
| Electric Ducted Fan | EDF Stumax SM100-45DF |
| Manufacturer | Stumax Aircraft |
| Power Input, $W$ | 3500-5500 |
| Fan Swept Area, $cm^2$ | 62.64 |
| Static Thrust, $lbf$ | 11-14.3 |
| Max Efficiency | 92-94% |
| Max RPM | 40000 |
| Shroud Diameter, $mm$ | 103 |
| Inside Diamter, $mm$ | 100 |
| Shroud Length, $mm$ | 100 |
| Overall Length, $mm$ | 200 |
| Weight, $lbf$ | 1.564 |

Two of these EDFs are mounted in the two nacelles of the aircraft to provide thrust. Each are connected to an electric speed controller and two six cell, lithium-polymer batteries. A picture of one of the EDFs is shown below in Fig. 5.2.1.

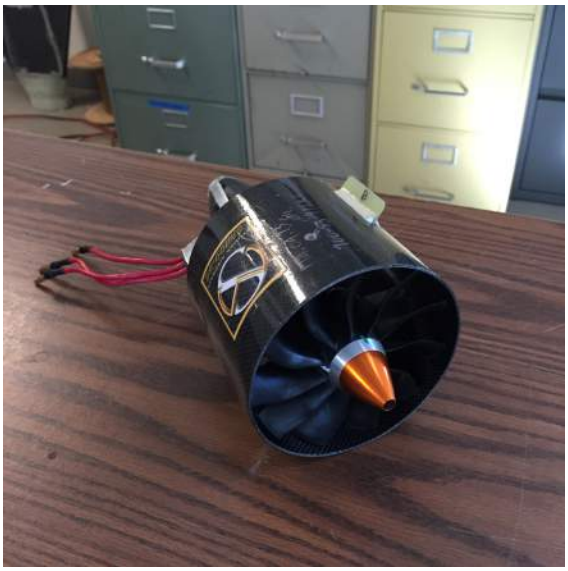

**Figure 5.2.1:** Stumax Electric Ducted Fan

## 5.3. Structural Layout

### *5.3.1. Wing Structure Optimization*

#### 5.3.1.1. Purpose

The optimization was used at this stage to develop a stronger, more scientific reasoning for the structural layout selected. Although the optimization did not give an accurate amount

overall (because of incorrect, non-varying material properties) it was a quick method for seeing what sections were highly loaded and which were not.

5.3.1.2. Loads Many of the load cases were outlined by the RFP supplied by Chet and Eli. These include the 4.5g lift and 3g landing load cases. Other loads applied that were not specifically included in the RFP were those such as a general drag load. In order to apply the lifting load in a spanwise distribution, an equation was used to describe the load on the bottom surface. Because aerodynamics had not yet developed an equation for the lift distribution, values from 2013 were used, in part because of wing similarities between 2015 and 2013. The linear interpolation for the lift distribution can be seen in Figure 5.3.1 below. It should be noted that the same profile was used, but the weight of the aircraft was set to $36lbf$.

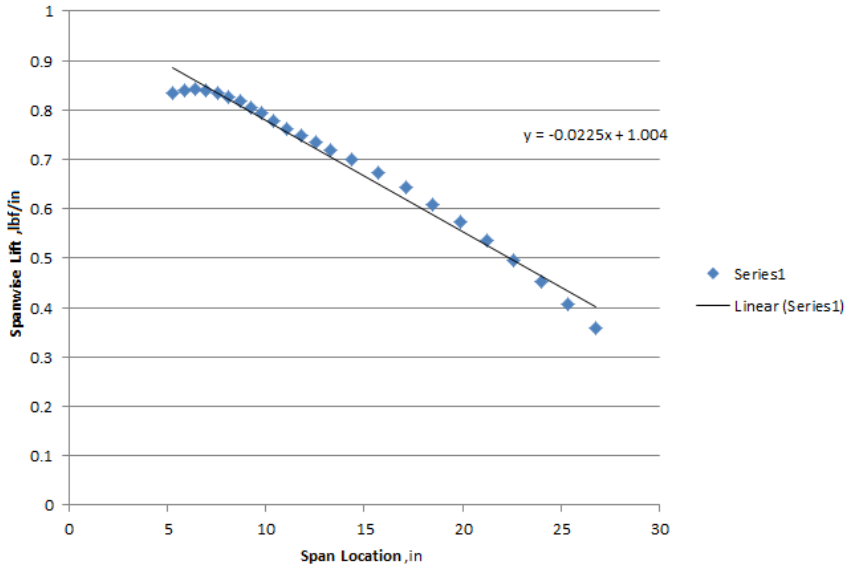


**Figure 5.3.1:** The graph above shows the lift distribution for the 2013 wing planform. Note that this goes from the centerline of the aircraft, and not the root of the wing.

In theory, integrating across the length of the wing would yield 1/2 of the total weight of the aircraft. Therefore, for the 4.5g lifting load the equation used to describe the lift can be seen below in Equation 5.3.1. Note that the notation of that equation is how it is accepted in Femap.

$$LiftingLoad = 4.5 * (1.004 - (0.0025 * !Y)) \tag{5.3.1}$$

Then, the load can just be set to a unit load in the Z-direction, but will be a function of the location along the span. It should be noted this method does not give a chordwise variation for the load. In the future it would be advantageous to get a function for the pressure on both the top and bottom surface as a function of the X and Y locations.

For the 3g landing, a simple inertial load was applied equal to 3 times the acceleration of gravity (applied in the Z-direction). Then, a landing gear load equal to 3/2 of the aircraft weight was applied near to elements at the location where the main, rear landing gear would

attach on that side. In the future in might be useful to apply mass loads where the EDFs would be located under the wing.

For the general drag load, a fraction of the lifting load was applied in the X-direction, due to the fact drag is a function of the lift being generated. Therefore, the drag load was selected to be 1/7 of the lift distribution equation because the lift-to-drag ratio was estimated to be around 7. This is likely a very rough method for getting a drag estimate, nevertheless it gave the optimization software an X-directional load to consider that was a fraction of the lift. This is another case where pressure distribution as a function of X and Y would be ideal.

#### 5.3.1.3. Constraints

The wing was fixed at the root face/inboard face. This did not appear to generate any divergence issues.

#### 5.3.1.4. Geometry and Meshing

The model was split such that the upper and lower surfaces of the wing were independent (as well as inboard and outboard). This allowed for the lifting to be applied on the bottom surface. In the case of the model that had the control surfaces removed, small holes were placed near the leading edge of said control surface to simulate the mounting. Then, a fraction of the lifting load was applied in each of the holes to simulate the load contribution from the control surfaces.

The auto-meshing capabilities present in Femap were used to mesh the solid with 3D, solid elements (tets). The mesh was refined to a very fine amount; a max element size in the range of 0.1in per side. For the most part, the mesh quality was acceptable by Femap's standards (surface mesh quality), but there were patches of poor elements around the trailing edge where the thickness was near-zero. In the future it would be best to trim the trailing edge to make it thicker and easier to mesh properly.

#### 5.3.1.5. Results

The results of the optimization runs can be seen in Figures 5.3.2 and 5.3.3 below.

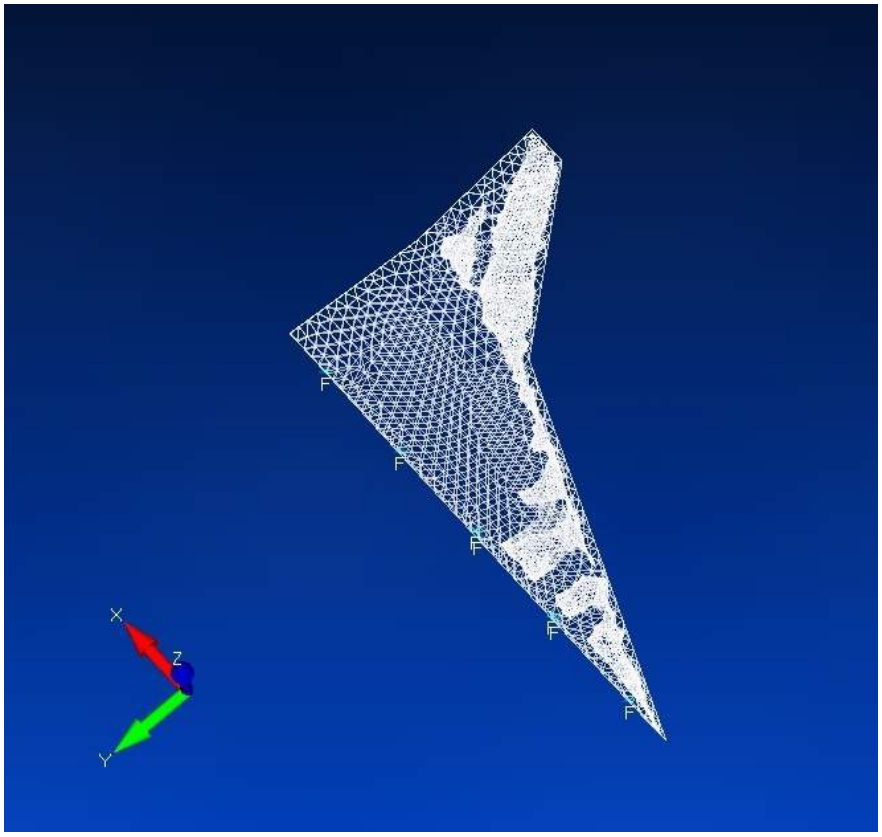


**Figure 5.3.2:** The image above shows the results of the first optimization run with the control surfaces/area of the surfaces providing structural assistance, which they would not do in reality.

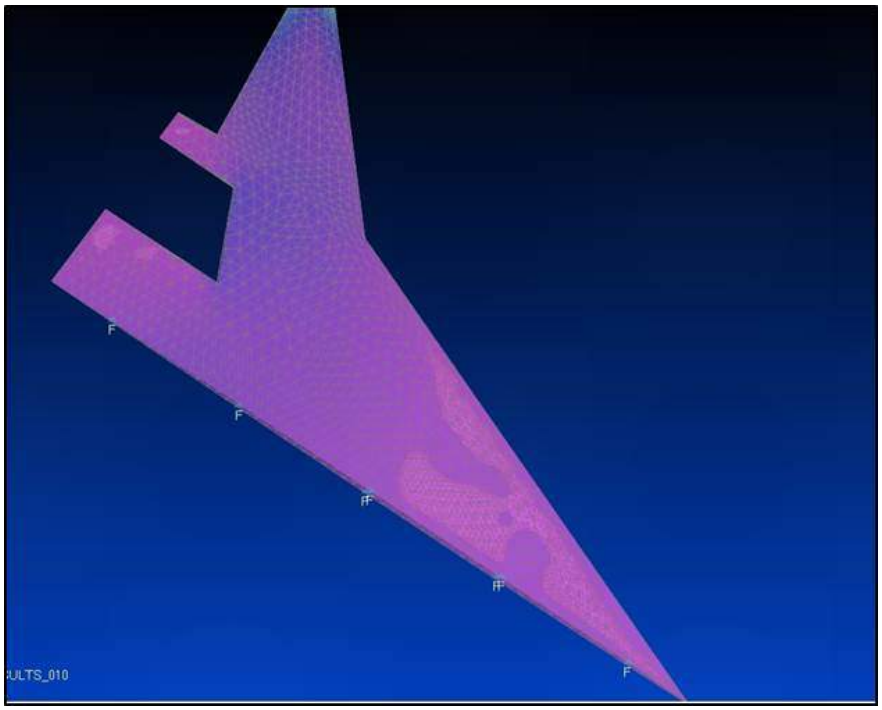

**Figure 5.3.3:** The image above shows the results of the second optimization run with control surfaces removed.

Note that the areas of lighter color, the bright white and pink in Figure 5.3.2 and 5.3.3, respectively, show the locations where material would be removed with minimal adverse effects to the stiffness of the wing. For the second run, which is more analogous to reality, the results indicate that less material can be used near leading edge area of the inboard wing section. Also, an area at the trailing edge of the inboard wing requires lesser material. From this, we might reason that running a primary spar/stringer just in front and tangent to the inboard control surface might carry the brunt of the wing loading most effectively (in terms of weight). Because of the tapering of the lifting load along the span, it would likely be best to taper the spar accordingly along the span. The exact size of the elements in the wing are something that would need to be calculated with accurate material properties and sizes.

### *5.3.2. Rapid Prototyping*

In the early stages of the design, it was useful to quick prototype various concepts. Taking full advantage of 3D printing capabilities available on campus, it was possible to develop and test PLA control surface designs, actuation devices, and bulkheads. One test that made it to production was the prototyping of the 3D printed bulkheads with removable, pinned hatches. The demonstration part can be seen below in Figure 5.3.4 below.

**Figure 5.3.4:** The image above shows a 3D printed bulkhead that was mocked up in a short fuselage section made with 2014's molds.

Other designs were not as successful, or at least did not make it to the final aircraft, such a 3D printed flaps and keyed, direct-drive servo linkages. Nevertheless, the ability to rapid prototype early in the design phases was crucial in validating the idea.

### *5.3.3. Summary of Preliminary Structural Design*

- Using simplified finite element models to get a grasp of how where the loads were naturally concentrated was very useful in developing an efficient structure. Being able to use optimization to get an even better idea of how to arrange the internal structure, and in a more refined manner than just running simulations over and over again, proved useful in justifying decisions in the later design stages.
- Rapid prototyping was a new venture that proved extremely useful for a project like this. Being able to take a Solidworks concept from part file to completion in a few

hours provided the opportunity to test innovative solutions to old problems.

#### *5.3.4. Recommendations for Future Preliminary Structural Design*

- Depending on the existing structural knowledge of the given type of aircraft/wing planform, it might be more useful to invest time running optimization on components rather than full assemblies. Nevertheless, optimization is a useful tool and has a clear place in design.
- Rapid prototyping should occur as quickly as possible and as frequently as possible. There should be no hesitation to model, manufacture, and test all sorts of new concepts and ideas. This allows for the design to be more creative while maintaining a level of completeness that is expected.
- Master design spreadsheets are extremely useful throughout the process, but can definitely be started as early as the preliminary design. If each member has their own spreadsheet it is much easier to document work, change values and update calculations, and develop presentable data than it would be with the classic pen-and-paper method. Despite dozens of attempts to encourage members to utilize these tools, they were not adopted. An example spreadsheet can be found in *Z/2015/Teams/Structures/Lead*.

### 5.4. Aerodynamics

#### *5.4.1. Airfoil Selection*

The process of selecting an airfoil for the wing had to take into account that we are using 2013 inboard wing for the wind tunnel test, so this will be a constraint. This inboard planform has the NACA 66-204-45 airfoil at the root and the NACA 66-206-45 airfoil at the crank. However, in our model we have a larger wing area because we have reduced the notch area. For the wind tunnel test we are going to extend the wing just as a flat plate. In the next image **??** we can see how the initial airfoil at the crank looked and how the wind tunnel model cross section at the crank looks.

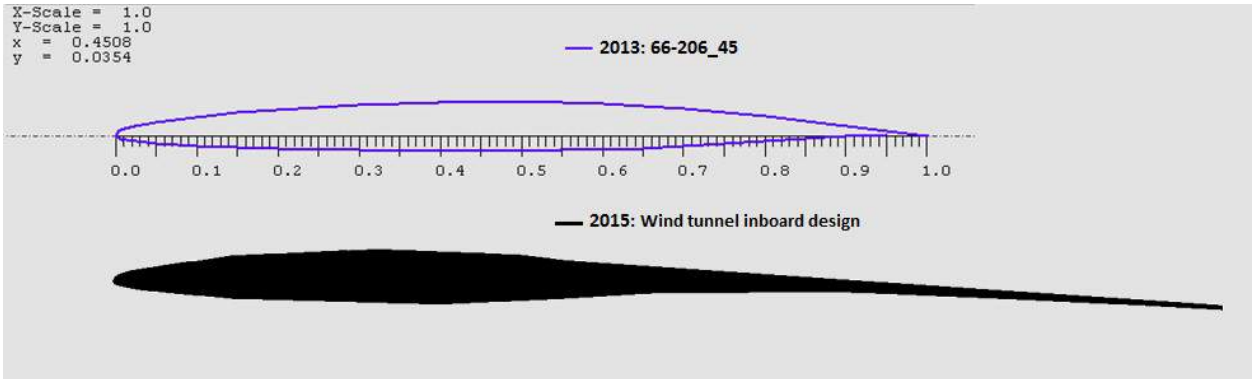


For the actual R-UAV, we need the airfoil that best matches the wind tunnel model. Then, at the root we will use the NACA 66-204-45 and at the tip of the inboard we will use the NACA 66-205-45, to account for the larger chord and keep the maximum thickness.

To make sure that the wind tunnel model was accurate, we made an analysis of the wind tunnel model cross section at the crank that is shown in the previous image and the selected NACA 66-205-45 airfoil for the R-UAV. We performed 2-D CFD simulations for subsonic regime and the study revealed optimistic wind tunnel results.

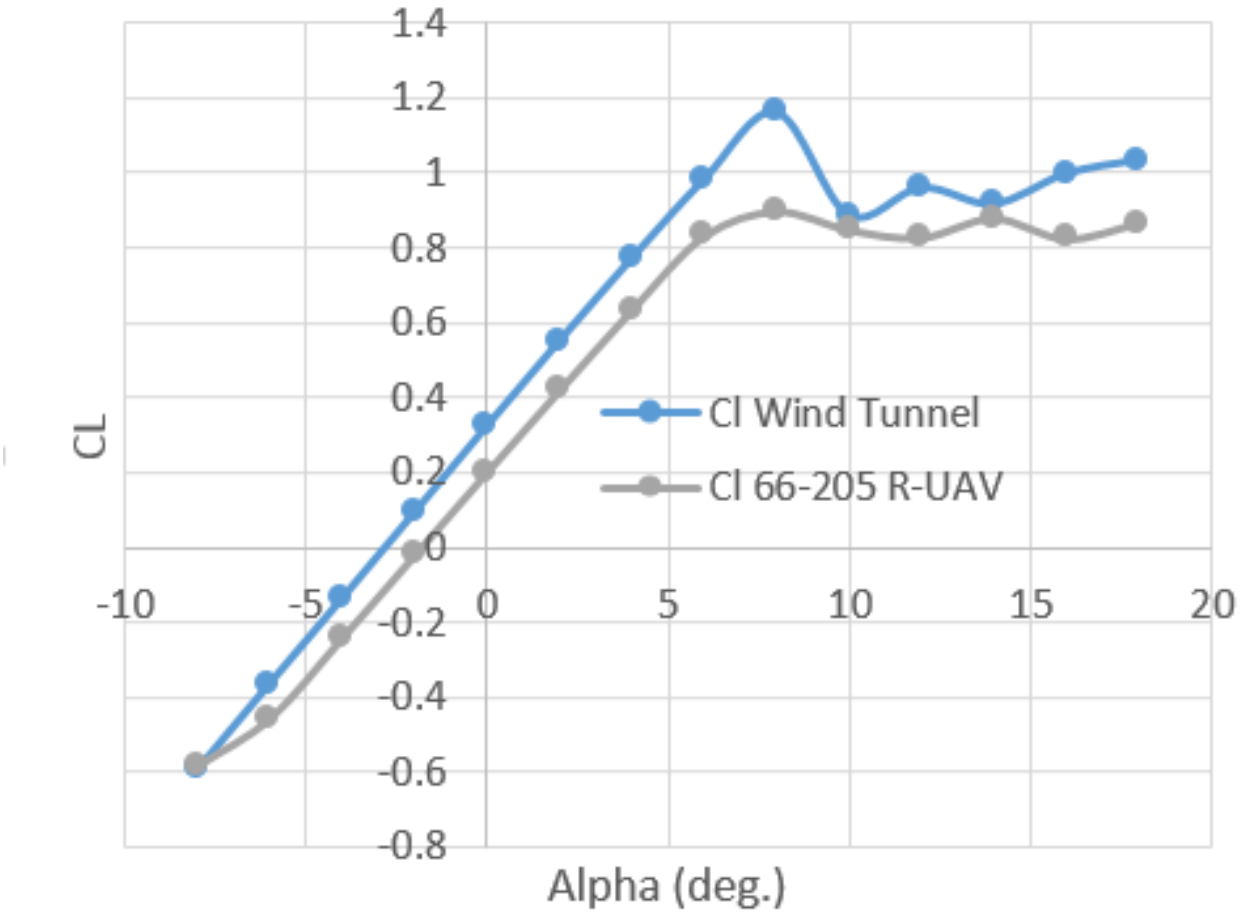


**Figure 5.4.1:** Comparison of $c_L$ between wind tunnel model and R-UAV.

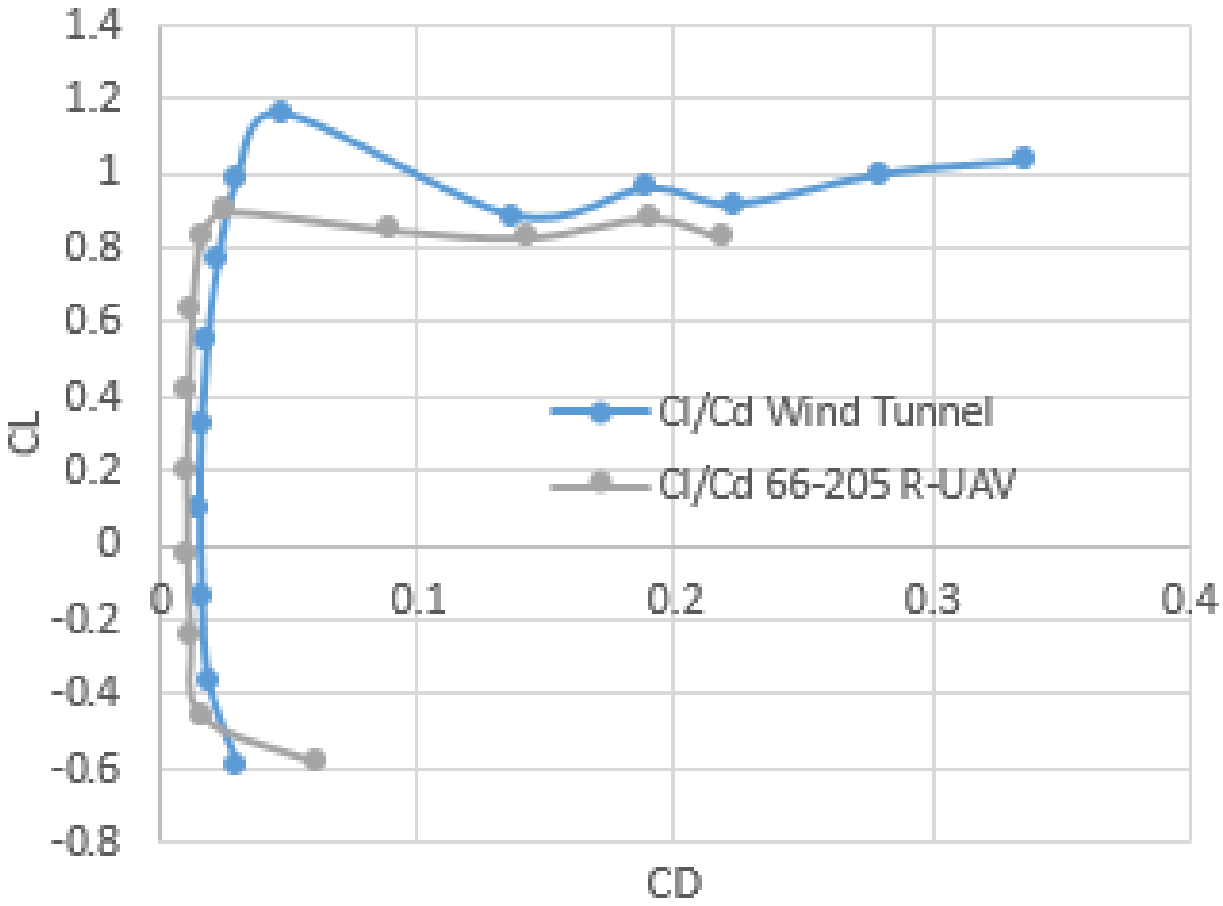


**Figure 5.4.2:** Comparison of drag polar between wind tunnel model and R-UAV.

To select the airfoil for the outboard wing we had to take into account that this region will be outside of the Mach cone. This means that a supersonic sharp airfoil will be needed to prevent the formation of a detached bow shock in front of the airfoil. In a supersonic regime, rounded subsonic airfoils increase the wave drag of the bow shock. In the other hand, supersonic airfoils are inefficient at low speeds, what means that high-lift devices will be used to generate enough lift at subsonic speeds. To find the desired airfoil for the outboard wing, NACA 64,65 and 66 series were tested in STAR-CCM+ in subsonic and supersonic regime. The usual range of 3.5

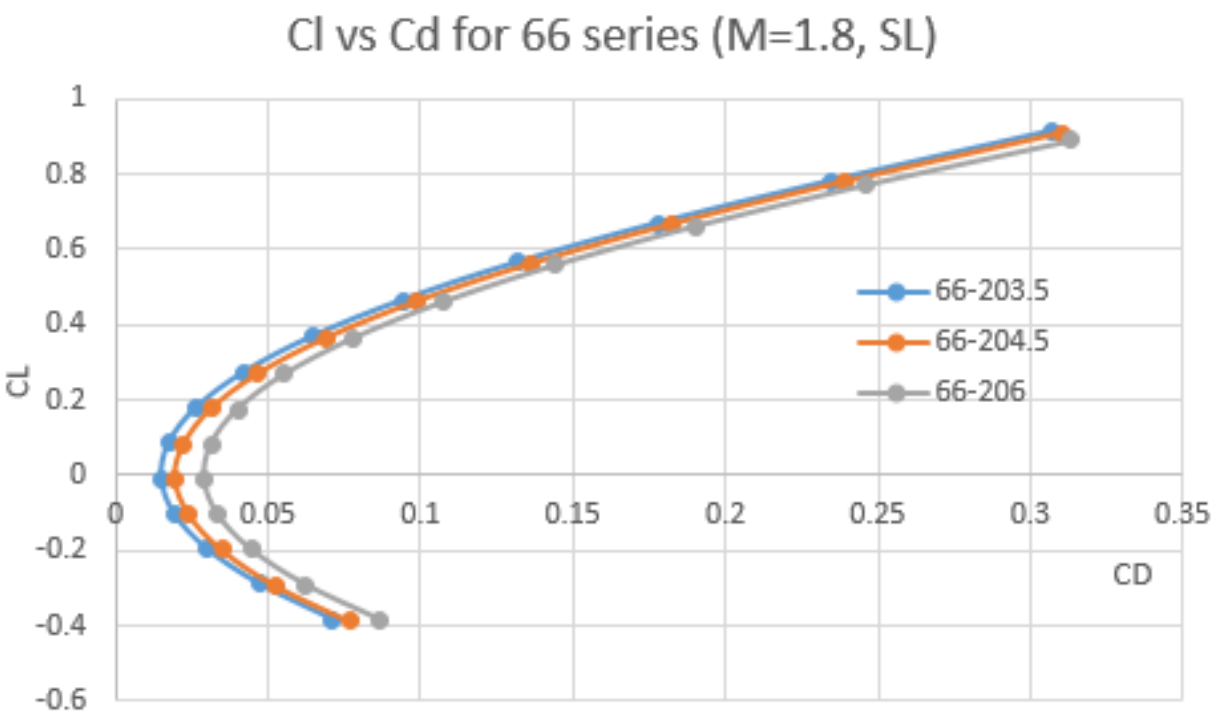


**Figure 5.4.3:** Thickness-to-chord ratio analysis for 66 series.

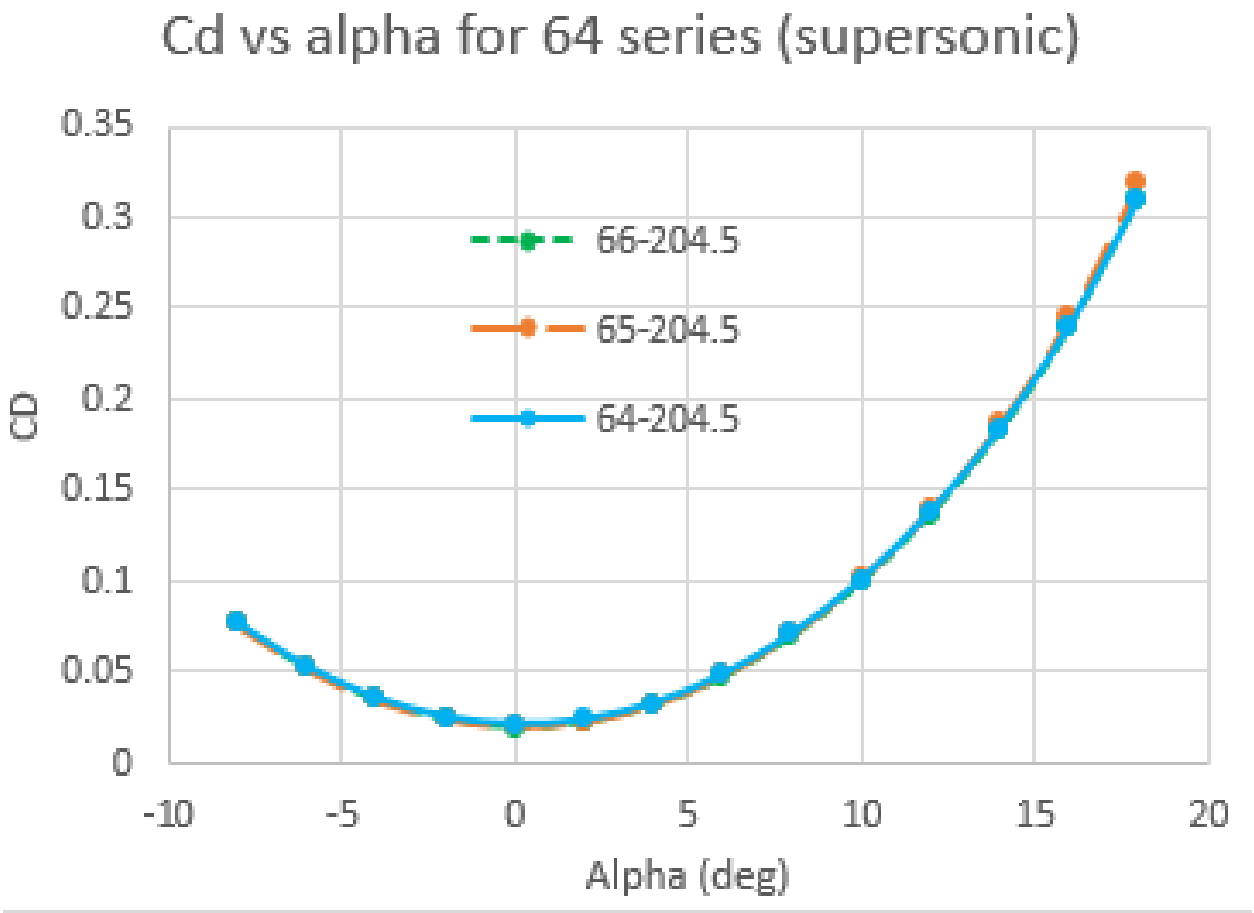


**Figure 5.4.4:** $c_D$ analysis for 64, 65 and 66 series for 4.5% $\frac{t}{c}$.

To match with the tip of the inboard, the root of the outboard will use the NACA 66-205-45 airfoil. For the tip, the same airfoil would be desired, but as the chord is decreasing, the maximum thickness will probably not be enough to meet the structural requirements needed. Because of this, the thickness to chord length ratio at the tip will be in the range of 6% to 8%.

### *5.4.2. Area Ruling*

#### 5.4.2.1. Introduction

The compressibility effects that appear during supersonic flight lead to the formation of shock and expansion waves. The associated drag created is called wave drag and is the major contributor to the supersonic drag build up. In the early fifties Whitcomb experimented with several different axisymmetric bodies and wing-body combinations in a transonic wind-tunnel [1]. He discovered that the drag created on these shapes was directly related to the change in cross-sectional area of the vehicle from the nose to the tail. The shape itself was not as critical in the creation of drag, but the rate of change in that shape had the most significant effect. Stated differently, the wave drag is related to the second-derivative (or curvature) of the volume distribution of the vehicle. During the 1950's there was an intense focus to

optimized volume wave drag. It was found that a Sears-Haack body produces the least amount of drag for a given volume or maximum radius.

#### 5.4.2.2. Procedure

The area rule seeks for the change in volume distribution that best approaches the Sears-Haack body by evaluating the vehicle cross sectional area along the Mach planes.

During sonic conditions the Mach planes are perpendicular to the direction of travel, for higher Mach numbers there is an infinite number of planes deflected to the free stream Mach angle for different positions along the Mach cone. For this purposes, previous years STAR-CCM+ macro was modified in order to compute Mach 1 and Mach 1.8 area distributions. A cylindrical free-stream was used with a mesh resolution of about 0.5 million cells.

For the Mach 1 case the frontal area report was directly used for different locations along the x-axis of the airplane, then it was compared with a reference area obtained by sectioning the freestream region upstream of the airplane. With this method, the local cross sectional area is computed. For the Mach 1.8 case 8 equally spaced Mach planes are created for each x-position along the Mach cone, an averaged area is taken and finally compared with a reference value to obtain the local area. Figure **??** shows a Mach plane for one of the last x locations.

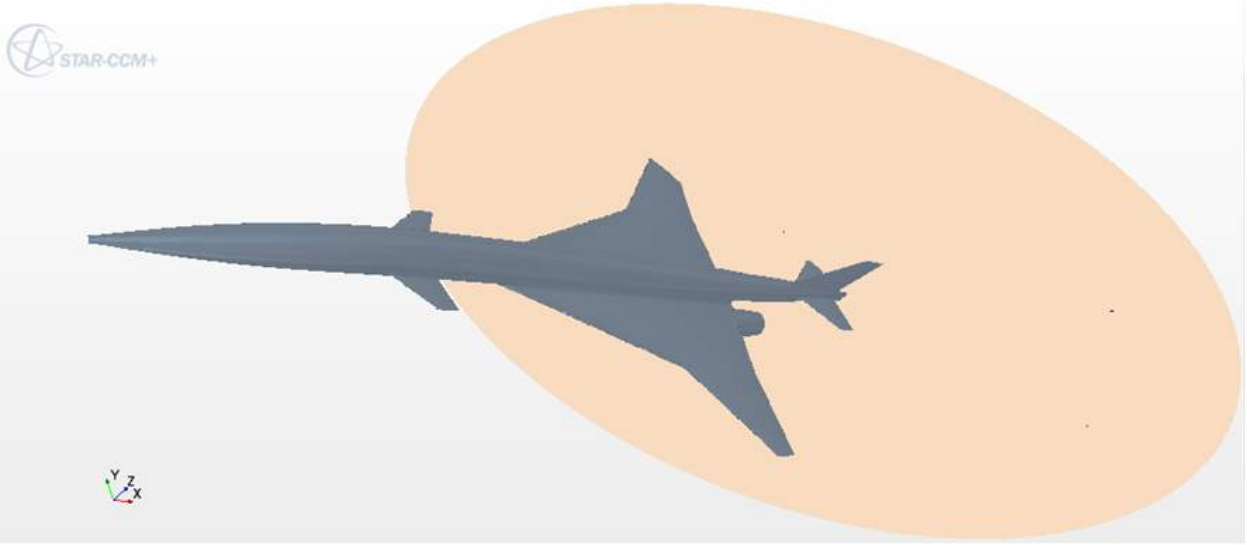


**Figure 5.4.5:** Geometry scene showing one of the Mach plane forming the Mach cone for the flight condition Mach = 1.8.

#### 5.4.2.3. Design Analysis

Area rule effects play an important rule on the design planform and must be taken into account early in the design process to account for appropriate modifications, this would help to avoid major design revisions in the future.

Throughout the early design process the cross-sectional area of the aircraft was monitored and changes were made to try and keep the results as close to a Sears-Haack body configuration as possible for the Mach 1 and 1.8 cases. The major design modifications performed early in the design process to account for area rule were the wing body intersection, engine

location along x-axis, fairing size, airfoil tapering, and fore body shaping, particularly, fuselage was accordingly narrowed where it joins the wings, the nacelles where properly moved forward, different tapering rations where evaluated.

The results of the mentioned design iterations resulted on an optimized design which cross sectional area distribution for Mach 1 and Mach 1.8 are shown in Figs. **??** and **??**.

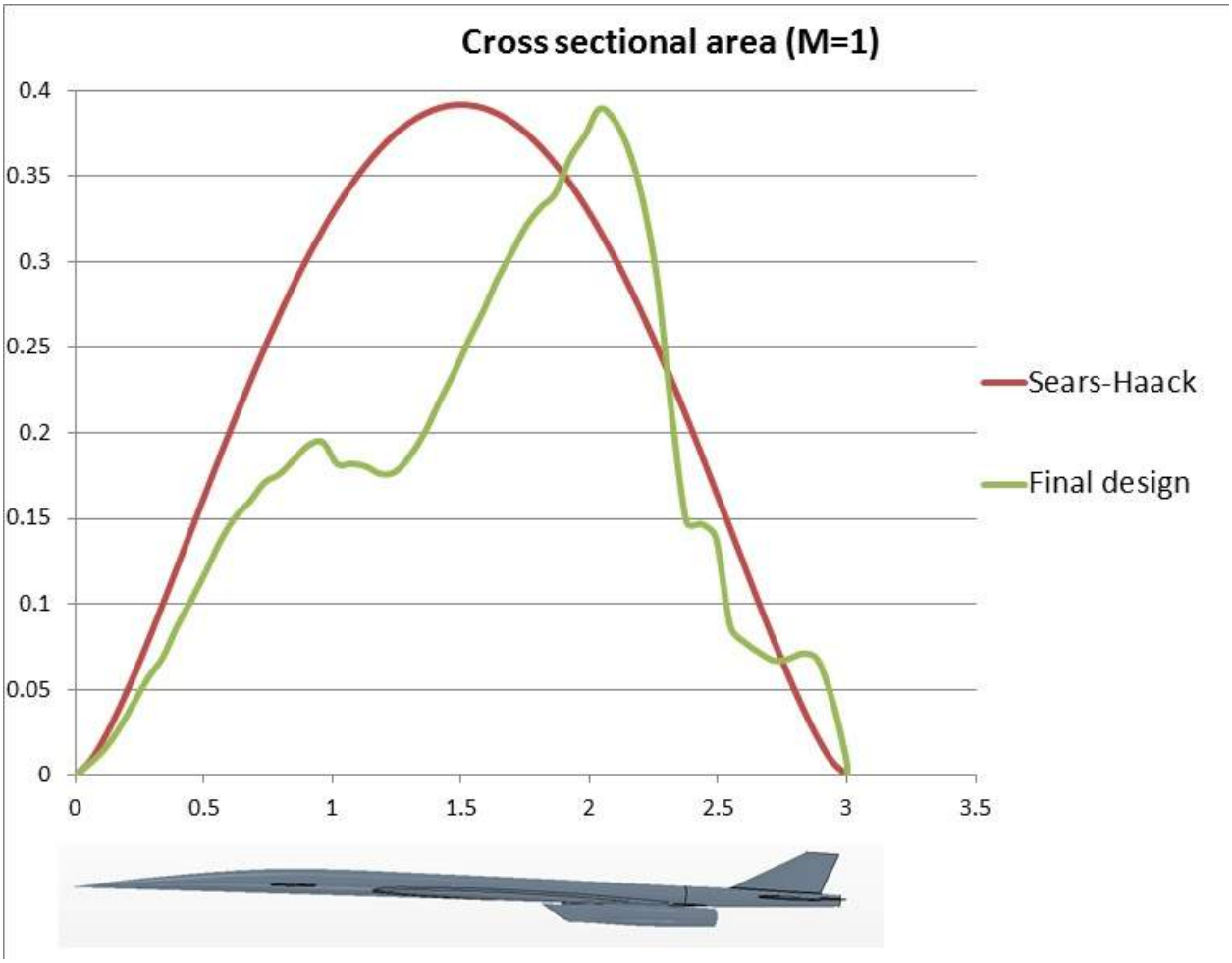


**Figure 5.4.6:** Cross-sectional area distribution along the x-axis.

Although the design cruise Mach number was set to 1.8, it is important to consider the area distribution at lower Mach numbers because the aircraft was required to fly through these speeds before it reached Mach 1.8. Since wave drag reaches its maximum during sonic conditions, the area distribution at Mach 1 was also examined. It can be seen that the actual distribution approaches the idealized Sears-Haack closely. The chosen configuration that includes an empennage section and a "fish" tail will allow for reduced wave drag for speeds close to Mach 1. A comparison with previous year's configurations is shown in Figure **??**. Finally, it can be seen that for M=1.8 the area distribution is flattened out reducing the cutoff around the nozzles, as a result a moderate drop in area is achieved allowing for optimum performance at the design cruise Mach number.

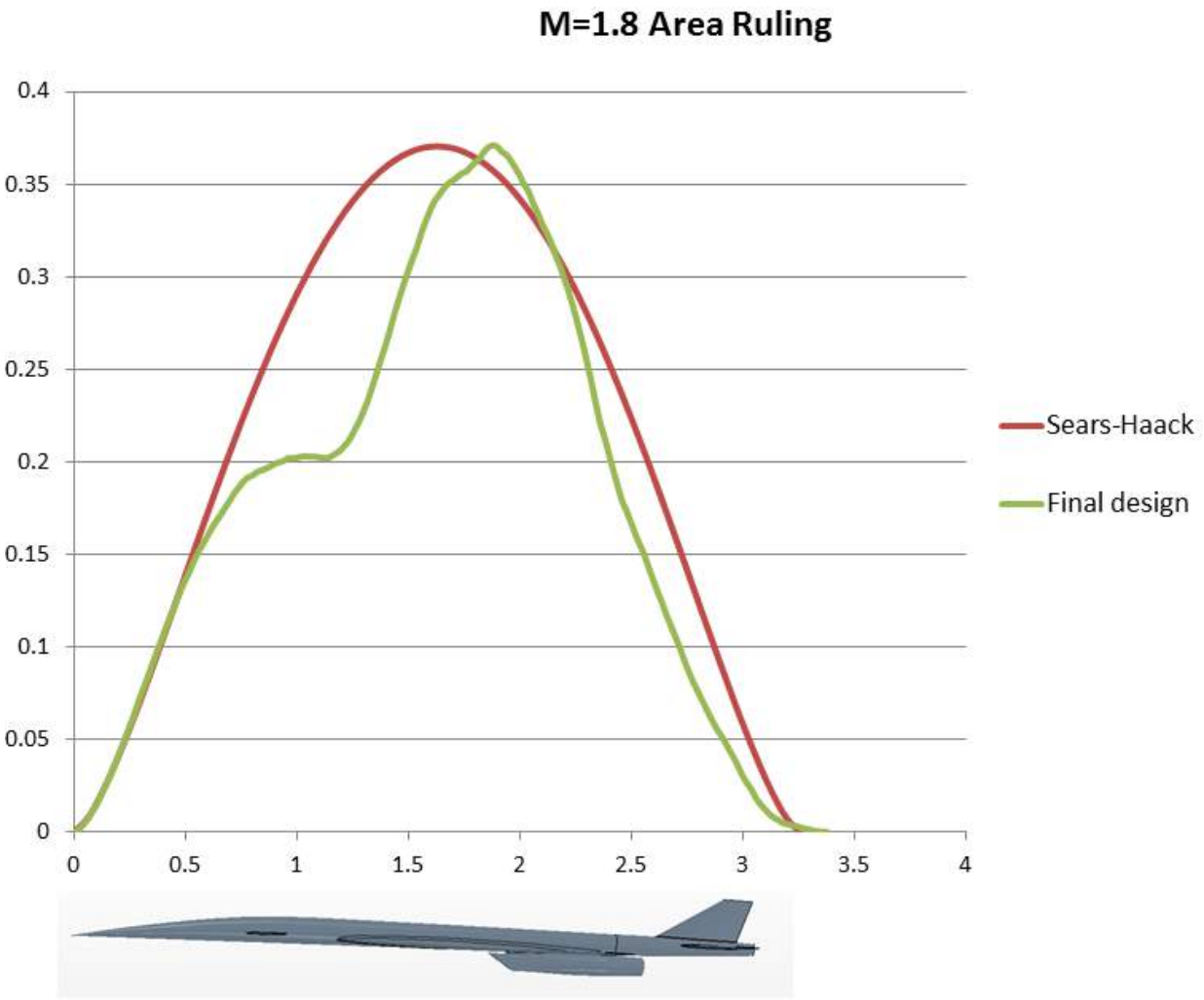


**Figure 5.4.7:** Mach cone average cross sectional area distribution along the x-axis for cruise Mach number of 1.8.

### *5.4.3. Drag Buildup*

The parasitic or zero-lift drag on the RUAV was calculated analytically using empirical methods from Raymer. Contributions from part of the aircraft to the frictional, form, and interference drag on the aircraft were calculated as shown in Eq. 5.4.1.

$$c_{D,0} = \frac{\Sigma(c_{f,c} F F_c Q_c s_{wet,c})}{s_{ref}} + c_{D,misc} + c_{D,LP}. \tag{5.4.1}$$

The flow is assumed to be turbulent over all surfaces, so the skin friction coefficient as calculated in Eq. 5.4.2 using a Reynolds number calculated in Eq. 5.4.3 using the MAC for the wings and control surfaces and the total length of the fuselage.

$$c_f = \frac{0.455}{(\log_{10} R)^{2.58}(1 + 0.144M^2)^{0.65}} \tag{5.4.2}$$

$$Re = \frac{\rho V l}{\mu} \tag{5.4.3}$$

The form factor for different sections of the airplane were calculated using Eqs. 5.4.4, 5.4.5, and 5.4.6.

$$FF = [1 + \frac{0.6}{(s/c)_m}\frac{t}{c} + (\frac{t}{c})^4][1.34M^{0.18}(\cos\Lambda)^{0.28}] \tag{5.4.4}$$

$$FF = 1 + \frac{60}{f^3} + \frac{f}{400} \tag{5.4.5}$$

$$FF = 1 + \frac{0.35}{f} \tag{5.4.6}$$

For the fuselage, the form factor is a function of the ratio of its length-to-cross-sectional area as shown in Eq: 5.4.7.

$$f = \frac{1}{d} = \frac{1}{\sqrt{(\frac{4}{\pi})A_{max}}} \tag{5.4.7}$$

Other sources of drag included leakage and protuberance drag and other miscellaneous sources such as the landing gear were also factored into the calculation. The L&P drag was assumed to be only 5

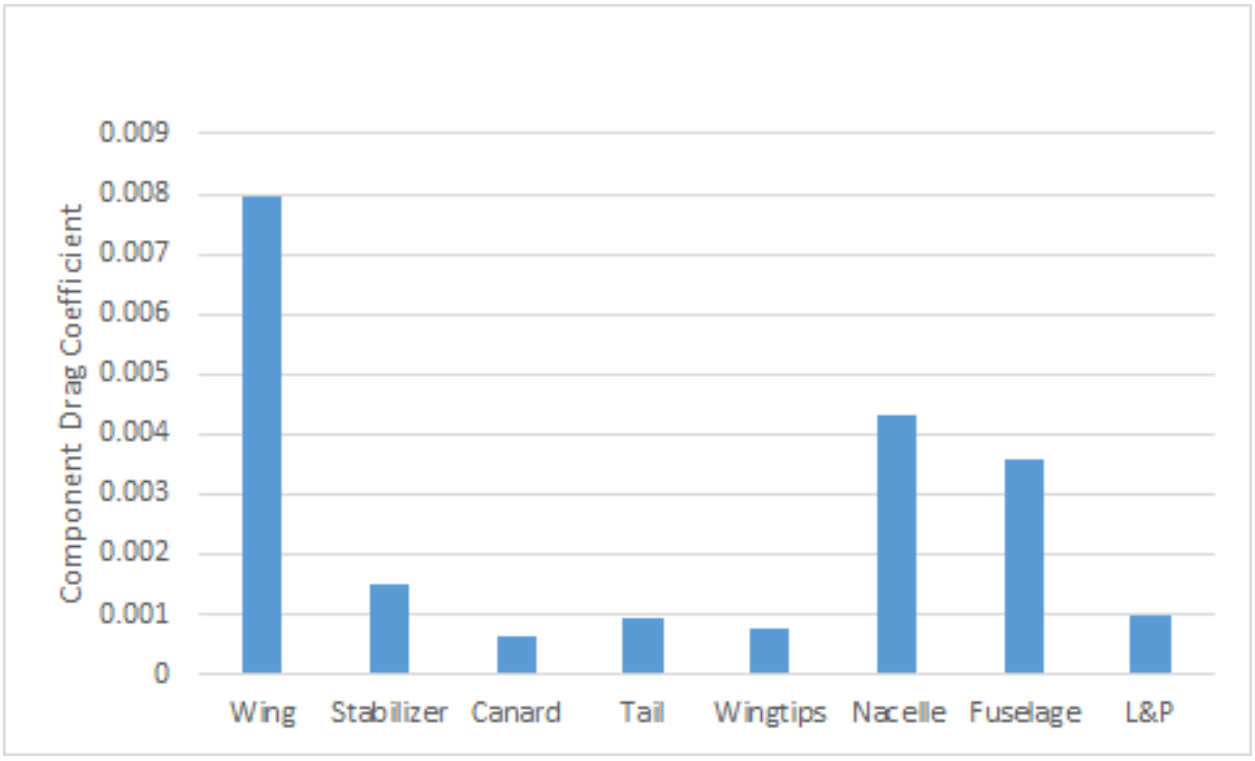

### *5.4.4. Hinge Moments*

In order to determine the size and strength of the servos required to deflect the control surfaces on the R-UAV it was necessary to calculate their hinge moments. The moment that the hinge needs to overcome is dependent on the moment arm as shown in Eq. 5.4.8.

$$x_{HA} = x_{AC} - x_{HL} \tag{5.4.8}$$

The aerodynamic center of the control surface was calculated using pressure data from VLAERO results for the canard and stabilator, while for the rest of the surfaces the aerodynamic center was estimated to be located at about the quarter chord line of the control surface. As shown in Eq. 5.4.9 the hinge moment coefficient is dependent on the lift curve slope of the control surface, which was estimated for the surfaces using results from VLAERO.

$$c_{m,hinge} = \frac{x_{HA}}{MAC} c_{L,AC} \tag{5.4.9}$$

The resulting hinge moment is determined by the dynamic pressure and maximum expected angle of deflection of the control surface as shown in Eq. 5.4.10. The resulting hinge moments are calculated in Table **??**.

$$M_{hinge} = q s_c MAC c_{m,hinge} \alpha \tag{5.4.10}$$

| **Surface** | $x_{HA}$ | $s_c$,in$^2$ | $M_{hinge}$,lb $\cdot$ ft |
|---|---|---|---|
| Canard | 0.25 | 18.60 | 0.70 |
| Stabilator | 0.30 | 52.7 | 2.38 |
| Aileron | 0.19 | 40.30 | 0.88 |
| Flap | 0.30 | 42.30 | 0.95 |

### *5.4.5. Spanwise Loads*

#### 5.4.5.1. Cruise Loads

The spanwise normal and axial loadings at various angles of attack were plotted for the final configuration using the accumulated force table command in STAR-CCM+. This feature allow the use pressure of and shear forces to directly compute force data in the normal and axial directions, so it was not necessary to correct with angle of attack. In order to get $c_n$ and $c_a$ (normal and axial force,respectively) data was normalized with respect to dynamic pressure and local chord length.

In Figs. **??** and **??** these coefficients are plotted with respect to the y-axis location of the airplane, $y = 0$ is the fuselage reference line.

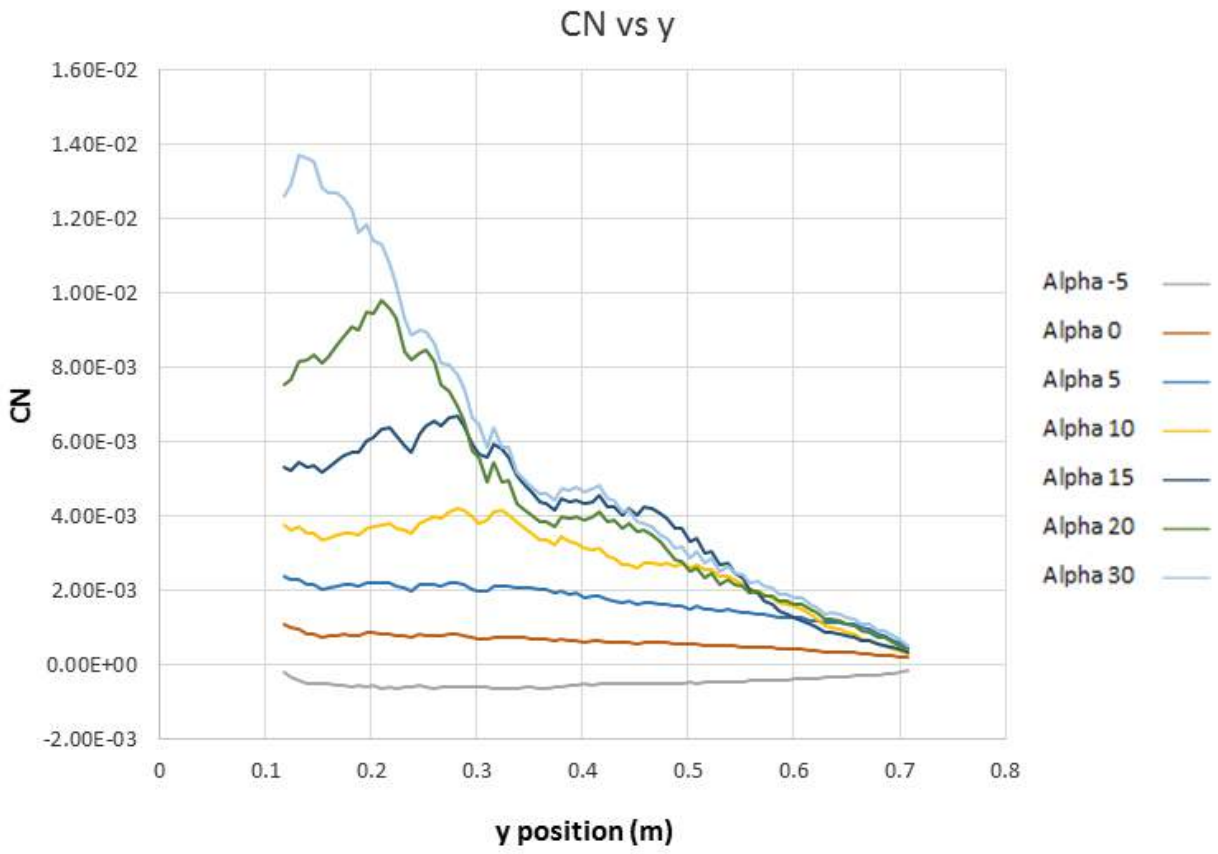


**Figure 5.4.8:** Normal force section coefficient distribution along the wingspan at different $\alpha$.

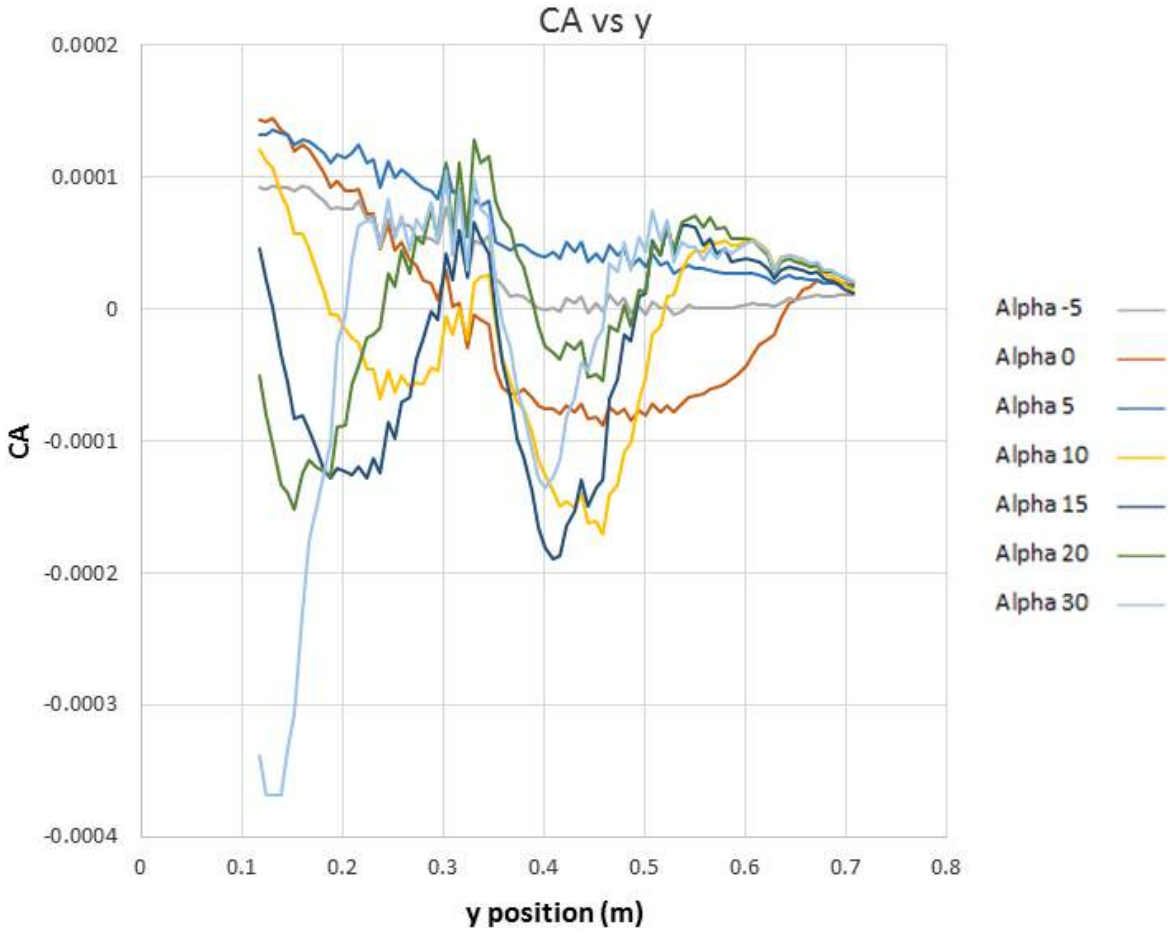


**Figure 5.4.9:** Axial force section coefficient distribution along the wingspan at different $\alpha$.

Note that the wing experiences positive normal force for values of alpha close to 0°and starts becoming negative when the alpha is about -5°. For angles of attack greater than 20°it can be seen that oscillation in the $c_n$ and $c_a$ values starts to appear and $c_n$ does not increase anymore at the outboard due to stall characteristics. In addition it can be noticed a sharp change in both, normal and axial forces that occurs right at the crank position, particularly, the axial force for low angles of attack goes from positive values towards the root to very small values or even negative values towards the tip. For angles of attack greater than 15°a sharp increase in $c_a$ can be noticed in Fig. **??** which will lead to a shear force in the x-y plane of the airplane, the integration of the normal and axial force data along the wing span can be used to obtain shear and bending moment diagrams for the wing.

#### 5.4.5.2. Design Loads

According to 2015 R-UAV Airworthiness Requirements the limit maneuver loads for the R-UAV must be one level more stringent for the corresponding full-scale aircraft's mission. As described on FAR 25.337, the minimum "utility category" maneuvering load factor for bizjet/Mil Handling Qualities Class 2 aircraft is set to 4.4g, a conservative value of 4.5g was used for this project. In order to simulate a 4.5g flight condition in STAR-CCM+ it was assumed that the performance characteristics of the R-UAV were enough to perform

a sustained 4.5g turn at a constant altitude and constant airspeed, this requires a bank angle of about 77°. A combination of lift coefficient and airspeed was selected in order to obtain a loading of 4.5g. An airspeed equal to the maneuver airspeed or corner airspeed shown in the V-N diagram on Figure **??** was selected, this is defined as the stall speed for standard configuration at 4.5g and corresponds to 33.50 $^{m}/_{s}$. The corresponding CLmax was selected since it was known from previous STAR-CCM+ runs for the standard configuration. The sectional normal and axial coefficients normalized with the local chord length along the wingspan are shown in Fig. **??**. Only wing regions were considered for the calculations, pressure and shear forces were considered, $y = 0$ is the fuselage reference line.

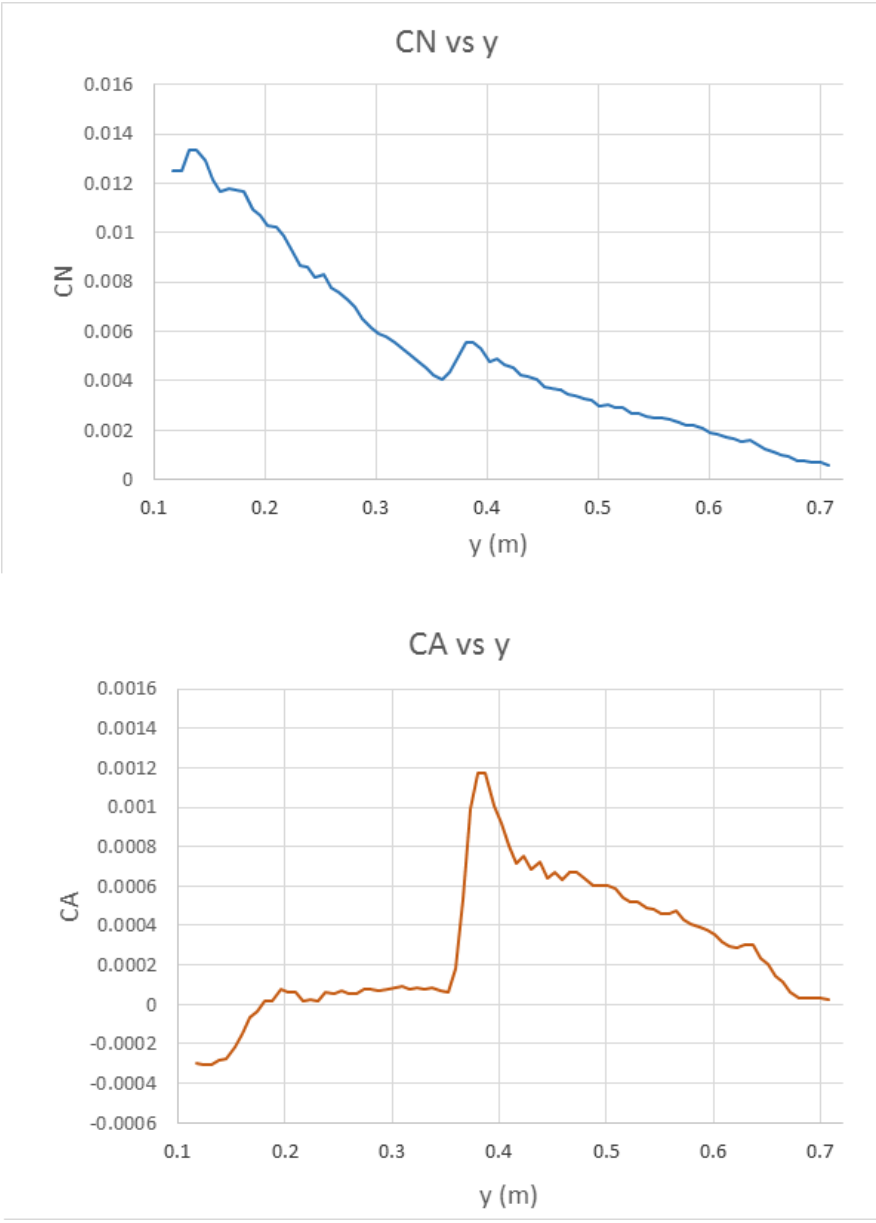


**Figure 5.4.10:** Normal and axial force section coefficient distribution along the wingspan for a 4.5g sustained turn flight condition.

### *5.4.6. Wind Tunnel Codes*

Matlab codes were developed to obtain the longitudinal and lateral-directional static stability derivatives based on the wind tunnel data runs. This has been used to evaluate the independent effect on the derivatives of the different control surfaces, as well as the changes in the whole plane configuration. The inputs that the codes need are the angle of attack you want the derivatives at and the run numbers to import the wind tunnel data needed to obtain the derivatives. The default of the code gives the derivatives at zero degrees of sideslip angle but that can be changed easily if another sideslip angle is desired. The codes were based on 2014 wind tunnel data to be able to have them ready for when our wind tunnel test was done. In the next table we can visualize what each code will provide.

**Table 5.4.1:** Static Stability Codes to Obtain Derivatives

| | Code name | Description |
|---|---|---|
| **Longitudinal** | Wind_Tunnel_Longitudinal_Analyzer | Longitudinal derivatives |
| | | Simple interpolation |
| | Wind_Tunnel_Elevator_Analyzer | Longitudinal elevator effect |
| | | Subtraction and interpolation |
| | Wind_Tunnel_Canard_Longitudinal_Analyzer | Longitudinal elevator effect |
| | | Subtraction and interpolation |
| **Lateral** | Wind_Tunnel_Lateral_Analyzer | Lateral-directional derivatives |
| | | Interpolation |
| | Wind_Tunnel_Flaperon_Analyzer | Lateral flaperon effect |
| | | Subtraction and interpolation |

Once this was ready, as 2015 design does not have all the previous complicated control surfaces, we implemented the changes needed to use the codes for our plane. Then, we ran the codes with the data from the wind tunnel test. The codes used and the derivatives obtained are shown in the next tables.

**Table 5.4.2:** Static Longitudinal Derivatives for the Baseline Configuration

| **Configuration W1+B1+N+LE4+V+C2+H2** | | | | | |
|---|---|---|---|---|---|
| **Longitudinal derivatives** | | | | | |
| Type | **Wind_Tunnel_Longitudinal_Analyzer** | | | | |
| RUNS | 212 | | | | |
| Comments | $\beta$=0, q=6.27 | | | | |
| $\alpha$ | CD,$\alpha$ | CL,$\alpha$ | CM15,$\alpha$ | CM20,$\alpha$ | CM25,$\alpha$ |
| 3 | 0.13585 | 2.94234 | -0.5107 | -0.36192 | |
| 12 | 0.7807 | 2.46093 | -0.25423 | -0.12668 | |

The derivatives were obtained for alphas of 3°and 12°because these values are near the cruise angle of attack and the alpha that provide a $c_L$ around 0.6. Thanks to these codes, we were able to obtain all the values shown above in a much reduced amount of time.

Table generated by Excel2LaTeX from sheet 'Sheet1'

**Table 5.4.3:** Static Longitudinal Derivatives for the Different Control Surfaces

| **Configuration W1+B1+N+LE4+V+C2+H2** | | | | | |
|---|---|---|---|---|---|
| **Longitudinal derivatives** | | | | | |
| Type | **Wind_Tunnel_Stabilator_Analyzer** | | | | |
| RUNS | 224 & 233 (No C2) | | | | |
| Comments | $\beta$=0, q=6.27, -15 (+ def, - moment) | | | | |
| $\alpha$ | CLs,$\delta$s | CDs,$\delta$s | CM15s,$\delta$s | CM20s,$\delta$s | CM25s,$\delta$s |
| 3 | 0.35347 | 0.03093 | -0.5269 | -0.50934 | |
| 12 | 0.32972 | -0.027 | -0.49158 | -0.4752 | |
| Type | **Wind_Tunnel_Flap_Analyzer** | | | | |
| RUNS | 136 & 137 | | | | |
| Comments | $\beta$=0, q=6.27, -21/-21 (+ def, - moment) | | | | |
| $\alpha$ | CLf,$\delta$f | CDf,$\delta$f | CM15f,$\delta$f | CM20f,$\delta$f | CM25f,$\delta$f |
| 3 | 0.54043 | 0.09611 | -0.20826 | -0.18106 | |
| 12 | 0.48344 | 0.16728 | -0.18304 | -0.15776 | |
| Type | **Wind_Tunnel_Canard_Analyzer** | | | | |
| RUNS | 199 & 200 | | | | |
| Comments | $\beta$=0, q=6.27, 10/10 (+ def, + moment) | | | | |
| $\alpha$ | CLc,$\delta$c | CDc,$\delta$c | CM15c,$\delta$c | CM20c,$\delta$c | CM25c,$\delta$c |
| 3 | -0.03777 | 0.01997 | 0.20797 | 0.20613 | |
| 12 | -0.00067 | 0.03342 | 0.04343 | 0.04374 | |

Table generated by Excel2LaTeX from sheet 'Sheet1'

**Table 5.4.4:** Static Lateral Derivatives for the Different Control Surfaces

| **Configuration W1+B1+N+LE4+V+C2+H2** | | | | | | | |
|---|---|---|---|---|---|---|---|
| **Lateral derivatives** | | | | | | | |
| Type | **Wind_Tunnel_Winglets_Analyzer** | | | | | | |
| RUNS | 150-154 & 156-160 (C5 instead of C2, dihedral) | | | | | | |
| Comments | $\alpha$=0, 10, 20, 24, 32 / b=0 / q=6.27 / 5/5 vs 10/10 (+def, - moment) | | | | | | |
| $\alpha$ | CN15w,$\delta$w | CN20w,$\delta$w | CN25w,$\delta$w | CR15w,$\delta$w | CR20w,$\delta$w | CR25w,$\delta$w | CYw,$\delta$w |
| 3 | -0.02537 | -0.02362 | -0.02171 | -0.00512 | | -0.00502 | 0.07793 |
| 12 | -0.01108 | -0.00989 | -0.0087 | 0.00769 | | 0.00807 | 0.05147 |
| Type | **Wind_Tunnel_Aileron_Analyzer** | | | | | | |
| RUNS | 214, 215, 217 & 180-182 | | | | | | |
| Comments | $\alpha$= 0, 10, 24 / b=0 / q=6.27 / -20/20 (+def, - moment) | | | | | | |
| $\alpha$ | CN15a,da | CN20a,da | CN25a,da | CR15a,da | CR20a,da | CR25a,da | CYa,da |
| 3 | -0.00534 | -0.00515 | -0.00493 | -0.12162 | | -0.12159 | 0.0081 |
| 12 | 0.01561 | 0.01583 | 0.01605 | -0.09753 | | -0.09741 | 0.00924 |

**Table 5.4.5:** Static Lateral Derivatives for the Baseline Configuration

| **Configuration W1+B1+N+LE4+V+C2+H2** | | | | | | | |
|---|---|---|---|---|---|---|---|
| **Lateral derivatives** | | | | | | | |
| Type | **Wind_Tunnel_Lateral_Analyzer** | | | | | | |
| RUNS | 213-218 | | | | | | |
| Comments | $\alpha$=-10, 0, 10, 20, 24, 32 / b=0 / q=6.27 | | | | | | |
| $\alpha$ | CN15,$\beta$ | CN20,$\beta$ | CN25,$\beta$ | CR15,$\beta$ | CR20,$\beta$ | CR25,$\beta$ | CY,$\beta$ |
| 3 | 0.09957 | 0.08777 | 0.07622 | -0.06894 | | -0.06992 | -0.50069 |
| 12 | 0.08133 | 0.07417 | 0.06711 | -0.1047 | | -0.10662 | -0.3075 |

## 5.5. Construction

### *5.5.1. P-38 Lightning*

Prior to the construction of R-UAV, two different construction projects were completed in order to familiarize the students to the skills required to build R-UAV and the system used in the R-UAV. The first project which was mainly done in the Winter Quarter was construction of the scaled down version of the Lockheed Martin P-38 Lightning. The purpose of it was to familiarize students with construction process specifically molding, lay ups, 3D printing, laser cutting, hot wire-cutting and the integration and actuation of avionics and instrumentation. The P-38 was made out of fiberglass, plywood and foam. Fig. 5.5.1 shows the airplane fully integrated.

**Figure 5.5.1:** Finished P-38 model.

### *5.5.2. Foamie*

Before starting to construct the R-UAV, the group built a prototype called "foamie". The main purpose of the foamie, shown in Fig. 5.5.2, was to validate and verify the feasibility of integrating vectored thrust to 2015 R-UAV. Due to deadlines, the foamie from the previous year was altered to meet the needs of 2015 design. Some of the changes that were done to 2014 foamie are the outboard wing to meet 2015 wingspan, smaller canards and smaller vertical tail. Also additional features were added to the foamie including: winglets, horizontal stabilator, nacelles and vectored thrust. The following figure shows the foamie integrated.

# 6. Testing

## 6.1. UWAL Testing

### *6.1.1. Wind Tunnel Model*

The wind tunnel model was mostly constructed by AeroTec although many of the parts of the wind tunnel model were manufactured in house due to budget and time constraints as well as unexpected delays from AeroTec. The parts that were manufactured with metal are: flaps, ailerons, canards, stabialtor and vertical tail. In addition, the idea of 3D printing leading edge droops and thrust vectoring paddles was explored. The model is shown in Fig. 6.1.1.


**Figure 5.5.2:** Foamie of 2015 model

**Figure 6.1.1:** Wind Tunnel Model

### *6.1.2. Initial Buildup and Flow Visualization*

Testing began with runs on just the wing and subsequently the wing-fuselage combination. The plane was then incrementally built up by adding components test by test. These initial tests were used primarily for flow visualization, baseline pitch- and yaw-stability testing, and baseline aerodyanmic forces and moments to be subtracted from other data to find the contributions of other components. The flow visualization for the winglets can be seen below in Fig. 6.1.2.

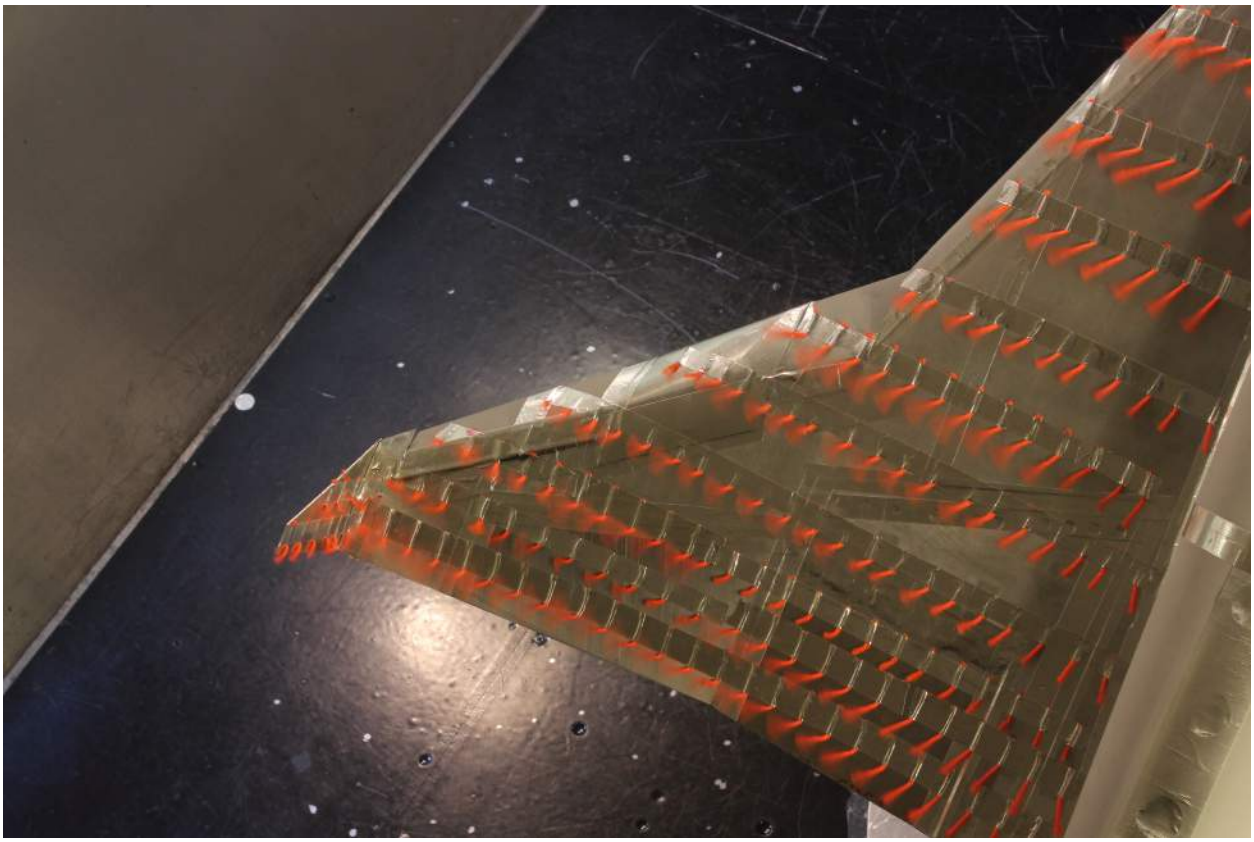

**Figure 6.1.2:** Turbulent flow appearing on the winglet.

The optimum leading-edge configuration included 30°leading-edge (fixed) droops on both the outboard and inboard wings. WHY? Comparisons plots can be seen below in Fig. 6.1.3.

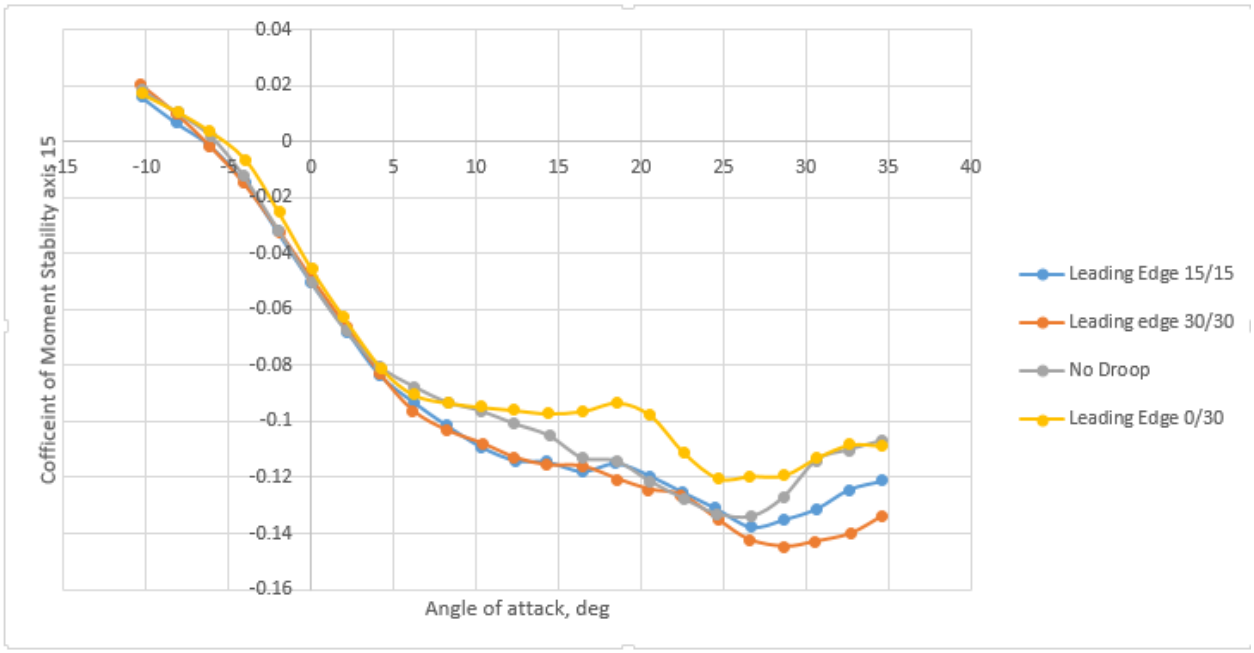


**Figure 6.1.3:** Pitching moment plots in which 30/30 shows the most negative slope.

### *6.1.3. Winglets*

Initial yaw tests showed positive yaw results for the winglets. The winglets provided a substantial increase in $C_n$. This can be seen in Fig. 6.1.4.

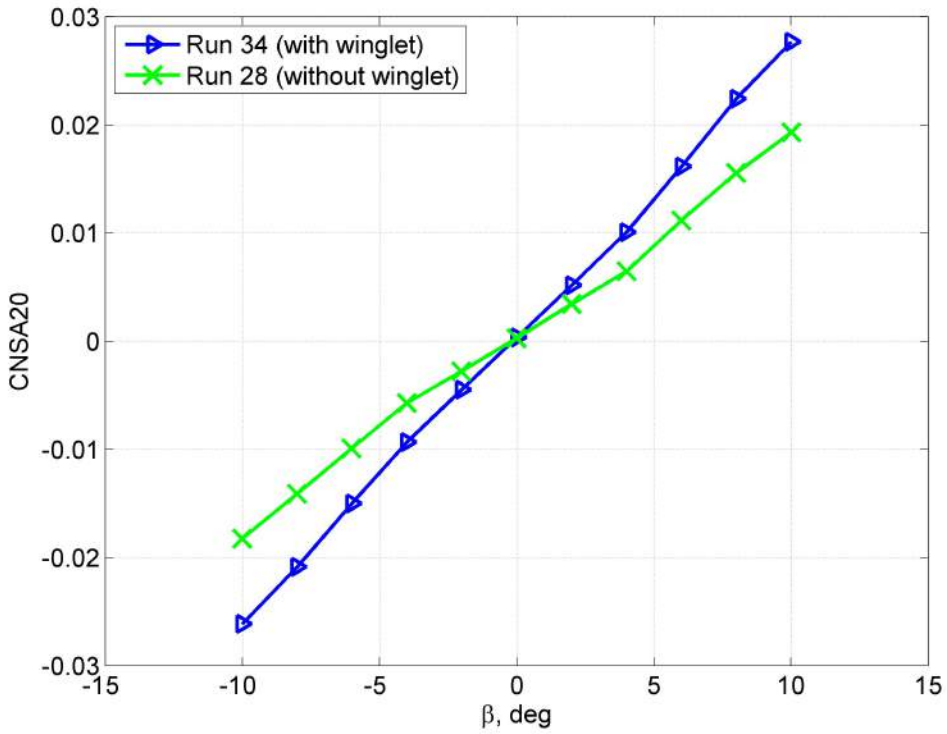


**Figure 6.1.4:** Beta sweeps for yaw coefficient(CNSA20) with q=6.27, psf and $\alpha = 0$, deg without nacelles.

Further yaw tests proved the winglets to be ineffective; the yaw stability contributed by the winglets initially was no longer present upon the addition of nacelles. In addition to the lack of yaw stability benefit, no substantial increase in sideforce (RIGHT?LOCAL CL ON THE WINGLETS?) was seen from the winglets. The lack of effectiveness is clear in Fig. 6.1.5. There are multiple theories as to why this occured. From initial flow visualization there appeared to be unclean flow over the winglets (FIGREFERENCE), which may have been caused by the drooped leading edge. A significant detriment to the effectiveness of the winglets was the usage of flat sheet-metal plates, which provided some yaw stability but not nearly enough to advance the use of the winglets. Having airfoiled winglets may have shown some improvement but these were not manufactured or tested due to time constraints and manufacturing (3-D printing or machining) difficulty of such small winglets. The sheet-metal winglets showed a tendency to stall at relatively low angles of incidence, severely limiting how far they could be effectively deflected at any appreciable angles of sideslip. A solution to this setback might have been to form sheathed airfoils around the plate winglets using pliable sheet metal, similar to what was done on the stabilator in order to artificially increase the size.

**Table 6.1.1:** Yaw Derivatives due to Winglet

| $\beta, deg$ | $CN_{\beta_{winglet}}, deg$, without Nacelle, $(10^{-3})$ | $CN_{\beta_{winglet}}$, with Nacelle, $(10^{-3})$ |
|---|---|---|
| -8 | 0.843 | 0.620 |
| -6 | 0.815 | 0.575 |
| -4 | 0.818 | 0.555 |
| -2 | 0.883 | 0.693 |
| 0 | 0.846 | 0.743 |
| 2 | 0.920 | 0.755 |
| 4 | 0.850 | 0.666 |
| 6 | 0.785 | 0.608 |
| 8 | 0.704 | 0.543 |

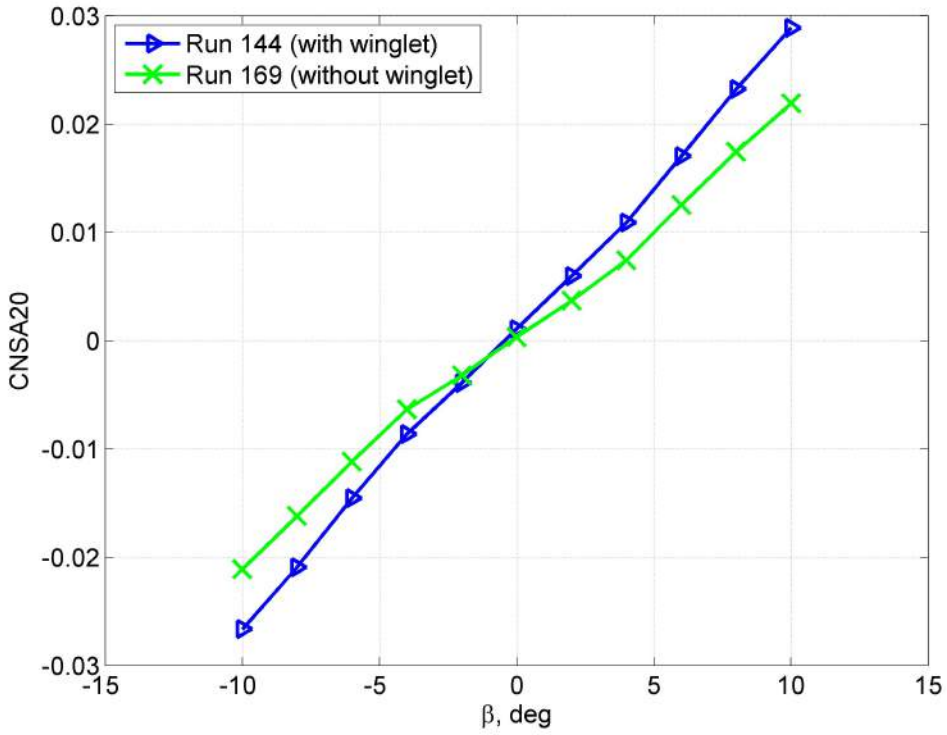


**Figure 6.1.5:** Beta sweeps for yaw coefficient(CNSA20) with q=6.27, psf and $\alpha = 0$, deg with nacelles.

The yaw stability derivatives due to the winglet for configurations with nacelles and without nacelles are shown in Table 6.1.1.

Even though Fig. 6.1.5 shows that the winglet slightly increases the yaw stability but from Table 6.1.1, it is clear that winglet becomes less effective with the configuration with the nacelles.

### *6.1.4. Lessons Canards and Stabilators*

For more detailed analysis see Stability and Controls, subsection Control surfaces.

Much of the analysis on the all-moving stabilizing surfaces was conducted via addition and subtraction of all aerodynamic coefficients of given components in given configurations. For example, to approximate the forces and moments on a configuration with both the canard and stabilator deflected, the effects of the stabilator (all-undeflected run subtracted from stabilator-deflected run) were superimposed on a canard-deflected run. This was necessary due to time constraints impeding the testing of many combinations of canard deflections and stabilator deflections. In the aforementioned case, the analysis does not take into consideration effects of the canard wake on the stabilator, which could be significant if the canard produces much lift and at either high or negative angles of attack where the canard wake could surpass the wing.

Ranges of canard configurations and deflections could have been more abundant during testing. Outside of a ground-rotation configuration during which the aircraft demands likely the most pitch-up authority from the control surfaces. The canard configurations that had the most usable and isolated data were canards C2 and C4, tested respectively at $\delta_C = 0°$, $15°$ and $\delta_C = -30°$, $-15°$, $0°$, $15°$, $30°$. The resolution on canard C2 was limiting in not being able to capture nonlinear effects in deflection (outside of those inferred from canard C4). The effectiveness did end up looking fairly linear at modest angles of incidence, but this did decrease confidence in the accuracy of the actual control derivative values (see Subsection 7.8.1.4).

A test that should have been conducted in the wind tunnel is a takeoff (flaps-down) configuration without the stabilator, which would allow more easily for the analysis of the downwash effects on stabilator effectiveness. When all of the flaps-down data incorporate the stabilator (even if undeflected), the additional lift on the stabilator due to additional downwash from the flaps is very difficult to separate from the additional lift on the main wing; this impedes the calculation of a zero-tail-lift stabilator deflection, which is important for specification of the change in downwash angle due to the flaps. Similarly, it is difficult to separate the change in pitching moment authority of the stabilator due to flap downwash from the addition wing pitching moment.

### *6.1.5. Thrust vectoring*

The powered runs in the wind tunnel showed an effect on the pitching characteristics of the aircraft. The overall pitching moment derivative proved to stay negative and thus the aircraft was stable at full throttle. The following figure, Figure shows this stability. Only a few data points were taken to conserve battery power.

**Purpose and Testing Procedure**

The Kirsten wind tunnel testing offered the propulsion team a unique opportunity to gain valuable data on the effectiveness of the thrust vectoring system for a full scale aircraft. The effectiveness of the thrust vectoring system would be reported in terms of the derivative of roll moment, yaw moment, and side force coefficients with respect to vane deflection angle. Also, to develop a richer understanding of how the thrust vectoring system would function in realistic flying conditions, tests were conducted for four different aircraft orientations. At each orientation, the aircraft were tested with no vane deflection, and with the vanes deflected at an angle of 30°. Table 6.1.2 below shows the aircraft orientation and vane deflection angle

for the tests focusing on vectored thrust effectiveness. Note that all tests were conducted at a nominal pressure of 6.27 psf and at full engine power.

**Table 6.1.2:** Breakdown of aircraft orientation and vane deflection angle for each run

| Run | Deflection Angle, deg | $\beta$, deg | $\alpha$,deg |
|---|---|---|---|
| 204 | 30 | 10 | 0 |
| 204 | 30 | 10 | 10 |
| 206 | 30 | 0 | 0 |
| 206 | 30 | 0 | 10 |
| 207 | 0 | 10 | 0 |
| 207 | 0 | 10 | 10 |
| 209 | 0 | 0 | 0 |
| 209 | 0 | 0 | 10 |

The vane deflection angle was adjusted by hand and measured using a protractor between runs. The mount for the aircraft had pressure sensors in all three axis. Using this information the data acquisition system reported the roll moment, yaw moment and side force coefficients. The data was then reduced and uploaded to a public folder. The EDF was powered by a bank of four 12-volt car batteries, which were held in a room directly below the testing platform. The batteries were connected in series and a long insulated wire was snaked around the sting mount and into the engine nacelle. The battery life, voltage, and amperage of the batteries were monitored closely to ensure that the EDF was properly powered and was within the manufacturer recommended operating voltage. Fig. 6.1.6 below shows how the wires connecting up to the EDF as well as the thrust vectoring vanes in the un-deflected orientation.

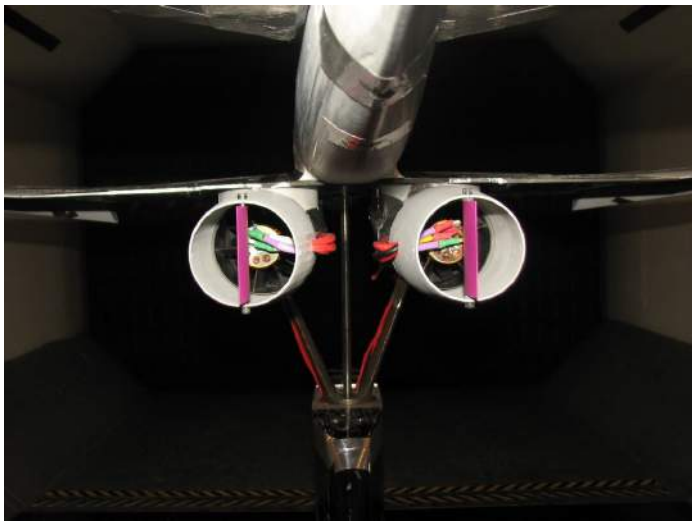

**Figure 6.1.6:** Kirsten Tunnel Model Nacelle Closeup

**Analysis**

Fig. 6.1.7 below shows the side force coefficient as a function of vane deflection angle. As

stated before the tests were conducted under a nominal dynamic pressure of 6.27 psf and powered up to full thrust.

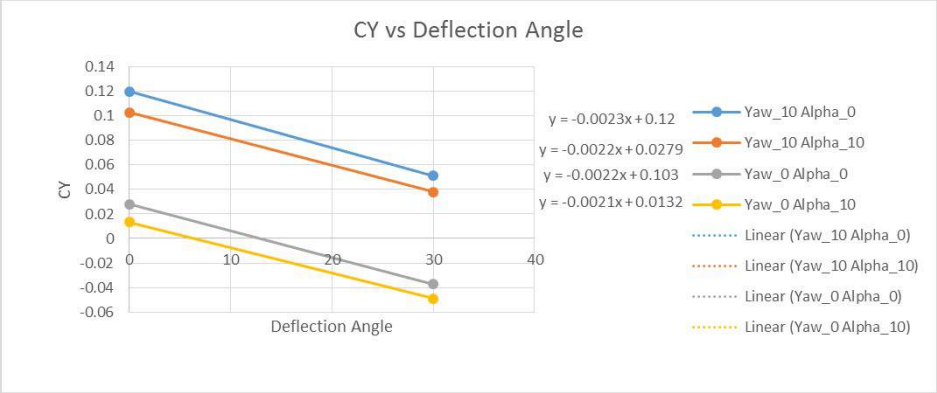


**Figure 6.1.7:** Side force as a function of vane deflection for various yaw and alpha angles at 6.27 psf nominal dynamic pressure

The graph shows that the alpha angle has a small effect on the side force while the beta angle has a much more significant effect. It was expected that the presence of the vertical tail would cause a significant side force when the beta angle was shifted ten degrees. The data shows that at zero alpha and vane deflection, an increase in beta angle of ten degrees increased the side force coefficient by 0.09984. In comparison, a vane deflection of 30 degrees at the zero alpha and beta angle orientation changed the side force coefficient by 0.06511. This shows the effectiveness of the trust vectoring system, and the potential for a functional aircraft with no vertical tail.

Fig. 6.1.8 below shows roll moment coefficient as a function of vane deflection angle. It was predicted that vane deflection would have little if any effect on roll moment as this was not the intended purpose of the thrust vectoring system.

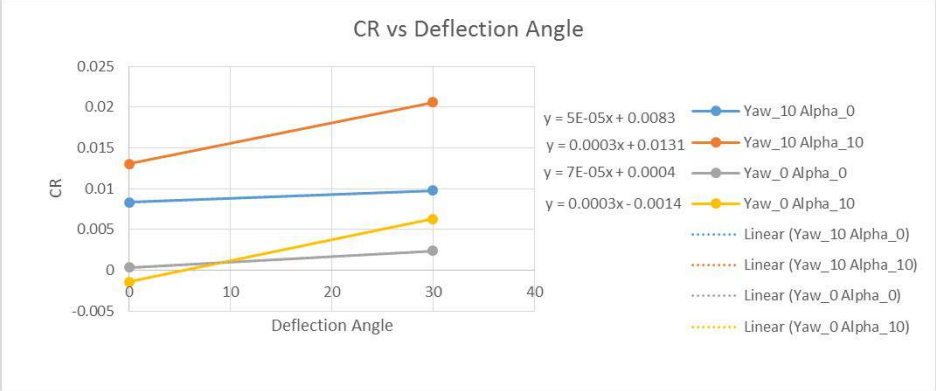


**Figure 6.1.8:** Rolling moment as a function of vane deflection angle for various yaw and alpha angles

The graph confirms the prediction that vane deflection would have little to no effect on roll moment coefficient. At zero and beta angle orientation, a vane deflection of 30 degrees caused a change of only 0.002035 in the roll moment coefficient. For contrast, at zero alpha

orientation and with no vane deflection, an increase in beta angle of ten degrees causes an increase in roll moment coefficient of 0.09129. Rolling moment coefficient change was 45 times greater for the beta angle deflection compared with the vane deflection. Interestingly, the change roll moment coefficient is less significant when the aircraft was in the ten degree beta and ten degree alpha orientation. Although interesting to note, the implications of this was out of the scope of the vectored thrust effectiveness study, thus it will not be further explored.

Fig. 6.1.9 below shows the yaw moment as a function of vane deflection angle. The ability to generate yaw moment is the greatest measurement of the effectiveness of the vectored thrusting system. The data in the graph below, is therefore the most important of the three graphs shown in this section.

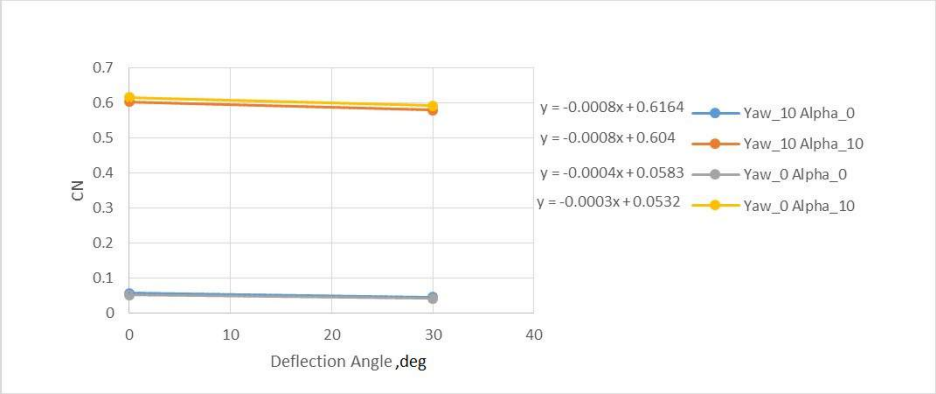


**Figure 6.1.9:** Yawing moment as a function of vane deflection for various yaw and alpha angles

Unsurprisingly, the graph shows that there was no significant yawing moment at zero beta angle orientation and zero vane deflection, regardless of the alpha angle orientation. When the RUAV was in the ten degree alpha and zero degree alpha orientation, the yaw moment coefficient jumps to about -0.025. Based on the side force data in figure 19, it is not surprising to see an increase in yaw moment coefficient with the increase in beta angle. The ten degree beta and ten degree alpha orientation had the most significant change in yaw moment coefficient at about -0.03. Note that the yaw moment only decreases as a function of alpha when the aircraft had a ten degree beta deflection, but not when there was no beta deflection. This was most likely due to a change in the aerodynamic behavior of the aircraft at this orientation.

When the aircraft was in the zero degrees alpha and beta orientation, a vane deflection of 30 degrees increased the yawing moment coefficient by 0.0334. This was about the same change in yaw moment coefficient caused by an alpha and beta deflection of ten degrees. This clearly shows that the thrust vectoring system has the ability to generate a yaw moment comparable to that of a vertical tail.

Table 4 below summarizes the differential yaw moment, roll moment, and side force coefficients with respect to vane deflection. Before the wind tunnel experiments took place, these three values were determined to be the most important to find. Table 6.1.3 below summarizes the differential yaw moment, roll moment, and side force coefficients with respect to vane deflection. Before the wind tunnel experiments took place, these three values were

determined to be the most important to find.

**Table 6.1.3:** Yaw moment, roll moment, and side force coefficients with respect to vane deflection angle

| Alpha | Beta | $Cy_{\delta_{T.V}}$ | $Cl_{\delta_{T.V}}$ | $Cn_{\delta_{T.V}}$ |
|---|---|---|---|---|
| 0 | 0 | 0.003896 | -0.12435 | 0.065661 |
| 10 | 0 | 0.014687 | -0.12214 | 0.062643 |
| 0 | 10 | 0.027693 | -0.13174 | 0.0699519 |
| 10 | 10 | 0.0144 | -0.12372 | 0.062281 |

The table shows that the yaw moment produced by the vectored thrust system was nearly independent of the orientation of the aircraft. This was an important criteria because consistency of the thrust vectoring system is critical for controlling the RUAV. Secondly the table shows that the side force was much more dependent of the orientation of the aircraft. This is not ideal, however, side force is much less important than yaw moment in terms of controlling the RUAV.**Problems and Potential Sources of Error**

In the middle of one of the runs, the temperature of the wire became hot enough to melt the solder connection such that the wire split in half. The power carrying wire had to be replaced, delaying the powered runs in the wind tunnel. It was determined that the cause of the wire separation was due to the thickness of the wire being too thin. The problem was solved by using a wire of greater thickness with a lower electrical resistance.

## 6.2. 3× 3 Wind Tunnel Testing

### *6.2.1. Overview*

The nacelle and the EDF were tested in the 3'×3' wind tunnel in order to measure thrust, drag, lift, and side force. The effects of the thrust vectoring vane deflections and EDF thrust performance were also studied through this test. The variables for this test were the angle of attack, sideslip angle, vane deflection, and throttle settings, each of which were changed individually every run.

### *6.2.2. Set Up*

The nacelle used for the 3× 3 testing was 3D printed in four sections of PLA. The EDF was housed in the 3-D printed nacelle's cowl and the 4 components of the nacelle was attached firmly using speed tape. The thrust vectoring vane was mounted in the nozzle using a screw and epoxy. The vane deflection angle was changed by hand and measured using a protractor. The nacelle was mounted onto the sting mount using two screws as shown in Fig. 6.2.1.

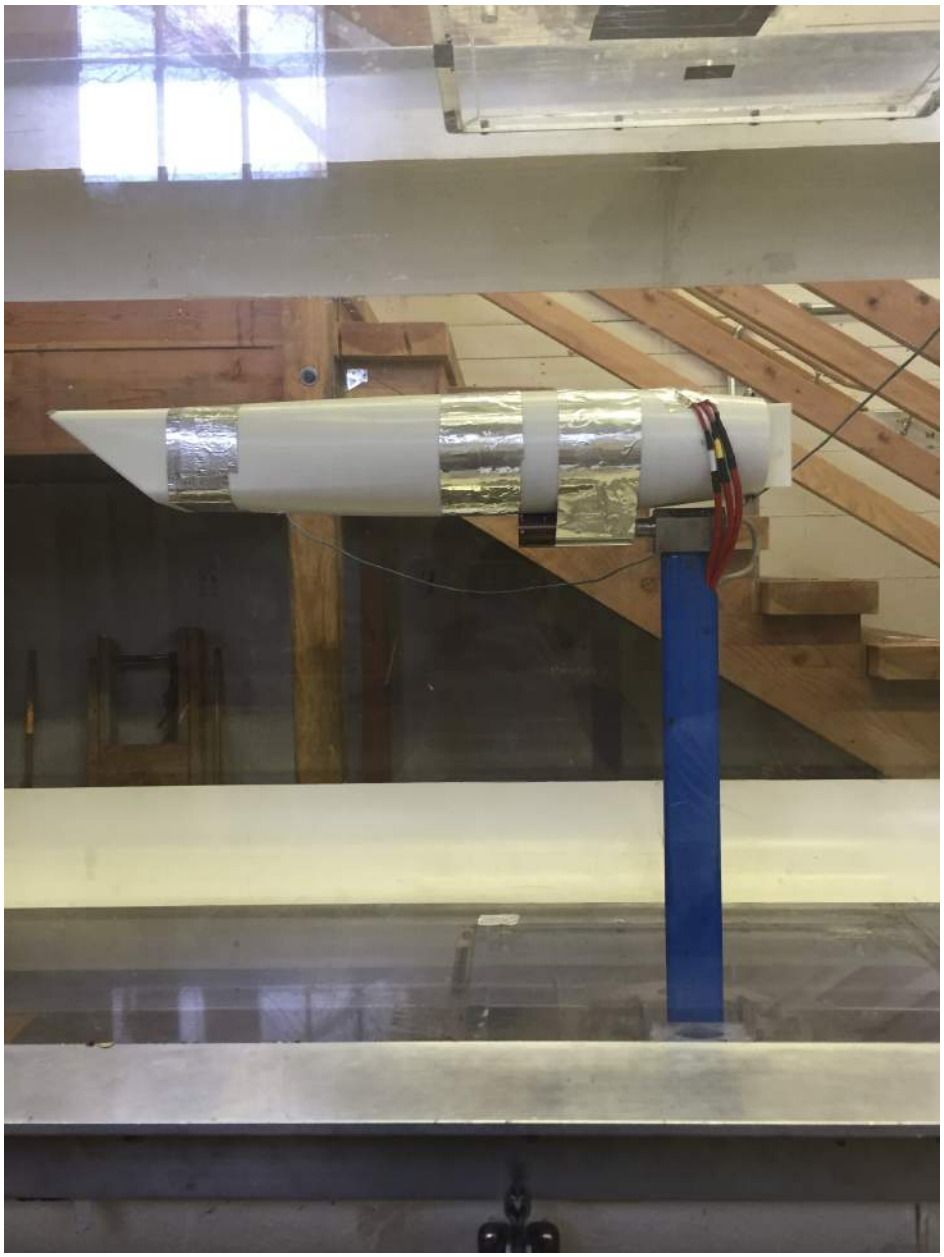

**Figure 6.2.1:** Set up of the nacelle in the 3× 3 wind tunnel

Although the EDF on the R-UAV will be powered by a six-cell Li-Po battery, the test was conducted by using four car batteries to avoid frequent charging between tests. The car batteries only required recharging once throughout the testing process. However, this caused some discrepancy in the data. The car batteries were fully charged such that each battery had a voltage well above 12.6 V. These batteries were connected in series and connected to the speed controller. The receiver lead of the speed controller was connected to the throttle port of the receiver. The receiver was powered by a two-cell Li-Po battery and was connected to the battery port of the receiver. The circuit for the EDF can be seen below in Fig. 6.2.2.

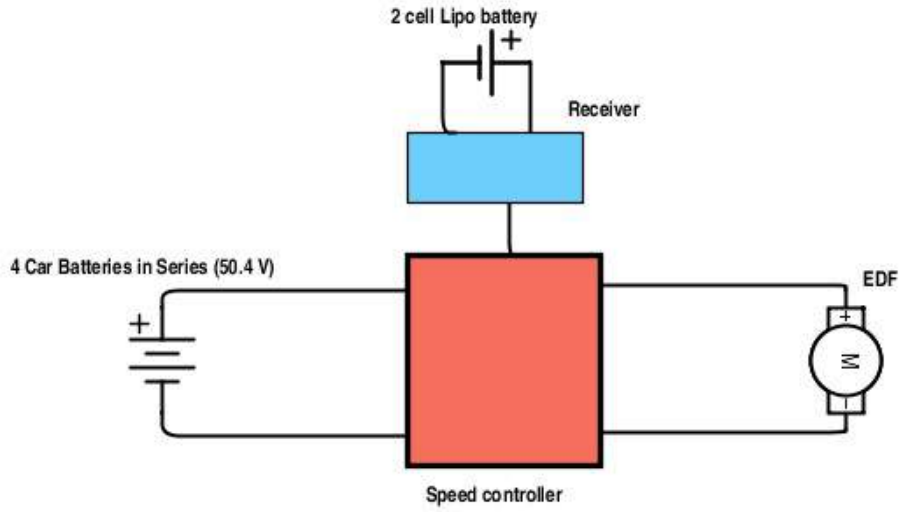


**Figure 6.2.2:** Circuit for EDF

All wires leading up to the EDF were harnessed inside the sting mount shaft, and anything outside of the shaft or the EDF pylon were taped to the nacelle using speed tape as shown in Fig. 6.2.3.

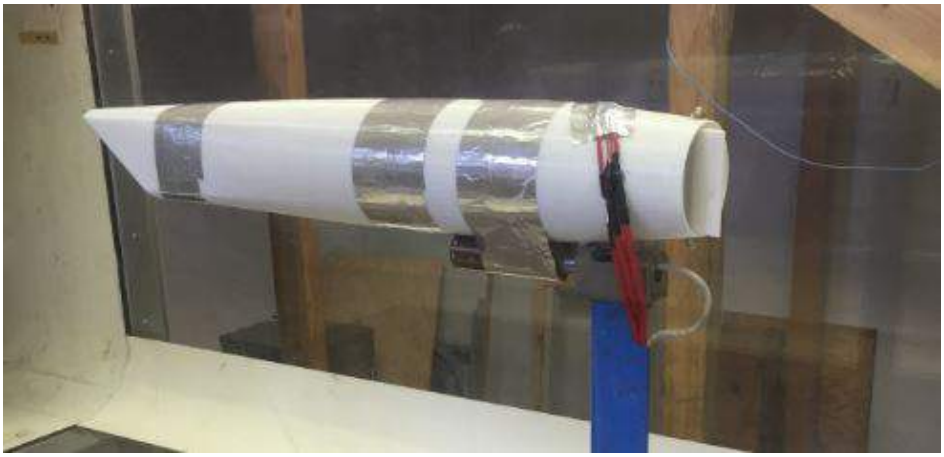

**Figure 6.2.3:** Wiring for the EDF

### *6.2.3. Procedure*

For each run, the following procedures were conducted:

First, the nacelle was set at the desired orientation and fastened to its position. Once the door of the wind tunnel test section had been closed and locked, the EDF throttle was brought up to the desired setting. Then the "record" button was then clicked on the data acquisition system (DAQ) and the wind tunnel was turned on. The dynamic pressure was slowly increases from 0 psf to 30 psf over a period of about 45 seconds. Once the dynamic pressure reached 30 psf, the "stop" button was clicked on the DAQ and the wind tunnel was turned off.

The alpha and beta angles were tested from $-5°$ to $+15°$ in $5°$ increments. The vane was

deflected from 0° to +40° in 5° increments. A tare run was also conducted. All of the tests were completed at both engine off and 5/6 throttle.

### *6.2.4. Discussion of Results*

**Beta Variation Un-Powered**

The testing of the nacelle side profile was performed in the same wind tunnel with similar methods as other tests. However, the EDF was left unpowered throughout the test. The nacelle was rotated through beta angles from 0° to 15° with a step of 5°. The drag was recorded and plotted in Fig. 6.2.4. There was no significant variation observed in the drag curve for different nacelle orientations. The difference of 0.1 lb of drag for 15° beta angle at 30 psf was considered non-substantial. However, it is important to bear in mind that these values only reflect the force component parallel to the length of the nacelle.

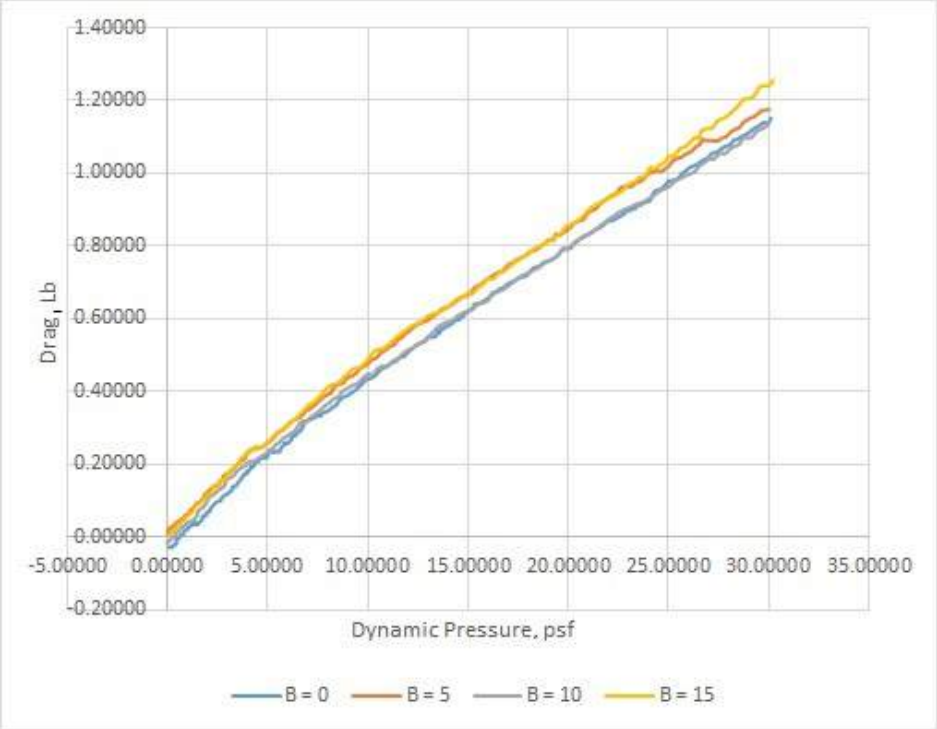


**Figure 6.2.4:** Drag of Nacelle

A more meaningful force component for the nacelle in beta angle would be the side force imposed during crosswinds. The value for this side force is somewhat expressed as a rolling moment due to the method the nacelle was set up during the experiment. However, by assuming the force to act at half the height of the nacelle, the side force can be obtained through the division of roll moment by the moment arm. The roll moment is plotted in Fig. 6.2.5.

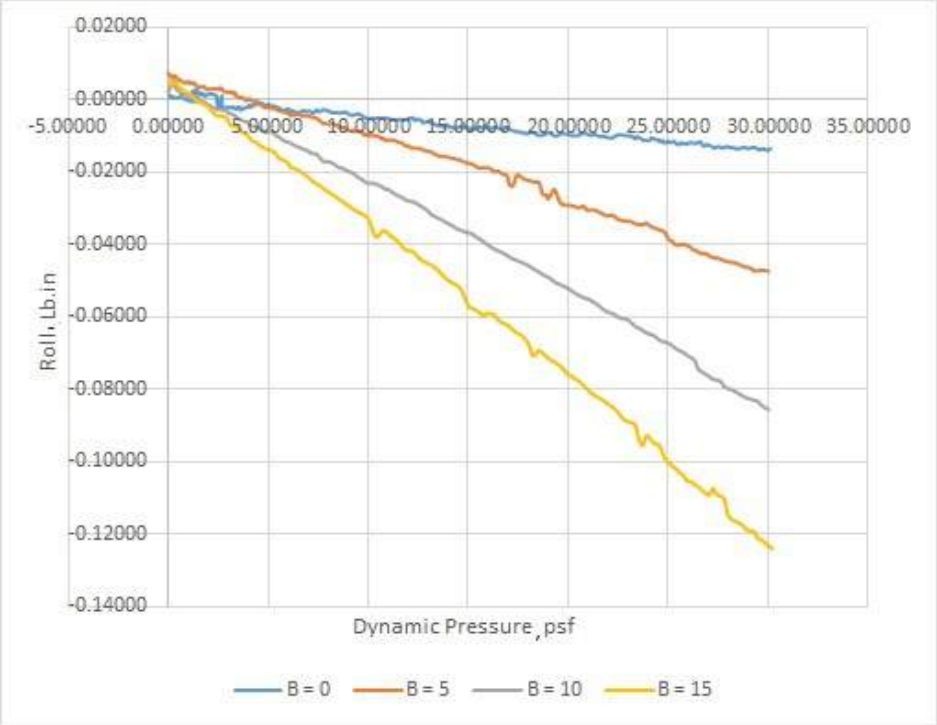


**Figure 6.2.5:** Rolling Moment of the Nacelle

**Vane Deflection, Un-Powered**

One of the goals of the thrust vectoring system was to ensure yaw control in a engine out scenario. Therefore, during testing in the wind tunnel, testing was done on varying angles of vane deflection at various dynamic pressures, with zero thrust from the EDFs. During each of the test runs, the drag and side force on the sting mount was recorded, in order to determine whether the side forces were strong enough to control the aircraft, as well as to make sure that the drag created by the vanes would not slow down the aircraft to the point of stalling. In each test, the vane was deflected in increments of 5°, starting at 0° and ending at 40°. The values of dynamic pressure during the test started at 0 psf and then increased gradually to 30 psf. The results for the drag for the varying vane deflections are shown below in Fig. 6.2.6

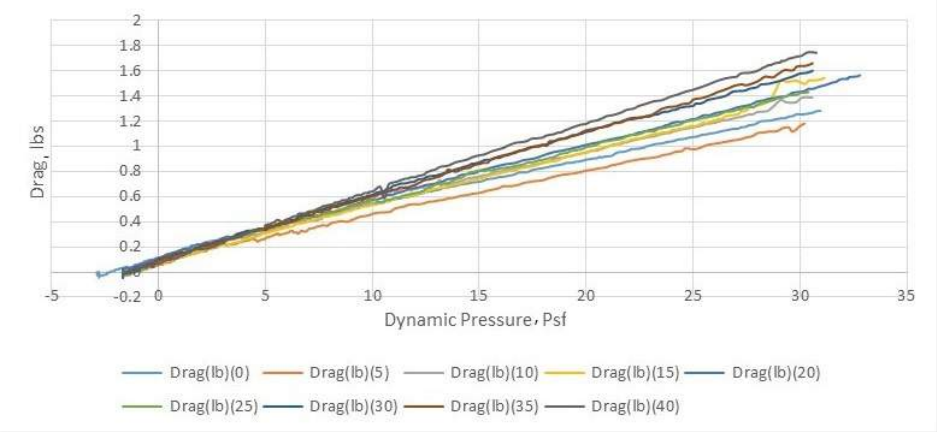


**Figure 6.2.6:** Dynamic Pressure vs Drag

As shown in Fig. 6.2.6, the increase in drag is directly proportional to the change in vane deflection. This is due to the increase of surface area exposed to the flow. Since drag is proportional to the surface area of the object in a flow, by changing the deflection of the vane, more of its area is shown to the flow, hence increasing the drag of the nacelle. This is very important to the performance of the aircraft because in an engine out situation, the pilot must balance the need for yaw control with the loss of airspeed.

The 3x3 wind tunnel tests also produced varying values of side force with the different vane deflections. This was important because it would allow the pilot to control the aircraft with the engine vanes even without the engines being on. The results for the side force are shown in Fig. 6.2.7.

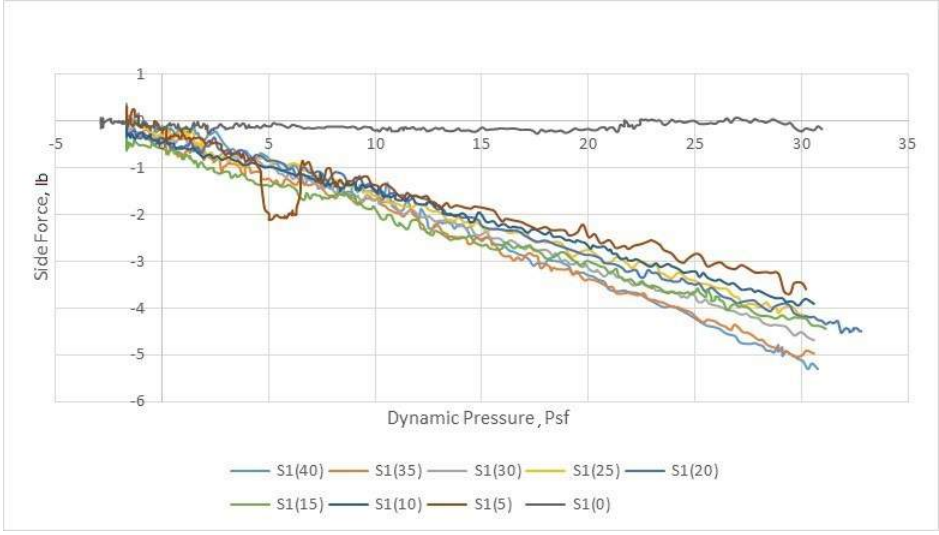


**Figure 6.2.7:** Side Force vs Dynamic Pressure for Thrust = 0

As shown by the test results, as you increase the deflection of the vane, a larger side force is being created. Assuming a dynamic pressure of 10 psf during flight, if the engine was to fail, the pilot could still produce up to 2 lbs of side force if fully deflecting just one of the engine vanes. Therefore, ideally if both engine vanes were deflected, the pilot could maintain

4 lbs of side force control on the aircraft at a dynamic pressure of 4 psf in an engine out situation. Using this side force, the pilot would be able to control the yaw of the aircraft using the vanes, even in an engine out situation.

**Angle of Attack variation, Powered**

Fig. 6.2.8 below shows the net axial force of the engine with varying angle of attack during a power-on test. Notice that the sting mount reads the drag as a positive force, therefore making the thrust a negative force. At q = 0 psf, it can be seen that the EDF generates different forces for each run without a dependence on angle of attack. Up to about 22 psf, all runs show a loss of thrust at about the same rate. However, when the dynamic pressure is increased above 22 psf, the drag decreases slightly for high angles of attack, whereas the small angle of attack continues to follow the same trend all the way up to 30 psf.

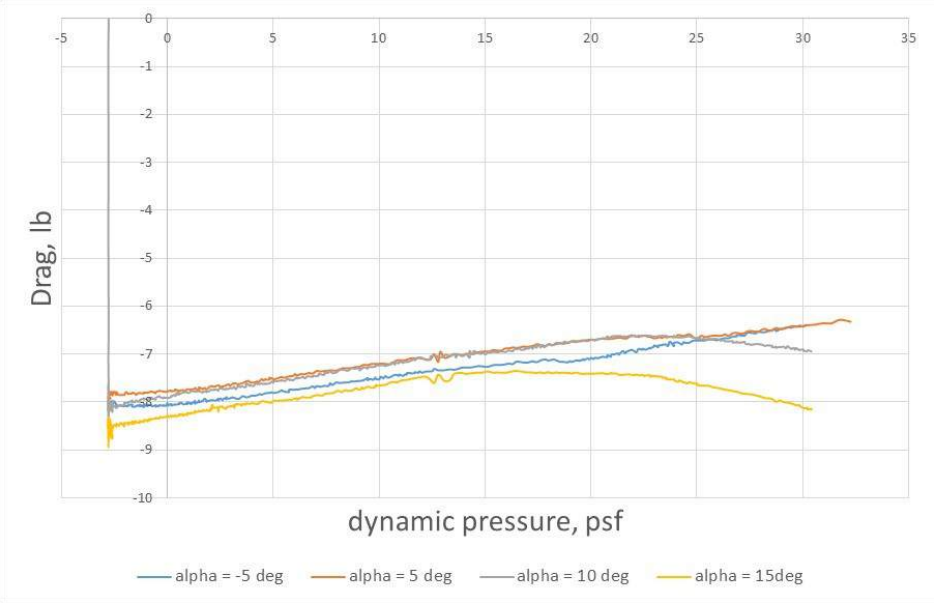


**Figure 6.2.8:** Dependence of drag on dynamic pressure at various angles of attack Throttle = 5/6, beta = 0°, vane deflection = 0°, Angle of attack variation = -5°, 5°, 10°, 15°

Fig. 6.2.9 is a plot of the lift versus the dynamic pressure. This data is expected, as the lift increases as the angle of attack increases.

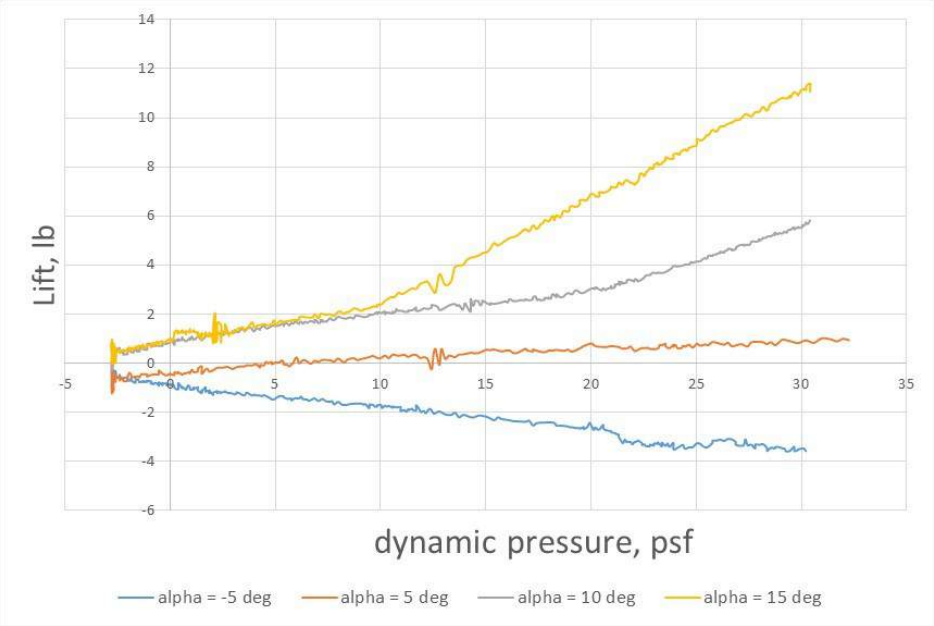


**Figure 6.2.9:** Dependence of lift on dynamic pressure at various angles of attack

**Vane Deflection, Powered**

In the 3×3 wind tunnel, the thrust vectoring was tested. The engine was run at 5/6 throttle and the wind speed was turned up from 0 to 30 psf dynamic pressure over about 1 minute. The thrust vectoring vane was deflected at various angles from 0 degrees deflection to 40° in intervals of 5°. To verify that deflecting the vane to the opposite side would generate the same forces but in the opposite direction, the angles of -20° and -40° were also tested. To analyze the data collected, the side force generated on the sting mount was observed over the range of dynamic pressure values. The side force is plotted vs. the dynamic pressure in Fig. 6.2.10. It can be seen that as dynamic pressure increases, the side force increases. This is to be expected because as the wind speed increases, there is more air being deflected by the vane. Also, as the vane angle increases, the side force also increases. This is also to be expected because as the vane deflects, a larger component of the thrust is being used to create a side force. However, above 20° deflection, this trend begins to vanish. The angles above 20° all generate a similar side force over the dynamic pressure range. This is most likely due to air separation at high deflection angles causing the airfoil shaped vane to stall.

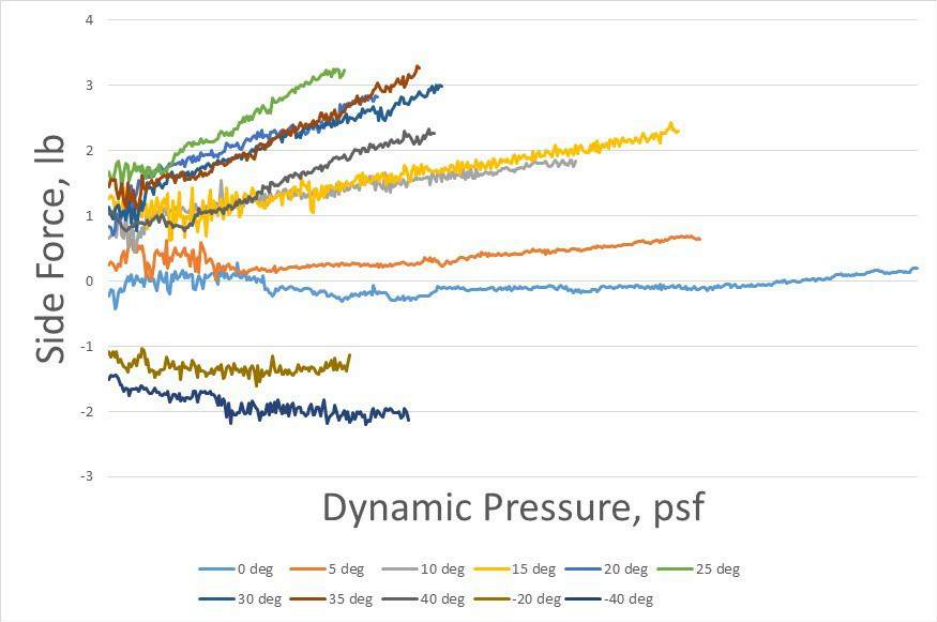


**Figure 6.2.10:** Side Force Results with Vane Deflection from 3×3 Testing

Next, the side forces for a given dynamic pressure value at varying deflection angles were then plotted to find the change in side force per degree of vane deflection. The dynamic pressure value of 16 psf was selected, as this translated to an airspeed of 80 mph, which is the approximate cruising speed. The deflection angles from 0° to 25° were selected. It can be seen in Fig. 6.2.11 that the side force increases by approximately 0.12 lb per degree of vane deflection.

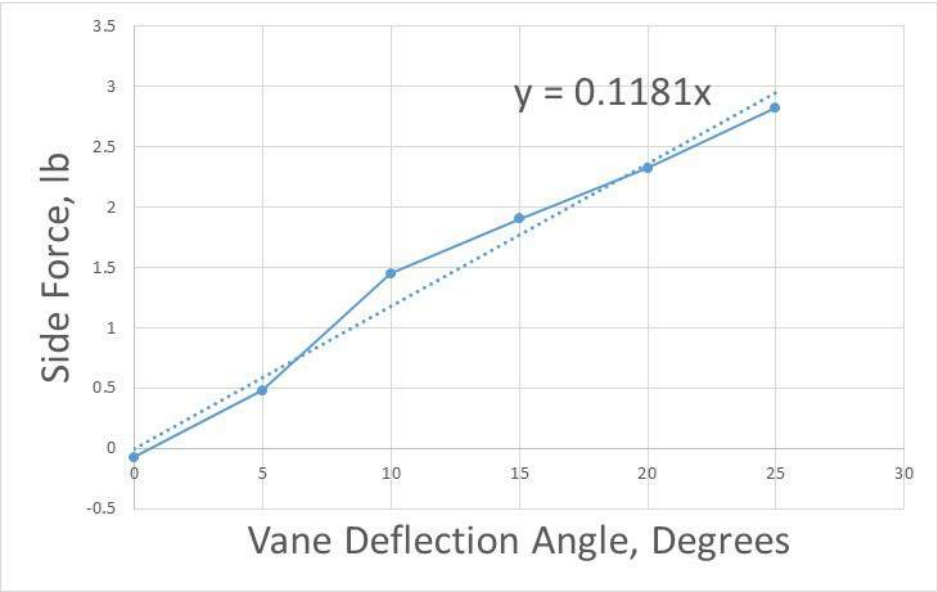


**Figure 6.2.11:** Side Force vs. Vane Deflection at $q = 16$ psf

### *6.2.5. Sources of Error*

Some possible sources of error during the 3×3 wind tunnel tests were damaged parts, inconsistent battery recharging, and non-uniform dynamic pressure increase.

During the 15° powered alpha test, the aluminum speed tape securing the duct to the cowl was torn which caused both the inlet and duct to detach and fly down the tunnel. This was due to the high dynamic pressure combined with the vibrations from the electric ducted fan. As a result of the in tunnel disassembly, the inlet lip was slightly damaged. This damage was patched with speed tape, and the amount of speed tape used to secure the duct to the cowl was increased from 1 strip to 2 strips of aluminum speed tape.

Next, using four 12 volt car batteries, it was difficult to discern the change and effect of the available voltage before and after recharging. Due this difference in voltage, there was a discrepancy in the thrust produced by the electric ducted fan over multiple test runs. Also, as the batteries were used from test to test, the available voltage decreased a small amount. This slightly affected the power output of the electric ducted fans between test runs.

Furthermore, there were a few sources of error due to human error. These include vane deflection measurement accuracy, electric ducted fan throttle consistency, and the uniformity of the dynamic pressure increase. To measure the vane deflection, a protractor was used, which inherently possesses error associated with its readability. Also, the throttle position on the DX-18 controller was set manually and was difficult to consistently tune to the same position. This could have resulted in a variation in thrust between power-on test runs. Finally, the dynamic pressure produced by the 3×3 wind tunnel was manually increased from 0 to 30 psf and the time taken to traverse this gradient varied from run to run. This may have affected the results. Another final source of error was that in alpha deflection cases, the nozzle of the nacelle touched the sting mount due to its sideways mounting position. This could have manipulated the measured normal force and drag.

## 6.3. Static Thrust Testing

In order to test the static performance of various nacelle designs "on the fly," the propulsion team developed a test stand that enabled accurate nacelle thrust measurements. Variables considered during static testing were EDF throttle setting, wire length between the EDF and the Li-Po batteries, as well as nacelle inlet and nozzle geometry. Two types of static testing were undertaken: endurance testing and performance testing. In order to determine battery endurance, and thus the flight time of the R-UAV, the EDF was run at a constant throttle setting while thrust, battery current, and battery voltage were monitored. In order to determine propulsion system performance, as well as thrust-specific charge consumption of the system, the EDF was run at multiple throttle settings from 5% to 100%. During the performance test, thrust, battery current, and battery voltage were measured.

### *6.3.1. Test Stand*

The EDF test stand is shown in Fig. 6.3.1. The test stand was constructed from a repurposed wood stand used during the 2014 project. The nacelle was hung with string from a digital force gage, which was located on the test stand. During initial testing, it was noticed that the nacelle tended to spin around the longitudinal axis due to torque from the motor. In order to alleviate this problem, a rod was positioned vertically in a guide rail on

the outside of the nacelle. The rod was held in place by hand during testing. The batteries used for testing were a pair of 6 cell Li-Po batteries.

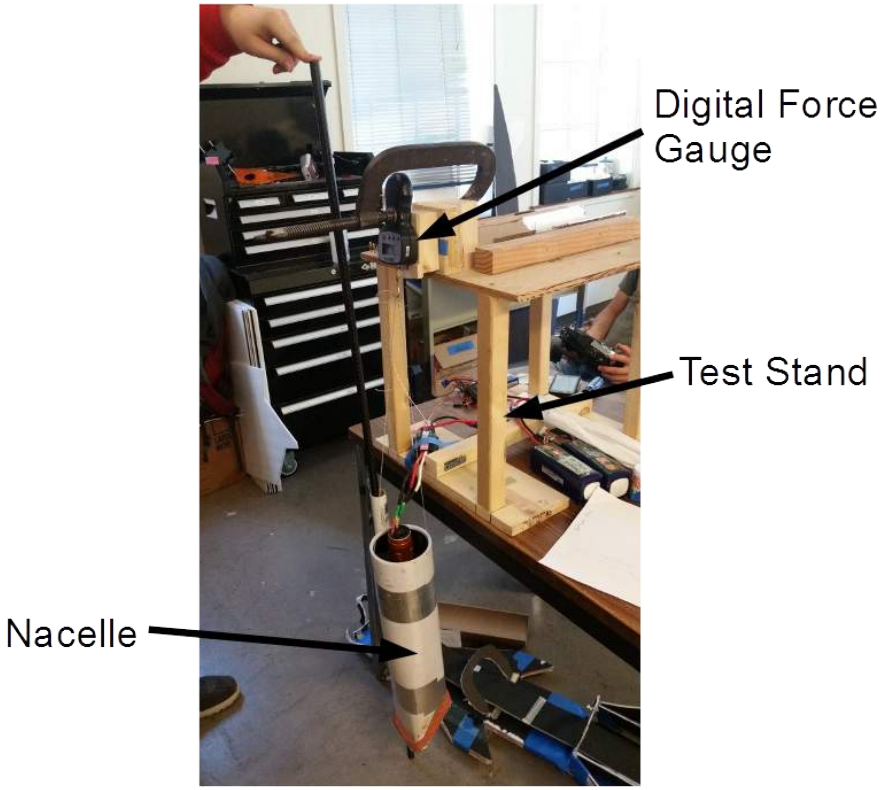


**Figure 6.3.1:** Static testing setup showing test stand, nacelle, and digital force gauge

### *6.3.2. Max Thrust*

Maximum thrust testing was performed by setting the throttle to full power and measuring the resultant thrust. The maximum thrust for various nacelle configurations can be seen in Table 6.3.1. This testing showed that the 3.4 inch diameter nozzle gave the best

**Table 6.3.1:** Propulsion system thrust based on nozzle diameter and throttle setting

| **Thrust (lbs)** | | | |
|---|---|---|---|
| | 3.1" Diameter Nozzle | 3.4" Diameter Nozzle | 4" Diameter Nozzle |
| 50% Throttle | 6.1 | 7.3 | 6.5 |
| 100% Throttle | 9.8 | 11.3 | 11.4 |

combination of mid-throttle and high-throttle performance.

All three EDFs were tested for thrust and endurance and were determined to have negligible differences. This ensured that there would be little thrust imbalance during flight and that each EDF would not have to go through the full range of testing.

Further performance testing was performed on three different nacelle configurations. In order to determine the EDF battery consumption at various throttle settings, the thrust at throttle settings between 5% and 100% were plotted versus battery current flow. The first configuration had a thin inlet lip, and the second two had a thicker, rounder inlet lip. The thinner inlet lip generally gave lower thrust for the static case due to airflow separating as it goes around the inlet lip and partially blocks the flow through the nacelle. The third nacelle configuration featured cable lengths between the battery and ESC that were representative of the lengths of cable that will be used on the R-UAV. The increase in cable length for this case had a negligible effect on the thrust of the propulsion system. Fig. 6.3.2 shows the performance of the propulsion system for all three configurations.

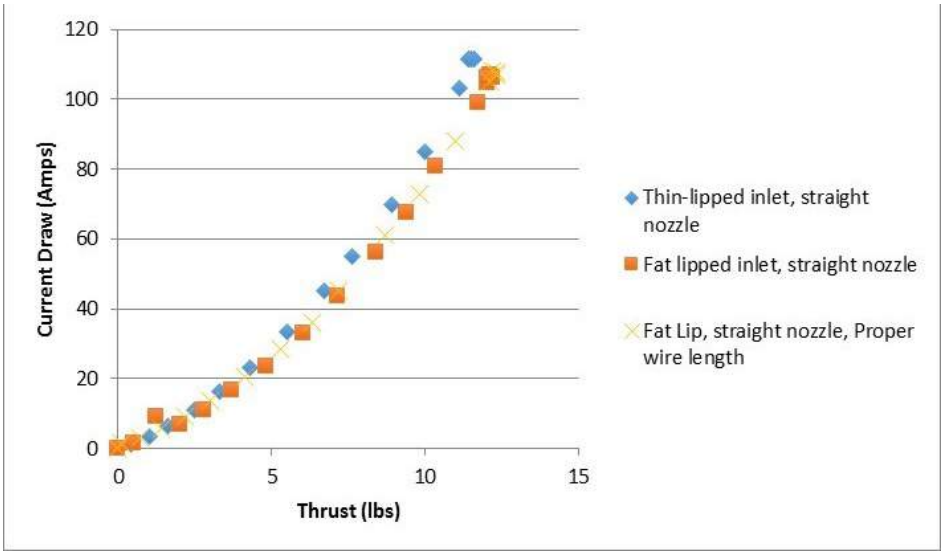


**Figure 6.3.2:** EDF thrust versus current draw for various nacelle configurations at throttle settings between 5-100%

### *6.3.3. Endurance*

Endurance testing was performed by setting the EDF to a constant throttle setting and measuring thrust, current, and voltage at 30 second intervals. The battery voltage was observed to sag while the EDF was running due to the internal resistance of the batteries, and to increase again when the EDF was turned off. In order to measure a more accurate battery voltage, the EDF was shut off every 30 seconds, and the steady-state, no-load voltage was recorded. In order to determine the endurance of the propulsion system at different throttle settings, the EDF was run until the no-load battery voltage reached 44.4 volts. This voltage was defined by the battery manufacturer as the indicator of a dead battery. The results for this testing are presented in Fig 6.3.3.

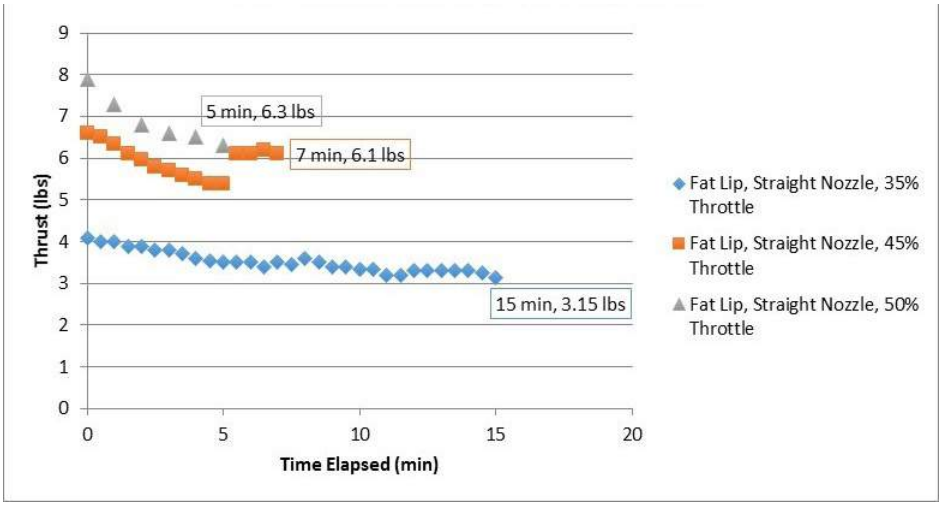


**Figure 6.3.3:** Thrust vs. elapsed time of EDF-nacelle configuration at various throttle settings

The results in Fig 6.3.3 gave the group invaluable knowledge about the endurance of the propulsion system and validated previously determined endurance estimates performed by the mechanical and electrical systems team. Furthermore, by reducing the throttle a small bit from 45% to 35%, the endurance was observed to increase by more that a factor of 2.

The voltage drop of the batteries is an indicator of the battery drain due to the EDF. This voltage drop is tabulated versus run time in Fig 6.3.4.

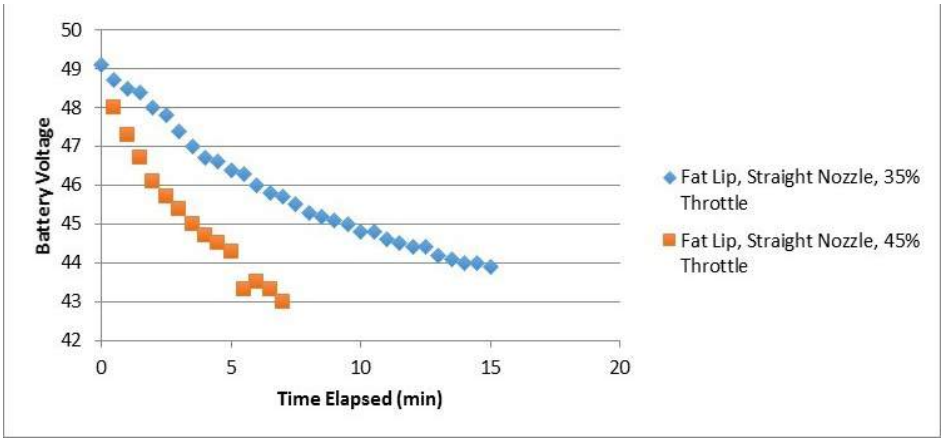


**Figure 6.3.4:** Voltage drop of batteries versus time during an endurance run

It can be seen that the voltage steadily decreases with time during periods of constant throttle setting. The timed rate of change of voltage is considerably greater for the 45% throttle case as compared to the 35% case. These throttle percentages were chosen because they were determined to be the approximate range of the minimum required thrust for the cruise configuration. This was based off of thrust required and thrust available data.

# 7. R-UAV Design

### *7.0.4. R-UAV Weights*

At this point, the next step for the weights group was to tally the total fixed weight for the R-UAV. This consists of the landing gears, EDFs, and systems components which totaled to approximately 12.4 lbf. The inital list was not fully complete, as some parts were subject to change, such as the size of the servos, the addition of FPV cameras, and wiring lengths. Knowing this was a lower limit to the systems, it was approximated that the total fixed weight would be closer to 15 or 16 lbf instead of the calculated 12.42 lbf.

It was imperative before finalizing the build plan was to analyze different material choices for each part and identify which materials were more viable based on their weight and also structural integrity. The material densities used in this analysis are listed in Table 7.0.2. Note in the table that measured indicates a coupon of the material was created, approximated indicates an assumption based on measured densities was carried through, and general means the value was taken from outside sources, such as the manufacturer.

**Table 7.0.2:** Area Densities of Prospective Build Materials

| **Material** | **Area Density (lbf/$ft^2$)** | **Calculation Technique** |
|---|---|---|
| Carbon Fiber T700 Weave | 6.31 x $10^{-2}$ | Measured |
| 0.75 oz/$yd^2$ fiberglass | 8.50 x $10^{-3}$ | Approximated |
| 2.0 oz/$yd^2$ fiberglass | 2.20 x $10^{-2}$ | Measured |
| 2.3 oz/$yd^2$ fiberglass | 2.61 x $10^{-2}$ | Approximated |
| 3.7 oz/$yd^2$ fiberglass | 4.19 x $10^{-2}$ | Approximated |
| Carbon fiber sandwich: | 3.48 x $10^{-1}$ | Measured |
| 2 ply CFRP + 1/4" honeycomb | — | — |
| Carbon fiber sandwich: | 2.27 x $10^{-3}$ | Measured |
| 1 ply CFRP + Dow Extruded Polystyrene | — | — |

**Table 7.0.3:** Densities of Prospective Build Materials

| **Material** | **Density (lbf/$ft^3$)** | **Calculation Technique** |
|---|---|---|
| Plywood | 1.14 x $10^{-5}$ | General |
| Balsawood | 7.41 x $10^{-6}$ | General |
| Dow Extruded Polystyrene | 5.27 x $10^{-7}$ | Measured |
| High Density Foam | 3.33 x $10^{-7}$ | Measured |
| PLA | 2.59 x $10^{-5}$ | General |

An important assumption made during the initial weight estimations was the weight addition due to epoxy. Time constraints in the project prevented analysis of coupons for each potential material, so assumptions were based of the limited coupons created. In particular, that of 2.0 $\frac{oz}{yd^2}$ fiberglass. The material alone is projected to have an area density of 0.01389 $\frac{lbf}{ft^2}$, however, coupons produced an area density of 0.022 $\frac{lbf}{ft^2}$. This indicates that epoxy essentially added 63.11% the weight of the fabric alone to the final part. This added amount is reflected in Table 7.0.3 was carried through the calculations.

The following figures display potential weights for the fuselage, wings, canards, horizontal stabilator, and vertical tail, respectively, based on material choices.

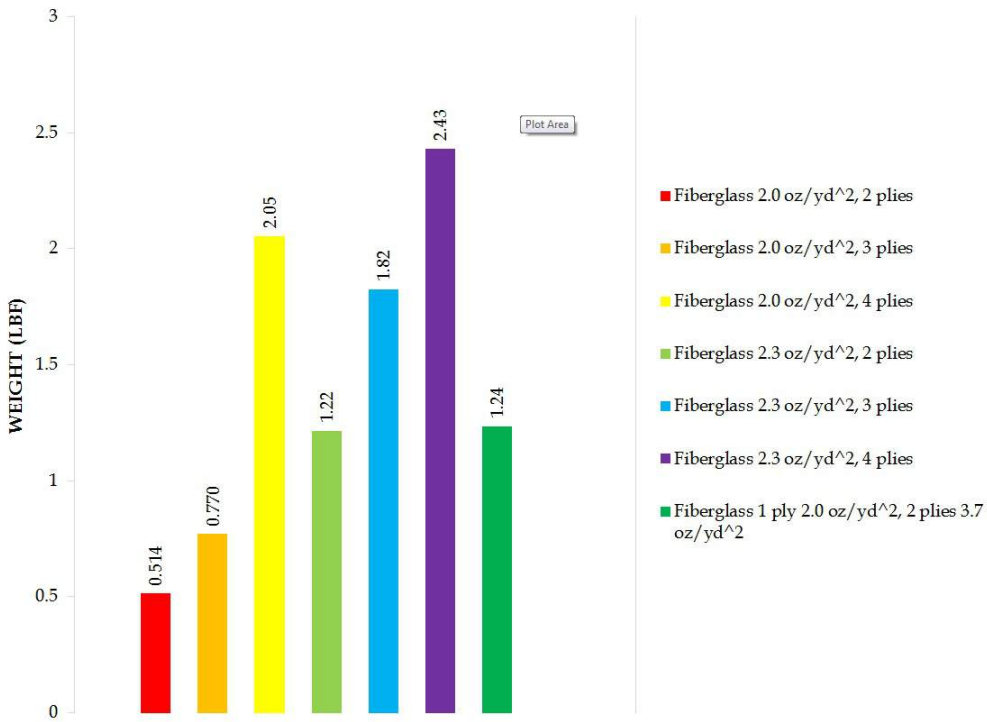


**Figure 7.0.5:** Comparison of weights based on material choices for the fuselage.

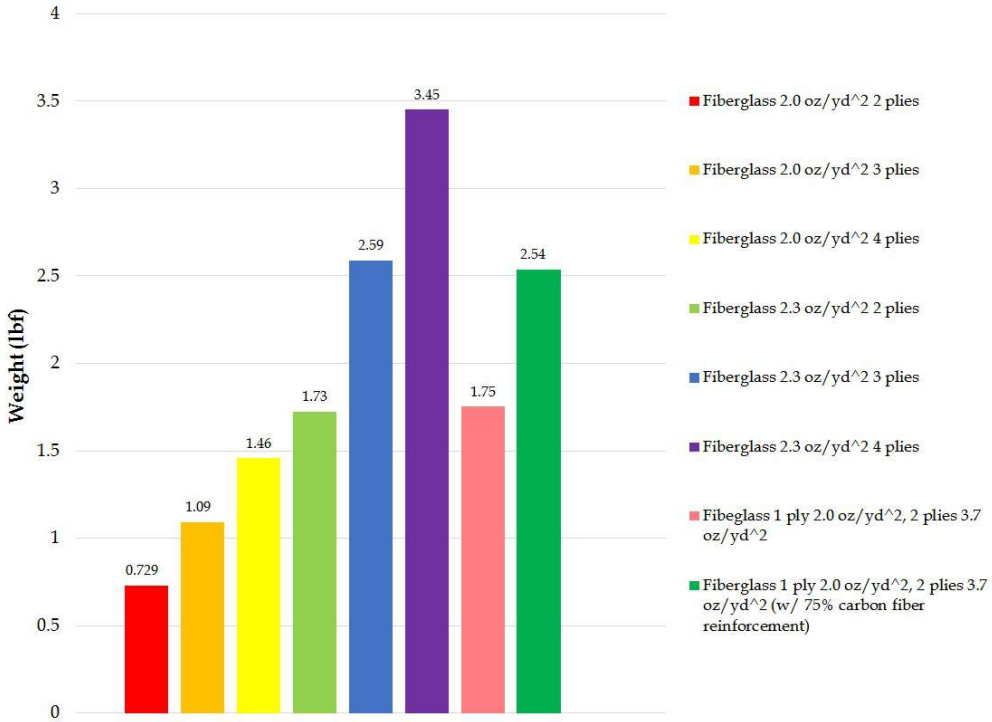


**Figure 7.0.6:** Comparison of weights based on material choices for the wings.

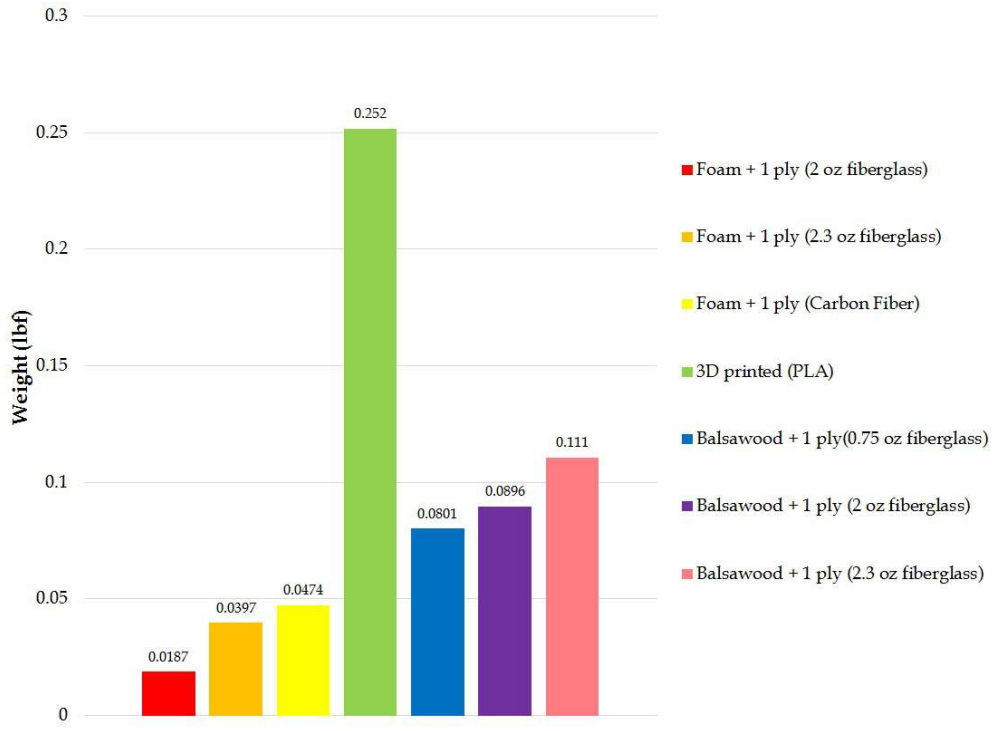


**Figure 7.0.7:** Comparison of weights based on material choices for the canards.

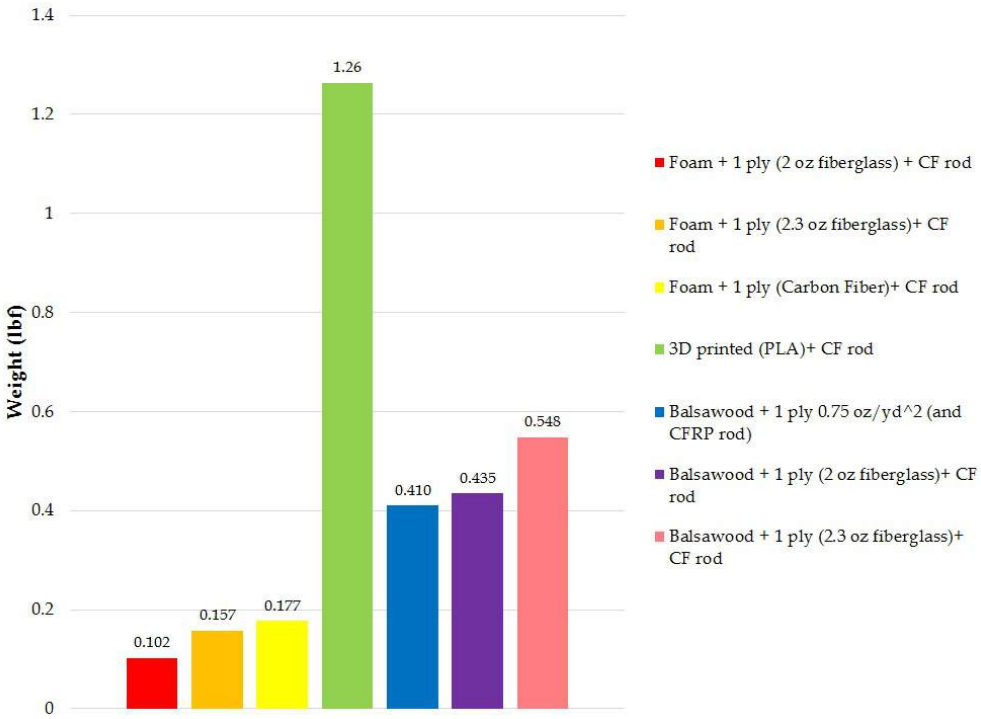


**Figure 7.0.8:** Comparison of weights based on material choices for the the horizontal stabilator.

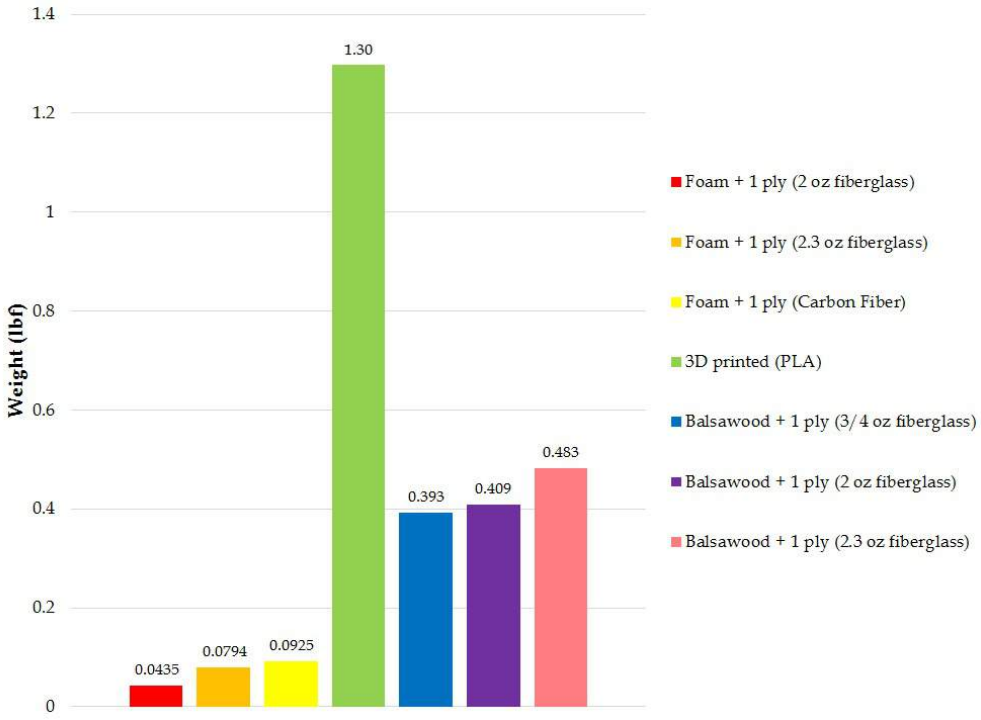


**Figure 7.0.9:** Comparison of weights based on material choices for the the vertical tail.

A balance between weight and structural integrity was taken into account when choosing

materials based on the previous figures. During the design phase, 3D printing materials was highly desirable for the time it would save and the improved accuracy in the parts. However, it is clear that it is harder to accurately estimate the weights of these parts. There are a variety of changes that can be made when manufacturing the part, such as infill percentages, that affect the weight. In future years, any experimentation with 3D printing should be done early, in order to have a better understanding and analysis of these parts. The final material choices for the R-UAV are summarized in Table 7.0.4.

**Table 7.0.4:** Material Choices for the R-UAV

| **Component** | **Material Choice** |
|---|---|
| Fuselage Skin | 4 plies of 2.0 $\frac{oz}{yd^2}$ fiberglass |
| Bulkheads/Spars | Carbon Fiber Foam Sandwich |
| Top Wing Skin | 1 ply of 2.0 $\frac{oz}{yd^2}$ + 2 plies of 3.7 $\frac{oz}{yd^2}$ w/ carbon fiber reinforcement |
| Bottom Wing Skin | 1 ply of 2.3 $\frac{oz}{yd^2}$ + 2 plies of 3.7 $\frac{oz}{yd^2}$ w/ carbon fiber reinforcement |
| Ribs | Carbon Fiber Foam Sandwich |
| Canards | Balsawood with 0.75 $\frac{oz}{yd^2}$ fiberglass |
| Horizontal Stabilator | Balsawood with $\frac{3}{4}$ $\frac{oz}{yd^2} fiberglass$ |
| Vertical Tail | Low Density Foam with $\frac{3}{4}$ $\frac{oz}{yd^2}$ fiberglass |

Weight was carefully monitored during the construction process to ensure the R-UAV would remain within the weight limitations. Fig. 7.0.10 depicts the differences in the various weight values calculated. Tabulated values including percent difference can be found in **APPENDIX STUFF AGAIN**.

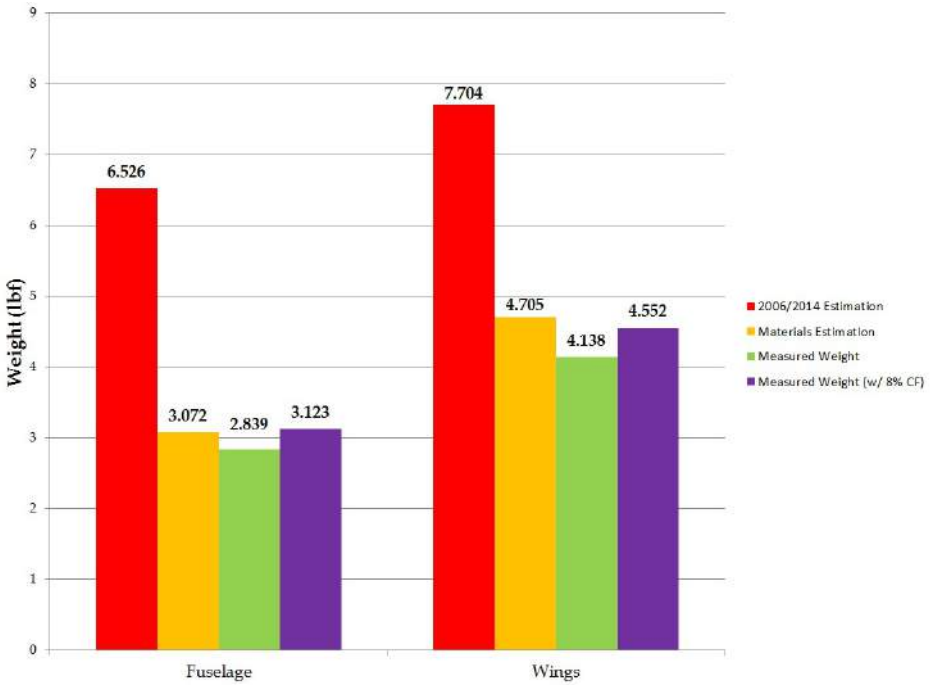


**(1)** Comparison of fuselage and wing weights.

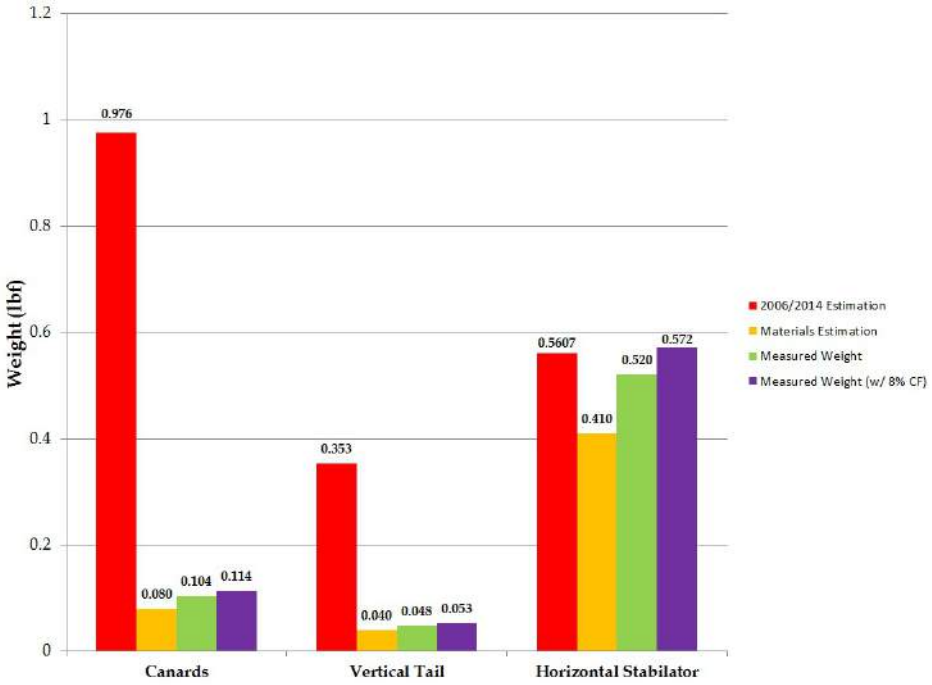


**(2)** Comparison of the canards, vertical tail, and horizontal stabilator weights

**Figure 7.0.10:** Weight Comparisons for Each Structural Component

It is evident that the initial estimation was not accurate to final measurements. One possibility for differences between these measurements are errors made in calculating between the 2006 and 2014 planes when finding area density. Another likely source is the distribution of reinforcements, fasteners, and material choices. Area density estimations assume that the weight within the wings and fuselage are distributed evenly along their skin, when in reality, it is concentrated based on where the structural supports are located. Lastly, because weight was actively trying to be reduced this year, different materials were used compared to 2014.

An important change to note in the weights analysis was the increase in nacelle weight. An estimation for nacelle weight was never calculated because it was initially assumed that the same nacelles from the 2014 design would be used. However, changes were made, mainly overall length and construction materials. A large portion of the nacelles are constructed from 3D printed PLA in order to hold the thrust-vectoring paddles and mount to the R-UAV. Alterations such as these were plausible throughout the entire design process, hence why an 8% correction factor minimum was always added to weight estimations.

Lastly, a total account for component weights is listed in Table 7.0.5. This includes all final structural weights (as of the date of this report) and fixed weights, such as the propulsion system, avionics, and landing gear. A 10% correction factor was included to account for any added weight as the R-UAV is completed. In particular, the servo connectors, additional weight from the servo arm attachments, epoxy from bonding parts together, and paint. Overall, it is evident that the R-UAV will meet the weight and performance requirements set forth at a weight of roughly 31 lbf.

**Table 7.0.5:** R-UAV Weight Breakdown

| Category | Component | Quantity | Weight Each (lbf) | Total Weight (l |
|---|---|---|---|---|
| Structures | Fuselage Skin | 1 | 1.775 | 1.775 |
| Structures | Bulkheads/Spars | 1 | 0.724 | 0.724 |
| Structures | Rig Frames | 5 | 0.0075 | 0.0375 |
| Structures | Wing Skin | 1 | 1.95 | 1.95 |
| Structures | Ribs | 1 | 1.208 | 1.208 |
| Structures | Horizontal Stabilator | 2 | 0.26 | 0.52 |
| Structures | Vertical Tail | 1 | 0.048 | 0.048 |
| Structures | Canards | 2 | 0.0518 | 0.104 |
| Structures | Nacelles | 2 | 1.11 | 2.22 |
| Structures | Ailerons | 2 | 0.0805 | 0.161 |
| Structures | Flaps | 2 | 0.0882 | 0.176 |
| Structures | Fasteners & Mounting Hardware | N/A | 0.1650 | 0.1650 |
| Propulsion | EDF | 2 | 1.534 | 3.068 |
| Propulsion | ESC | 2 | 0.532 | 1.064 |
| Propulsion | ESC/Battery Wires | 2 | 1.294 | 1.294 |
| Propulsion | ESC/EDF Wires | 4 | 0.0750 | 0.454 |
| Propulsion | 6S LiPo Battery | 4 | 1.254 | 5.016 |
| Avionics | Pitot Tube | 1 | 0.0198 | 0.01978 |
| Avionics | Current Measuring Device | 1 | 0.0639 | 0.0639 |
| Avionics | GPS Module | 1 | 0.0595 | 0.0595 |
| Avionics | Telemetry Radio | 1 | 0.0573 | 0.0573 |
| Avionics | Buzzer | 1 | 0.0088 | 0.0088 |
| Avionics | Switch/Push Button | 1 | 0.0044 | 0.0044 |
| Avionics | RC Encoder | 1 | 0.0154 | 0.0154 |
| Avionics | Pixhawk | 1 | 0.1860 | 0.1860 |
| Avionics | Alpha-Beta Sensor | 1 | 0.132 | 0.132 |
| Avionics | Arduino Mega Pro | 1 | 0.0875 | 0.0875 |
| Avionics | Breakout Board | 1 | 0.0374 | 0.0374 |
| Avionics | 1S LiPo Battery | 1 | 0.108 | 0.108 |
| Receiver | RX | 1 | 0.05 | 0.05 |
| Receiver | Battery | 1 | 0.3625 | 0.3625 |
| Receiver | Antenna | 1 | 0.2112 | 0.2112 |
| Servos | Horizontal Stabilator | 1 | 0.17 | 0.17 |
| Servos | Canards | 1 | 0.12125 | 0.12125 |
| Servos | Flaps | 2 | 0.130 | 0.260 |
| Servos | Ailerons | 2 | 0.048 | 0.096 |
| Servos | Thrust Vectoring | 2 | 0.048 | 0.096 |
| Servos | Rudder | 1 | 0.124 | 0.124 |
| Servos | Nose Gear | 1 | 0.124 | 0.124 |
| Landing Gear | Main Gear | 2 | 0.42 | 0.84 |
| Landing Gear | Nose Gear | 1 | 0.474 | 0.474 |

*7.0.5. Balances*

Results from the wind tunnel tests indicated that the aircraft should fly between 15% and 22% MAC, with the optimal position being 18% MAC. Based on a LE position at 60.2“ from the nose and MAC of 26”, a range of possible CG locations were calculated, as shown in Table 7.0.6.

**Table 7.0.6:** CG Locations of the R-UAV

| MAC Value | CG position (in inches from the nose) |
|---|---|
| 15% | 64.10 |
| 18% | 64.88 |
| 22% | 65.92 |

The specific CG of the R-UAV based on known positions was calculated via Eq. 7.0.1 and is summarized in Table 7.0.7

$$CG_{total} = \frac{CG_{component} W_{component}}{W_{total}} \tag{7.0.1}$$

**Table 7.0.7:** CG Locations of the R-UAV

| Axis | Location (in) |
|---|---|
| x | 64.68 (17.24% MAC) |
| y | -0.001 |
| z | 0.4410 |

For pure symmetry, the y-position of the CG should be on the y-axis, however, slight assymmetries in the overall configuration (such as servo mounts being off-axis) cause the CG to be mildly left to the centerline. This was such a small value, that it was approximated to be zero in all future calculations.

Another important component related to the balance of the R-UAV are the moments of inertia. They are critical components to analyzing the dynamic stability of the aircraft. By assumed symmetry of the aircraft, $I_{xy}$ and $I_{yz}$ are zero. However, each of the other terms was calculated based on the mass of individual components and their tabulated locations (from SolidWorks), according to Eq. 7.0.2.

$$I = mass * distance^2 \tag{7.0.2}$$

Tabulated values of each component, their, locations and individual moment of inertia values used for these calculations can be found in **MORE APPENDIX NONSENSE THAT I NEED TO KNOW ABOUT**. A summarized list is shown in Table 8.3.11.

**Table 7.0.8:** Moments of Inertia of R-UAV Components (Units: slugs/$in^2$)

| **Category** | **Component** | $I_{xx}$ | $I_{yy}$ | $I_{zz}$ | $I_{xz}$ |
|---|---|---|---|---|---|
| Structure | Total Structure | 10.42 | 63.24 | 74.66 | -21.8 |
| Propulsion | EDFs (2) | 1.235 | 32.34 | 33.57 | -32.9786 |
| Propulsion | ESCs (2) | 0 | 8.840 | 8.840 | -8.840 |
| Propulsion | Nacelles (2) | 0.8935 | 5.987 | 6.882 | -6.420 |
| Propulsion | Batteries (4) | 0.2286 | 37.97 | 38.20 | 38.08 |
| Propulsion | Component Wiring | 0.04444 | 5.193 | 5.237 | -3.330 |
| Avionics | Alpha-Beta Sensor | 0 | 13.81 | 13.81 | 13.81 |
| Avionics | Pixhawk System | 8.33 | 8.4 | 0.5384 | 19.09 |
| Avionics | Arduino Mega Pro | 7.394 x $10^-5$ | 0.01368 | 0.01375 | -0.01371 |
| Avionics | Arduino Battery | 0.0001391 | 0.02573 | 0.02587 | -0.02580 |
| Avionics | Breakout Board | 1.096 x $10^-5$ | 0.002026 | 0.002037 | -0.002032 |
| Receiver | Overall System | 0 | 9.062 | 9.062 | 9.062 |
| Servos | Overall System | 1.038 | 177.8 | 1.861 | 11.01 |
| Landing Gear | Nose Gear | 0 | 22.79 | 22.79 | 22.79 |
| Landing Gear | Main Gears (2) | 2.210 | 0.5063 | 2.716 | -1.166 |
| **TOTAL** | **Overall R-UAV** | **16.94** | **229.7** | **241.4** | **2.038** |

To ensure the R-UAV could meet these CG limits, the positions and weights of every component in the R-UAV were tabulated in Excel. The components which contributed the largest changes to the CG location were the internal structure, landing gear placement, and 6S LiPo battery placement. The internal supports and landing gears were determined based on structural necessities of the aircraft, thus the batteries were shifted as necessary to accommodate the desired CG location. In the R-UAV, the batteries ballast along the length of R-UAV via velcro attachments on the floor to change the CG depending on flight test requirements.

Another strict requirement on the placement of components were the moments of inertia. Based on previous years, it was known that these types of supersonic configurations are sensitive to changes in the moments of inertia of the aircraft. It was important to ensure calculations were accurate, thus two methods were used as checks against one another. The first was through modeling components in SolidWorks and using the properties in the model to determine moments of inertia of the components and overall aircraft. The other method was to do these calculations by hand. Another potential method would be to use Femap.

# For the Appendix

**Table 7.0.9:** 2006 Weights Information

| Category | Component | Quantity | Total Weight |
|---|---|---|---|
| Structure | Fuselage | 1 | 3.897 |
| Structure | Wings | 1 | 5.286 |
| Structure | Canards | 1 | 0.612 |
| Structure | Horizontal Stabilator | 2 | 0.462 |
| Structure | Vertical Tail | 1 | 1.011 |
| **Total** | | | **14.754** |
| **Total without H. Stab or Nacelles** | | | **10.806** |
| Propulsion | Overall System | 1 | 7.4 |
| Systems | Servo Batteries & Receiver | 1 | 0.871 |
| Systems | Nose Gear | 1 | 0.63 |
| Systems | Main Gear | 1 | 1.88 |
| Systems | Servos for Stabilators | 2 | 0.38 |
| Systems | Telemetry/Transmiterr | 1 | 0.132 |
| **Total** | | | **26.26** |

**Table 7.0.10:** 2006 Structural Weight Percentage Breakdown

| Component | Percentage |
|---|---|
| Fuselage | 26.41 |
| Wings | 35.82 |
| Canards | 4.148 |
| Nacelles | 23.62 |
| Horizontal Stabilator | 3.131 |
| Vertical Tail | 6.852 |

**Table 7.0.11:** 2014 Projected Weight Breakdown

| **Component** | **Projected Weight (lbf)** |
|---|---|
| Fuselage | 4.322 |
| Wings | 5.863 |
| Canards | 0.6788 |
| Nacelles | 0.8818 |
| Horizontal Stabilator | N/A |
| Vertical Tail | 1.121 |

**Table 7.0.12:** 2015 Component Sizes

| **Component** | **Surface Area $ft^2$)** | **Volume ($ft^3$)** |
|---|---|---|
| Fuselage | 11.67 | N/A |
| Wings | 16.56 | N/A |
| Canards | 0.698 | 3.36 x $10^{-3}$ |
| Horizontal Stabilator | 1.83 | 1.57 x $10^{-2}$ |
| Vertical Tail | 1.194 | 1.73 x $10^{-2}$ |

**Table 7.0.13:** Fuselage Weight Breakdown

| **Component** | **Material** | **Weight (lbf)** |
|---|---|---|
| Skin | 4 plies of 2.0 $\frac{oz}{yd^2}$ fiberglass | 1.775 |
| Bulkheads/Spars | Carbon Fiber Foam Sandwich | 0.2989 |
| Bulkheads # 3 & #11 | PLA | 0.242 |
| Rig Frame | Plywood | 0.0375 |
| Floor | Carbon Fiber Honeycomb Sandwich | 0.4856 |
| Hatch Fasteners | PLA + metal | 0.1625 |
| Landing Gear Mount | PLA | 0.1 |
| **Total** | | **3.064** |
| **Total w/ 10% Correction Factor** | | **3.3704** |

**Table 7.0.14:** Wing Weight Breakdown

| **Component** | **Material** | **Weig** |
|---|---|---|
| Top Skin | 1 ply of 2.0 $\frac{oz}{yd^2}$ fiberglass + 2 plies of 3.7 $\frac{oz}{yd^2}$ fiberglass w/ CF reinforcement | 1. |
| Bottom Skin | 1 ply of 2.3 $\frac{oz}{yd^2}$ fiberglass + 2 plies of 3.7 $\frac{oz}{yd^2}$ fiberglass w/ CF reinforcement | 1. |
| Spars | Carbon Fiber Foam Sandwich | 0. |
| Ribs | Carbon Fiber Foam Sandwich | 0 |
| Servo Mounts | Plywood | |
| Aileron Supports | Pink Insulator Foam | 0 |
| LE Droops | Pink Insulator Foam | 0. |
| Nacelle Mounts | Sheet Metal | |
| **Total** | | **4.** |
| **Total w/ 10% Correction Factor** | | **4.** |

**Table 7.0.15:** Moments of Inertia of R-UAV Components

| **Category** | **Component** | **x position** (in) | **y position** (in) | **z position** (in) | $I_{xx}$ (slugs-$in^2$ |
|---|---|---|---|---|---|
| Structure | Fuselage Skin | 53.7 | 0 | 2.51 | 0 |
| Structure | Wing Skin | 66.3 | 5.99 | 0.859 | 1.485 |
| Structure | LE Droop | — | — | — | — |
| Structure | Canards | — | —- | —- | —- |
| Structure | Vertical Tail | — | —- | —- | — |
| Structure | Horizontal Stabilator | — | —- | —- | —- |
| Structure | Bulkhead 1 | 10 | 0 | 1.16 | 0.025 |
| Structure | Bulkhead 2 | 22 | 0 | 2.22 | 0.422 |
| Structure | Bulkhead 3 | 29 | 0 | 4.21 | 3.10 |
| Structure | Bulkhead 4 | 37 | 0 | 4.69 | 2.44 |
| Structure | Bulkhead 5 | 42.5 | 0 | 2.75 | 1.69 |
| Structure | Bulkhead 6 | 55 | 0 | 2.06 | 5.48 |
| Structure | Bulkhead 7 | 67 | 0 | 1.5 | 13.2 |
| Structure | Bulkhead 8 | 70 | 0 | 1.35 | 14.7 |
| Structure | Bulkhead 9 | 76 | 0 | 1.17 | 16.1 |
| Structure | Bulkhead 10 | 80 | 0 | 1.16 | — |
| Structure | Bulkhead 11 | 89 | -0.05 | 2.25 | 0 |
| Structure | Bulkhead 12 | 97 | 0 | 2.0 | — |
| Structure | Bulkhead 13 | 106 | 0 | 2.31 | — |
| Structure | Rig Frame 1 | — | — | — | — |
| Structure | Rig Frame 2 | — | — | — | — |
| Structure | Rig Frame 3 | — | — | — | — |
| Structure | Rig Frame 4 | — | — | — | — |
| Structure | Rig Frame 5 | — | — | — | — |
| Structure | Rib 0.5 | — | — | — | — |
| Structure | Rib 1 | — | — | — | — |
| Structure | Rib 2 | — | — | — | — |
| Structure | Rib 3 | — | — | — | — |
| Structure | Rib 4 | — | — | — | — |
| Structure | Rib 5 | — | — | — | — |
| Propulsion | EDF | 83 | 3.55 | -2.45 | 331 |
| Propulsion | Forward ESC | 77.9 | 0 | 1.9 | 100 |
| Propulsion | Aft ESC | 84 | 0 | 1.89 | 117 |
| Propulsion | Nacelles | 74 | 3.55 | -1.96 | 190 |
| Propulsion | Forward Batteries | 40 | -1.0 | 2.24 | 87.4 |
| Propulsion | Aft Batteries | 48 | -1.0 | 2.21 | 128 |
| Propulsion | Battery/ESC Connectors | — | — | — | — |
| Propulsion | ESC/EDF Connectors | — | — | — | — |
| Avionics | Alpha-Beta Sensor | — | — | — | — |
| Avionics | Current Measure Device | — | — | — | — |

**Table 7.0.16:** Comparison of Initial Estimated Weight to Measured Weight

| Component | Initial Estimated Weight (lbf) | Measured Weight w/ 10% CF | Measured Weight (lbf) | % Diffe |
|---|---|---|---|---|
| Fuselage (skin + support) | 6.526 | 3.072 | 2.839 | -109 |
| Wings (skin + support) | 7.704 | 4.138 | 4.552 | -69.2 |
| Canards | 0.976 | 0.1036 | 0.1140 | -756 |
| Vertical Tail | 0.353 | 0.048 | 0.0528 | -569 |
| Horizontal Stabilator | 0.561 | 0.5200 | 0.5720 | 1.97 |

**Table 7.0.17:** Comparison of Material Estimated Weight to Measured Weight

| Component | Material Estimated Weight (lbf) | Measured Weight (lbf) | Measured Weight w/ 10% CF (lbf) | % Differe |
|---|---|---|---|---|
| Fuselage | 3.072 | 2.839 | 3.123 | 1.630 |
| Wings | 4.705 | 4.138 | 4.552 | -3.365 |
| Canards | 0.08015 | 0.1036 | 0.1140 | 29.68 |
| Vertical Tail | 0.03973 | 0.048 | 0.0528 | 24.75 |
| Horizontal Stabilator | 0.4080 | 0.5200 | 0.5720 | 28.36 |

## 7.1. Structural Design

### *7.1.1. Coupon Preparation and Testing*

#### 7.1.1.1. Carbon Plate and Sandwich Panel

A small sample of test coupons were manufactured and strained to failure to obtain the material properties needed for hand calculations and FEA analyses. Ten T800
3900 coupons were manufactured and five honeycomb sandwich panels were cut from bulk material purchased from ACP Composites. Because the T800/3900 is a composite material the compressive and tensile moduli are expected to be notably different, however the samples manufactured were only tested under tensile loading. The tensile coupons produced were water-jetted from an 8 ply specially orthotropic laminate, because the plain weave itself is specially orthotropic the laminate layup was simply [ 04 ]s. The geometry of the coupons was dictated by AMTAS D3039 standards, and plastic tabs were added to reinforce the coupons at the gripping locations per these standards. No specifications are prescribed for the epoxy which bonds these tabs to the specimen, standard procedure is to use a trial and error approach for the epoxy. AMTAS standards can be obtained online or by contacting either Mark Tuttle or Bill Kuykendal in the Mechanical Engineering Department. The geometry

used for the tensile specimen and plastic tabs appear in Fig. 7.1.1 below, where dimensions are in inches.

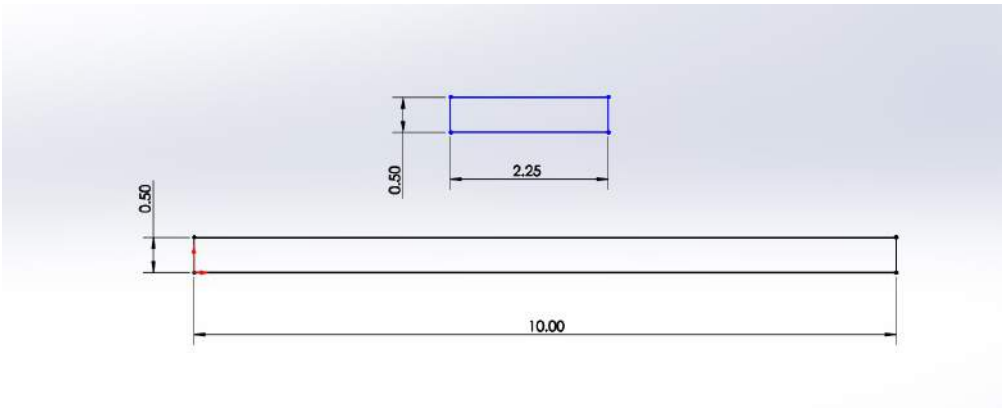


**Figure 7.1.1:** Tensile Coupon Geometry

The tensile coupons were water-jetted from a panel made using the ME departments hot press machine. Two major errors occurred at this stage and can be easily avoided in the future. First the manufacturer's autoclave cure cycle cannot be directly substituted for a hot press cure cycle. Secondly, when dealing with donated fiber the supplier should be contacted directly to verify the fiber/resin system and to obtain the correct cure cycle. Misinformation related to the fiber/resin system and an improper hot press cure cycle resulted in improperly manufactured specimens. Tensile testing was accomplished by installing the coupons in the ME departments Instron machine and applying tensile loading to failure. The transverse poisons ratio was measured using a video extensimeter which tracked the displacements of dots painted on the coupon prior to testing. This method did not provide reliable values for the poison's ratio, which likely occurred due to bowing of the sample during testing. To obtain better data the width of the specimen could be increased, or strain gauges could be used. Fig. 7.1.2 below shows the test setup for the tensile specimen. The data analysis for the tensile testing was minimal due to the error in manufacturing technique, therefore only the stress – strain data is included below. (table is only here to orient the figures)

**(1)** Tensile Testing Setup

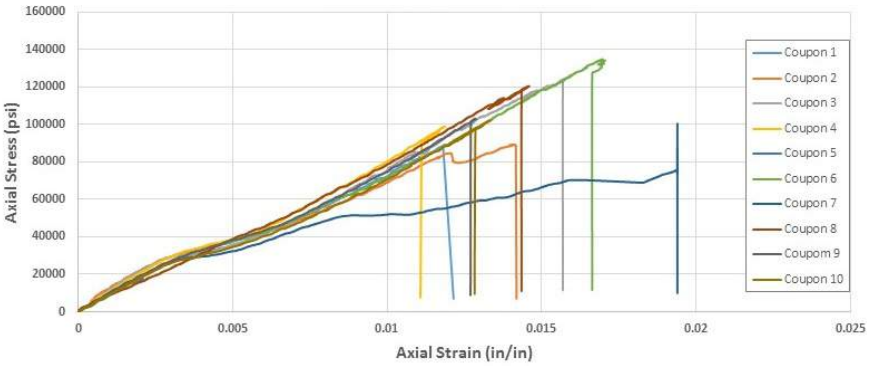


**(2)** Tensile Testing Results

**Figure 7.1.2:** Example Subfigures

More effort was dedicated to determining the flexural modulus of the sandwich panels as shown in Fig. 7.1.3 below.

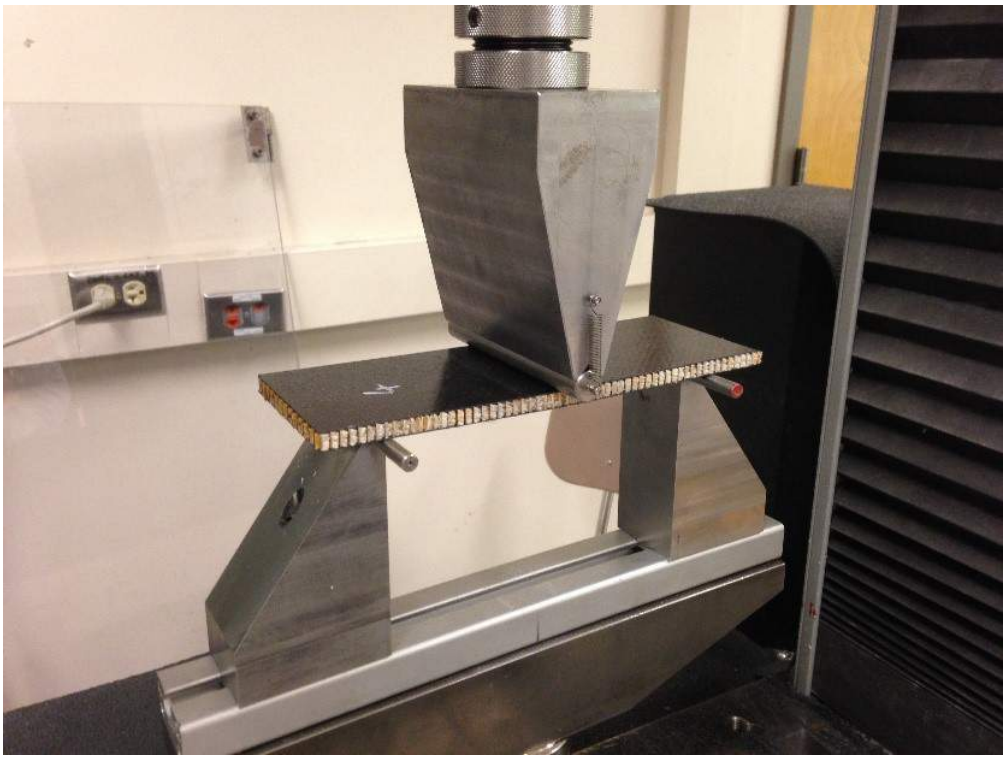

**Figure 7.1.3:** Honeycomb 3-pt Bend Testing

#### 7.1.1.2. Fiberglass Coupons

In order to find Young's modulus of fiberglass, simple tensile coupon testing was performed. Since the number of layers of fuselage and skin were undetermined at this time, 8 layers of fiberglass coupons were manufactured. The size of coupon specimen were followed

by ASTM standard which was 10" depth and 1" width. Each end of specimen were clamped using sandpapers to prevent damaging the specimen from the Instron machine. Figure 7.1.4 shows the test specimen after ultimate load.

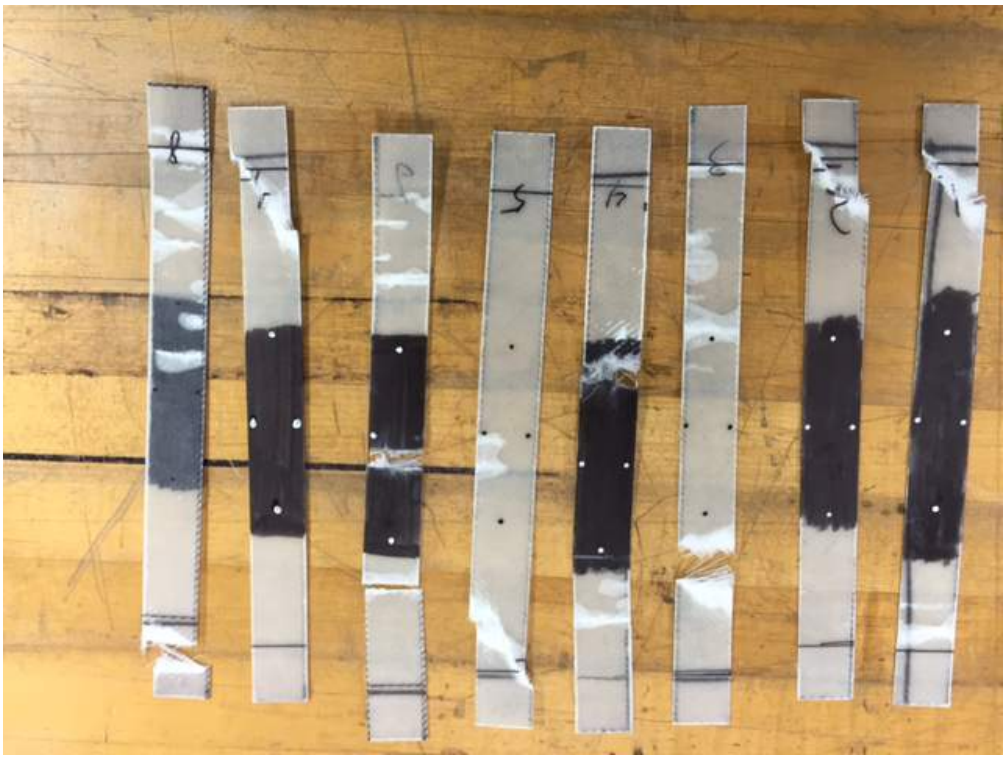

**Figure 7.1.4:** Fiberglass tensile specimens

The Figure 7.1.5 shows the results of the tensile test from specimen 1 to 8. Neglecting two extreme specimen data, the average Young's modulus is 2.4 Msi and Poisson's ratio is 0.117.

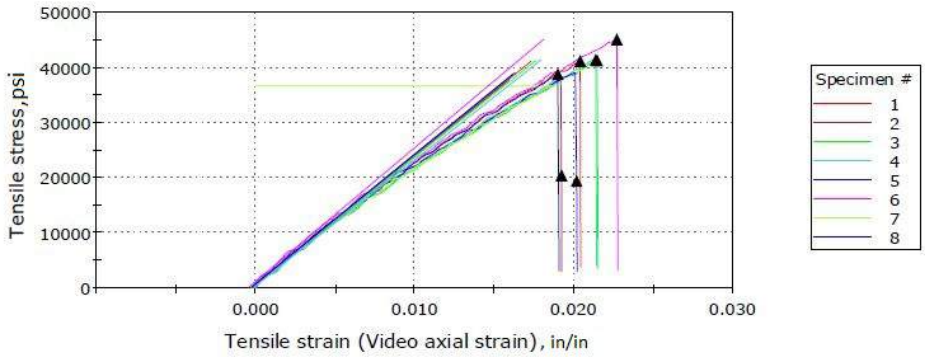


**Figure 7.1.5:** Instron results for fiberglass samples in tension.

Unlike metals, composite laminates have different Young's modulus in flexural property. Since the loading conditions of fuselage or skin will be from flexural, bending loads, it was

important to find Young's modulus in flexural mode. Three point bending test of different layers of fiberglass coupons (0.024 and 0.032" thickness) were performed. The size of coupons were followed by ASTM standard which was width of 1.67" and support span of 1". The Instron test provided loads (lbf) and deflections (inch) of the coupons. Using the data from the Instron test, FEMAP analysis were made to find the Young's modulus. First, the isotropic, plate type coupon was created. Second, pinned the location separated by span width. Third, apply loads from the Instron data. Finally, compare the deflection of the results and try to match it with the test data by adjusting the Young's modulus. Using the Young's modulus from the tests, the interpolation equation was calculated to assume the Young's modulus of different numbers of layers. The Figure 7.1.6 shows the FEMAP model of 3 point bending test.

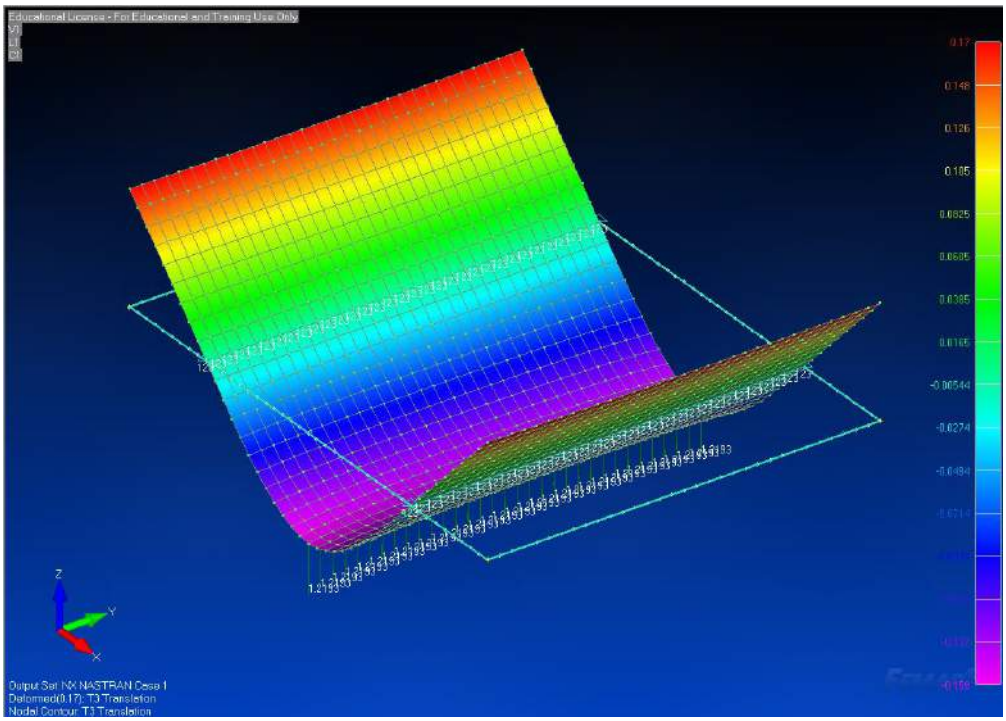


**Figure 7.1.6:** Femap modeling of the fiberglass samples undergoing a 3-point bending test.

The results of the test, including interpolation for actual skin layup is listed on Table 7.1.1.

In order to determine the flexural shear modulus of the fiberglass we are using, torsional test was conducted on a rectangular fiberglass plate. This is a coarse material test to obtain the rough estimate of the flexural shear modulus due to the limitation of time and experimental apparatus.

The test specimen is made from eight plies of 4 in x 6 in 2oz fiberglass to have a total 16 ounces, or 0.032 in thickness. The setup of the test is shown in Figure 7.1.7. With one end of the specimen fixed on a vise, two deflection gauges are located at the two remaining free corner to measure the displacement during testing. Wood sticks are glued to the free end of the specimen so that the moment applied can be uniformly distributed. With a small clamp is placed in the center of the free end, it acts as a moment arm so that normal force can be applied at the other end of the clamp using a digital force gauge. Various forces are applied

**Table 7.1.1:** Fiberglass 3-point bending test results.

| Specimen | Thickness (in) | Total weight (oz) | Modulus (Msi) | Interpolated modulus (Msi) |
|---|---|---|---|---|
| 6 plies | 0.024 | 12 | 1.69 | - |
| 8 plies | 0.032 | 16 | 1.61 | - |
| Actual skin (lower wing) | 0.0194 | 9.7 | - | 1.736 |
| Actual skin (other) | 0.0188 | 9.4 | - | 1.742 |

and the corresponding end deflection are measured and recorded.

**Figure 7.1.7:** The actual torsion test setup used.

After acquiring data from torsional test, FEMAP was used to model the test assuming isotropic material properties, shown in Figure **??**. Similar to the previous fiberglass bending test modeling, by applying the same loading condition as the actual physical test, the material properties are adjusted so that the deflections match the ones recording in the physical test.

The flexural shear modulus is determined to approximately be 0.9 Msi. The results of these tests can be seen in Table 7.1.2 below.

**Table 7.1.2:** Fiberglass torsion test results.

| Property | 2014 (tensile test) | 2015 (flexural test) |
|---|---|---|
| Elastic Modulus (Msi) | 1.97 | 1.74 |
| Shear Modulus (Msi) | 0.84 | 0.90 |

2014 Fiberglass material test uses tensile test to obtain its normal material properties. However, since fiberglass is mostly used as the airplane's skin for the design, it is more appropriate to test for its flexural properties in respond to its real loading. Therefore, it is reasonable that this year's elastic modulus is lower than last year's while the shear modulus is higher. These numbers are used in finite element analysis for fiberglass as isotropic material for simplicity. Also, the Poisson's ratio should be left in blank since it is not really applicable in this case, and FEMAP can automatically calculate it eventually.

**Figure 7.1.8:** Femap modeling of the fiberglass samples undergoing a torsion test.

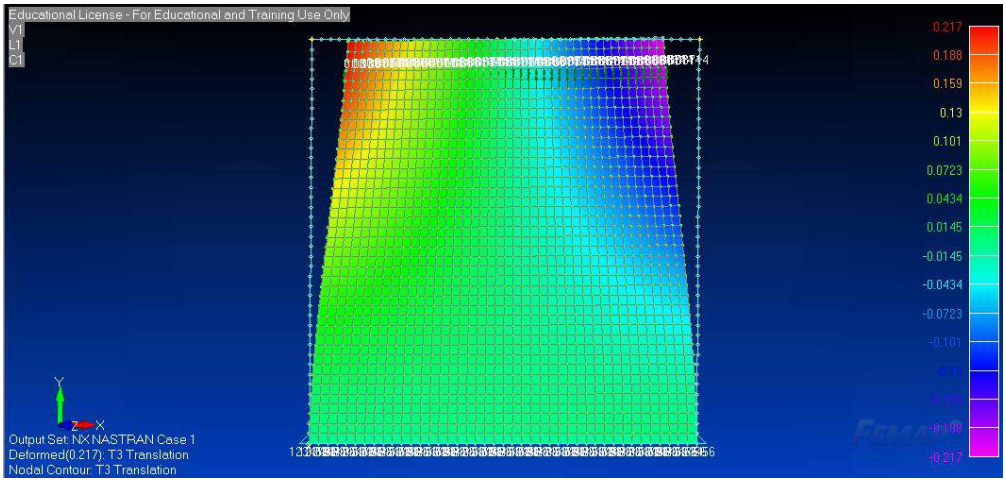


### 7.1.1.3. Developing Allowables

A goal was set to use the data collected from Instron testing to develop allowable basis values that could be used in the design process. Although there is not a vast array of samples available, the practice of defining basis values gives gives a statistically more sound design. To create the basis values, the mean and standard deviation were calculated. From there, it was possible to calculate what points were outliers (if they were greater than a deviation out). Looking at each of these outliers it was possible to determine if the coupon should be kept within the data or removed. Examples of times when data should be removed include:

- If the plastic tabs on the specimen fail.
- If the material fails outside the desired testing area (such as around or under the tabs).
- If external damage exists that was not intended or undesired.
- If there is slipping of the coupon or tabs in the Instron grips.

Because the failure criteria/mode is important in determining if the data is legitimate or not, they should be noted during testing. Once the has been cleaned up, the coefficients for each basis can be calculated using statistically determined values found in handbooks. The B-basis coefficient equation can be seen in Equation 7.1.1.

$$k_{bj} = Z_b\sqrt{f}Q + \sqrt{1}C_B n_j + (b_B/(2c_B))^2 + (b_B/(2c_B)) \tag{7.1.1}$$

As was mentioned, all the values used to determine the coefficient are provided in handbooks. Taking this coefficient, the usable basis values are calculated using Equation 7.1.2

$$\sigma_{B-basis} = \sigma_{mean} - k_{bj}\sigma_{stddev} \tag{7.1.2}$$

Using this process, the allowable values produced for the materials tested can be seen in Tables 7.1.3 through 7.1.5.

**Table 7.1.3:** Basis values found for the honeycomb sandwich panels (ACP) in bending.

| Item | Value |
|---|---|
| $\sigma_{A,flex}$ (ksi) | 5.38 |
| $\sigma_{B,flex}$ (ksi) | 5.69 |
| $\epsilon_{A,flex}$ (in/in) | 0.0058 |
| $\epsilon_{B,flex}$ (in/in) | 0.0067 |

**Table 7.1.4:** Basis values found for the T700 tension specimens.

| Item | Value |
|---|---|
| $\sigma_{A,T}$ (ksi) | 42.1 |
| $\sigma_{B,T}$ (ksi) | 68.6 |
| $\epsilon_{A,T}$ (in/in) | 0.0044 |
| $\epsilon_{B,T}$ (in/in) | 0.0084 |

**Table 7.1.5:** Basis values found for the 2oz fiberglass tension specimens.

| Item | Value |
|---|---|
| $\sigma_{A,T}$ (ksi) | 31.4 |
| $\sigma_{B,T}$ (ksi) | 34.5 |
| $\epsilon_{A,T}$ (in/in) | 0.0159 |
| $\epsilon_{B,T}$ (in/in) | 0.0178 |

These values can be applied to later stress to aid in determining an accurate, safe factor of safety.

### *7.1.2. Component Level Testing*

#### 7.1.2.1. Canard Test

The purpose of canard deflection testing was to determine which material will provide the most desirable characteristics. The type of canards tested were carbon-foam, fiberglass-balsa, fiberglass-foam, and PLA. Each test was carried out using the same procedure. The canards were clamped at the root. The loading point attachment was positioned 5 inches from the middle of the fixed root. Once the canards were secure, loading commenced until failure. While loading, the deflection was measured to collect Load-Deflection data to find out which material provided the best strength characteristics. The carbon-foam canard was the third best in terms of strength before failure. The maximum load before failure was 4.23 pounds. This load caused a deflection of 0.70 inches. Fig. 7.1.9 and Fig. 7.1.10 below shows the setup of the canard and various loading weights and its correlated deflection.

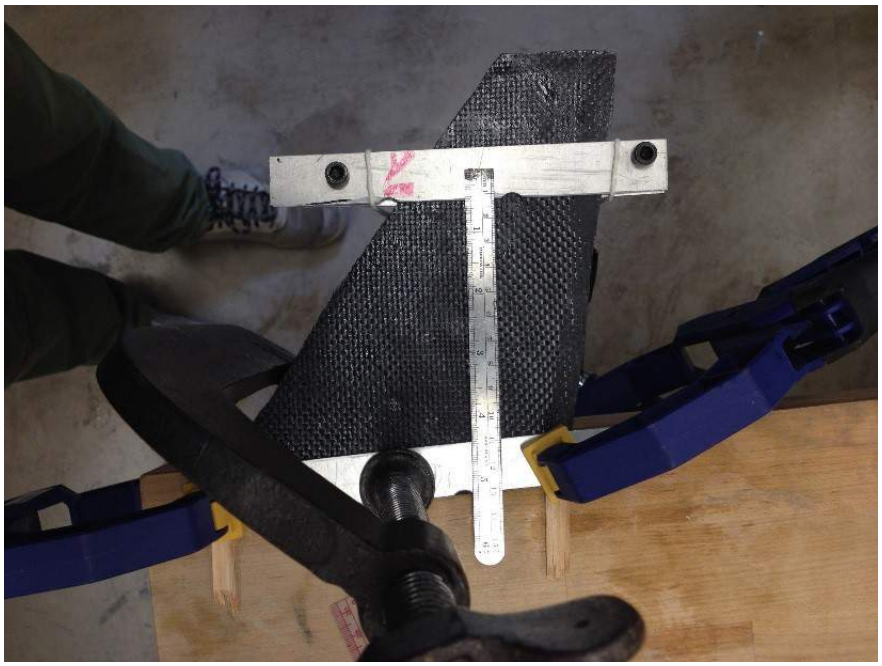

**Figure 7.1.9:** Carbon-foam Canard

**(1)** Carbon-foam Canard Deflection w/ Light Weights

**(2)** Carbon-foam Canard Deflection w/ Heavier Weight

**Figure 7.1.10:** Carbon-foam Deflections

The fiberglass-balsa canard was the second best in terms of strength. Final failure occurred at about a load of 6.8 pounds with a 0.9 inch deflection. Fig. 7.1.11 (1) below shows the setup of the test and Fig. 7.1.11 (2) displays the failure of the canard.

**(1)** Test Setup

**(2)** Fiberglass-balsa Failure

**Figure 7.1.11:** Fiberglass-balsa Deflection

The fiberglass-foam canard performed the worst. The fiberglass-foam canard delaminated at around 1.242 pounds at a deflection of about 0.98 inches. As can be seen from Fig. 7.1.12 below, the delamination points are outlined in blue marker.

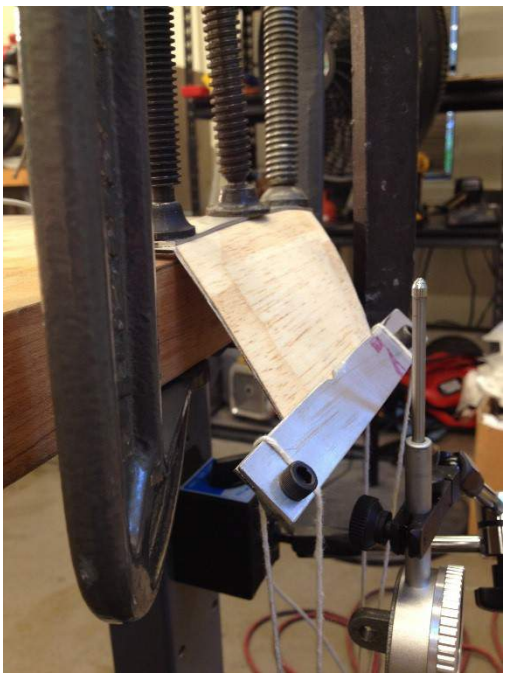

**Figure 7.1.12:** Fiberglass-foam Delamination Points

The PLA canard was the best material for the canard in terms of strength. The PLA canard testing ended before failure due to the high load causing the weight bracket to fall off. This happened at a weight of 29.59 pounds at a deflection of 1.205 inches. As can be seen from the data, the canard is very stiff. Testing for this canard can be seen below in Fig. 7.1.13.

**Figure 7.1.13:** PLA Canard Testing

Fig. 7.1.14 below is a Load-Deflection plot of all the tested canards.

**Figure 7.1.14:** Canard Load vs. Deflection

As can be seen from the chart, PLA is the material that will be used for the canards due

to its high strength properties.

### *7.1.3. Canard Mount Design*

The canard mount was designed with the purpose of joining the canard with the actuation system in the aircraft. The canard shape extension is to be inserted into the middle of the canard such that the root of the canard is flush with the base of the canard mount. This applies to both canards. Once the canards are attached, both canard mounts from each side will be connected in the middle and connected to actuators to control the desired deflection during flight. The dimensions of the bar for the canard mount is 0.25 inches. The canard mount insert to the canard has a thickness of 0.05 inches and is lofted such that the taper of the mount follows the taper of the wing. The base of the mount is the same size as the cross section of the canard root. The base is extruded 0.1 inches to form a solid base for the canard. The canard mount will be made out of PLA and 3d printed. Fig. 7.1.15 below shows an isometric view of the system.

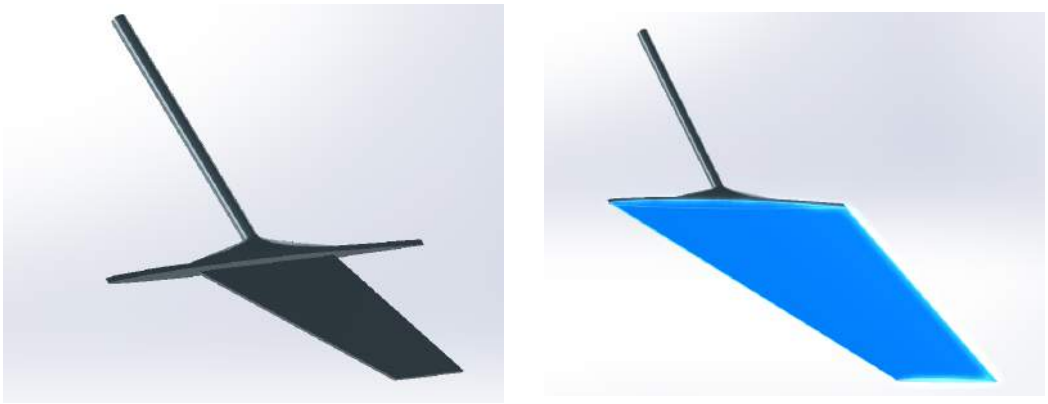

**(1)** Canard Mount w/o Canard

**(2)** Canard Mount w/ Canard

**Figure 7.1.15:** Canard Mount

### *7.1.4. Full Model Finite Element Analysis*

#### 7.1.4.1. Model Preparation and Meshing

To model the aircraft in FEMAP the inboard wing skin must be meshed. The FEMAP model was greatly delayed while this section went through multiple iterations due to the complexity of this task, and misdirection from the structural advisor. To speed up progress in the future an overview of the multiple meshing options is included in this section.

The general process for creating the inboard wing mesh is as follows. First surfaces must be generated on the top and bottom faces of the wing. This is accomplished by creating lines. It is also useful to mesh a curve to place nodes on that curve, and then form a different curve by splining those nodes. After the desired curve has been produced the nodes used to form it can be deleted. Once all curves running along the edge of a surface have been created they can be used to form a surface. These surfaces are then meshed using a mesh control command to size along the edge curves. To produce a "structured mesh" which will be approved by Marat you will need to remove the angle restrictions when meshing as shown in Figs. 7.1.16 and 7.1.17 below. Analysis will be added after obtaining data

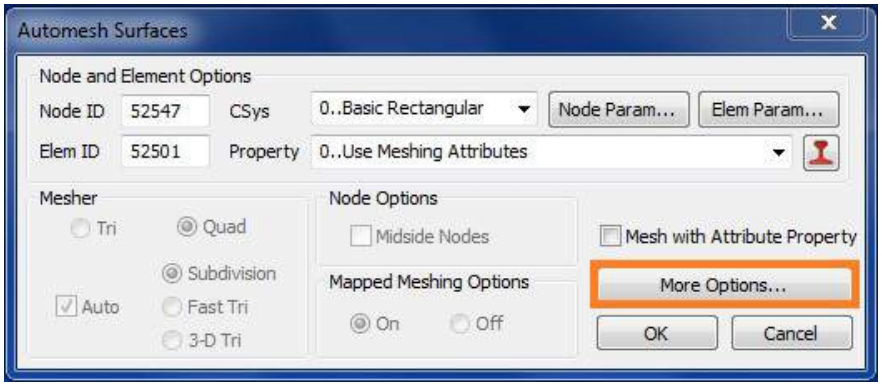


**Figure 7.1.16:** Aeroelastic mesh

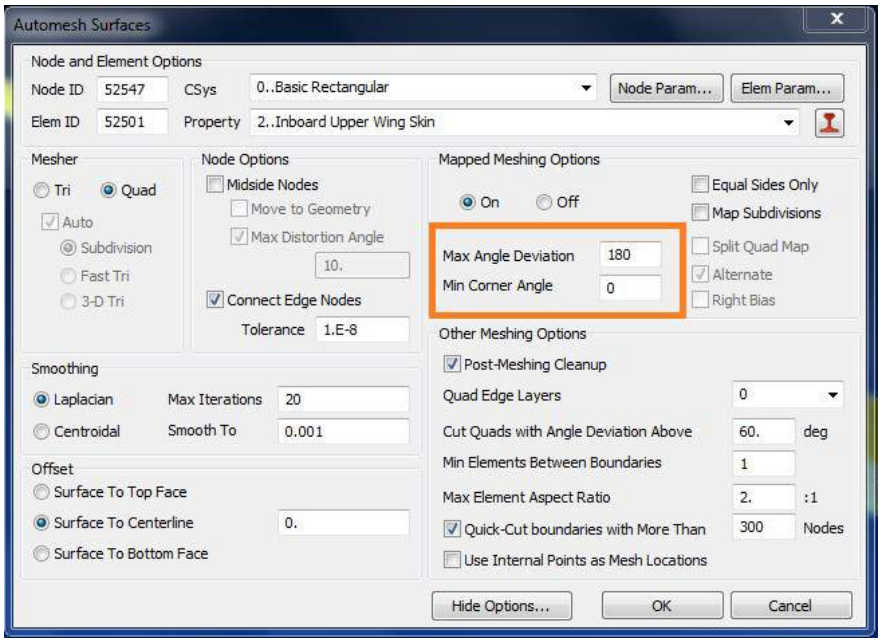


**Figure 7.1.17:** Removing Surface Mesh Angle Restrictions

Above is the general procedure for creating the inboard wing meshing, however there are some additional steps that may be taken to produce a more useful meshing. The surface meshing used to form the wing skin will provide the nodes ultimately used to model the internal structure. Therefore the top and bottom surfaces of the wing must have identical meshing. This occurs naturally for other sections of the model, however, because the bottom surface of this year's R-UAV wing is flush with the bottom of the fuselage an extra step must be taken for the wing. The lower surface must be divided using a command like slice (geometry => Curve From Surface => Slice) so that top and bottom nodes are vertically aligned. This will create an irregular surface which must be free meshed. Fig. 7.1.18 below shows the meshing for the upper wing skin highlighted in yellow, and Fig. 7.1.19 shows the irregular surface produced from the slicing operation highlighted.

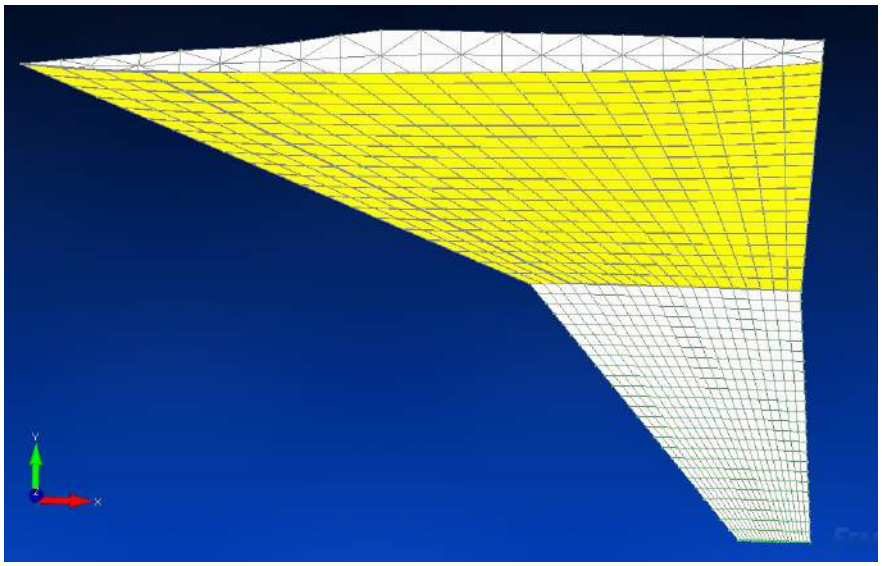

**Figure 7.1.18:** Upper Wing Skin

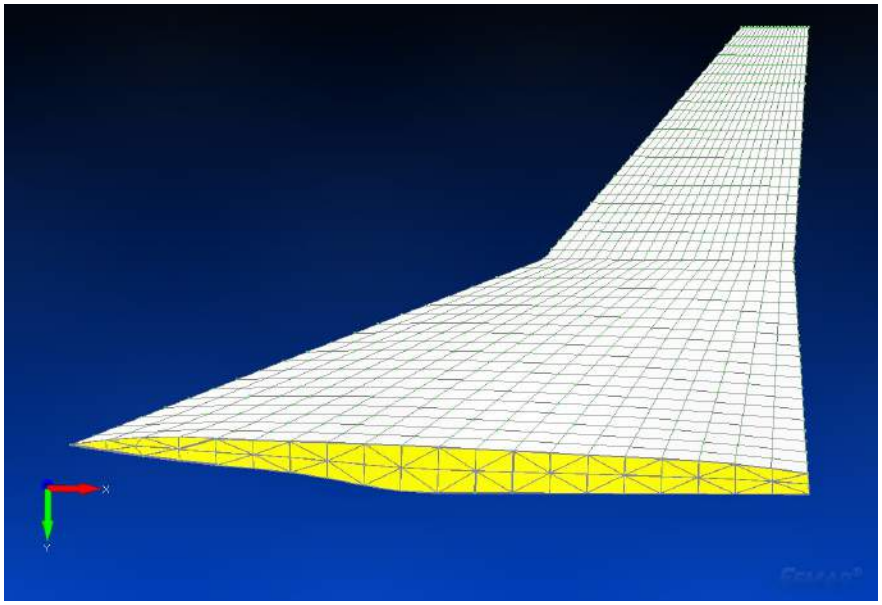

**Figure 7.1.19:** Irregular Mesh On Lower Wing Skin

After the inboard wing skin is meshed the internal structure can be added. This was accomplished by using a clipping plane for better viewing. This feature can be accessed as shown in Fig. 7.1.20 below.

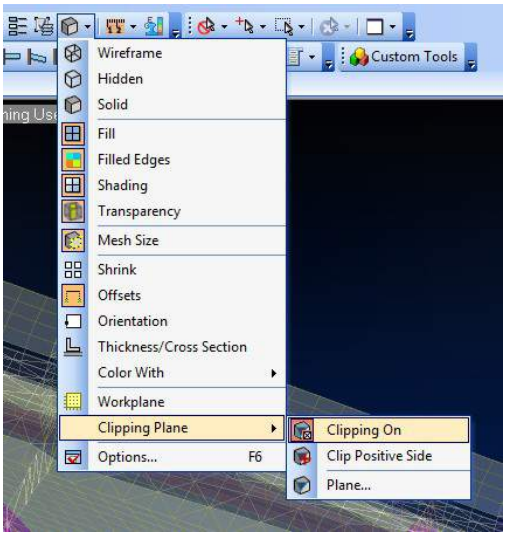


**Figure 7.1.20:** Clipping Plane View Tool

Once the clipping plane is setup as desired the internal structure can be meshed using triangular elements. It would be better to use quad elements since the strain is not continuous along the edge of triangular elements, however, we were advised to mesh all internal structure using triangular elements. Meshing the internal structure can be accomplished by manually adding elements and either maximizing refinement as shown in Fig. 7.1.21, or by skipping available nodes to produce the straightest internal component possible as shown in Fig. 7.1.22. The second method was used.

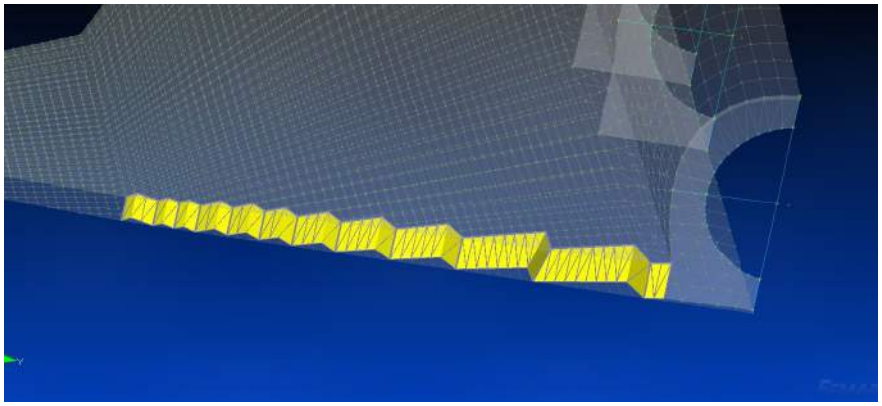

**Figure 7.1.21:** Maximum Refinement of Internal Components

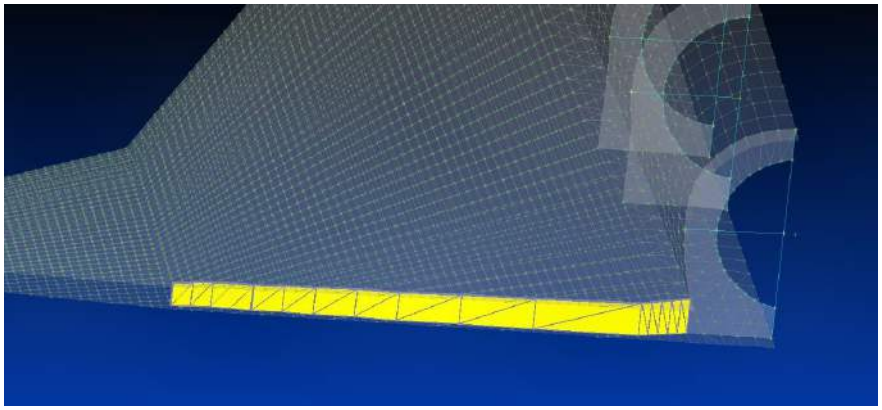

**Figure 7.1.22:** Straight Internal Components

The figures above show that the meshing used for the wing skin will influence how the internal layout will appear. If it's known in advance how the internal layout will be, then the surface meshing for the wing could defined differently over multiple surfaces to enable the internal structure to be located correctly. Similarly the size of the surface mesh will influence the spar cap size in the model, therefore a highly refined skin mesh would be useful so that spar cap modeling can be more representative of the actual structure. Fig. 7.1.23 below shows the internal structure with spar caps highlighted in purple.

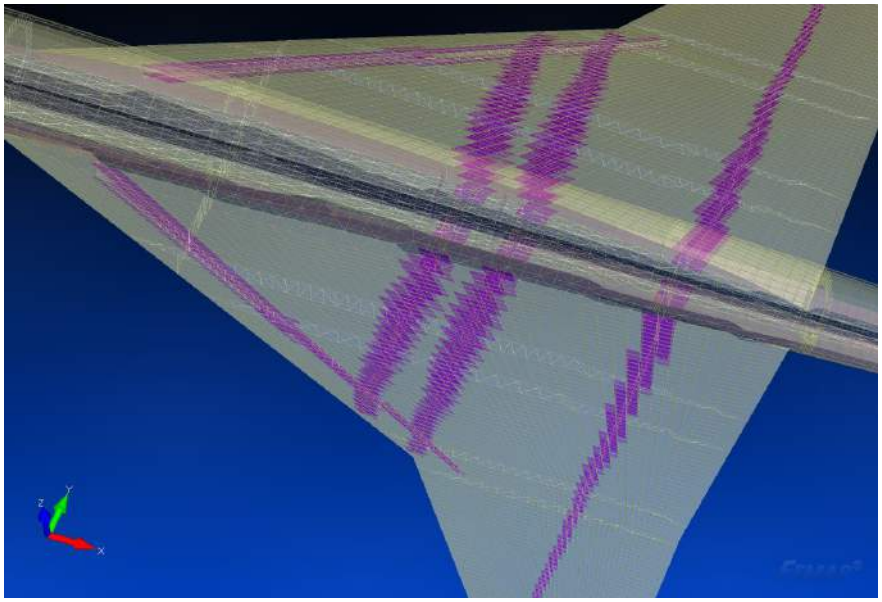

**Figure 7.1.23:** Internal Structure for Inboard Wing

#### 7.1.4.2. Inboard Wing Mesh

As part of the overall structural mesh for the aircraft, the inboard wing was meshed to provide accurate analysis of stress and deflection in response to aerodynamic loading and point loads. The mesh was created such that the majority of elements were quad elements and triangular elements were used to fill in gaps between transition regions. This was to ensure that surface meshes were not too refined but still provided an accurate structural analysis. An image of the final inboard wing mesh in FEMAP is shown below in Fig. 7.1.24.

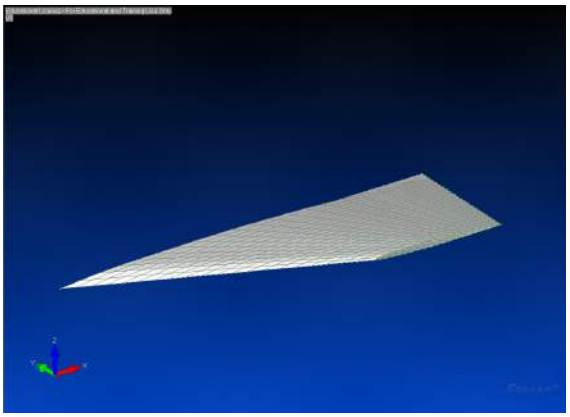

**(1)** Inboard Wing Mesh

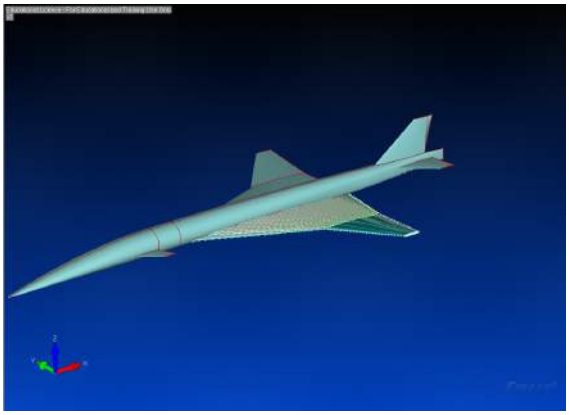

**(2)** Inboard Wing mesh w/ Surface Geometry Overlayed

**Figure 7.1.24:** Inboard Wing Figures

#### 7.1.4.3. Horizontal Tail Mesh

The structural mesh is a vital part of the analysis portion. It allows the team to accurately model and test our final structure to specific desired characteristics. A structural mesh allows for inexpensive material testing with accurate result by using finite element analysis software. Figure 7.1.25 below displays the window into the FEMAP program with a structural mesh for one side of the horizontal tail.

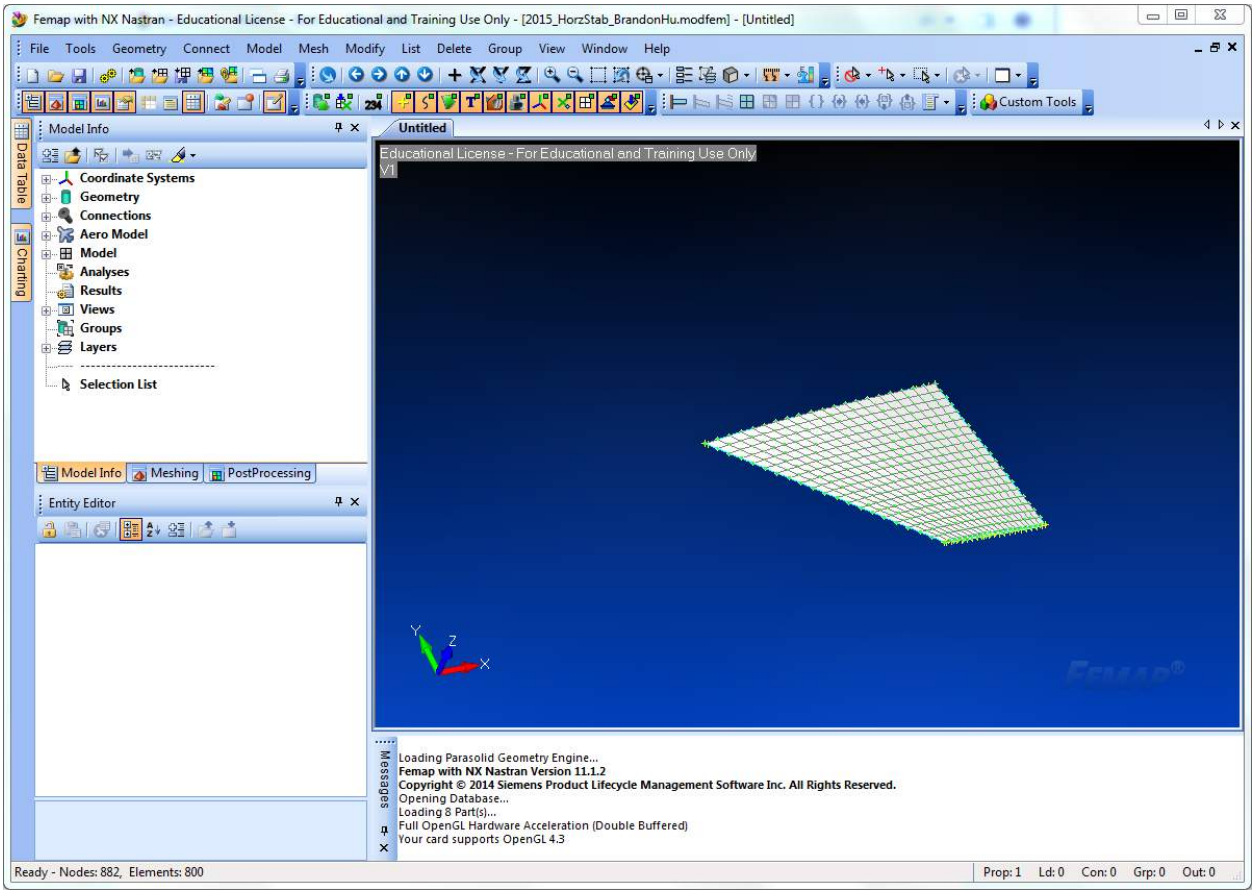


**Figure 7.1.25:** Horizontal Tail Mesh

#### 7.1.4.4. Aeroelastic Mesh

In addition to the structural mesh, an aeroelastic mesh was created for flutter/vibration analysis. Aero panels/bodies were first created by measuring lifting surface dimensions and applying them in FEMAP. An image showing the aero panels is shown below in Fig. 7.1.26.

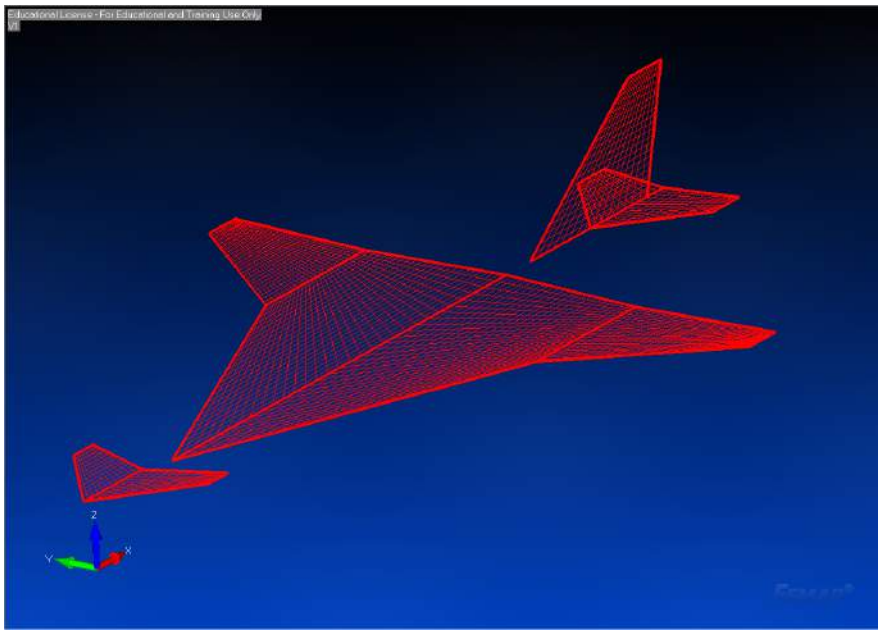

**Figure 7.1.26:** Aeroelastic Panels

Aero splines were then made to relate forces from the aircraft body to the aero panels. This allowed for flutter/vibration analysis to be done given loadings and load locations. A picture showing the aeroelastic mesh is shown below in Fig. 7.1.27.
Analysis will be added after obtaining data

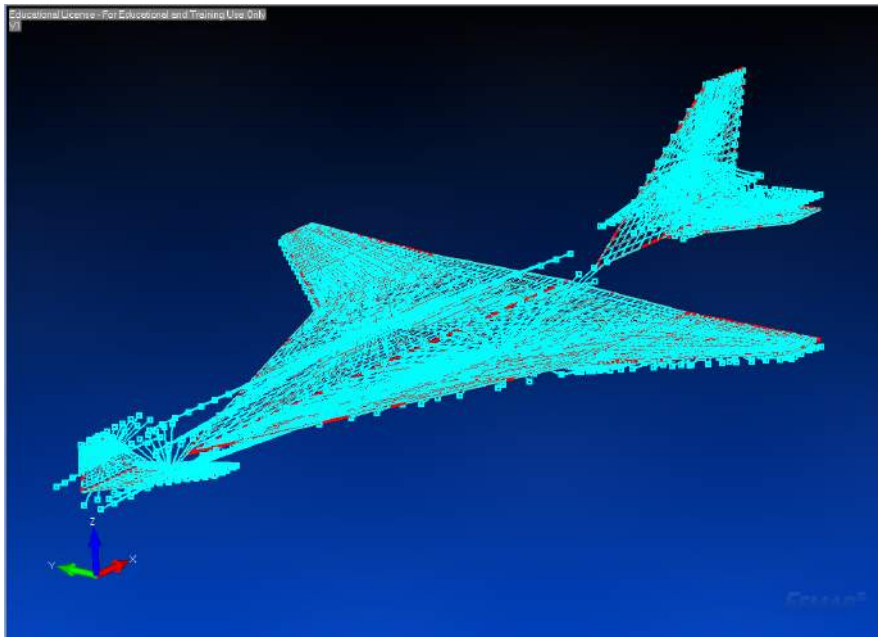

**Figure 7.1.27:** Aeroelastic Mesh

#### 7.1.4.5. General Meshing Resources

There are a number of strong resources online related to analysis in FEMAP. However, to supplement the process specific to this course, a hand full of instructional videos outlining

the processes used in meshing and creating the finite element model were created and are located on the Z-drive (*Z/2015/Team/Structures/Femap Files/Femap Meshing Tutorials*). These may prove useful in speeding up the initial development process, thus allowing more time to run analysis.

#### 7.1.4.6. Finished Structural Layout

After completing all the external surfaces using the methods outlined earlier and then creating the internal structure manually, element by element, the model appeared as seen in Figures 7.1.28 and 7.1.29.

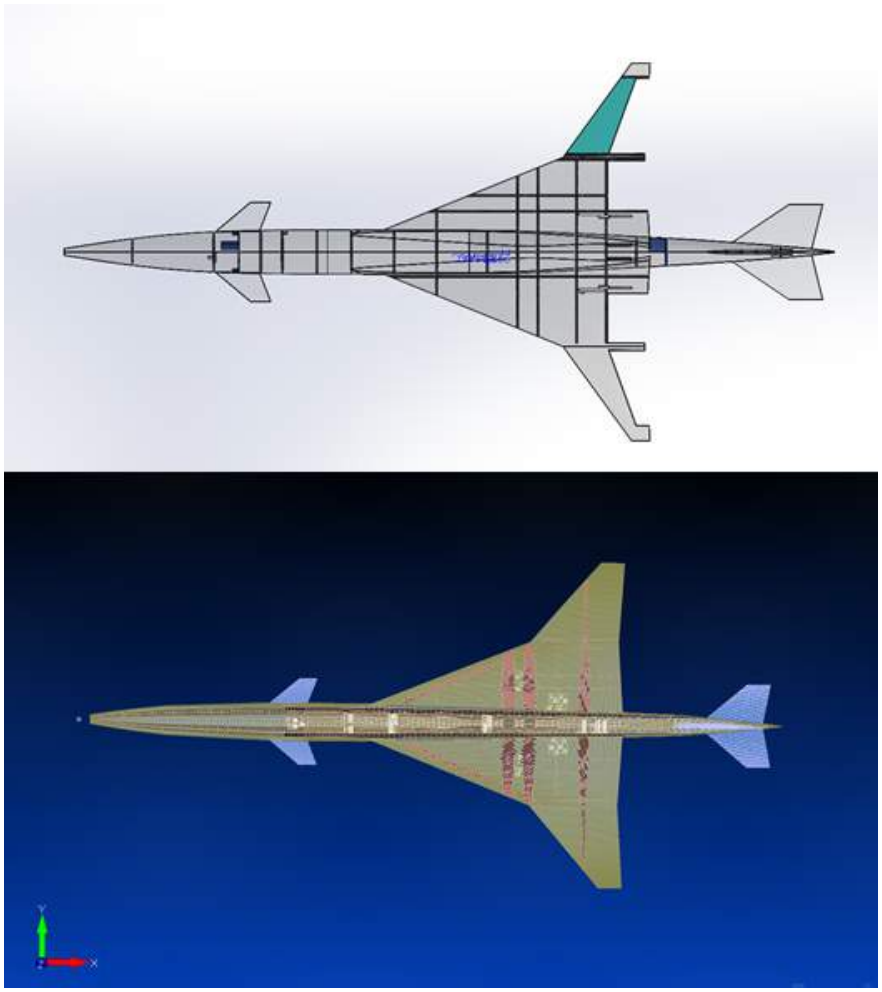

**Figure 7.1.28:** The structural geometry modeled in both Solidworks and FEMAP, as seen from the top.

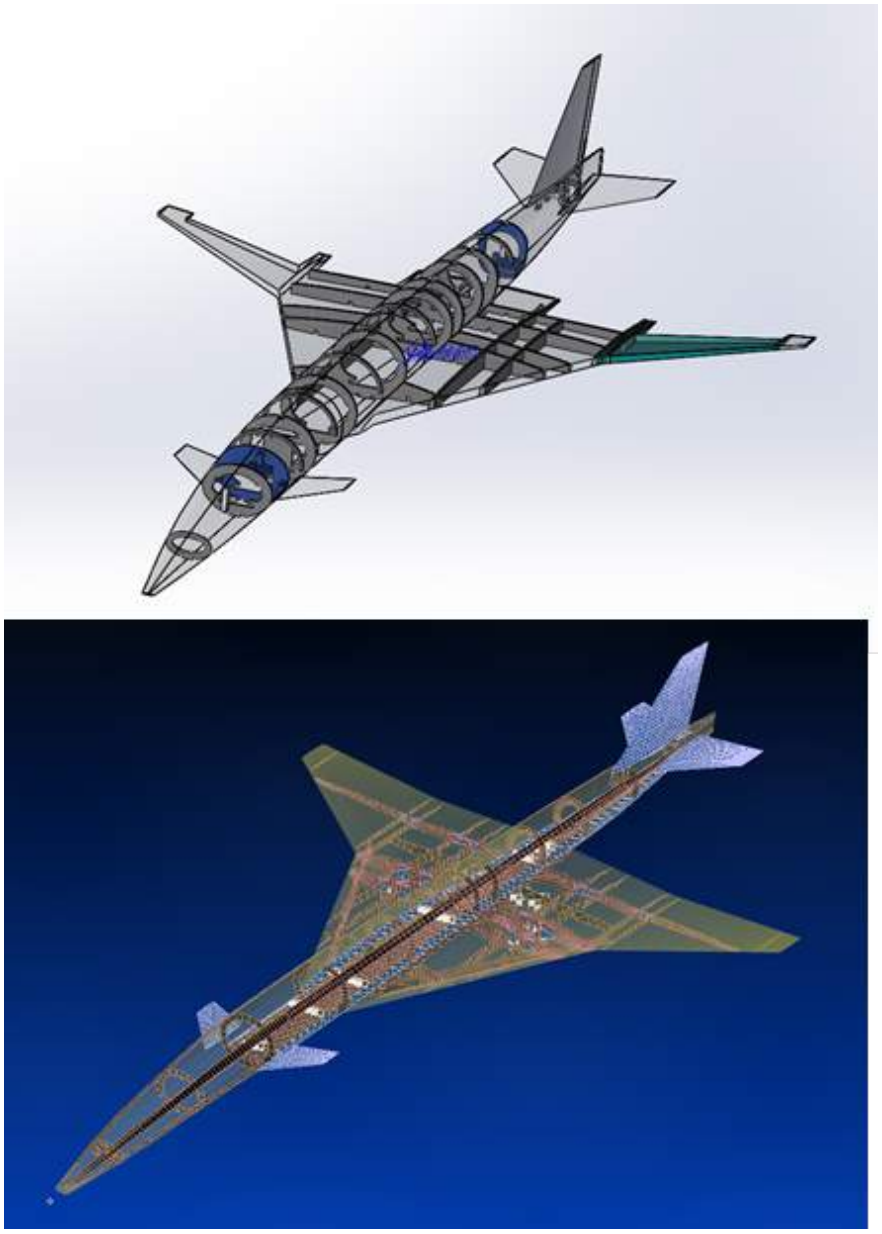

**Figure 7.1.29:** The structural geometry modeled in both Solidworks and FEMAP, as seen from an isometric view.

As can be seen, the main wing was designed such that the landing gear was secured to two of its own spars, as well as two ribs. Because the landing load must be considered on a single wheel when at 3g's, that scenario is the greatest concentrated load applied to the aircraft (with the intention of it surviving). Then, as was outlined by optimization, a large fraction of the lifting stress was carried by the rear spars, as that is the area of the wing that it concentrates to. That is why two spars were added close to the trailing edge of the wing. The outboard wing utilized a design common in many production supersonic aircraft; a relatively thick carbon wing with foam sandwich material. This was done because of the spacial challenges present in the outboard wing.

In terms of materials and properties, the plane utilized over 20 materials and more than

40 properties. The whole goal of the modeling was to make the finite element model as close to reality as possible. Thus, the material breakdown of the model was very close to what we planned in reality, and can be seen in Figure below.

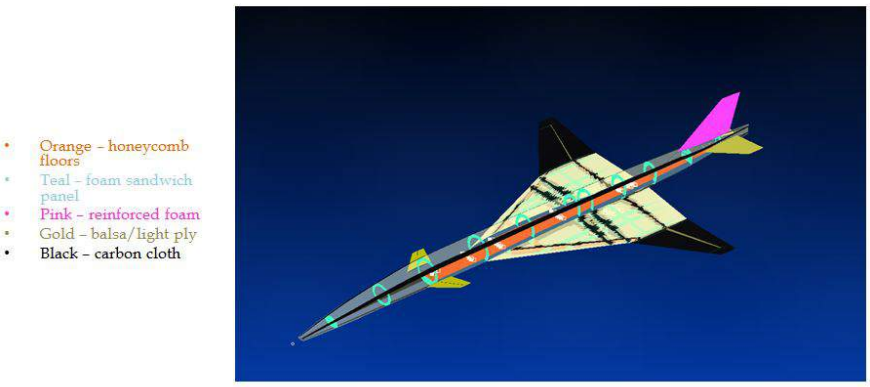


**Figure 7.1.30:** A breakdown of which materials were used in FEMAP and the final aircraft.

#### 7.1.4.7. Eigenvalue Analysis

Upon completion of the structural model, it is possible to begin running eigenvalue analysis on the plane. This is extremely useful in quickly determining weak spots of aircrafts internal structures, sections prone to buckling, or places with incomplete or disjointed element connections. In the first few runs of eigenvalue analysis, the plane had extremely floppy control surfaces (canards and stabilizer) and a lot of displacement in the aft fuselage due to the size of the control surfaces there, as well as the slenderness of the fuselage. When buckling was found near the empennage of the aircraft, recommendations were made to reinforce the area by adding carbon fiber cloth to the skin and extending the honeycomb floor (to limit the displacement) because of the severity of the apparent buckling. This case can be seen in Figure 7.1.31 below.

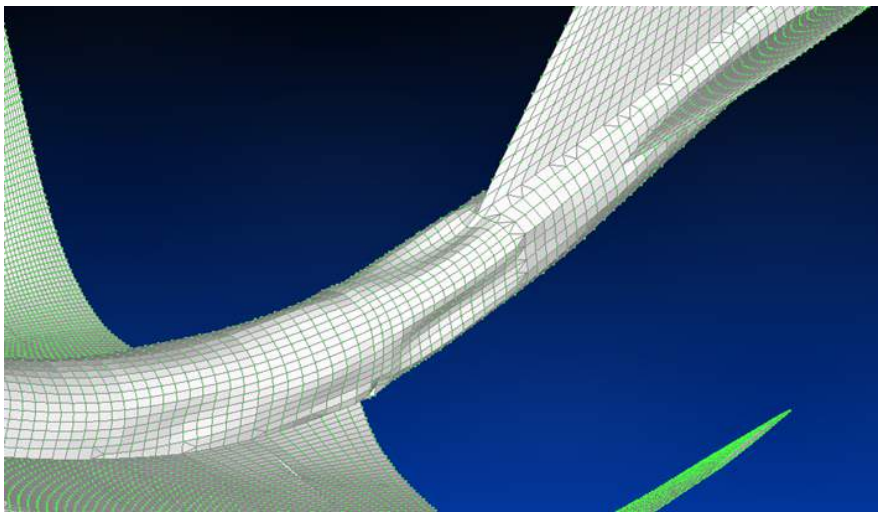

**Figure 7.1.31:** A buckling mode found near the tail that lead to additional skin thickness and localized reinforcements during the construction process.

However in other cases, the buckling was found to be fairly mild and not near any vital structural or control elements (not to mention at very high frequencies), so nothing was done to remove it. An example of this can be seen in Figure 7.1.32.

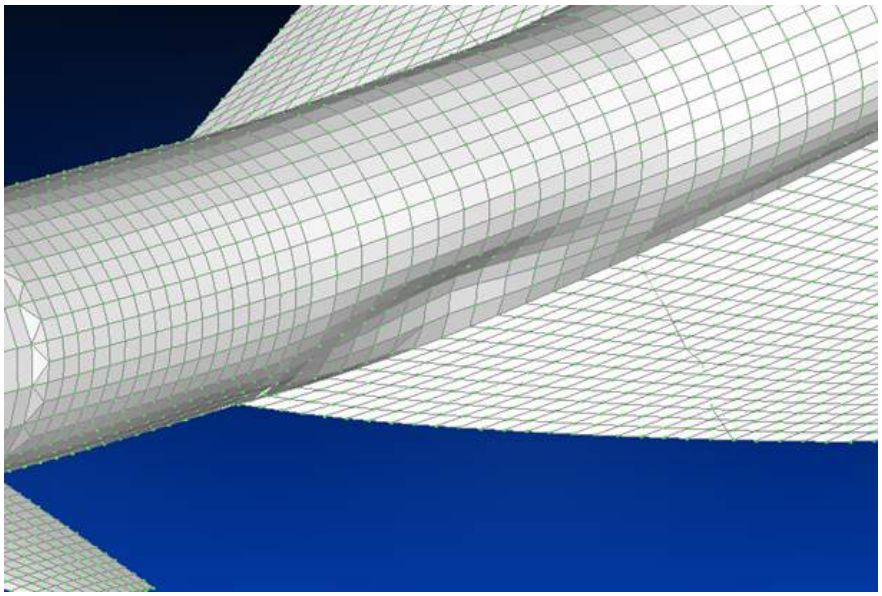

**Figure 7.1.32:** A buckling mode found ahead of the wing that was very mild and at a high frequency, so it was disregarded.

After all changes were completed, the modes found can be seen outlined in Table

**Table 7.1.6:** First seven usable eigenvalues found.

| Frequency (Hz) | Wing Mode | Fuselage Mode | Symmetric? | Notes |
|---|---|---|---|---|
| 50.4 | First | - | Yes | First wing bending |
| 69.8 | Second | First | No | Empennage deflection |
| 86.1 | Second | First | No | Greater empennage deflection |
| 90.1 | First | First | Yes | Fuselage bending |
| 128 | Second | First | No | Empennage torsion |
| 148 | Third | First | Yes | Some buckling |
| 151 | Second | Second | No | Heavy fuselage deflection |

#### 7.1.4.8. Static Analysis

To get a more complete idea of how stress was transitioned in the near-finalized structure, static loading cases were applied to the model by fixing it along the centerline and then applying landing gear loads or distributed lift along the nodes. As was outlined by the load provided in the RFP, the aircraft needed to be take 4.5g lifting values (limit load) and a 3g landing. These were some of the critical cases for the internal wing structure. When the static 4.5g lifting load was applied, it was easy to see that the stress congregated to the rear spar (as well as the landing gear ones) near the base of the wing/moment. This can be seen in Figure 7.1.33 below.

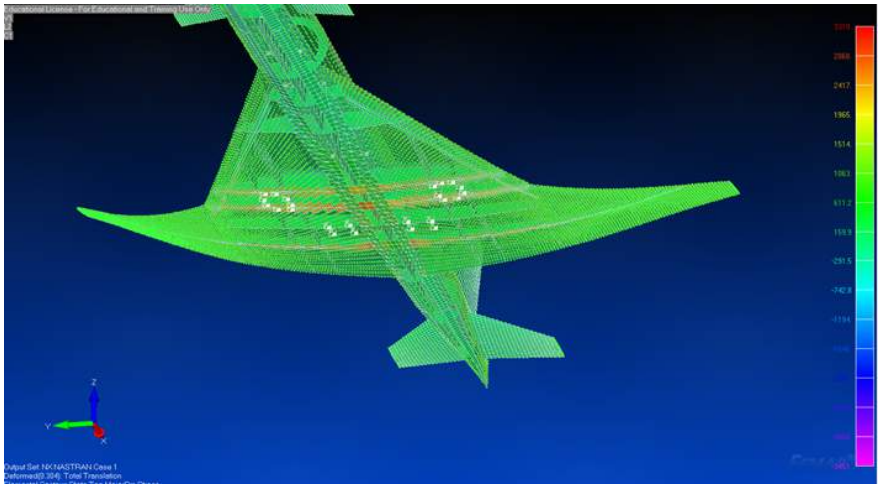

**Figure 7.1.33:** The stress seen in the spar caps when a 4.5g lifting load was applied across the aircraft.

From this, it was possible to determine what areas of the internal structure were vital in the lifting scenario and thus make recommendations in the construction process to avoid removing load carrying structures.

When a 3g landing was applied, a 3g inertial load was placed on all the nodes and a force equal to 3 times the total aircraft weight was applied to a single landing gear location (along some of the nodes).

***Aero Model Calibration***

In order to verify that the aerodynamics model is functioning accurately for the flutter analysis, the model needs to be calibrated. To do so, multiple trim tests were run on the model at various angles of attack and then compared back to the wind tunnel results. The exact lift value produced by NASTRAN, which was found as $CZ$ in the .f06 file, was corrected by adding on the $C_{L0}$ value, because the NASTRAN model assumes no lift at 0 degrees angle of attack. For this specific case, the NASTRAN model was run at 3 points that corresponded to points from run 212 of UW2128. From these values, the aerodynamics model was deemed accurate enough for use in the flutter analysis that came later.

***Flutter Analysis***

Flutter analysis was run using the structural model alongside the aerodynamics model that was previously calibrated. The goal was to determine that the flutter speed was greater than 1.25 times the dive velocity. Table below shows the flutter velocities that were found.

| Flutter Velocity (ft/s) | Frequency (Hz) | Notes |
|---|---|---|
| 1100 | 145 | Second wing mode |
| 1500 | 150 | Relate to empennage torsion |

Clearly, the flutter velocity found is well above the designed cruise speed. Thus, the aircraft was analytically determined to be safe for flight. However, to verify these analytical results it would be necessary to perform a Ground Vibration Test (GVT).

*7.1.5. Supplemental Handbook Calculations*

To determine and validate material/structure strength required to maintain structural integrity in steady-level flight, a conservative analysis was conducted. The conservative approach required simplification of the actual internal structure of the wing. The actual internal structure of the wing is shown below in Fig. 7.1.34, (1). It contains many ribs and smaller spar-like supports. For the conservative analysis, the entire internal structure was assumed to be one straight, box-beam spar. An image of the conservative approach is shown in Fig. 7.1.34, (2) (the spar outline is highlighted by red). This allowed for a simple analysis to be conducted concerning the max bending stress at the root of the wing.

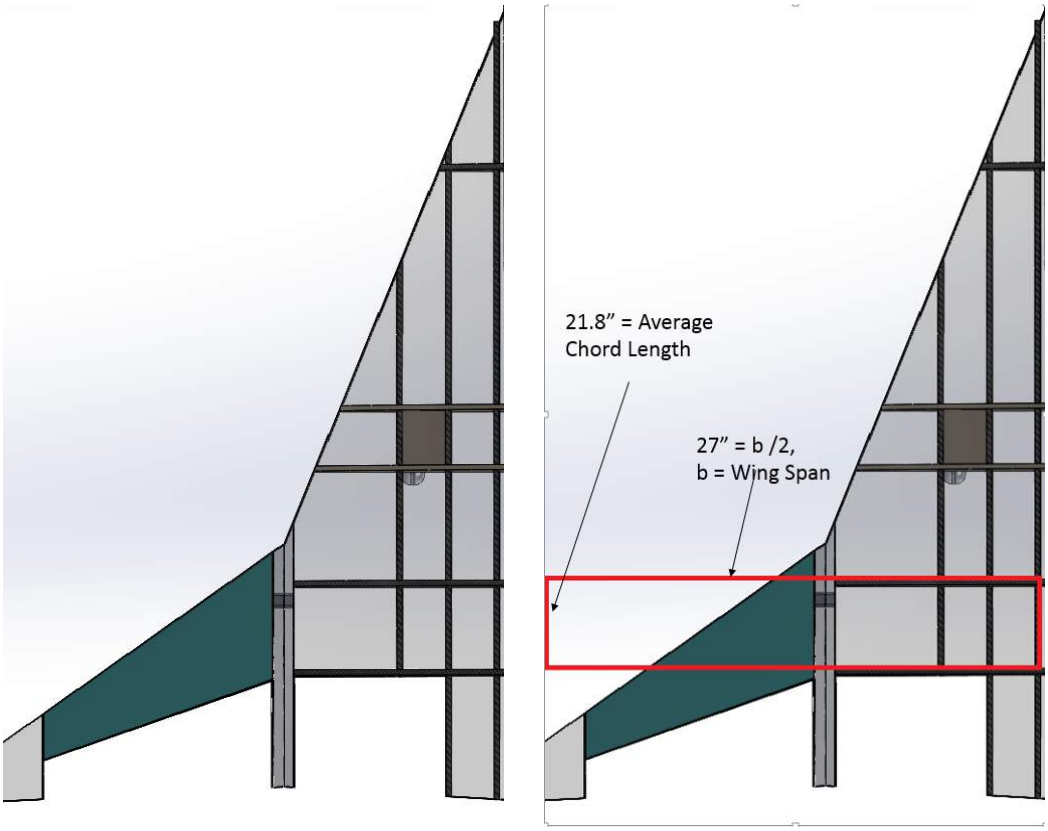


**(1)** Actual Internal Structure of the Aircraft Wing

**(2)** Simplified Internal Structure of the Aircraft Wing

**Figure 7.1.34:** Actual and Simplified Internal Layouts

The bending stress in the beam was computed through Eq. 7.1.3

$$\sigma = \frac{Mz}{I} \tag{7.1.3}$$

where M is the bending moment as a function of the y distance (longitudinal direction) from the wing root, z is the vertical distance from the neutral axis of the beam, and I is the moment of inertia of the beam cross section.

For the conservative approach, the aerodynamic loading was assumed to be equally distributed along the simplified spar. A picture of the distribution is shown in Fig. 7.1.35.

The value of the loading was roughly approximated by dividing the aircraft weight by the span of the wings as shown in Eq. 7.1.4.

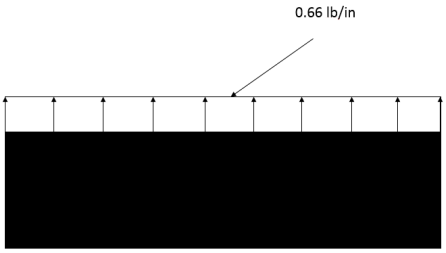


**Figure 7.1.35:** Equally Distributed Load Along Spar

$$q = \frac{W}{b} = \frac{36lb}{54in} = 0.66lb/in \tag{7.1.4}$$

This load distribution was used to calculate the moment about the root of the wing using Eq. 7.1.5

$$\sum M_{@cut} = M + qy\frac{y}{2} = q\frac{y^2}{2} = \frac{0.66}{2}(27^2) = 243lb - in \tag{7.1.5}$$

where y is the direction along the wing starting from the root and M is an arbitrary moment on the beam (zero in this case). This produced a moment of 243 lb-in at the root of the wing.

To solve for z, the distance above the neutral axis, a constant beam height in the x-z plane was computed. NACA 66204 airfoil coordinate data was used to find a weighted average for the height of the airfoil above the midchord and below. This can be expressed as Eq. 7.1.6 for both the top and bottom of the airfoil.

$$\bar{z} = \frac{(h_i)(A_i)}{TotalArea} \tag{7.1.6}$$

where $h_i$ is the z value on the airfoil above or below the midchord and $A_i$ is the area between each pair of successive z values. After finding weighted z values for both the top and the bottom, the two values were added to find the average height of the flange (i.e. the total height of the rectangular beam). The average height came out to be 0.8898 in. This value was divided by 2 to get the z value required for Eq. 7.1.3.

The last part of Eq. 7.1.3 involved the moment of inertia of the cross section of the beam, I. The moment of inertia was calculated using the derived equation for a rectangular cross section and the parallel-axis theorem. I is found from Eq. 7.1.7

$$I = 2 * (\frac{1}{12}c_{average}h^3 + c_{average}t\frac{h}{2}^2) \tag{7.1.7}$$

where $c_{average}$ is the average of the average chord lengths of the wing cross sections, t is the thickness of the flanges, and h is the height of the beam in the z direction. $c_{average}$ was found

as a weighted average between the average chord lengths along the length of the wing. Eq. 7.1.8

$$c_{average} = \frac{\sum c_i A_i}{TotalWingArea} \tag{7.1.8}$$

gives the formulation of $c_{average}$ with $c_i$ equal to the average chord length at the ith cross section and $A_i$ equal to the area of the wing (bird's eye view) of the ith area between successive cross sections. The thickness, t, was varied between values of 0.001“ and 0.003” in increments of 0.0001 due to the uncertainty in manufacturing processes. The bending stress was then calculated using Eq. 7.1.3 as a function of t. A plot showing the results is shown below in Fig. 7.1.36.

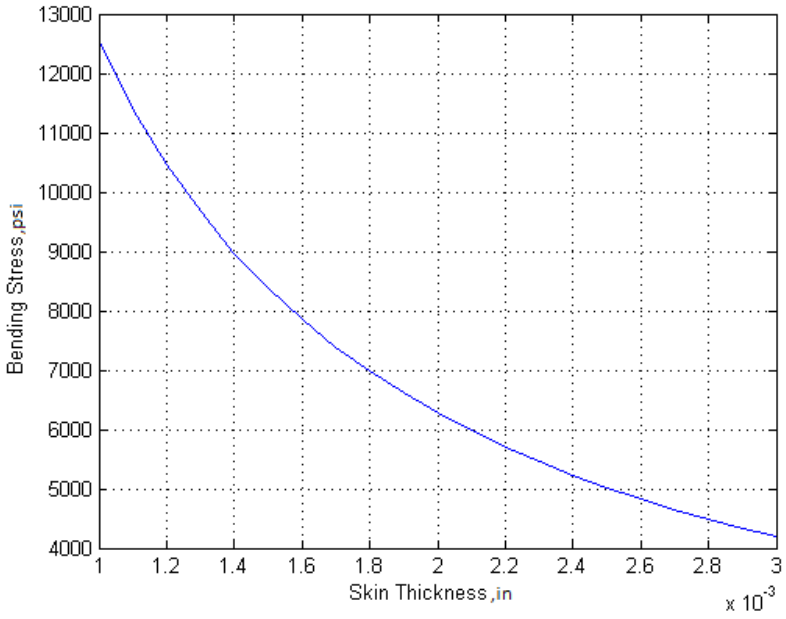


**Figure 7.1.36:** Bending Stress vs. Thickness

From the graph, it can be seen that the max bending stress at the root of the wing occurs with the smallest thickness of 0.001 in. with a value of $1.2558 * (10^4)$ psi.

### *7.1.6. Manufacturability*

The usage of 3D printing was not just for rapid prototyping, but also for production parts because of its reliability and tolerance capability. Also, for 3D printing in particular, it is a single step from CAD to finished part – meaning a greater number of the team members can contribute to the manufacturing and design process. In general, the product will likely come out better if automated machines and systems can be used for the manufacturing process rather than the traditional, hand-fabrication methods. The rule of thumb often used is that everything takes 3 times longer than you initially think. This is especially true for techniques like hand sanding or filing. However, automated/CNC manufacturing techniques are far more predictable and usually are able to hold much high tolerances. Thus, when possible, a focus

was put on using 3D printing, laser cutting, and other automated techniques rather than relying on extensive, time-consuming methods.

### *7.1.7. Frames and Internal Structure*

The internal structure is the backbone of our airplane. It provides the strength and framework for the shape of our aircraft. In addition to structural uses of the internal structure, the frames also dictate the amount of internal space that is available for the systems that need to be integrated into the aircraft.

The manufacturing of the carbon fiber sandwich board consisted of a wet layup vacuum bagging technique. 4 plies of 3.7 oz cross-ply carbon fiber was used on each side.They are made from a carbon-foam sandwich. The composition of the sandwich was 4 plies of 3.7 oz. cross-ply fiber on each side of the Dow polystyrene. The total thickness of the frame was about half an inch. To cut the frame geometry from the sandwich board, the job was outsourced and cut by West Coast Waterjet. Figure **??** and Figure **??** below show a couple of the frames that were made from the carbon fiber sandwich board.

**Figure 7.1.37:** frame1

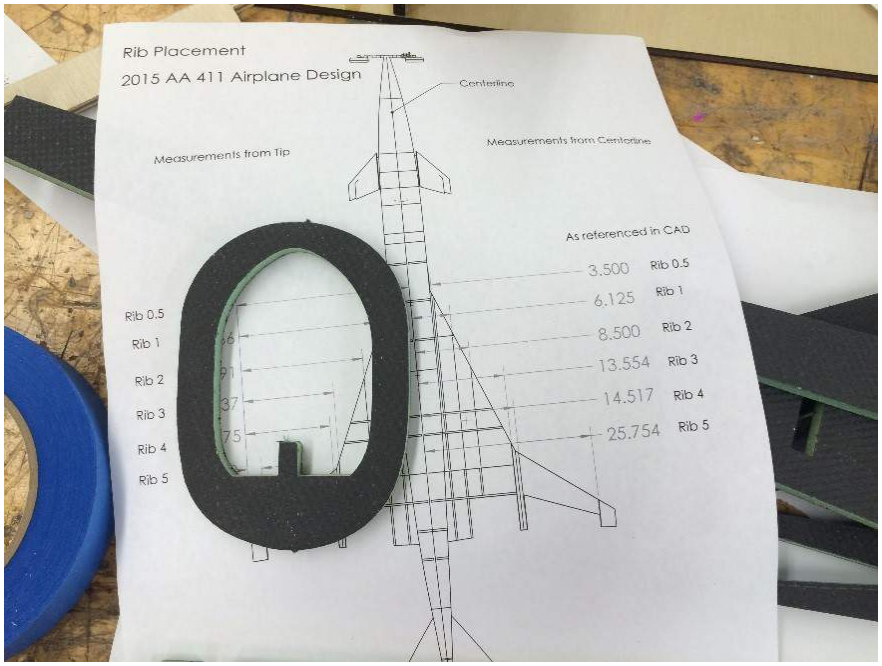


**Figure 7.1.38:** frame2

### *7.1.8. Summary*

- A lot of effort was put into properly characterizing the materials used, as well as developing usable basis values.
- Component level testing was performed to develop and understanding of the applicability of materials to individual components, from a structural and manufacturing standpoint.
- A full model was created in FEMAP to prove the structural capabilities of the full model, from static loads to flutter analysis. Static loads were only able to show where potential stress concentrations where and how loads were distributed. The flutter analysis and eigenvalue analysis provided useable values and proved the aircrafts dynamic capabilities.
- Component level analysis was used to prove the capabilities of individual, primary structural elements (PSE). This was done both with hand calculations and with finite element stress software such as ANSYS Workbench.

### *7.1.9. Recommendations for Future Improvement*

- Try to start material testing as soon as possible, and as many tests as possible.
- It might be a better option to put more time and emphasis on proving the structural capability of individual components using stress analysis software, as it is less labor intensive and provides quicker results, than to spend months developing a full scale model for aeroelastic analysis.

- If possible, the creation of a full model in FEMAP should be started as soon as possible by using the tutorials created and uploaded to the Z-drive (in the 2015 folder).
- As was mentioned before, master design spreadsheet should be used team wide to document work and begin basic, handbook calculations right at the beginning.

## 7.2. Propulsion

### *7.2.1. Nacelle Location*

One of the major design options considered by the propulsion team, the vehicle integration team, and the class as a whole was the number and location of the aircraft nacelles. Many different aspects had to be considered when deciding where to place the nacelles, including noise reduction, engine performance and efficiency, structural implications, yaw stability, and engine out situations. For noise considerations, it would be best to have the nacelles located on top of the airplane. This would allow the body of the airplane to muffle the noise before it could reach the ground during flight. However, for aircraft performance, it would be best to have the nacelles on the bottom of the airplane. This would allow for cleaner airflow through the nacelles, especially at high angles of attack. For structural considerations, it would be best to have the nacelles as close to the fuselage centerline as possible. This would create a smaller moment arm and less of a moment load on the internal wing support structures. Also, if there was an engine failure during flight, it would be best if the nacelles were close to the fuselage centerline. The closer the nacelle is to the center, the less it would create an imbalance in the aircraft's yaw moment in an engine out situation.

Our class also looked at the design process of the 2013 and 2014 airplanes. The 2013 class decided to put their airplanes on top of the fuselage in a vertically stacked arrangement. The 2014 class decided to put their engines in a more traditional configuration with the nacelles under the wing, horizontally separated from each other. After considering all these factors, it was decided to place the nacelles under the wing in a similar design to the 2014 aircraft. This was chosen mainly because noise was less of a consideration this year when compared to the past, and because the 2013's vertically stacked nozzles had a significant loss in thrust due to their complex geometry. The 2015 nacelle locations are shown in Fig. 7.2.1.

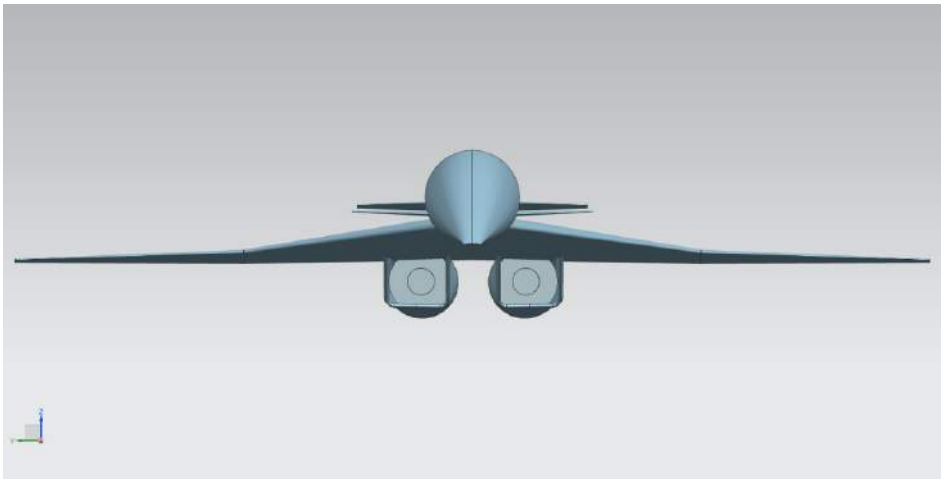

**Figure 7.2.1:** Nacelle Location Design from Initial CAD Model

### *7.2.2. Nacelle Design*

The propulsion team was tasked with designing the two nacelles which would house the electric ducted fans. The 2015 project goal was to design and test a supersonic business jet and analyze its performance at subsonic speeds while focusing on minimizing the vertical control surfaces with thrust vectoring. Therefore, the nacelle design had to be a balance between an optimal supersonic nacelle design and designing to provide maximum thrust and efficiency at subsonic speeds, which would be the regime where the aircraft is actually flying.

Because the mission requirements were similar and the electric ducted fans were the same as the 2014 project, the propulsion team decided to base the nacelles off of the 2014 nacelle design. Modifications would be made based off the results from 2014 testing and new static and wind tunnel testing done by this year's propulsion team. The 2014 nacelle utilized a 2-D ramp inlet. This is the type of inlet used on many supersonic engines, such as the inlet system on the Concorde. This type of inlet is used to generate a shock wave starting on the front upper lip of the inlet to aid in the compression process of the flow at supersonic speeds.

After talking to advisors and reviewing the 2014 design, it was decided to increase the lip radius of the nacelle and decrease the size of the trailing edge of the nacelle nozzle. The increase in lip radius was intended to help increase the static thrust. The decreased nozzle trailing edge was intended to help decrease flow separation like the trailing edge of a wing. The increase in lip radius was a tradeoff to increase thrust because a supersonic inlet would have a much sharper lip than a subsonic inlet. The initial nacelle design is shown below in Fig 7.2.2.

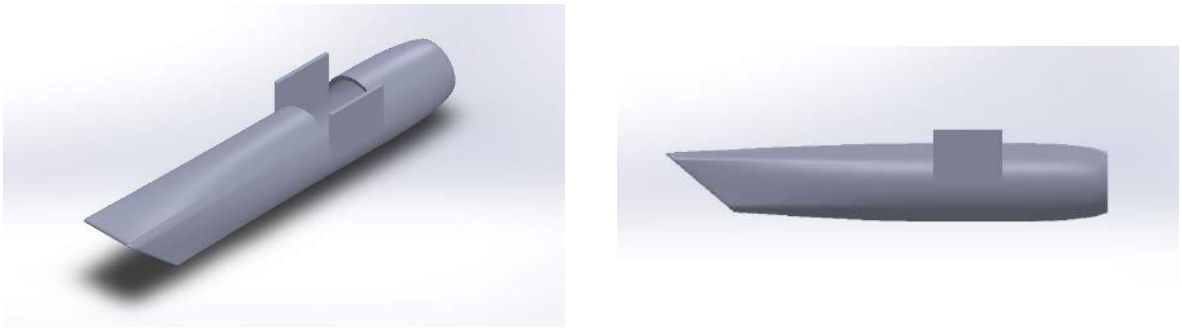

**Figure 7.2.2:** Nacelle Location Design from Initial CAD Model

### *7.2.3. Supersonic Inlet Design*

As stated earlier in the report, the goal of this project was to create an R-UAV based on our design for a supersonic business aircraft. This provided a unique challenge for the propulsion group, as it required the design of an inlet that would be used on a supersonic aircraft, but would fly only at speeds well below Mach 1. It was therefore determined that the propulsion group would design two different inlets. One inlet would be for use on the R-UAV, and would bear the same outer shape of the supersonic inlet, but would not contain the supersonic interior and would simply include a straight tube running to the EDF. The other inlet design would be for the designed supersonic aircraft.

One of the requirements for the aircraft was that the designed supersonic aircraft would have a cruising speed of Mach 1.8. After passing through the shock at the wing, it was

estimated that the speed of the air entering the inlet would be approximately Mach 1.6. However, in order to increase the efficiency of the aircraft, the flow at the engine face had to be reduced to a speed below Mach 0.5. Therefore, the flow traveling through the inlet had to be reduced through a series of shockwaves and diffusers. To design the full scale supersonic nacelle, the diameter of the full scale engine was needed. The engine chosen was the JT8D-219 which was the engine selected by the 2014 aircraft design class to meet their project requirements.

Prior to designing the supersonic inlet, the group studied the concepts put forward by the class textbook "Aircraft Design: A Conceptual Approach" by Raymer. The group also researched inlet designs from past supersonic transport aircraft, such as the Concorde, and applied design ideas from these aircraft to construct our own design concepts. Through the research done by the group, a series of inlet designs were suggested that would allow the goals of the project to be achieved while getting the maximum performance out the engines. A few of the common inlets researched from the Raymer text are shown in Fig. 7.2.3.

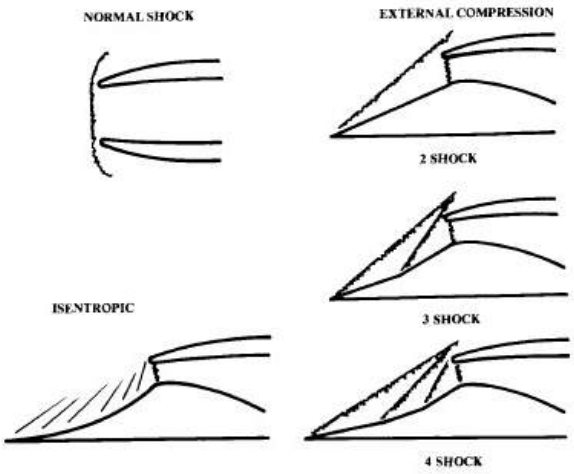


**Figure 7.2.3:** Supersonic Inlets

In order to reduce the speed of the flow before it reached the engine face it was determined that the inlet would be designed using a mixed compression 3 shock system. This dictated that the supersonic flow approaching the engine face would travel through 3 shock waves in order to reduce its speed. Although the flow could be reduced to an acceptable value using normal shock waves, it was determined that this would cause an unwanted drop in pressure recovery, which would severely affect the performance of the engine. Therefore, our group designed an inlet that created 2 oblique shockwaves, followed by a normal shock wave and a diffuser, which would reduced the speed of the flow at the engine face to the desired level. The proposed design is shown in Fig. 7.2.4.

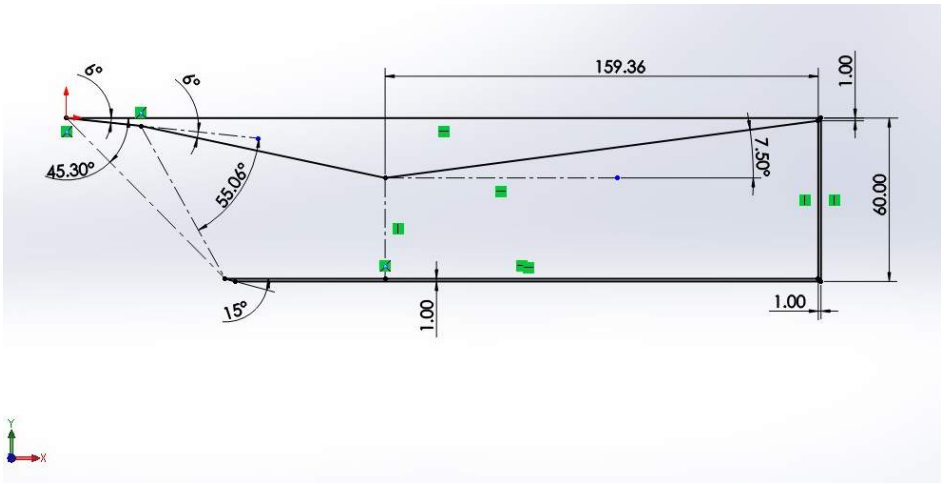


**Figure 7.2.4:** Supersonic Inlet Design

As shown in Fig. 7.2.4, the inlet is designed with two 6° wedges, which cause oblique shockwaves to form. As the flow travels through these shockwaves, the speed of the flow reduces, from Mach 1.6 to Mach 1.39 and then to Mach 1.165. The oblique shockwaves have angles of 45.3° and 55.06° from the horizontal. The lower lip of the inlet was placed so that it was located where the two oblique shockwaves met.

The pressure recovery through these two oblique shocks was much greater than it would have been than if it had gone through 2 normal shocks, with the $P_{o2}/P_{o1}$ value for the first shock being 0.997 and the second shock being .997 as well. However, the flow was not reduced to below 1 Mach yet so a final shock wave, this one normal to the flow, was added. Since the flow velocity was very low at this point though, the pressure recovery was much better. After passing through the normal shock, the flow velocity was at Mach 0.864, with a $P_{o2}/P_{o1}$ value of .995. This gave the inlet an overall pressure recovery of .989. As stated in "Aircraft Design: A Conceptual Approach", a decrease in 1% in the total pressure corresponds to a drop of about 1.3% in the overall thrust of the engine. Due to this, the design of our inlet means that we will be losing about 1.43%. Based on data from other supersonic aircraft, as well as in Raymer's book, it was determined by the group that this was an acceptable value.

At this point, the flow entered a diffuser, which allowed it to slow further until it had dropped below 0.5 Mach at the engine face. The diffuser dimensions were determined using the equation shown below assuming incompressible flow.

$$A_1 v_1 = A_2 v_2 \tag{7.2.1}$$

Using the area of the engine face for $A_2$, 0.5 Mach as $v_2$ and 0.864 Mach as $v_1$, the area of the diffuser entrance was determined to be 19.63 $ft^2$. A major concern with designing the diffuser was that the flow would separate if the diffuser angle was too large, which would severely worsen the performance of the turbo fan. Therefore, the diffuser was designed with an angle of 7.5deg, which would allow the flow to expand without separating. Using this angle, and the desired dimensions for the areas at either end of the diffuser, the length of the diffuser was determined to be 159.36 inches.

### *7.2.4. Thrust Vectoring*

The challenge of all supersonic aircraft is to have the lowest drag possible during supersonic cruising. One way of achieving this is to minimizing the frontal cross sectional area of the aircraft and protruding parts such as the vertical tail. It is only logical that decreasing the size of vertical tail, or even eliminating it altogether, will reduce drag significantly. However, losing a vertical tail means losing yaw capability. This is where the thrust vectoring system plays its role. By repositioning a vane directly behind each of the engine exhausts, one can deflect the flow coming out of the exhaust. Since aerodynamic forces are proportional to the square of velocity, one can expect the yaw control vane to be smaller to accomplish a similar task.

This choice of thrust vectoring is not without long consideration. It is important to bear in mind that the goal was to achieve yaw stability. Several concepts were examined in the early design phase. Initially a gimballing fan was proposed due to its effectiveness and multiple degrees of freedom. However, given the large size of the fan used and its rigid attachment to the driving motor, this was deemed impossible. Furthermore, since the design team decided to incorporate a nacelle for each engine, the propulsion team decided it was best to deflect the thrust at the nozzle section. Considering the time constraint for the propulsion system design, and the sole requirement of providing yaw stability, the design is simplified into a simple, 1 degree of freedom thrust vectoring system.

A NACA 0015 airfoil section was used as the vane for the thrust vectoring system. It was chosen because of its large thickness and symmetry. This would allow for symmetrical flow displacement vertically while also providing structural support for the deflection rod. Ideally, the vane would be entirely exposed outside the nozzle. Due to structural and construction issues, a small part of the leading edge needed to be placed inside the nozzle. The vane is hinged by a rod running through the wall on the top and bottom of the nozzle, where it will be joined to a servo pushrod. A little clearance was intentionally made on each side to allow for movement. The entire nozzle assembly will be manufactured using a 3-D printing technique. The advantages of this thrust vectoring system are:

- Smaller vanes eliminates the need for a large vertical tail, allowing design team to take advantage of the new CG position
- In general less yaw and roll coupling, reducing complexity
- Smaller side profile, consequently better stealth capability
- Significantly less drag. Fuel saving permit for cheaper fares

Inevitably, there are several disadvantages associated with thrust vectoring such as:

- Failure of an engine could potentially cripple the entire plane
- In a worst case scenario, loss of all engine means loss of airplane control
- More complexity in an attempt to design an inherently stable aircraft in yaw
- Dependency on throttle as opposed to airspeed, leave concern for operation during descent and landing

- Fluctuation in forward thrust
- The entire system could potentially weigh more

### *7.2.5. Nacelle Re-Design*

As shown below in Fig.7.2.5, the initial type of nacelle chosen as the most viable for our project is shown. It was determined that the shape of our nacelles would follow the general size and shape as the 2014 RUAV who used a more rounded and thicker lipped version of the Concorde's under wing mounted nacelles. The size of the nacelles are not to scale with the Concorde because of the thrust required for this RUAV and the corresponding required diameter of electric ducted fan needed to meet this requirement.

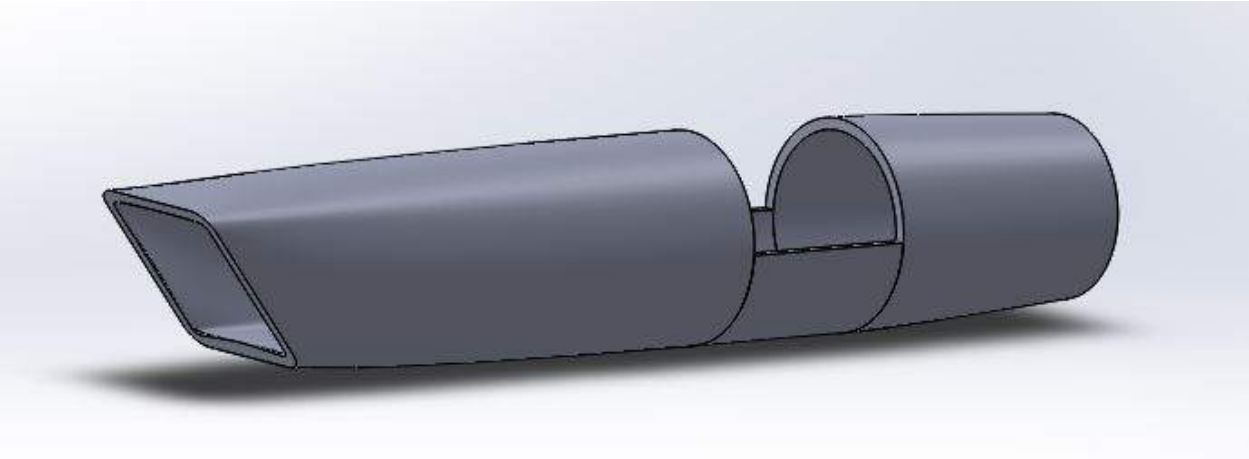

**Figure 7.2.5:** Rough initial design

After determining the initial design shape and location, a model of the 2014's nacelle was made. This is shown below in Fig.7.2.5. The location of the nozzle, and inlet with respect to the electric ducted fan as well as the inlet area to fan area ratio, and nozzle area to fan area ratio were calculated with respect to a supersonic configuration. Two differences between this and a purely supersonic is that the inlet lip is not a sharp edge and the inlet corners are rounded. In supersonic conditions, the larger inlet lip, and smoother corners provide greater leading edge suction on the lips and less separation at the corners. This combination provides a more desirable thrust profile for a subsonic RUAV than the traditional supersonic nacelle design seen on aircraft such as the Concorde.

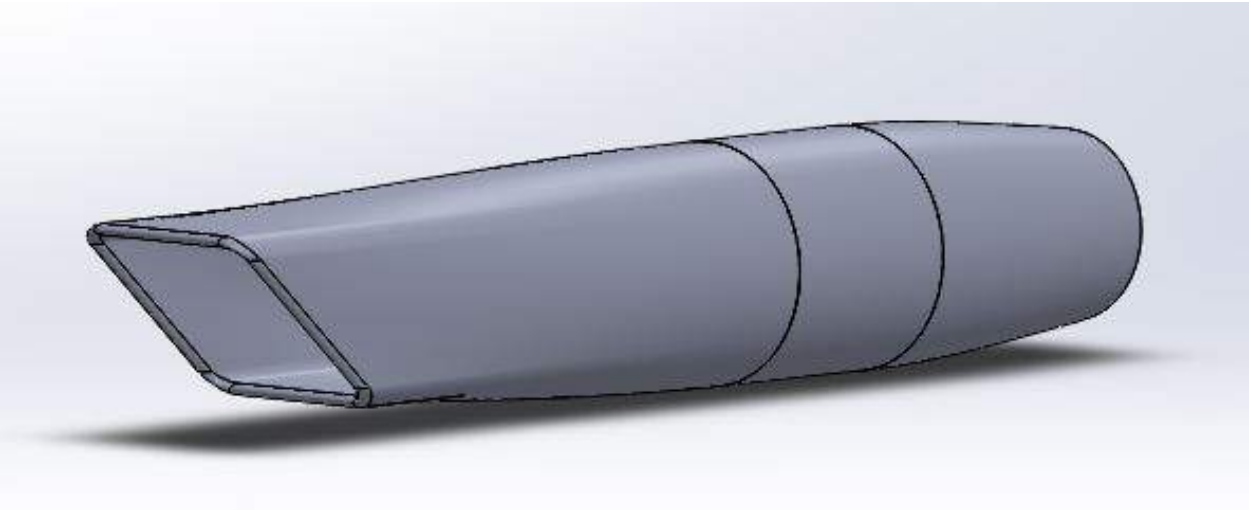

**Figure 7.2.6:** Initial design with inlet rim

Shown below in Fig.7.2.7 a visual representation of the area ratios of inlet, cowling and nozzle can be clearly seen.

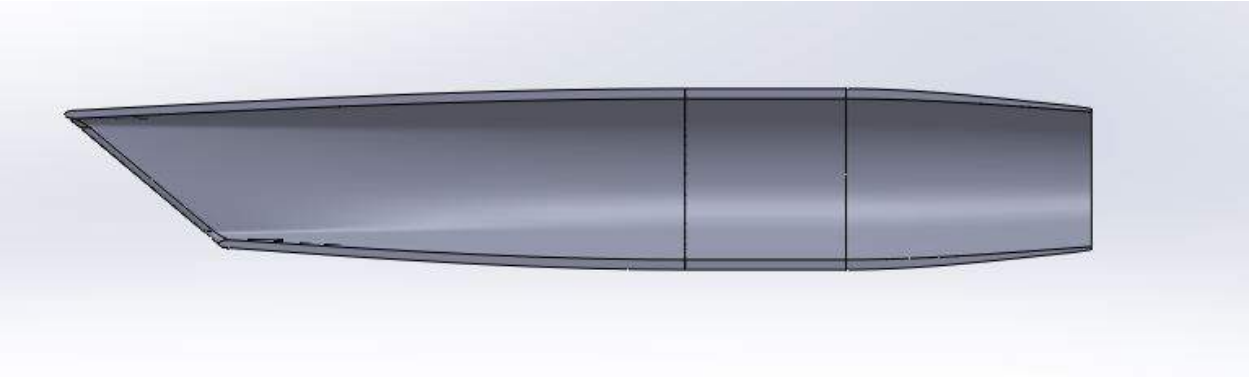

**Figure 7.2.7:** Initial design with inlet rim side view

As shown below in Fig.7.2.8, the inlet lip radius and depth are 0.1in and 0.25in respectively.

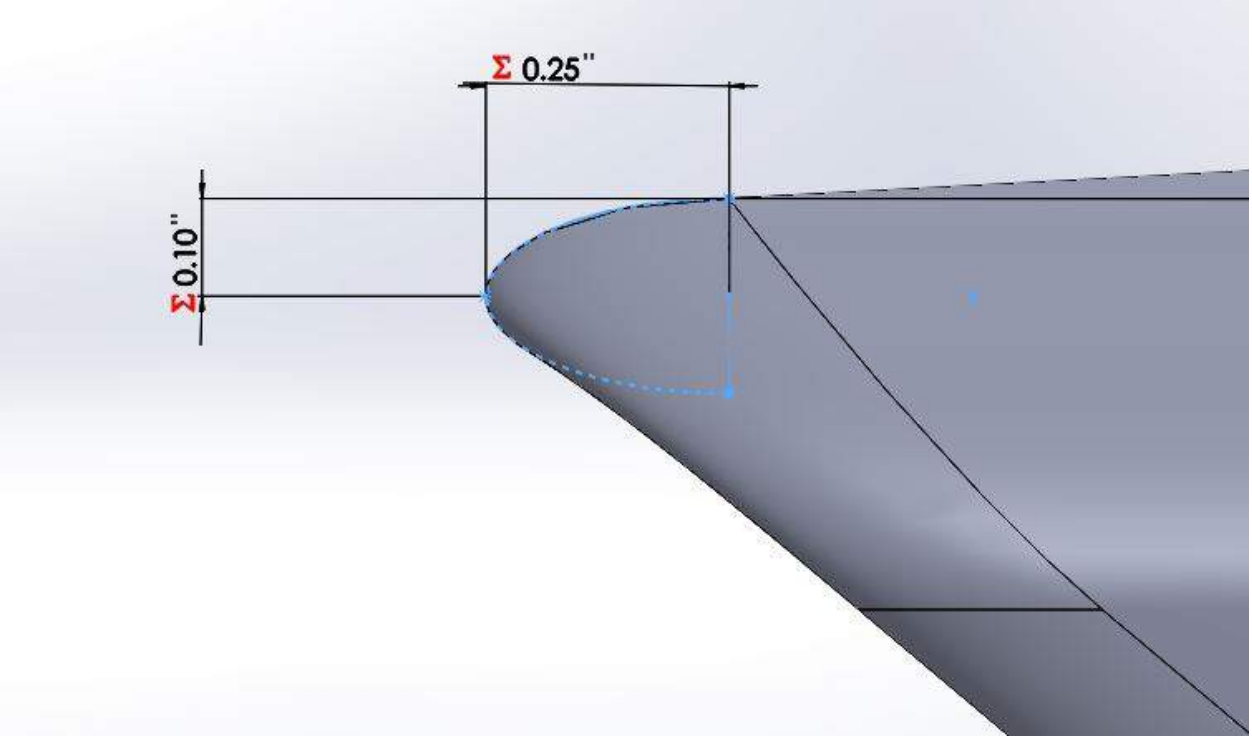


**Figure 7.2.8:** Initial design with inlet rim, geometry

Using the nacelle, geometry shown above in Fig.7.2.8, static testing was completed. In a variation of this testing, a rim of clay was attached to the nacelle. It was found that with this configuration, the maximum static thrust was measured. Using this as an idea to increase the thrust to weight ratio, the nacelle shown below in Fig.7.2.9 was created.

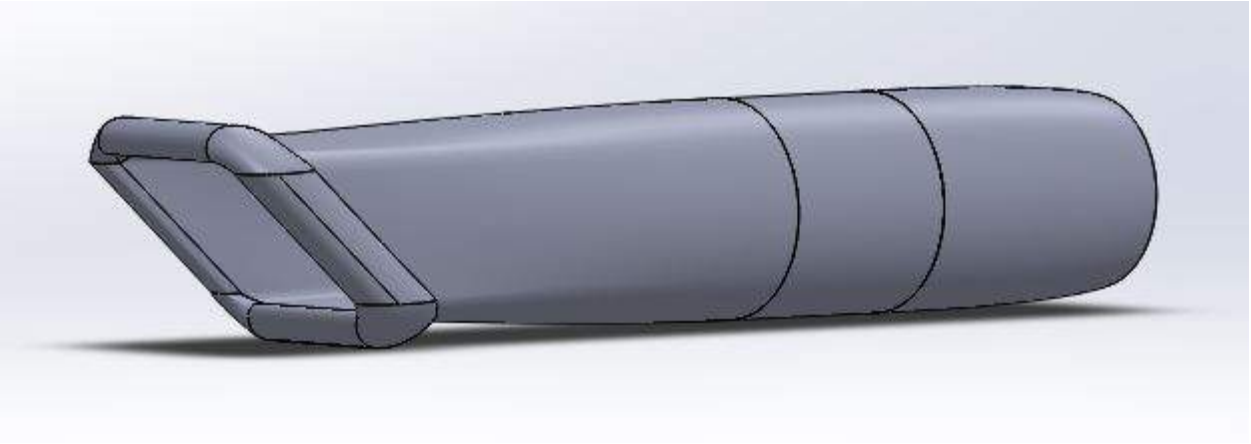

**Figure 7.2.9:** Large bulged rim configuration

As shown below in Fig.7.2.10, the additional lip geometry is shown.

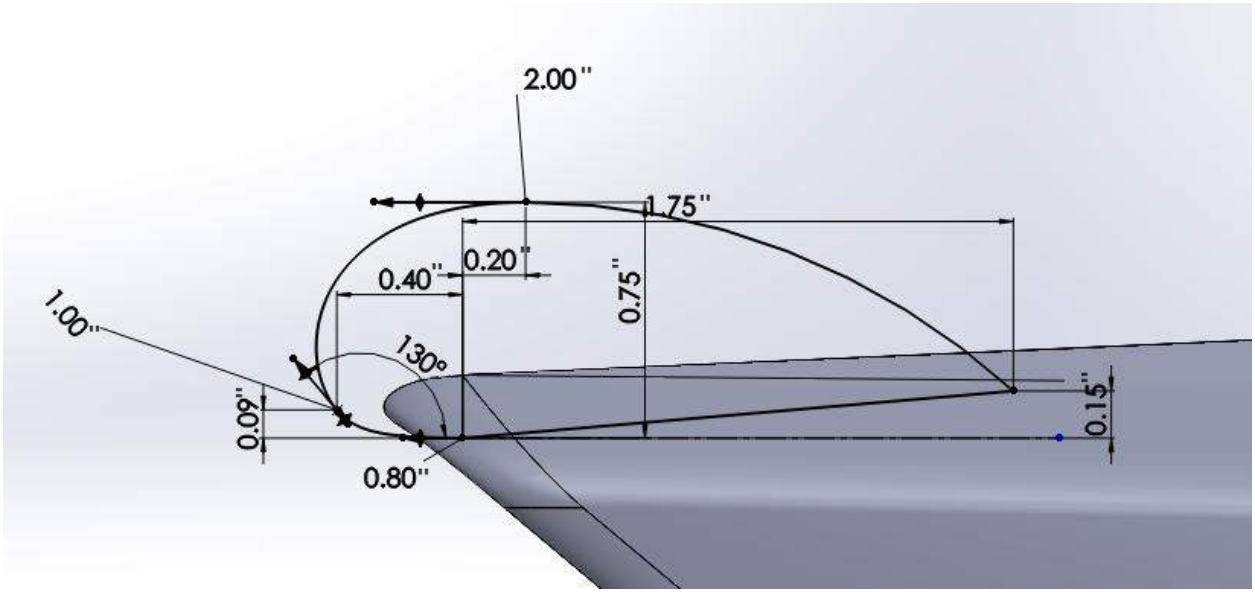


**Figure 7.2.10:** Large bulged rim configuration geometry

During static testing, different nozzle sizes were tested. It was determined that a 95% nozzle exit area to fan highlight area was best for thrust performance. Also, the inlet area was also increased by roughly the same amount as the nozzle area to help maximize mass flow. Shown below in Fig.7.2.11 a visual representation of the area ratios of inlet, cowling and nozzle can be clearly seen.

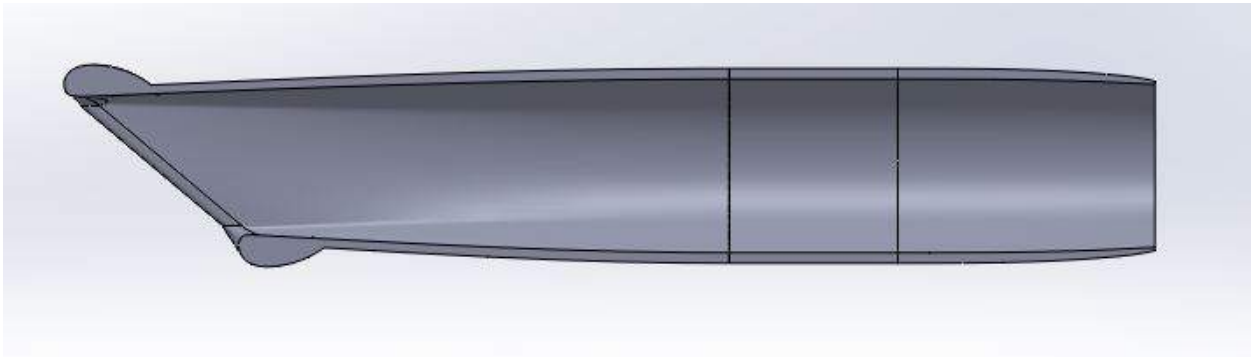

**Figure 7.2.11:** Large bulged rim configuration side view

However, after further deliberation, it was determined that even though the nacelle shown above in Fig.7.2.9 may be optimal for static thrust, the problems it may cause during flight may counteract any gains. This is because, the rim would separate the flow and then cause additional drag on the aircraft as well as the nacelle when at non-zero dynamic pressure states. Because of this, a compromise was made, and the nacelle design shown below in Fig.7.2.12 was created. This design has an larger lip than the 2014's design while maintaining a smooth contour from the lip to the nozzle exit unlike the previous design shown in Fig.7.2.9. It also included the same area ratio design parameters as the nacelle shown in Fig.7.2.9 allowing for greater mass flow rate.

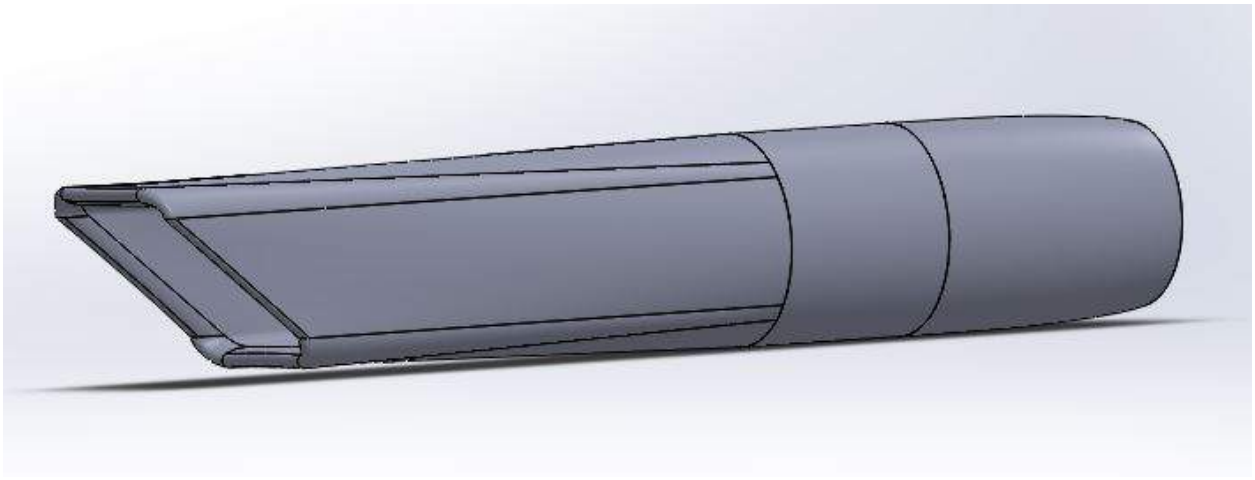

**Figure 7.2.12:** Smoothed inlet

As shown below in Fig.7.2.13, the smoothed lip geometry is shown.

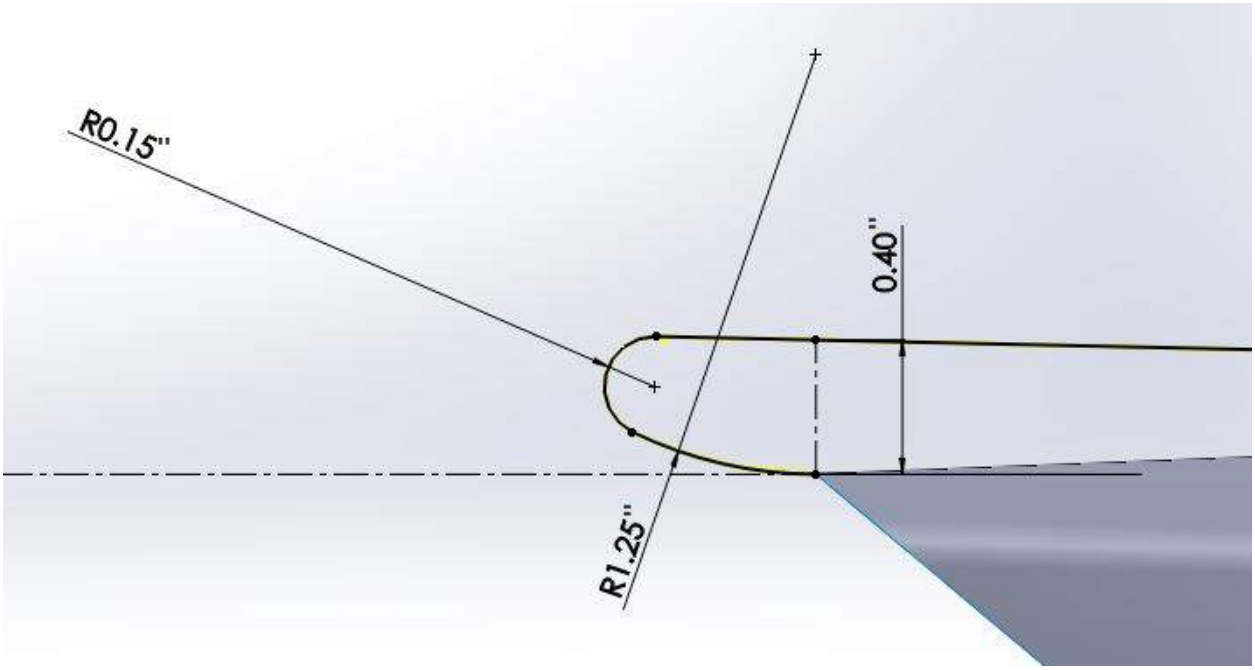


**Figure 7.2.13:** Smoothed inlet geometry

Shown below in Fig.7.2.14, a visual representation of the area ratios of inlet, cowling and nozzle can be clearly seen, as well as the filled lip cross section.

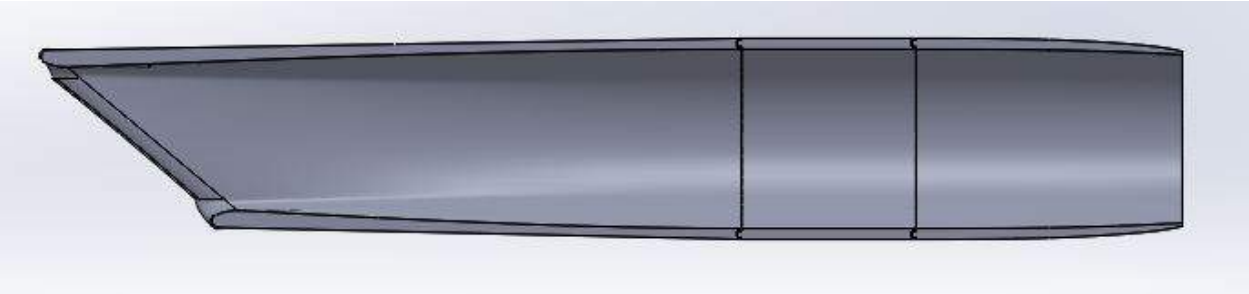

**Figure 7.2.14:** Smoothed inlet side view

Next, the mass properties of the materials were added to the nacelle design as can be shown below in Fig.7.2.15. Plywood is going to be used as both the bulkheads as well as a platform to hot wire cut the duct and front three quarters of the nozzle from high density foam. The nozzle tip, EDF cowl, and inlet are made from 3-D printing ABS plastic.

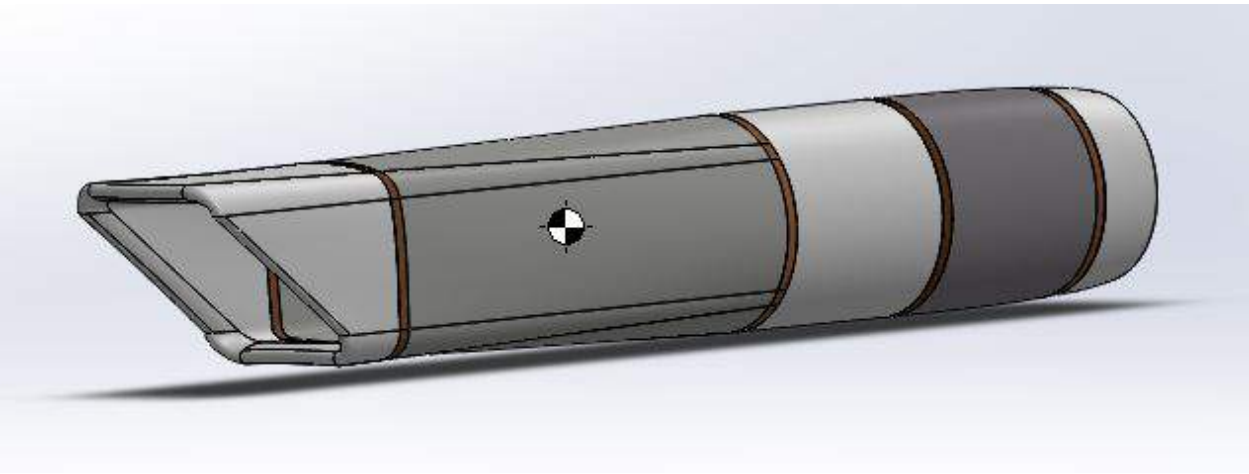

**Figure 7.2.15:** Final configuration including mass properties

As shown below in Fig.7.2.16, the center of mass for the nacelle can be clearly seen.

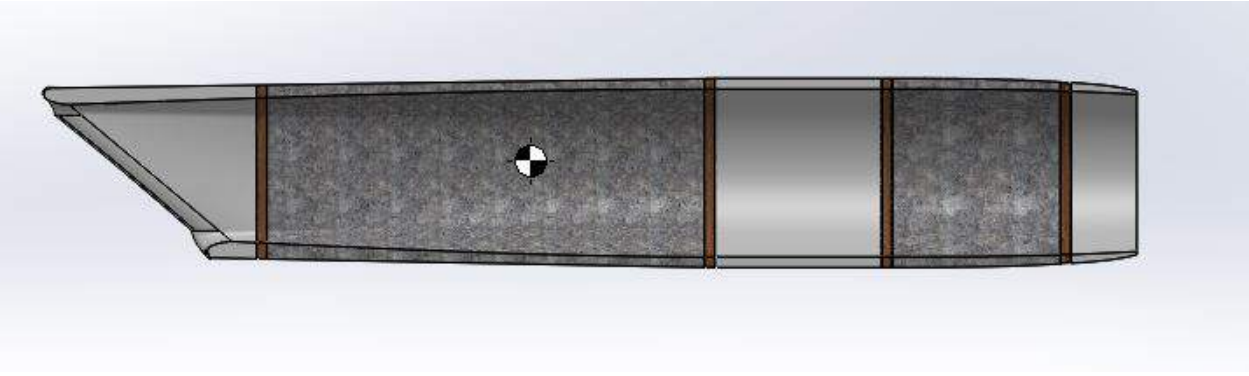

**Figure 7.2.16:** Final configuration including mass properties side view

As shown below in Fig.7.2.17, the shape of the ramp can be seen.

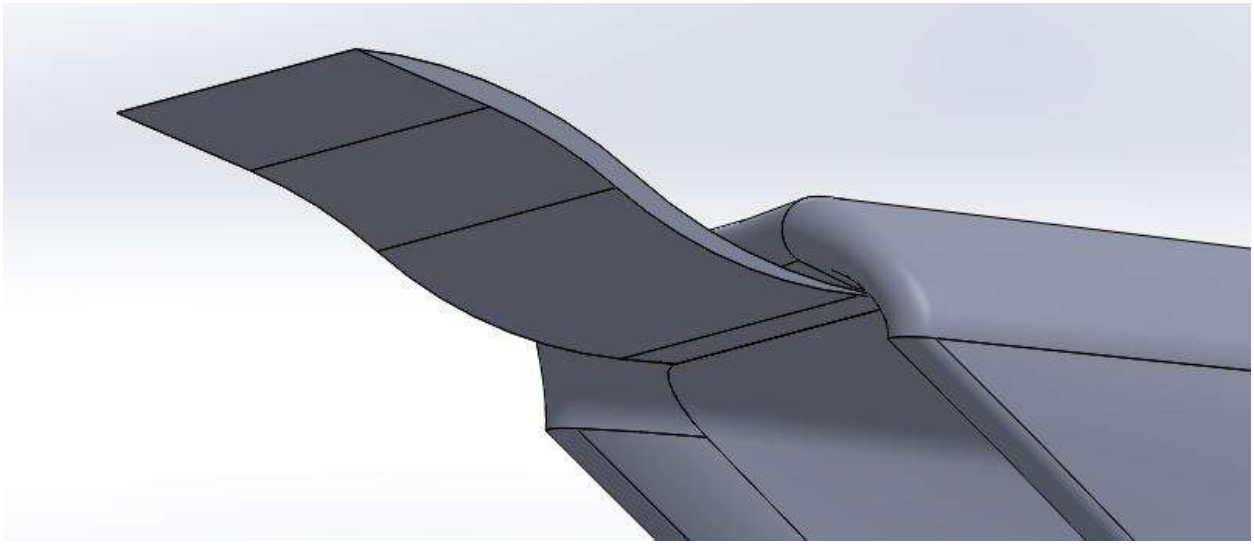

**Figure 7.2.17:** Initial ramp design

This ramp is designed to smoothly connect the upper lip of the nacelle to the underbelly of the wing. This is meant to decrease drag. The ramp connects the inside of the lip and is tangential to the interior wall of the nacelle.

Shown below in Fig.7.2.18, the completed design and integration geometry of the ramp can be seen.

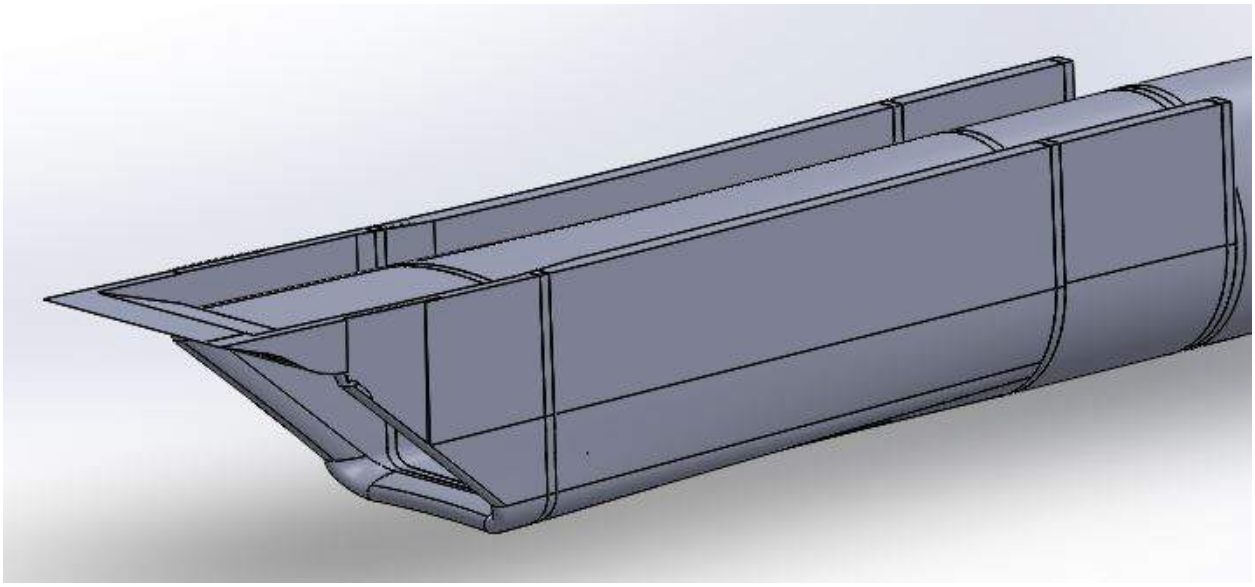

**Figure 7.2.18:** Ramp integration and extension

This completed design uses the same geometry as seen in Fig.7.2.17 and then has added structure coming up from the side walls of the nacelle as well as above the ramp to add structural support. Furthermore, the side walls will decrease form drag due to the pocket of space between the underside of the wing and the top of the nacelle by blocking off this pocket to dynamic flow.

### *7.2.6. Nacelle Mounts*

The nacelles containing the EDF are relatively heavy compared to many other parts of the wing, with the total nacelle weighing over 3 lbs. Not only that, but while the EDF is running, it causes a large amount of vibration through the nacelle. Finally, when the EDF is running, the thrust causes the EDF to pull itself forward inside the nacelle. Therefore, the nacelle mount had to be able to withstand the vibration of the EDF, as well as keeping the engine from flying forward out of the nacelle.

In order to keep the EDF from flying forward into the nacelle, two measures were taken. First, a series of 3D printed pins were place around the interior of the nacelle in front of the engine. These helped to keep the EDF in place. The other measure was to very slightly decrease the diameter of the connecting inlet pieces and the nozzle pieces, which also keep the EDF in place. In order to attach the nacelle to the plane, the nacelle was attached at two points. At the 3D printed portion of the inlet and ahead of the foam, a small mount was attached to the top of the nacelle. This piece went through the bottom of the wing, and was screwed in place into the forward spar. This mount provides support to the 3D printed portion of the lip and the forward portion of the inlet. Since this portion is made of foam and the lip itself is relatively light, the forward mount does not have to support as much weight, and therefore does not have to be as strong. The second mount is a rear mount, attached at the cowl, which houses the EDF. The mount, and attached cowl, are shown in Fig. 7.2.19.

**Figure 7.2.19:** Rear Nacelle Attachent

As shown in Fig. 7.2.19, the attachment consists of two pieces of 3D printed material, which attach at the cowl, and then run upward through the lower surface of the wing, and attach to a rib inside the wing.

The rear mount had to be much stronger than the forward mount. The rear mount supports the weight of the EDF, nozzle, cowl, and the back portion of the inlet. Not only that, it also has to deal with the constant vibration of the engine, as well as keeping the engine from pushing the nacelle forward and ripping off from the bottom portion of the wing. In order to accomplish this, three holes were drilled into each of the 2 supporting 3D printed pieces, and screws were run through them into the rib that it was attached to. The rib itself was a bit thicker than the other ribs in the wing, and is designed specifically for the support of the nacelle. The proximity of the fuselage structure to the nacelles also allow supporting structure to be built into the fuselage, further supporting the nacelles.

## 7.3. Overview

Each component needs to coordinate with other components to build the system which fulfills the requirements for the project. The schematic of the system is shown in Fig. 7.3.1.

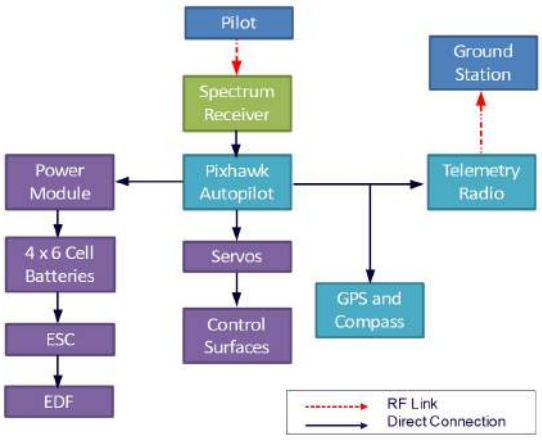


**Figure 7.3.1:** The schematic of the electrical system

As shown in Fig. 7.3.1, the systems is the integration of many components such as electric speed controllers(ESC) and servos.

## 7.4. Selection of Components

In order to design a robust system, reliable components must be chosen with an extra care. The following is the list of components selected with explanation of reasons.

1. Pixhawk

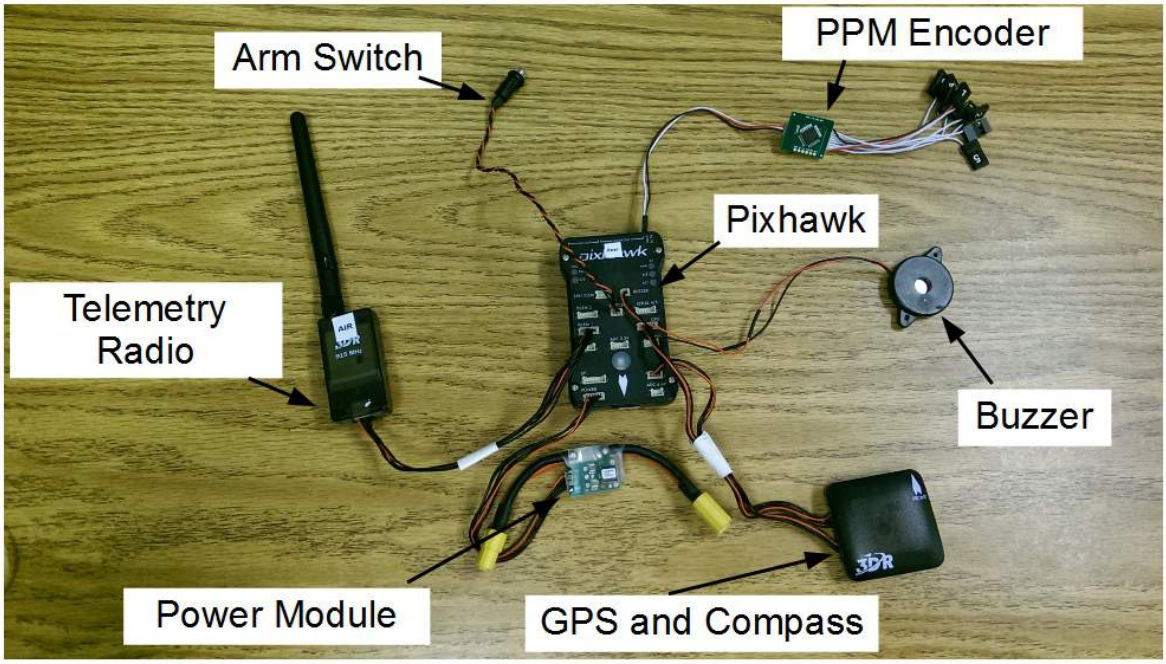


**Figure 7.4.1:** Pixhawk and its accessories

Pixhawk was chosen as the data gathering devise for the R-UAV. It collects flight data such as the Euler angles, airspeed, altitude, and many other useful parameters. The Pixhawk is also capable of activating autopilot. Also, by coordinating with a computer hardware such as Arudino, it is possible to install an active control system, specifically for sideslip correction. There are several parts which acts as components of the Pixhawk. The Pixhawk and its accessories are shown in Fig. 7.4.1. The explanation of the accessories are shown below.

- Telemetry Radio
  The telemetry radio receives the signal from the ground station and sends the information about aircraft which the Pixhawk measures.
- GPS and compass
  It receives the position data from the Global Positioning System. It also has a compass embedded, which enhances the location information.
- Buzzer
  It is an user interface that enables the users recognize the errors with Pixhawk.
- Arm Switch
  This switch is used for "arming" and "disarming" the airplane. When the airplane is "armed", Pixhawk disseminates signals to servos so that the flight mode is activated. On the other hand, when it is "disarmed", the Pixhawk has the information about the flight mode but servos do not.
- Power Module
  The power module measures the current and voltage values from the battery.
- PPM Encoder
  The PPM encoder allows the signal to be transmitted between PWM-only RC equipment to PPM-only autopilot system.

2. DX-18(Fig. 7.4.2)


**Figure 7.4.2:** DX-18

This is a controller that allow pilots to program the control. This is a sophisticated radio which was inherited from 2014 Storm project.

3. Spektrum receiver(Fig. 7.4.3)

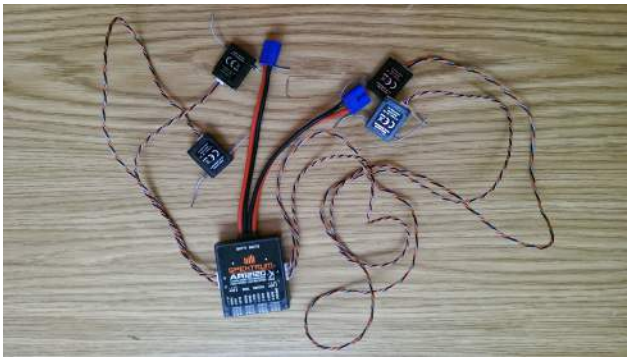

**Figure 7.4.3:** Spektrum radio receiver

This receiver was chosen due to the compatibility with the DX-18 controller.

4. Electronic Speed Controller(ESC) (Fig. 7.4.4)

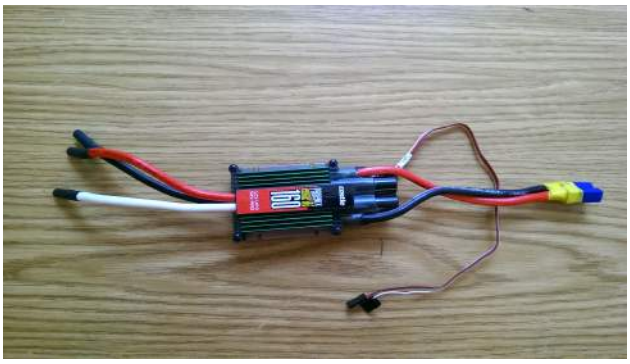

**Figure 7.4.4:** Electronic speed controller

ESC can control the speed of the electronic motors which are installed to the R-UAV. This ESC was chosen based on the maximum current amperage the electric motor requires.

5. Landing gear brake (Fig. 7.4.5)


**Figure 7.4.5:** Landing Gear Brake

An electrical landing gear brakes was chosen to be used for R-UAV. The merits of using the electrical landing gear brakes are that the same power source for other components can be used and that there is no special procedure required for using it whereas air must be charged for the air landing gear brakes.

## 7.5. Programming of Controllers

Pixhawk and the DX-18 controller were programmed to meet the requirements of the project. The programming of Pixhawk the DX-18 channels are included in Table 7.5.1 and Table 7.5.2, respectively.

**Table 7.5.1:** Channels of the Pixhawk

| Pixhawk Channel | Actuators |
|---|---|
| RC1 | Aileron |
| RC2 | Horizontal Stabilizer |
| RC3 | Throttle |
| RC4 | Thrust Vectoring |
| RC5 | Canard |
| RC6 | Nose Wheel and Rudder |
| RC7 | Flap |
| RC8 | Breaks |

**Table 7.5.2:** The channels and programmings for DX-18 controller

| Actuator | DX18 | Acronym |
|---|---|---|
| Throttle | THRO | THR |
| Aileron | AILE | AIL |
| Horizontal Stabilizer | ELEV | ELE |
| Thrust Vectoring | RUDD | RUD |
| Nose Wheel &Rudder | GEAR | RUD |
| Flap | AUX1 | ELE |
| Canard | AUX2 | FLP |
| Nose Wheel | AUX3 | AX3 |
| Brakes | AUX5 | AX5 |

The mixing of the channels are shown in Table 7.5.3.

**Table 7.5.3:** Mixing Settings of Channels for DX18

| Mixing | Parts | Channel | Percentage |
|---|---|---|---|
| Mix 1 | Rudder | AUX 3 | 50% / 50% |
| Mix 2 | Canard | AUX 2 | 50% / 50% |
| Mix 3 | H | AUX 5 | 100%/ 100% |
| Mix 4 | RKn | AUX 3 | 20%/ 20% |

## 7.6. Sizing of servos

The servos were chosen based on the torque required for deflecting the control surfaces. The expected torque required were found based on the calculations done by Flight Dynamics team. The expected torque and generatable torques are shown in Table 7.6.1.

**Table 7.6.1:** The expected torque for each component which utilizes a servo and the torque and mass information about servos

| Component | Expected Torque, kg-cm | Torque Generated by Servos, kg-cm | Mass, g |
|---|---|---|---|
| Thrust Paddle | 8.3 | 8.6 | 28.4 |
| Canard | 9.7 | 13 | 49 |
| Horizontal Stabilizer | 32.5 | 40 | 170 |
| Flap | 13.3 | 16 | 57 |
| Aileron | 12.3 | 8.6 | 29 |
| Nose Wheel | Unknown | 16 | 57 |
| Rudder | Unknown | 16 | 57 |

Nose wheel is meant to steer the airplane when it is on the ground. However, there is

not enough information to calculate the torque required for steering of the wheel. Also, the initial designs did not include a rudder thus the calculations has not finished yet for the torque required for the rudder.

## 7.7. Ground Station

In order to collect the flight information from Pixhawk, a software called Mission Planner needs to be used.

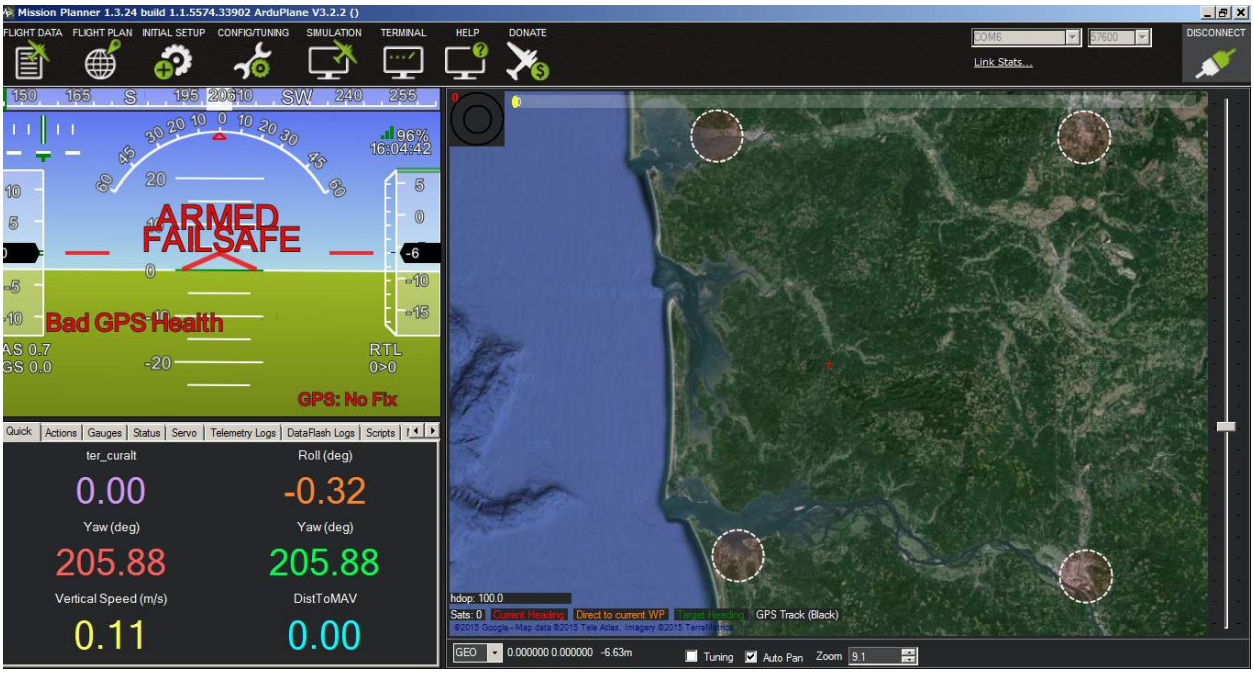


**Figure 7.7.1:** Interface of the Mission Planner

The interface of Mission Planner is shown in Fig. 7.7.1. As shown in the figure, six different flight information can be displayed in the main interface. The types of information to be displayed can be changed. Also, all of the information is recorded with the location of the aircraft based on the GPS information. After a flight, the information recorded can be displayed with Google Earth along with the flight path. The software can be downloaded from the link shown below. The website has more detailed information about the software. Mission Planner Home

## 7.8. Stability and Control

### *7.8.1. Control Surfaces*

#### 7.8.1.1. Flaps

Flaps were added to the inboard wing to increase lift at takeoff and landing. As can be seen in (figure of lift), deflecting the flaps to -30° and -20° caused the inboard wing to stall out at higher angles of attack, reducing the gain in lift. It was decided to still use flaps but to only deflect them to -10° to minimize stalling and maximize lift at high angles of attack. The amount of lift provided at takeoff from the flaps deflected to -10° is interpolated from

the configurations with flaps deflected to 0° and is likely to be only a conservative estimate of the effect.

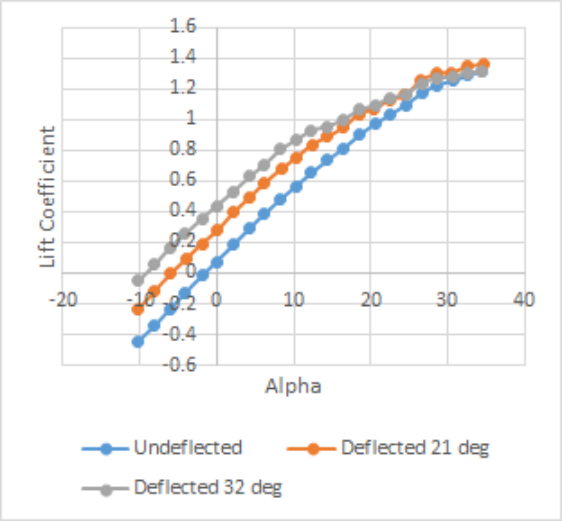


**Figure 7.8.1:** Lift of Flaps

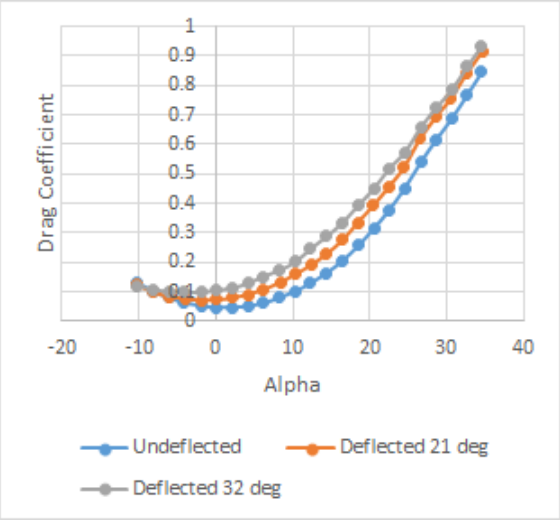


**Figure 7.8.2:** Drag of Flaps

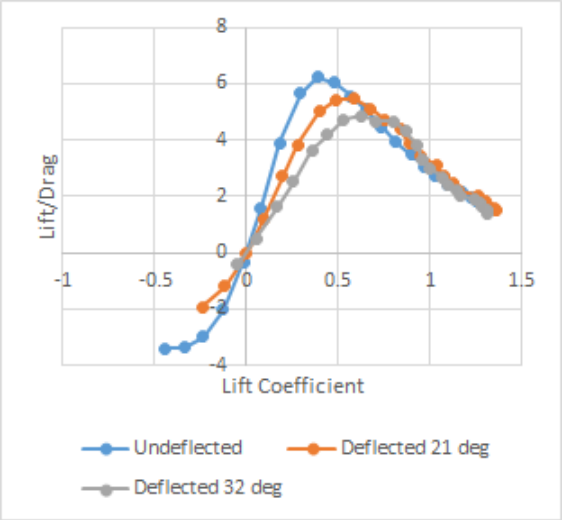


**Figure 7.8.3:** L/D of flaps

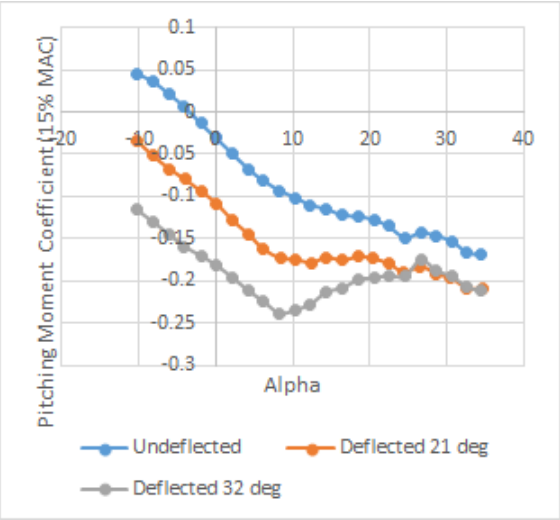


**Figure 7.8.4:** Pitching Moment

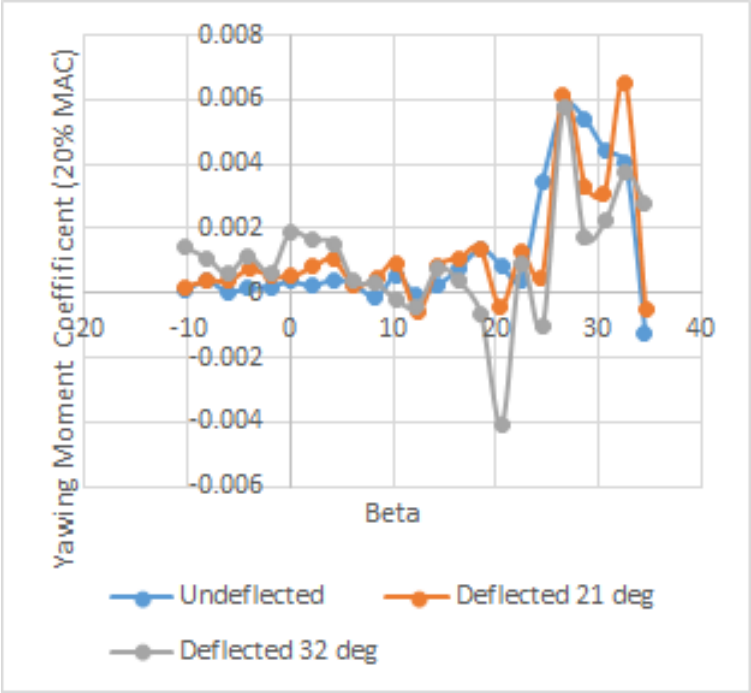


**Figure 7.8.5:** Yawing Moment of Flaps about 20%CG

7.8.1.2. Ailerons

The ailerons were split into two parts in case one of them needed to be used as a flaperon, but because the flaps on the inboard wing were so effective, the ailerons on the outboard wing could be used only for roll control. The ailerons were tested at +/-10° and +/-20° and the rolling moment increment was used to find their effectiveness. Because the ailerons change effectiveness based on their deflection angle, their control derivative was taken as an average effectiveness between 0° and 20° deflection.

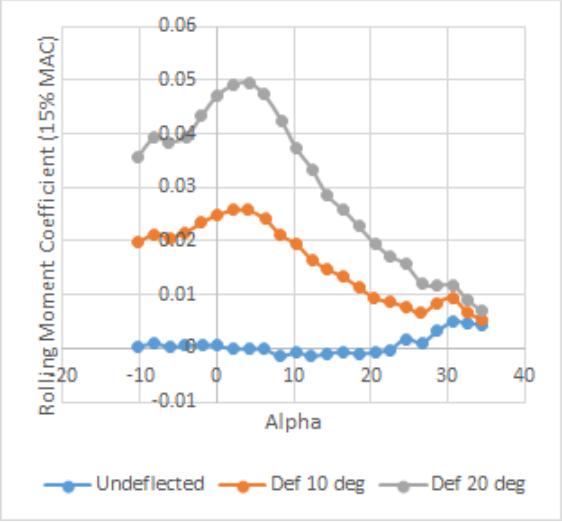


**Figure 7.8.6:** Rolling Moment of Aileron

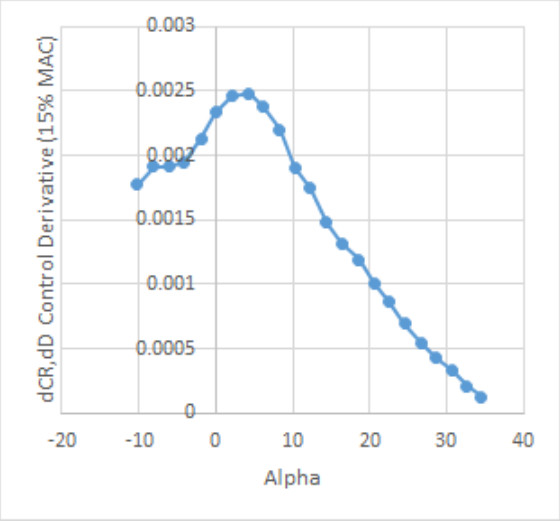


**Figure 7.8.7:** Control Derivative of Ailerons

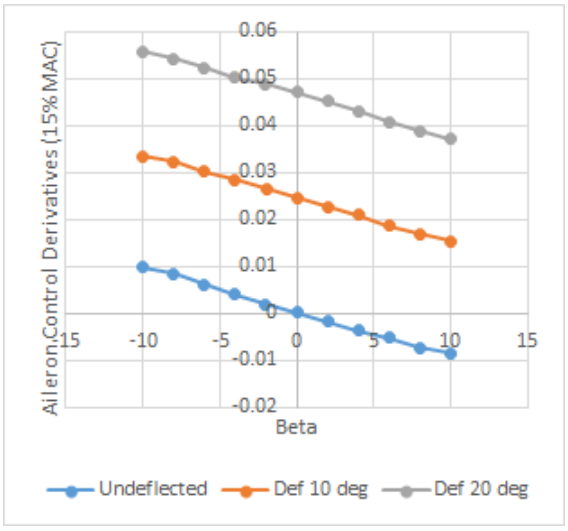


**Figure 7.8.8:** Control Derivative of Ailerons at Alpha = 0

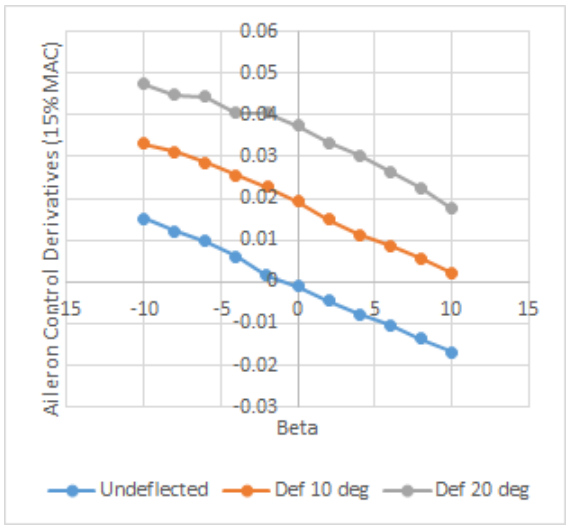


**Figure 7.8.9:** Control Derivative of Ailerons at Alpha = 10

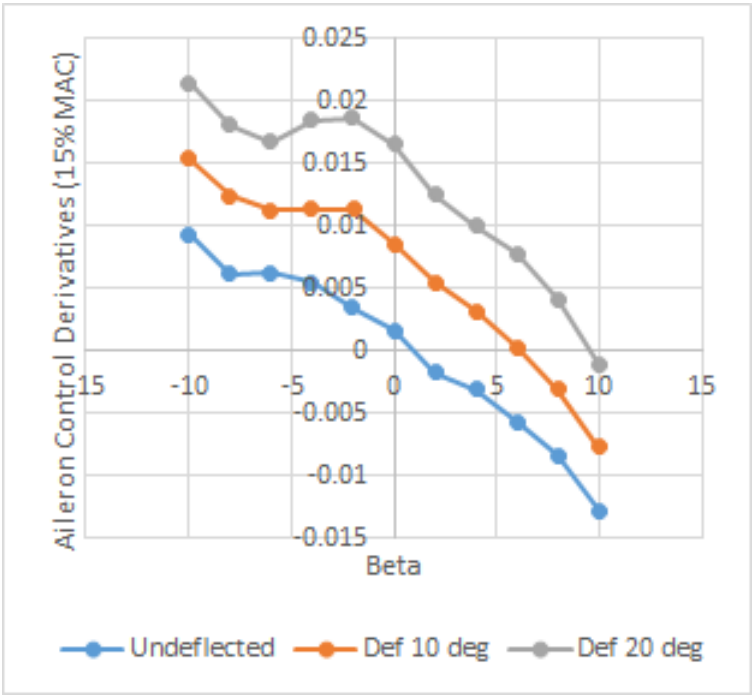


**Figure 7.8.10:** Control Derivative of Ailerons at Alpha = 24

#### 7.8.1.3. Stabilator

Fig. 7.8.11 shows the trimmed angles of attack for a few tested stabilator deflections. The difference at $\delta_H = 0°$ is small but is quite significant at $\delta_H = -15°$, indicating that the control authority advantage of stabilator H2 deflection angle is large. To trim at modest angles of attack ($\alpha < 10°$), stabilator H1 could be required to deflect up to -15°with no canard deflection. Stabilator H2, on the other hand, has enough authority to trim well beyond the normal range of $\alpha$ at no more than -15°deflection even without the canard deflected. The

horizontal stabilizer H2 was chosen for the final RUAV configuration due to the insufficiency of stabilator H1, a premise that significantly outweighed the extra parasitic drag incurred by having a larger stabilator surface.

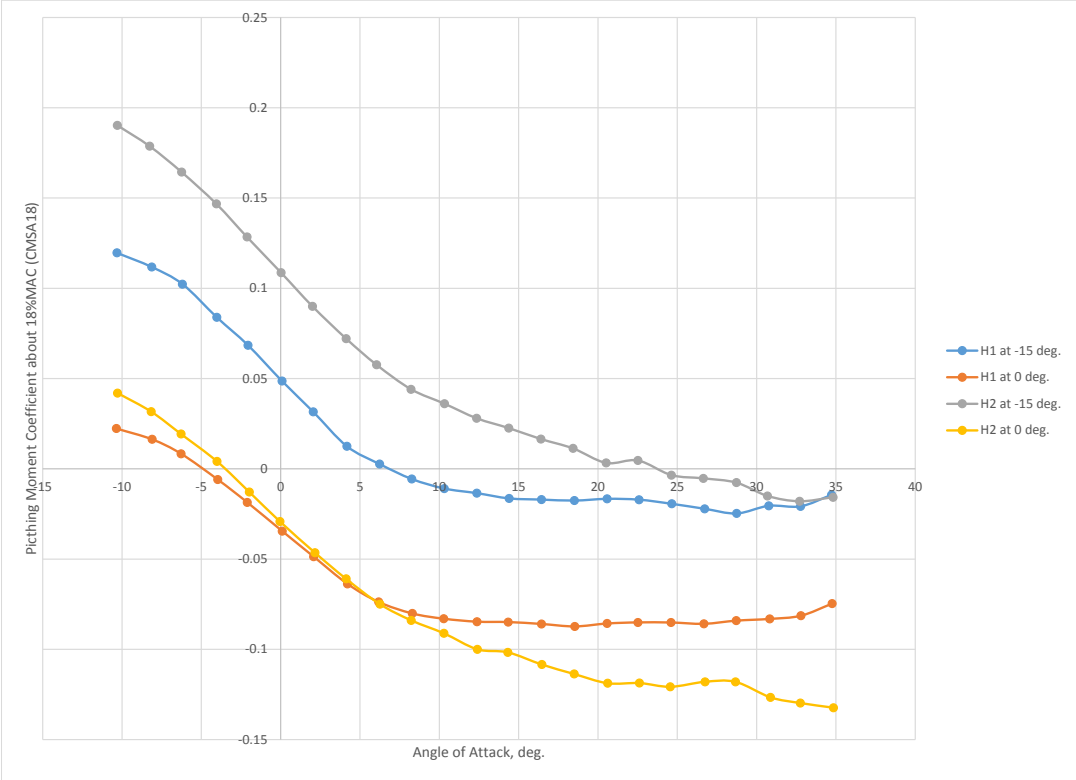


**Figure 7.8.11:** Moment coefficient curves for stabilators H1 and H2 at $\delta_H = 0°$ and $0°$.

The pitching moment contribution for each stabilator configuration is shown in Fig. 7.8.121 at various angles of attack. Judging by the increased moment for stabilator H2 at $\delta_H = -5°$ above what a linear relationship between $\delta_H = 0°$ and $\delta_H = -15°$ would suggest, the linear moment contribution over $-15° < \delta_H < 0°$ for stabilator H1 shown in Fig. 7.8.12 is likely conservative. Regardless, the stabilator H2 shows close to 150% of the pitching moment authority of stabilator H1 at negative deflection angles. Average values for the control derivatives $\frac{\partial c_M}{\delta_H}$ for both configurations are shown in Fig. 7.8.13 as functions of angles of attack.

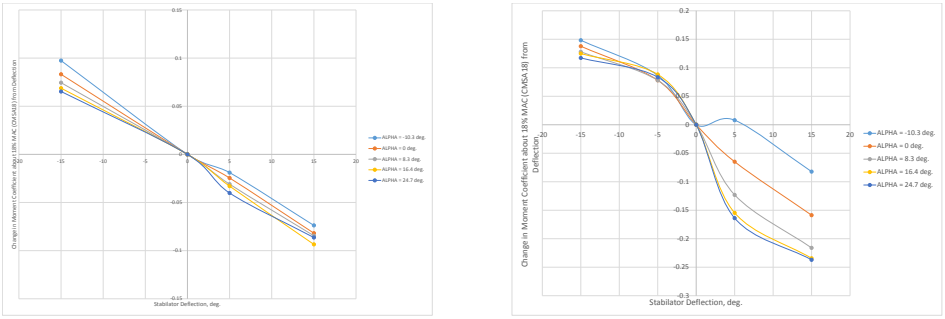


**(1)** Stabilator H1 **(2)** Stabilator H2

**Figure 7.8.12:** Change in pitching moment coefficient (about 18%MAC) relative to zero-deflection value versus stabilator deflection $\delta_H$.

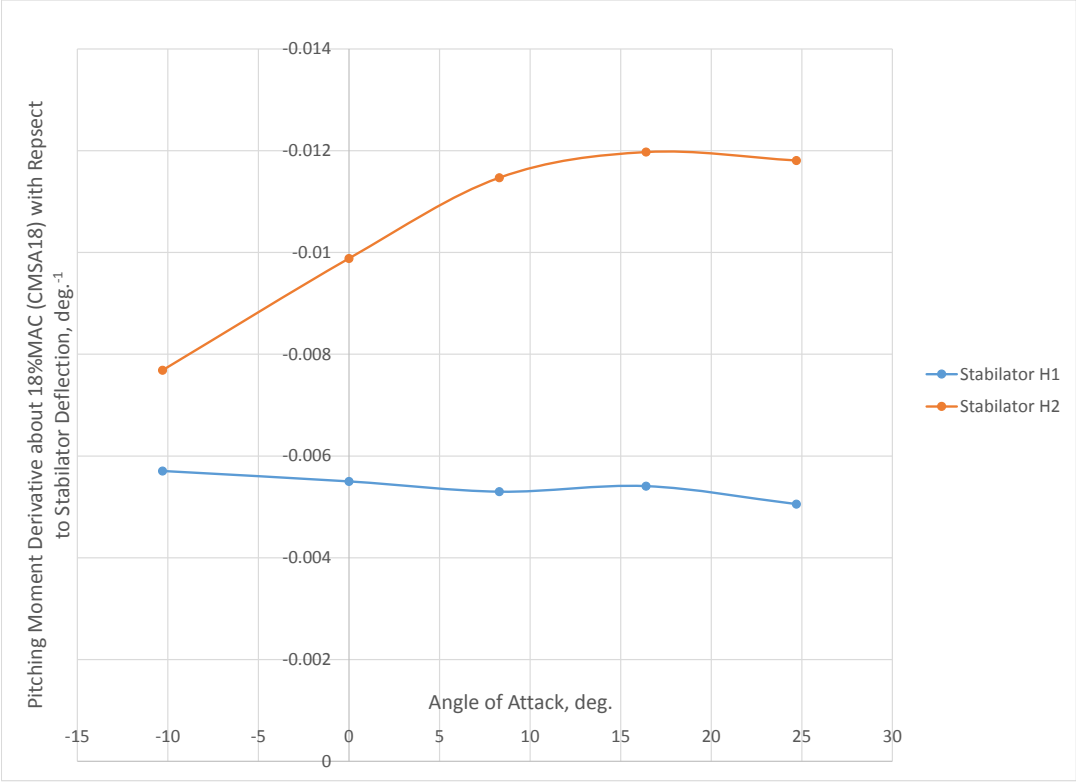


**Figure 7.8.13:** Pitching moment control derivative $\frac{\partial c_M}{\partial \delta_H}$ versus $\alpha$ for both stabilator configurations.

The contributions of lift and drag from just the final stabilator H2 are shown in Figs. 7.8.14

and 7.8.15.

#### 7.8.1.4. Canard

The most thoroughly tested canard configurations included a more forward canard, referred to as canard C2, and a larger canard farther aft, referred to as canard C4. Fig. 7.8.18 shows the difference in pitching moment about 15%MAC for the aircraft with each canard deflected to 15°.

Fig. 7.8.16 demonstrates some unexpected results for canard C4, particularly for the $\delta_C = 15°$ run over the range $2° < \alpha < 10°$ where the 15°canard produces more pitching moment than the 30°canard. This, at a first glance, would suggest that the 30/degree canard stalls out and loses lift around $\alpha = 2°$ thus decreasing the pitching moment below what the 15°canard with attached flow at the same $\alpha$ would produce, a reasonable result considering the high angle of incidence between the canard and oncoming flow ($\alpha+\delta_C > 30°$). The increase in pitching moment with angle of attack over $0° < \alpha < 5°$ is most surprising, particularly since canard C2 deflected at 15°does not display this phenomenon, shown in Fig. 7.8.17. Barring some very anomalous aerodynamic effects, the positive slope seen for C4 demonstrates some combination of very high lift on (and attached flow over) the canard and relatively low pitch-down stability on the rest of the airplane, possibly due to downwash from the high lift on the (larger) canard. This is still rather unexpected, since Fig. 7.8.18 shows the canard C4 as being more stable in pitch at the same deflections over $5° < \alpha < 18°$.

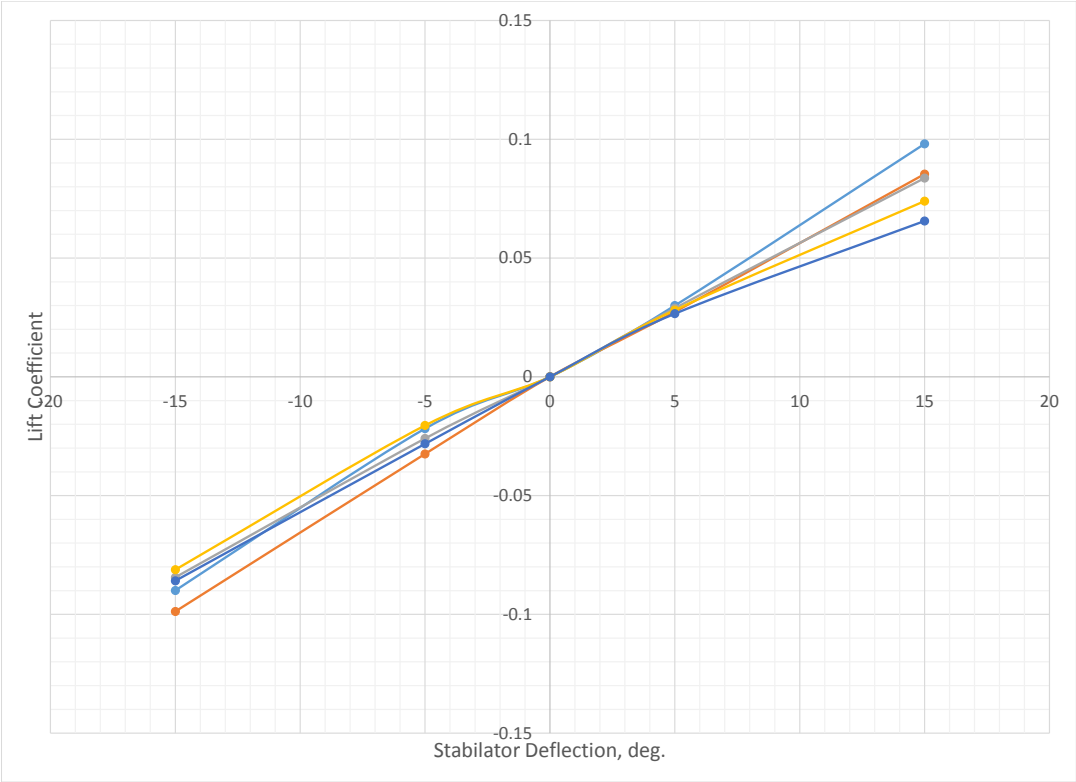


**Figure 7.8.14:** Contribution of lift coefficient from stabilator H2 as a function of deflection angle at several angles of attack.

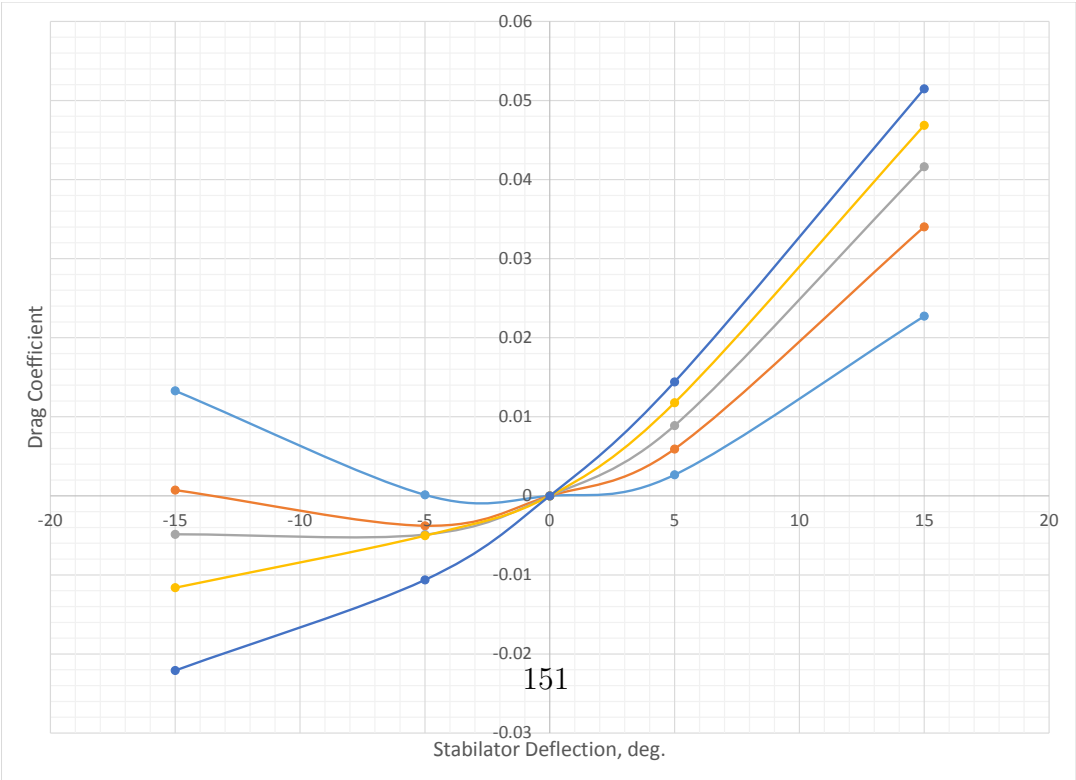

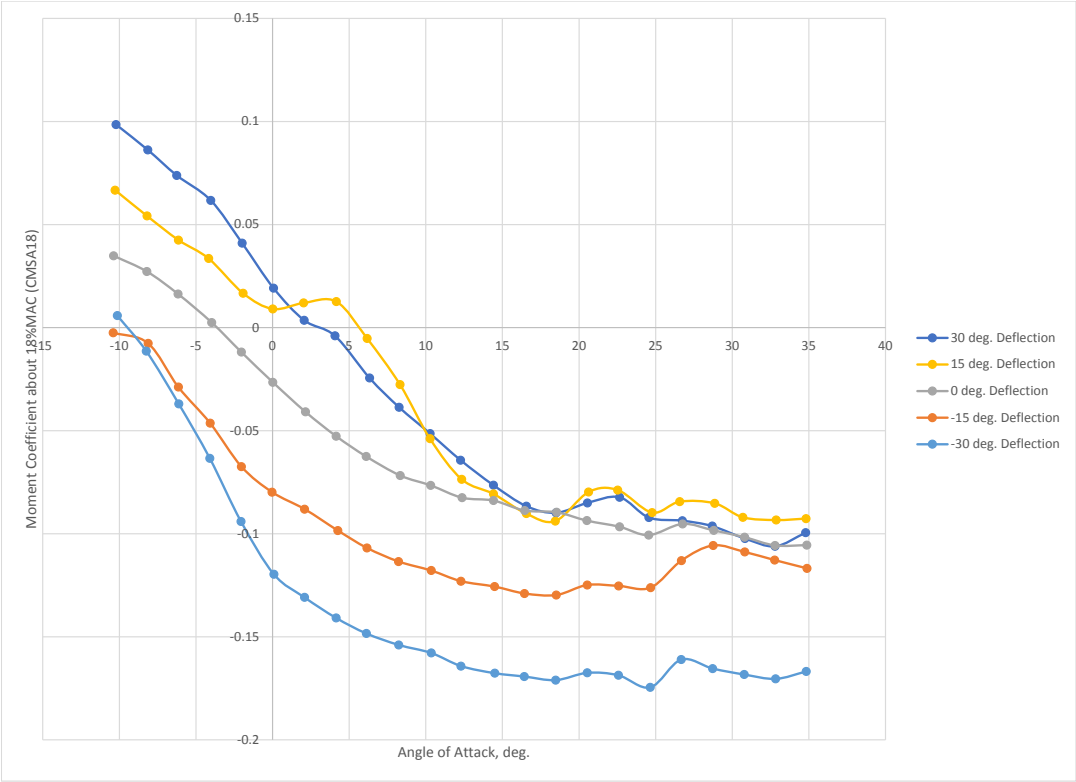


**Figure 7.8.16:** Moment coefficient $c_m$ about 18%MAC for canard C4 configurations tested at various angles.

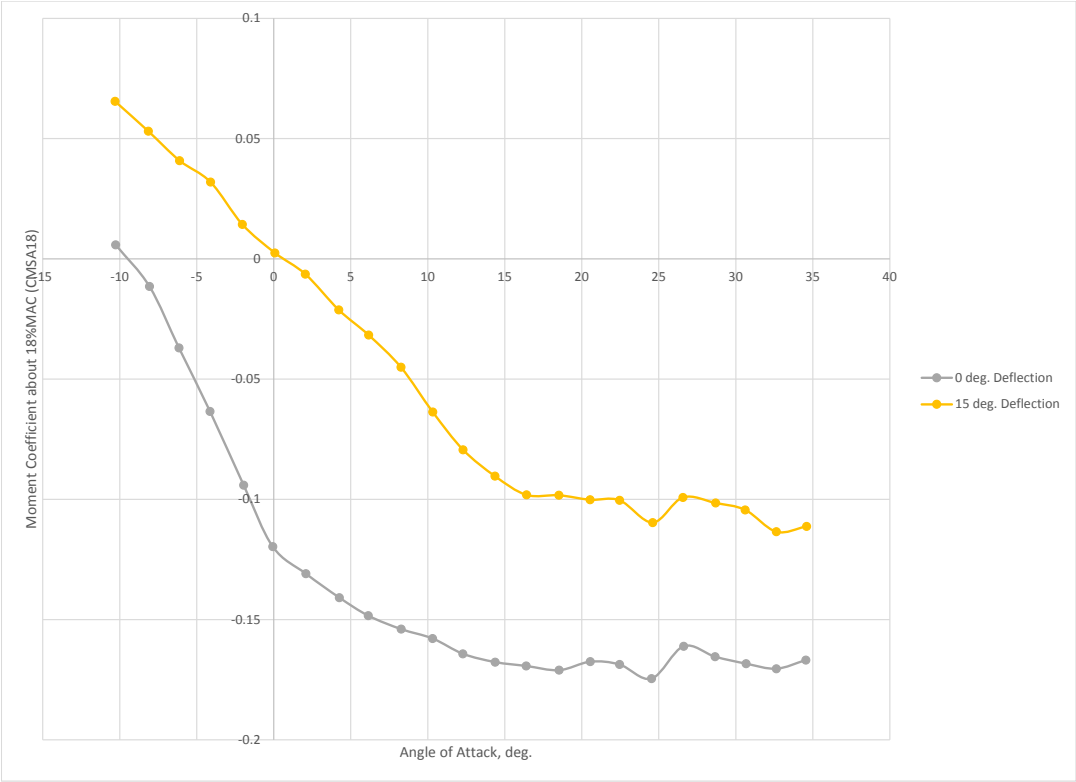


**Figure 7.8.17:** Moment coefficient $c_m$ about 18%MAC for canard C2 configurations tested at various angles.

Canard C4 proved to be less destabilizing in pitch, as shown by the more negative slope in the $c_m$-$\alpha$ curve. Canard C4 also showed some local instabilities at higher angles of attack as well as a region of neutral pitch stability at very shallow angles of attack.

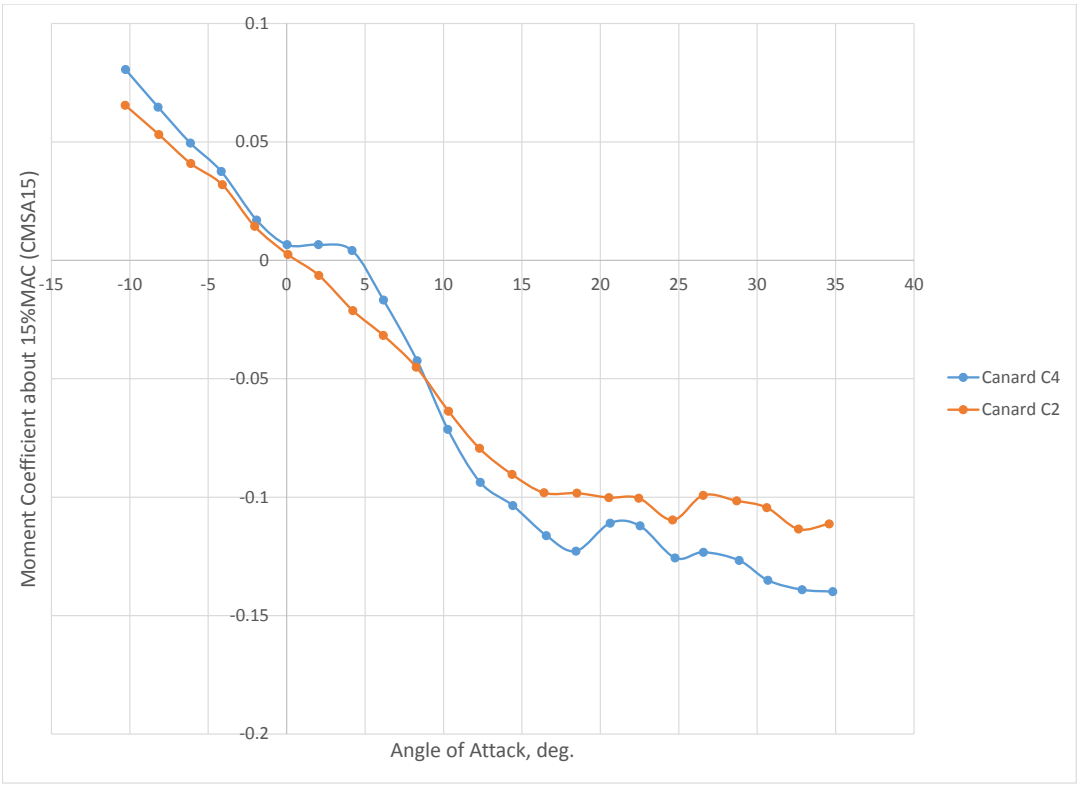


**Figure 7.8.18:** Moment coefficient $c_m$ about 15% MAC versus $\alpha$ for the entire aircraft with canards C2 and C4, each deflected to 15°.

Canard C2 was more aerodynamically efficient for the entire aircraft when the canards were deflected at the same angles, particularly over a range of modest angles of attack (about $5° < \alpha < 15°$), which is seen in Fig. 7.8.19.

In order to characterize the primary canard pitch control derivative $\frac{\partial c_m}{\partial \delta_C}$, particularly as a function of angle of attack, the trend of the pitching moment versus deflection for canard C4 (tested at five deflection angles) was assumed to be similar to the trend for canard C2 (a comparatively sparse data set that was only tested at two deflections). The two deflections would provide a linear slope $\frac{\partial c_m}{\partial \delta_C}$, and the viability of using this derivative for further analysis can be justified by comparison with the more populated data set.

Fig. 7.8.20 shows the pitching moment $c_m$ 'contribution' ($c_m$ for a given $\delta_c$ minus $c_m$ at $\delta_C = 0°$) versus that deflection $\delta_C$. The pitching moment contribution with respect to deflection is generally less for canard C2 (shown by a single deflection of $\delta_C = 15°$). This does not necessarily refute the conclusions from Fig. 7.8.18 that canard C2 is more effective, but does show that canard C2 effects a greater pitching moment at zero deflection. This does, however, mean that the canard will have to be deflected slightly more to trim out the same $\delta c_m$.

Also, the linearity of the $c_m$ versus $\alpha$ relationship for canard C2 in Fig. 7.8.18 reinforces

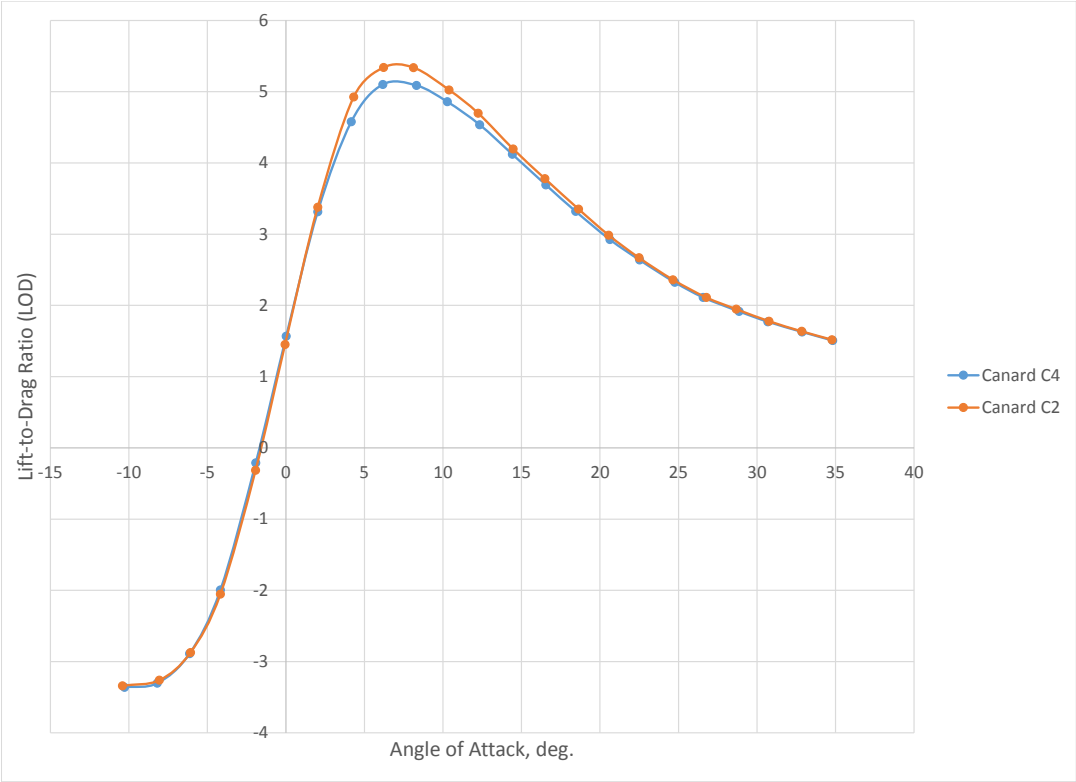


**Figure 7.8.19:** Lift-to-drag ratio versus angle of attack $\alpha$ for canards C4 and C2, both deflected at 15°.

the notion that the relationship between $c_m$ and deflection should also be linear. Both of these angles represent the realignment of the canard relative the freestream, and the only difference in the aerodynamics of the canard between a given $\Delta\alpha$ and a given $\Delta\delta_C$ would be from the angle of the nose of the aircraft, which is unlikely to negate the linearity of these relationships at shallow angles.

For usable angles of attack (such as $\alpha = 0°$ and $\alpha = 10.3°$ in Fig. 7.8.20) the relationship between $c_m$ contribution and $\delta_C$ for $-15° < \delta_C < 15°$ looks approximately linear (specific nonlinearities were beyond the scope of testing). This justifies the assumption that a constant derivative $\frac{\partial c_m}{\partial \delta_C}$ (i.e. a linear fit) for canard C2 would be sufficiently accurate despite only have two data points for $c_m$ at deflection angles 0°and 15°.

For canard C2, these linear-fit $\frac{\partial c_m}{\partial \delta_C}$ values were taken, whereas for canard C4, a spline fit for each of the curves in Fig. 7.8.20 was differentiated to yield functions of $\frac{\partial c_m}{\partial \delta_C}$ versus $\delta_C$. Average values of $\frac{\partial c_m}{\partial \delta_C}$ were taken for ranges of $/delta$ corresponding to modest canard angles of incidence (i.e. $-15° < \alpha + \delta_C < 15°$). These are plotted versus $\alpha$ in Fig. 7.8.21. The corresponding linear-fit values for canard C4 using just $\delta_C = 0°$ and $\delta_C = 15°$ are also displayed. The erratic spike in effectiveness of canard C4 around $\alpha = 6°$ correlates with

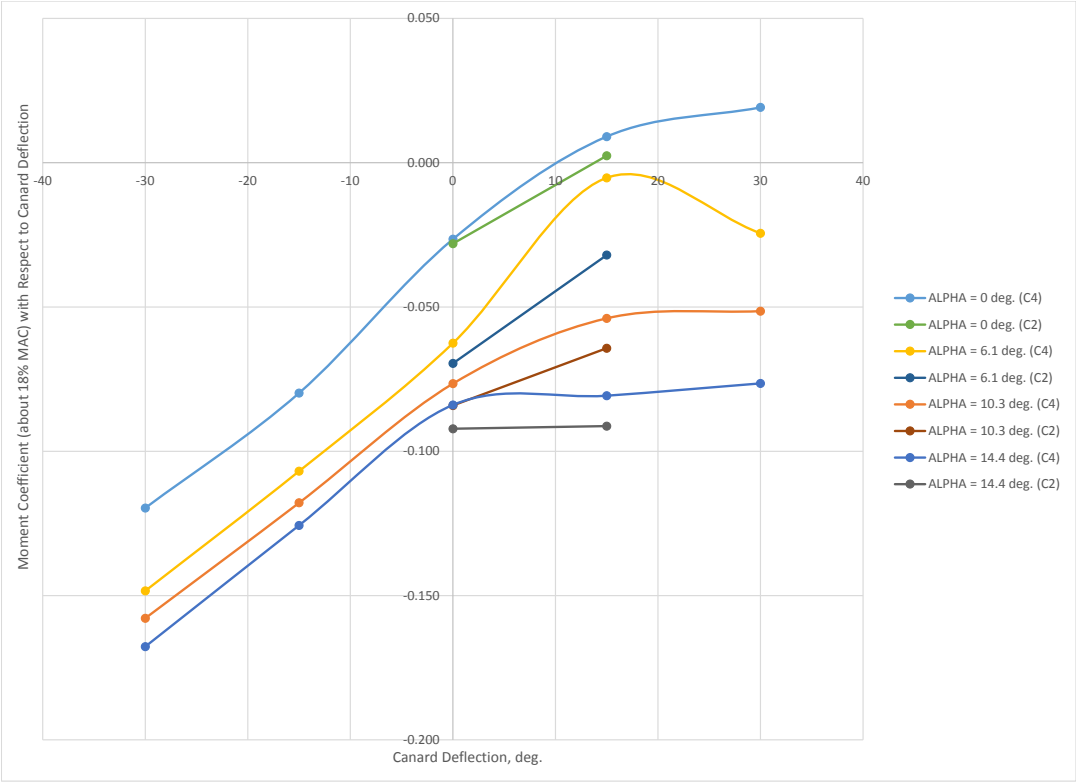


**Figure 7.8.20:** Pitching moment contribution from canard deflection only (i.e. test data with zero-deflection forces and moments subtracted out) for both canards C2 and C4.

the peak in pitching moment at $\delta_C = 15°$ seen in Fig. 7.8.16. In the interest of finding a derivative $\frac{\partial c_m}{\partial \delta_C}$ that is more general throughout the range of small angles of attack (i.e. $\alpha > 0°$), the spline-average derivatives at $\alpha = 0°$ and $\alpha = 6.1°$ incorporate values of $\frac{\partial c_m}{\partial \delta_C}$ over $-15° > \delta_C > 15°$ while the values at $\alpha = 10.3°$, $\alpha = 14.4°$, and $\alpha = 18.5°$ use only $-30° > \delta_C > 0°$ for low canard angles of incidence. This curve in Fig. 7.8.21 circumnavigates the some of the irregular aerodynamic behavior around $\alpha = 5°$.

Approximate stability derivatives can be taken for any usable angle of attack via this same method and by referring to the interpolation between the plotted angles. As expected, the effectiveness of the canard decreases dramatically toward the upper range of angles of attack (unless $\delta_C$ is either less than zero or very small). Additionally, for both canard configurations, the effectiveness is greatest at small positive angles of attack, which are applicable to trim at higher airspeeds.

Fig. 7.8.22 shows necessary trim deflections as functions of airspeed. Trimming out unbalanced pitching moments from the wing can be achieved with a number of combinations of canard and stabilator deflections. The stabilator deflections necessary for canard deflections

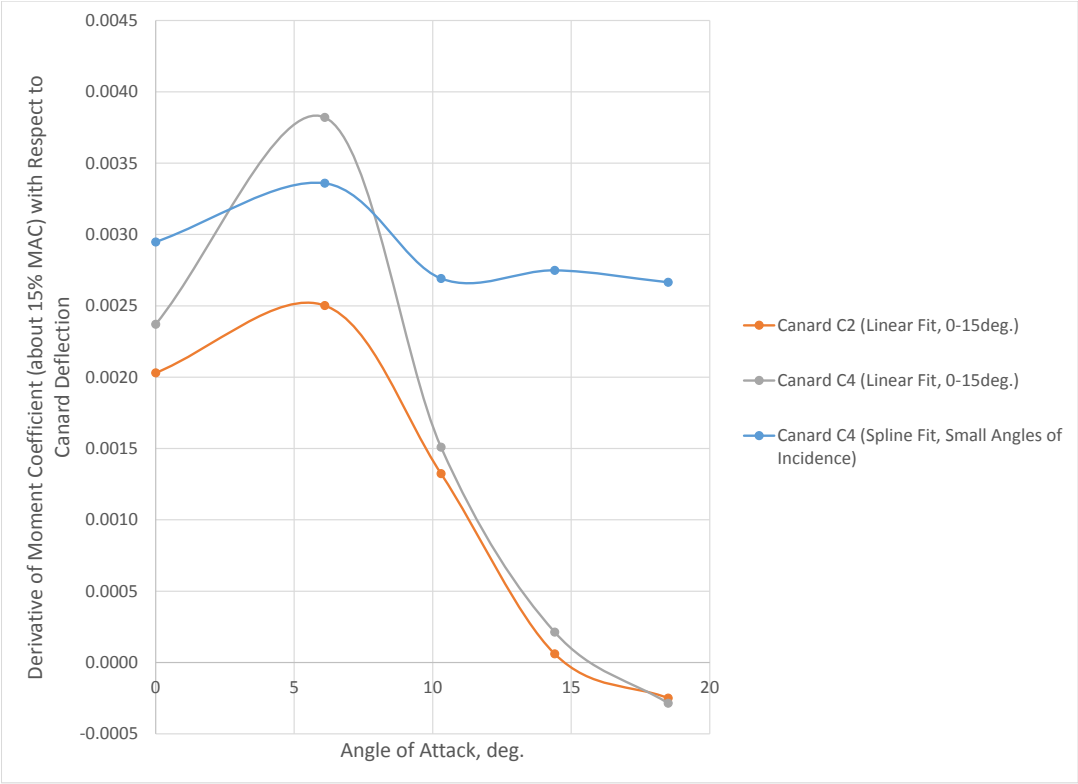


**Figure 7.8.21:** Canard pitching moment control derivative $\frac{\partial c_m}{\partial \delta_C}$ versus $\alpha$.

of 0°and 15°are shown. It is clear from Fig. 7.8.22 that either canard configuration would be sufficient to trim the aircraft at reasonably small stabilator deflections over a large range of airspeeds, and neither configuration particularly extends the range of trimmable airspeeds in either direction. For small canard deflections, canard C4 requires noticeably less stabilator deflection to trim at a given airspeed, whereas at larger canard deflections the difference is pronounced. Canard C4 is expected to be more efficient in trim (particularly at cruise s) due to requiring less stabilator deflection and resultant added drag (or, alternatively, a lesser $\delta_H$ for given $\delta_C$). A larger canard will experience more drag per se at the same deflection angle (see Fig. 7.8.19), but this effect is significantly less pronounced than the drag reduction of deflecting the stabilator a few to several degrees less. Furthermore, using canard C4 opens up the possibility of trimming the aircraft at airspeeds of interest (¡100mph) without requiring the stabilator to produce negative lift, which contributes to the efficiency of the aircraft (provided that the highly-deflected canard does not produce too much drag to negate this benefit).

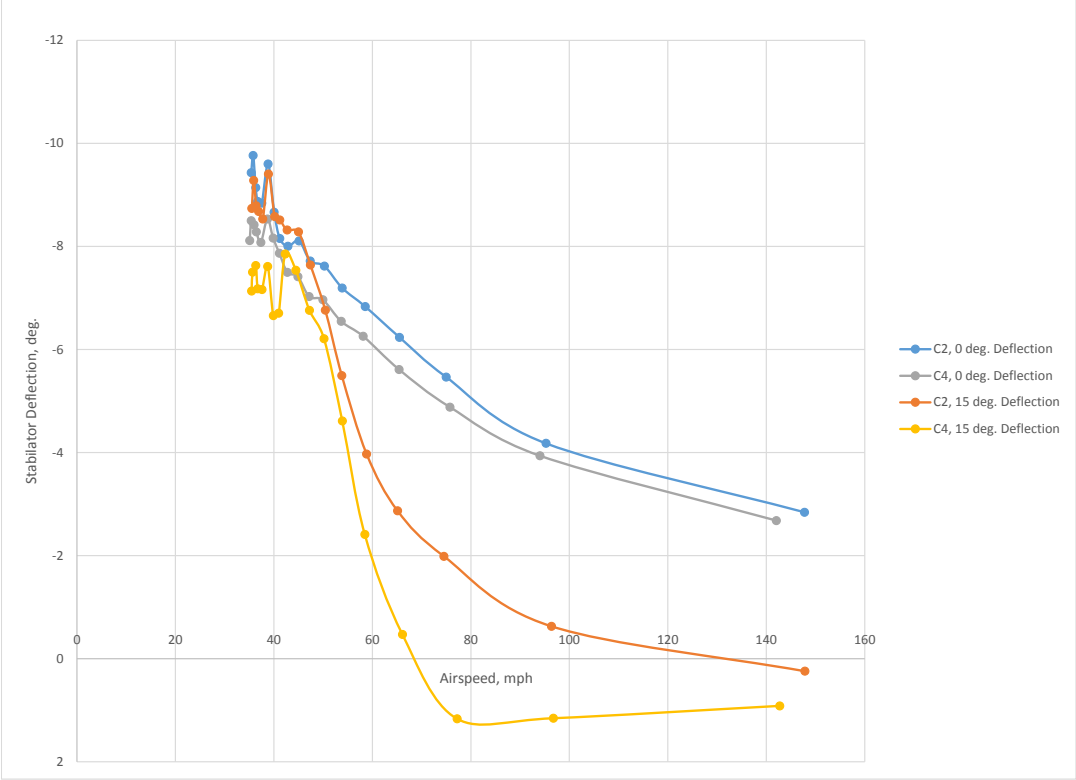


**Figure 7.8.22:** Stabilator deflections necessary for trimmed flight at different airspeeds, shown with canard deflected and undeflected.

Table 7.8.23 shows drag coefficients at two different trimmed airspeeds, each with canard deflections (for both canards) $\delta_C = 0°$ and $\delta = C = 15°$ and the corresponding trimmed stabilator deflections. Canard C4 proved to be more efficient in terms of drag when each canard was deflected at $\delta_C = 15°$ by approximately 8 drag counts, while the difference was minimal (within a drag count) with the canard undeflected.

**Figure 7.8.23**

| Airspeed, mph | $\delta_C$, deg. | $c_D$ (C2) | $c_D$ (C4) |
|---|---|---|---|
| 65.5 | 0 | 0.06642 | 0.06638 |
| | 15 | 0.05436 | 0.05358 |
| 75.5 | 0 | 0.07428 | 0.07438 |
| | 15 | 0.06080 | 0.05993 |

In addition to the more thorough testing of canard configuration C4 (large, middle position) and the similar option C2 (small, forward position), a canard configuration C5 (large, forward position) was tested in pitch at $\delta_C = 0°$ and $\delta_C = 15°$. Considering that both canard

options C2 and C4 provided plenty of pitch control to trim the aircraft and take off, the extra pitch authority added by moving C4 forward or (equivalently) increasing the area of C2 was considered extraneous. The smaller canard in the forward position (C1) was implemented in early tests building up the configuration but was not tested at any deflections.

Intuitively, having a larger canard decreases efficiency per say by generating more skin friction drag as well as generating more induced drag and downwash on the main wing implied by more lift on the canard itself. More canard authority, however (either by having a larger or more forward canard) should decrease drag from the stabilator due to requiring a lesser stabilator deflection to trim the aircraft. These counteracting means of increasing and decreasing efficiency necessitate further analysis of the actual efficiency at various trim conditions in order to determine which canard is actually more efficient in trimmed flight.

Figs. 7.8.24 and **??** show the drag for both canard configurations as functions of trimmed airspeed and lift coefficient. Despite the low resolution of data with respect to canard deflection (particularly for canard C2), canard C2 performs more efficiently in drag for most airspeeds of interest, and is only outperformed by canard C4 at trimmed airspeeds less than 55mph, corresponding to a lift coefficient of about $c_L = 0.6$. This indicates that, generally, the extra drag for a higher stabilator deflection while trimming with canard C2 is less than increased parasitic drag and drag due to lift and downwash while trimming with canard C4.

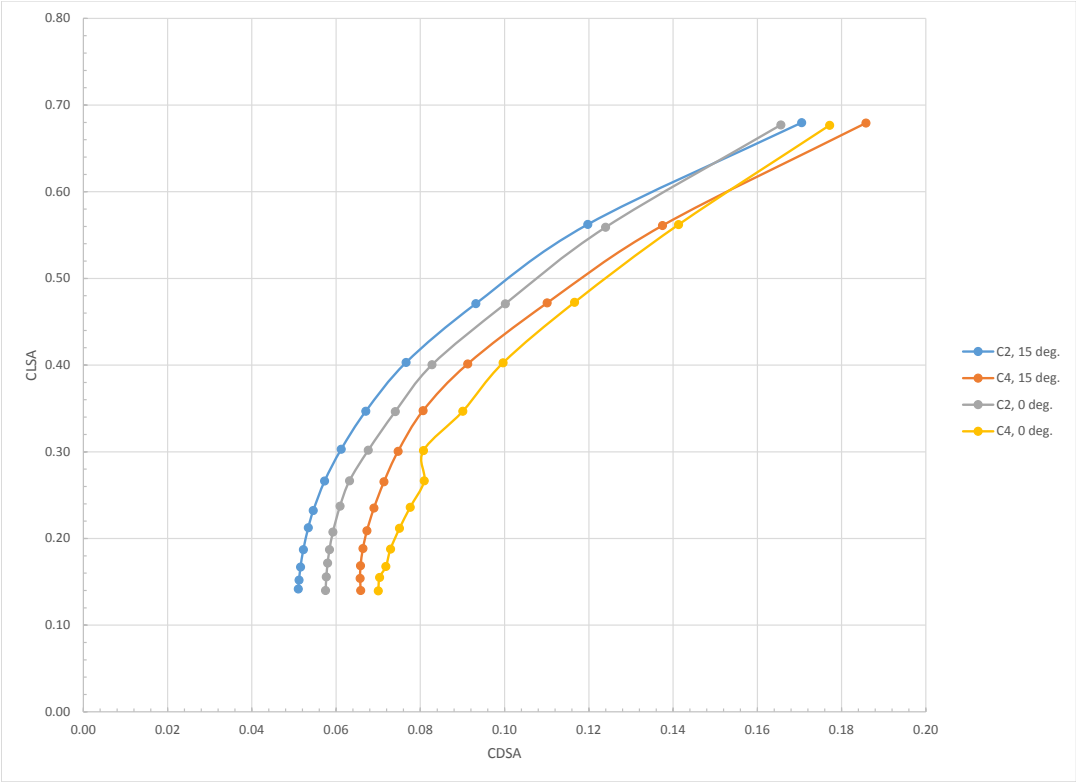


**Figure 7.8.24:** Trimmed drag polar for both canard configurations deflected at tested angles $\delta_C = 0°$ and $\delta_C = 15°$.

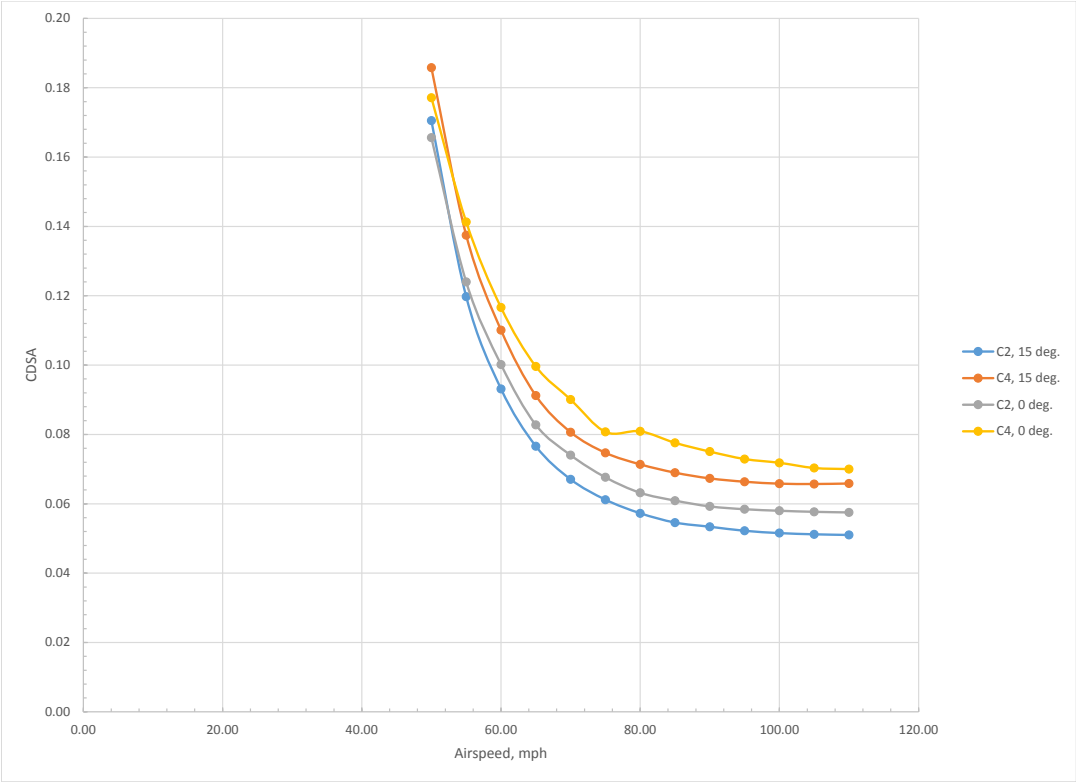


**Figure 7.8.25:** Trimmed drag versus airspeed for both canard configurations deflected at tested angles $\delta_C = 0°$ and $\delta_C = 15°$.

Results for trimmed flight in takeoff configuration with each canard cannot be confided in due to the necessity of tail-off data that was not taken. Flap effects could be superimposed on the above clean-trimmed conditions by superimposing the effects (firstly) of changes in aerodynamic forces on the main wing and (secondly) the subsequent change in downwash on the stabilator from having the flaps down. Finding the downwash increment, however, would require data with the flaps down and the stabilator removed in order to account for the lift on the stabilator itself, which was not obtained in the wind tunnel (see Section 6.1.1).

The above results do, in any case, suffice to specify a canard configuration for the final RUAV design. Canard C4 was chosen due to its higher efficiency in clean-configured cruise. Its control authority per deflection angle proved to be less than that of canard C2, but it was shown that either would be sufficient for the pitch authority commanded by the performance requirements.

Finally, for the final canard configuration, the lift and drag contributions at various angles of attack and deflection angles are shown in Figs. 7.8.26 and 7.8.27.

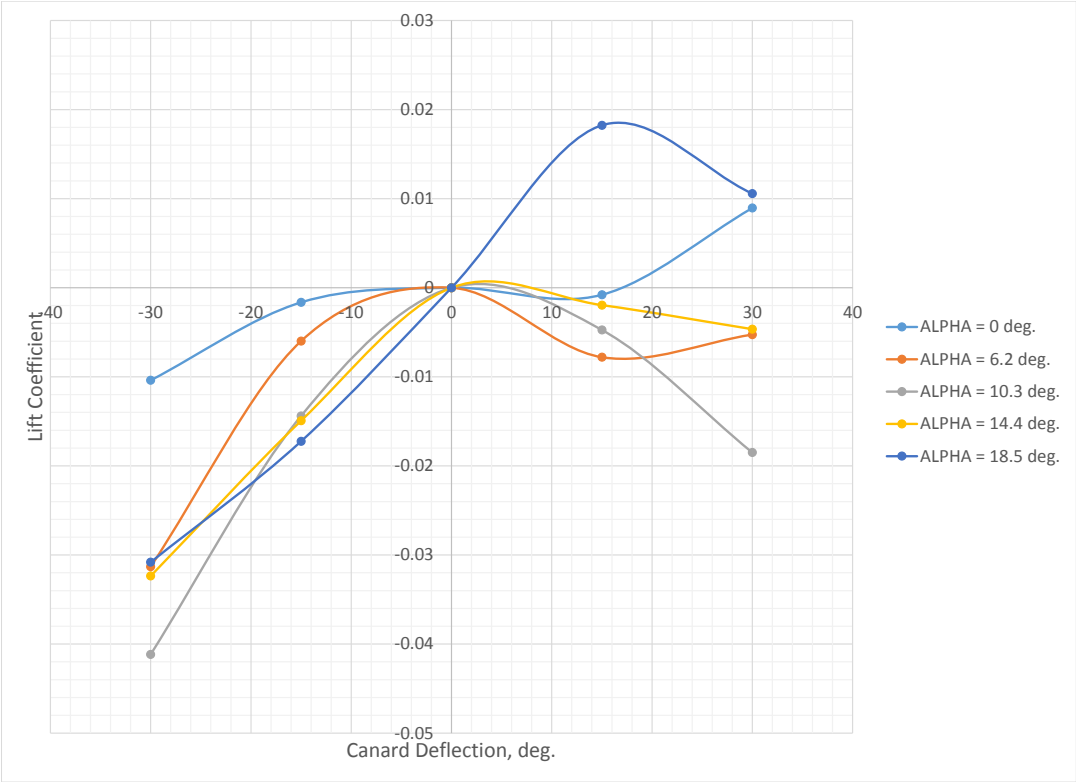


**Figure 7.8.26:** Lift coefficient contribution from canard C4 as a function of deflection at various angles of attack.

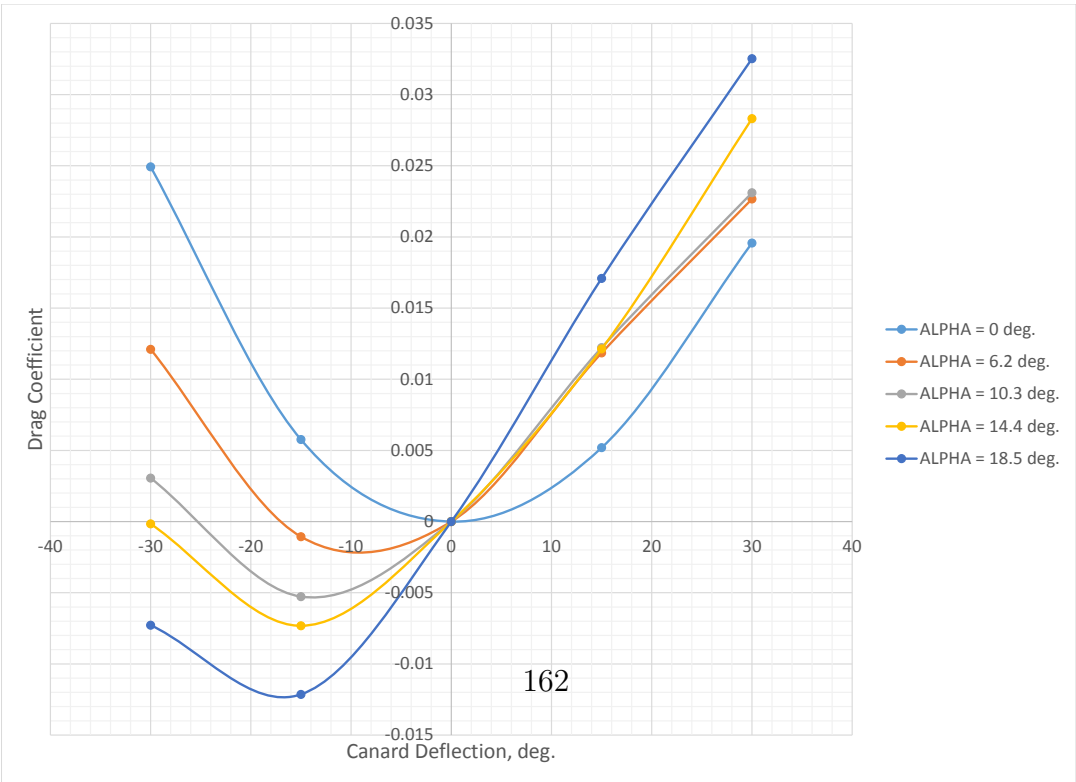

*7.8.2. Dynamic Modeling*

7.8.2.1. Calculations of the Dimensional Stability Derivatives from the Non-Dimensional Stability Derivatives

The linearized aircraft's equations of motion with assumptions that perturbations are small are shown in Eq. 7.8.7.

$$\begin{aligned}
&\Delta X(t) - mg(cos(\Theta_0))\theta(t) = mV_0(\tfrac{\dot{u}}{V_0}) \\
&\Delta Y(t) + mg(cos(\Theta_0))\phi(t) = mV_0(\dot{\beta} + r) \\
&\Delta Z(t) - mg(\sin(\Theta_0))\theta(t) = mV_0(\dot{\alpha} - q) \\
&\Delta L(t) = I_x\dot{p} - I_{xz}\dot{r} \\
&\Delta M(t) = I_y\dot{q} \\
&\Delta N(t) = I_z\dot{r} - I_{xz}\dot{p}
\end{aligned} \tag{7.8.1}$$

The aerodynamic forces and moments shown in Eq. 7.8.7, such as $\Delta X(t)$ and $\Delta L(t)$, are function of many aerodynamic parameters like angle of attack. With Taylor series expansions, each aerodynamic force and moment can be expressed with several terms. For example, $\Delta X(t)$ can be expanded to

$$\Delta X(t) = \Delta X_u(\frac{u(t)}{V}) + \Delta X_\alpha\alpha(t) + \Delta X_{\dot{\alpha}}\dot{\alpha}(t) + \Delta X_q q(t) + \Delta X_\delta\delta(t) \tag{7.8.2}$$

The similar expansion can be done for $\Delta X(t)$ and $\Delta M(t)$. For $\Delta Y(t)$ , the expansion is

$$\Delta Y(t) = \Delta Y_\beta(t)\beta(t) + \Delta Y_p(t)p(t) + \Delta Y_r(t)r(t) + \Delta Y_\delta(t)\delta(t) \tag{7.8.3}$$

The same expansions can be done for $\Delta L(t)$ and $\Delta N(t)$. As shown in Eq. 7.8.8 and Eq. 7.8.9, the equations of motion can be categorized in the longitudinal equation of motion and lateral equations of motion.

1. Longitudinal Equations of Motion
   Substituting the expanded parameters described by Eq. 7.8.8 back into Eq. 7.8.7, the longitudinal equations of motions becomes

$$\begin{aligned}
&V(\tfrac{\dot{u}}{V}) = VX_u(\tfrac{\dot{u}}{V}) + X_\alpha\alpha - g\cos(\Theta_0)\theta + X_\delta\delta \\
&(V - Z_{\dot{\alpha}})\dot{\alpha} = VZ_u(\tfrac{u}{V}) + Z_\alpha\alpha + (V + V_q)q - gsin(\Theta_0)\theta + Z_\delta\delta \\
&-M_{\dot{\alpha}}\dot{\alpha} + \dot{q} = VM_u(\tfrac{u}{V}) + M_\alpha\alpha + M_q q + Z_\delta\delta
\end{aligned} \tag{7.8.4}$$

   For longitudinal equations of motions, a state matrix is created by letting the state vector be $\{x\} = [\frac{u}{V}\ \alpha\ q\ \theta]^T$ with the form of $[I_n]\{\dot{x}\} = [A_n]\{x\} + \{B_n\}\delta$ where

$$I_n = \begin{pmatrix} V & 0 & 0 & 0 \\ 0 & (V - Z_{\dot{\alpha}}) & 0 & 0 \\ 0 & -M_{\dot{\alpha}} & 1 & 0 \\ 0 & 0 & 0 & 1 \end{pmatrix}$$

$$A_n = \begin{pmatrix} VX_u & X_\alpha & 0 & -g\cos(\Theta_0) \\ VZ_u & Z_\alpha & (V+Z_q) & -g\sin(\Theta_0) \\ VM_u & M_\alpha & M_q & 0 \\ 0 & 0 & 1 & 0 \end{pmatrix}$$

and

$$\{B_n\} = [X_\delta \; Z_\delta \; M_\delta \; 0]^T$$

.

By simplification, the equation can be changed to

$$\{\dot{x}\} = [A]\{\dot{x}\} + B\delta$$

where

$$[A] = [I_n]^{-1}[A_n]$$
$$[B] = [I_n]^{-1}[B_n]$$

The dimensional derivatives, such as $X_u$ and $X_\alpha$, are related to aerodynamic coefficients and non-dimensional derivatives like $C_{D_\alpha}$. The conversions from the non-dimensional derivatives to the dimensional derivatives for longitudinal direction are shown in the Appendix.

2. Lateral Equations of Motion
The lateral equations of motion simplified with the expansion in Eq. 7.8.9 substituted into Eq. 7.8.7 are shown in Eq. 7.8.11.

$$\begin{aligned} V\dot{\beta} &= Y_\beta\beta + Y_p p + g\cos(\Theta_0)\phi + (Y_r - V)r + Y_\delta\delta \\ \dot{p} - \tfrac{I_{xz}}{I_x}\dot{r} &= L_\beta\beta + L_p p + L_r r + Y_\delta\delta \\ -\tfrac{I_{xz}}{I_z}\dot{p} + \dot{r} &= N_\beta\beta + N_p p + N_r r + N_\delta\delta \end{aligned} \tag{7.8.5}$$

Similar to the longitudinal equations of motions, the state matrices can be constructed. However, for the lateral direction, the state vector is $\{x\} = [\beta \; p \; \phi \; r]^T$. The state matrices have the same form as the longitudinal direction state matrices($[I_n]\{\dot{x}\} = [A_n]\{x\} + \{B_n\}\delta$), with

$$I_n = \begin{pmatrix} V & 0 & 0 & 0 \\ 0 & 1 & 0 & -\frac{I_{xz}}{I_x} \\ 0 & 0 & 1 & 0 \\ 0 & -\frac{I_{xz}}{I_z} & 0 & 1 \end{pmatrix}$$

$$A_n = \begin{pmatrix} Y_\beta & Y_p & g\cos(\Theta_0) & (Y_r - V) \\ L_\beta & L_p & 0 & L_r \\ 0 & 0 & 0 & 0 \\ N_\beta & N_p & 0 & N_r \end{pmatrix}$$

and

$$\{B_n\} = [Y_\delta \; L_\delta \; 0 \; N_\delta]^T$$

Similar to the longitudinal direction, the equation can be simplified to

$$\{\dot{x}\} = [A]\{\dot{x}\} + B\delta$$

The conversions from the non-dimensional derivatives to the dimensional derivatives for lateral direction are shown in the Appendix.

### *7.8.3. Dimensionless Stability Derivatives*

#### 7.8.3.1. Approximated Dimensionless Stability Derivatives

To obtain an estimate of the dynamic stability derivatives, approximate values were computed from the equations and assumptions made in "Introduction to Aircraft Flight Dynamics" by Louis V. Schmidt. For the aerodynamic coefficients computed from this textbook, the linear form of the Taylor series formula is considered, implying that second and higher-order partial derivatives are not taken into account. The textbook also uses a linearized form of calculating the coefficients in which the values are calculated using a set trim point and perturbations of the deflection surfaces from that trim point. Values computed for angles of attack of 3 deg, 12 deg, and 17.3 deg are shown below in Tables 7.8.1, 7.8.2, 7.8.3.

**Table 7.8.1:** Dimensionless Stability Derivatives Calculated from Schmidt at 3 deg AoA

| Item | Value |
|---|---|
| $C_{y_r}$ | 0.2102 |
| $C_{l_r}$ | 0.0358 |
| $C_{n_r}$ | -0.1126 |
| $C_{y_p}$ | 0 |
| $C_{l_p}$ | -0.2321 |
| $C_{n_p}$ | -0.0286 |
| $C_{y_\beta}$ | -0.50069 |
| $C_{l_\beta}$ | -0.06943 |
| $C_{n_\beta}$ | 0.08777 |

**Table 7.8.2:** Dimensionless Stability Derivatives Calculated from Schmidt at 12 deg AoA

| Item | Value |
|---|---|
| $C_{y_r}$ | 0.0151 |
| $C_{l_r}$ | 0.1331 |
| $C_{n_r}$ | -0.0081 |
| $C_{y_p}$ | 0 |
| $C_{l_p}$ | -0.1985 |
| $C_{n_p}$ | -0.0673 |
| $C_{y_\beta}$ | -0.30750 |
| $C_{l_\beta}$ | -0.10568 |
| $C_{n_\beta}$ | 0.07417 |

**Table 7.8.3:** Dimensionless Stability Derivatives Calculated from Schmidt at 17.3 deg AoA

| Item | Value |
|---|---|
| $C_{y_r}$ | 0.2102 |
| $C_{l_r}$ | 0.1906 |
| $C_{n_r}$ | -0.1126 |
| $C_{y_p}$ | 0 |
| $C_{l_p}$ | -0.1809 |
| $C_{n_p}$ | -0.1060 |
| $C_{y_\beta}$ | 0.09828 |
| $C_{l_\beta}$ | -0.13401 |
| $C_{n_\beta}$ | 0.08857 |

In the case of roll damping derivatives, values were estimated using wing strip theory. This was done to account for both spanwise and chordwise lift distributions along the wing as well as for symmetric and asymmetric loading. The approximation was made using Eq. 7.8.6.

$$C_{l_p} = -\frac{b}{2S}\int_0^1 (\frac{\partial c_l}{\partial \alpha})_{wing} c(\eta)(\eta)^2 d\eta \tag{7.8.6}$$

#### 7.8.3.2. Dimensionless Dynamic Stability Derivatives Calculated from ZAERO

After a rough approximation of the dynamic derivatives using equations from Schmidt, the dynamic derivatives of the aircraft were calculated through ZAERO aerodynamic analysis to verify and check the approximate values. Dynamic derivatives for the aircraft are shown below in Tables 7.8.4, 7.8.5, and 7.8.6 for both high and low angles of attack.

**Table 7.8.4:** Dimensionless Yaw Damping Stability Derivatives from ZAERO at Both High and Low Angles of Attack

| Item | Value |
|---|---|
| $C_{y_r}$ | 0.4618 |
| $C_{l_r}$ | 0.03114 |
| $C_{n_r}$ | -0.3541 |

**Table 7.8.5:** Dimensionless Roll Damping Stability Derivatives from ZAERO at Both High and Low Angles of Attack

| Item | Value |
|---|---|
| $C_{y_p}$ | 0.03475 |
| $C_{l_p}$ | -0.2081 |
| $C_{n_p}$ | -0.01446 |

**Table 7.8.6:** Dimensionless Lateral-Directional Stability Derivatives from ZAERO at Both High and Low Angles of Attack

| Item | Value |
|---|---|
| $C_{y_\beta}$ | -0.2965 |
| $C_{l_\beta}$ | -0.00939 |
| $C_{n_\beta}$ | 0.1546 |

Comparing the derivatives calculated from Schmidt and ZAERO, it can be seen that there are discrepancies between values. Values calculated using equations from Schmidt provide decent approximations for the derivatives but are not satisfactory when implementing detail into the model. ZAERO values were found to be much more accurate and were used to define the state-space representation of the aircraft in Matlab/Simulink. From the ZAERO dynamic derivative values, some conclusions were made. Based off of the yaw damping dimensionless derivatives, the side force on the aircraft in the y-direction and the moment about the z-axis of the aircraft are mainly affected. A smaller effect takes place with the moment about the x-axis of the aircraft. Analysis of the roll damping dimensionless derivatives led to the idea that the moment about the x-axis was mainly affected while the side force in the y-direction and the moment about the z-axis were not as dependent upon the roll rate of the aircraft. Lastly, values of the lateral-directional dynamic stability derivatives with respect to change in side slip angle, $\beta$, led to the conclusion that the side force in the y-direction and the moment about the z-axis were primarily affected. The small value of the roll moment dimensionless coefficient indicated small change in moment about the x-axis with respect to change in side slip angle.

*7.8.4. State Space Model of the Aircraft*

7.8.4.1. Calculations of the Dimensional Stability Derivatives from the Non-Dimensional Stability Derivatives

The linearized aircraft's equations of motion with assumptions that perturbations are small are shown in Eq. 7.8.7.

$$\begin{aligned}
&\Delta X(t) - mg(cos(\Theta_0))\theta(t) = mV_0(\tfrac{\dot{u}}{V_0}) \\
&\Delta Y(t) + mg(cos(\Theta_0))\phi(t) = mV_0(\dot{\beta} + r) \\
&\Delta Z(t) - mg(\sin(\Theta_0))\theta(t) = mV_0(\dot{\alpha} - q) \\
&\Delta L(t) = I_x\dot{p} - I_{xz}\dot{r} \\
&\Delta M(t) = I_y\dot{q} \\
&\Delta N(t) = I_z\dot{r} - I_{xz}\dot{p}
\end{aligned} \tag{7.8.7}$$

The aerodynamic forces and moments shown in Eq. 7.8.7, such as $\Delta X(t)$ and $\Delta L(t)$, are function of many aerodynamic parameters like angle of attack. With Taylor series expansions, each aerodynamic force and moment can be expressed with several terms. For example, $\Delta X(t)$ can be expanded to

$$\Delta X(t) = \Delta X_u(\frac{u(t)}{V}) + \Delta X_\alpha\alpha(t) + \Delta X_{\dot{\alpha}}\dot{\alpha}(t) + \Delta X_q q(t) + \Delta X_\delta\delta(t) \tag{7.8.8}$$

The similar expansion can be done for $\Delta X(t)$ and $\Delta M(t)$. For $\Delta Y(t)$ , the expansion is

$$\Delta Y(t) = \Delta Y_\beta(t)\beta(t) + \Delta Y_p(t)p(t) + \Delta Y_r(t)r(t) + \Delta Y_\delta(t)\delta(t) \tag{7.8.9}$$

The same expansions can be done for $\Delta L(t)$ and $\Delta N(t)$. As shown in Eq. 7.8.8 and Eq. 7.8.9, the equations of motion can be categorized in the longitudinal equation of motion and lateral equations of motion.

1. Longitudinal Equations of Motion
   Substituting the expanded parameters described by Eq. 7.8.8 back into Eq. 7.8.7, the longitudinal equations of motions becomes

$$\begin{aligned}
&V(\tfrac{\dot{u}}{V}) = VX_u(\tfrac{\dot{u}}{V}) + X_\alpha\alpha - g\cos(\Theta_0)\theta + X_\delta\delta \\
&(V - Z_{\dot{\alpha}})\dot{\alpha} = VZ_u(\tfrac{u}{V}) + Z_\alpha\alpha + (V + V_q)q - gsin(\Theta_0)\theta + Z_\delta\delta \\
&-M_{\dot{\alpha}}\dot{\alpha} + \dot{q} = VM_u(\tfrac{u}{V}) + M_\alpha\alpha + M_q q + Z_\delta\delta
\end{aligned} \tag{7.8.10}$$

   For longitudinal equations of motions, a state matrix is created by letting the state vector be $\{x\} = [\frac{u}{V}\ \alpha\ q\ \theta]^T$ with the form of $[I_n]\{\dot{x}\} = [A_n]\{x\} + \{B_n\}\delta$ where

$$I_n = \begin{pmatrix} V & 0 & 0 & 0 \\ 0 & (V - Z_{\dot{\alpha}}) & 0 & 0 \\ 0 & -M_{\dot{\alpha}} & 1 & 0 \\ 0 & 0 & 0 & 1 \end{pmatrix}$$

$$A_n = \begin{pmatrix} VX_u & X_\alpha & 0 & -g\cos(\Theta_0) \\ VZ_u & Z_\alpha & (V+Z_q) & -g\sin(\Theta_0) \\ VM_u & M_\alpha & M_q & 0 \\ 0 & 0 & 1 & 0 \end{pmatrix}$$

and

$$\{B_n\} = [X_\delta \; Z_\delta \; M_\delta \; 0]^T$$

.

By simplification, the equation can be changed to

$$\{\dot{x}\} = [A]\{\dot{x}\} + B\delta$$

where

$$[A] = [I_n]^{-1}[A_n]$$
$$[B] = [I_n]^{-1}[B_n]$$

The dimensional derivatives, such as $X_u$ and $X_\alpha$, are related to aerodynamic coefficients and non-dimensional derivatives like $C_{D_\alpha}$. The conversions from the non-dimensional derivatives to the dimensional derivatives for longitudinal direction are shown in the Appendix.

2. Lateral Equations of Motion
The lateral equations of motion simplified with the expansion in Eq. 7.8.9 substituted into Eq. 7.8.7 are shown in Eq. 7.8.11.

$$\begin{aligned} V\dot{\beta} &= Y_\beta\beta + Y_p p + g\cos(\Theta_0)\phi + (Y_r - V)r + Y_\delta\delta \\ \dot{p} - \tfrac{I_{xz}}{I_x}\dot{r} &= L_\beta\beta + L_p p + L_r r + Y_\delta\delta \\ -\tfrac{I_{xz}}{I_z}\dot{p} + \dot{r} &= N_\beta\beta + N_p p + N_r r + N_\delta\delta \end{aligned} \tag{7.8.11}$$

Similar to the longitudinal equations of motions, the state matrices can be constructed. However, for the lateral direction, the state vector is $\{x\} = [\beta \; p \; \phi \; r]^T$. The state matrices have the same form as the longitudinal direction state matrices($[I_n]\{\dot{x}\} = [A_n]\{x\} + \{B_n\}\delta$), with

$$I_n = \begin{pmatrix} V & 0 & 0 & 0 \\ 0 & 1 & 0 & -\frac{I_{xz}}{I_x} \\ 0 & 0 & 1 & 0 \\ 0 & -\frac{I_{xz}}{I_z} & 0 & 1 \end{pmatrix}$$

$$A_n = \begin{pmatrix} Y_\beta & Y_p & g\cos(\Theta_0) & (Y_r - V) \\ L_\beta & L_p & 0 & L_r \\ 0 & 0 & 0 & 0 \\ N_\beta & N_p & 0 & N_r \end{pmatrix}$$

and

$$\{B_n\} = [Y_\delta \; L_\delta \; 0 \; N_\delta]^T$$

Similar to the longitudinal direction, the equation can be simplified to

$$\{\dot{x}\} = [A]\{\dot{x}\} + B\delta$$

The conversions from the non-dimensional derivatives to the dimensional derivatives for lateral direction are shown in the Appendix.

7.8.4.2. Stability Derivatives From the wind tunnel experiment, the static stability derivatives such as $C_{L_\alpha}$ and $C_{D_\alpha}$ are directly found from the data. Analysis were done on two flight conditions, at high angle of attack($\alpha = 17.3°$) and at low angle of attack($\alpha = 3°$). The high angle of attack was calculated based on the approach speed, that is 35 mph, and lift coefficient of the airplane. The dynamic stability derivatives such as $C_{L_{\dot{\alpha}}}$ were initially found with rough estimations and later found with CFD. Static derivatives were calculated for each angle of attack but the same dynamic derivatives were used for each case. The list of non-dimensional derivatives at angle of attack at 3 degrees for longitudinal and lateral direction dynamics are shown in Table 7.8.7 and Table 7.8.8, respectively. *These values are to be confirmed and decided*

**Table 7.8.7:** Non-Dimensional Derivatives for Longitudinal Directions at $\alpha = 3°$

| Drag Derivatives | Value | Lift Derivatives | Value | Pitch Derivatives | Value |
|---|---|---|---|---|---|
| $C_D$ | 0.0489 | $C_L$ | 0.2289 | | |
| $C_{D_M}$ | 0 | $C_{L_M}$ | 0 | $C_{m_M}$ | 0 |
| $C_{D_\alpha}$ | 0.1359 | $C_{L_\alpha}$ | 2.942 | $C_{m_\alpha}$ | -0.3619 |
| $C_{D_{\dot{\alpha}}}$ | 0.0783 | $C_{L_{\dot{\alpha}}}$ | 2.186 | $C_{m_{\dot{\alpha}}}$ | -1.151 |
| $C_{D_q}$ | 0.1637 | $C_{L_q}$ | 5.296 | $C_{m_q}$ | -4.173 |
| $C_{D_{\delta_s}}$ | -0.0309 | $C_{L_{\delta_s}}$ | 0.3535 | $C_{m_{\delta_s}}$ | -0.5093 |
| $C_{D_{\delta_f}}$ | 0.0961 | $C_{L_{\delta_f}}$ | 0.5404 | $C_{m_{\delta_f}}$ | -0.1811 |
| $C_{D_{\delta_c}}$ | 0.0200 | $C_{L_{\delta_c}}$ | -0.0378 | $C_{m_{\delta_c}}$ | 0.2061 |

*These values are to be confirmed and decided*

**Table 7.8.8:** Non-Dimensional Derivatives for Lateral Directions at $\alpha = 3°$

| Side-Force Derivatives | Value | Roll Derivatives | Value | Yaw Derivatives | Value |
|---|---|---|---|---|---|
| $C_{y_\beta}$ | -0.5007 | $C_{l_\beta}$ | -0.0694 | $C_{n_\beta}$ | 0.0986 |
| $C_{y_p}$ | 0.03475 | $C_{l_p}$ | -0.2081 | $C_{n_p}$ | -0.01446 |
| $C_{y_r}$ | 0.4618 | $C_{l_r}$ | 0.03114 | $C_{n_r}$ | -0.3541 |
| $C_{y_a}$ | 0.0044 | $C_{l_a}$ | -0.1274 | $C_{n_a}$ | -0.0052 |
| $C_{y_{T.V.}}$ | -0.1227 | $C_{l_{T.V.}}$ | 0.0069 | $C_{n_{T.V.}}$ | 0.0620 |

The non-dimensional stability derivatives found in Longitudinal and Lateral directions are listed in Table 7.8.9 and Table 7.8.10, respectively.

**Table 7.8.9:** Non-Dimensional Derivatives for Longitudinal Directions at $\alpha = 17.3°$

| Drag Derivatives | Value | Lift Derivatives | Value | Pitch Derivatives | Value |
|---|---|---|---|---|---|
| $C_D$ | 0.2270 | $C_L$ | 0.8463 | | |
| $C_{D_M}$ | 0 | $C_{L_M}$ | 0 | $C_{m_M}$ | 0 |
| $C_{D_\alpha}$ | 1.4331 | $C_{L_\alpha}$ | 2.3549 | $C_{m_\alpha}$ | -0.00055 |
| $C_{D_{\dot{\alpha}}}$ | 0.0783 | $C_{L_{\dot{\alpha}}}$ | 2.186 | $C_{m_{\dot{\alpha}}}$ | -1.151 |
| $C_{D_q}$ | 0.1637 | $C_{L_q}$ | 5.296 | $C_{m_q}$ | -4.173 |
| $C_{D_{\delta_s}}$ | 0.06093 | $C_{L_{\delta_s}}$ | 0.30577 | $C_{m_{\delta_s}}$ | -0.50934 |
| $C_{D_{\delta_f}}$ | 0.20220 | $C_{L_{\delta_f}}$ | 0.37845 | $C_{m_{\delta_f}}$ | -0.181 |
| $C_{D_{\delta_c}}$ | 0.03081 | $C_{L_{\delta_c}}$ | 0.00288 | $C_{m_{\delta_c}}$ | 0.2061 |

**Table 7.8.10:** Non-Dimensional Derivatives for Lateral Directions at $\alpha = 3°$

| Side-Force Derivatives | Value | Roll Derivatives | Value | Yaw Derivatives | Value |
|---|---|---|---|---|---|
| $C_{y_\beta}$ | 0.09828 | $C_{l_\beta}$ | -0.13401 | $C_{n_\beta}$ | 0.08857 |
| $C_{y_p}$ | 0.03475 | $C_{l_p}$ | -0.2081 | $C_{n_p}$ | -0.01446 |
| $C_{y_r}$ | 0.4618 | $C_{l_r}$ | 0.03114 | $C_{n_r}$ | -0.3541 |
| $C_{y_a}$ | 0.0000305 | $C_{l_a}$ | 0.0767 | $C_{n_a}$ | -0.0348 |
| $C_{y_{T.V.}}$ | -0.114 | $C_{l_{T.V.}}$ | 0.0197 | $C_{n_{T.V.}}$ | 0.0516 |

#### 7.8.4.3. State Space Models

Based on the theory shown in Section 7.8.4.1, the state space models were generated with the dimensional stability derivatives. The calculated state matrices for low angle of attack and high angle of attack are shown below. Note that for each angle of attack two directions, lateral and longitudinal, were considered. Generation of these state matrices were done by using MATLAB codes in Section 8.1.3.1.

**Longitudinal($\alpha = 3°$)**

$$[A]_{Longitudinal} = \begin{pmatrix} -0.1224 & 0.1165 & 0 & -0.2927 \\ -0.5583 & -3.6479 & 0.9099 & 0 \\ 1.164 & -58.78 & -9.4538 & 0 \\ 0 & 0 & 1 & 0 \end{pmatrix}$$

$$[B]_{Longitudinal} = \begin{pmatrix} -0.0387 & -0.1204 & -0.0250 \\ -0.4311 & -0.6591 & 0.0461 \\ -92.5246 & -31.8362 & 37.7125 \\ 0 & 0 & 0 \end{pmatrix}$$

**Lateral($\alpha = 3°$)**

$$[A]_{Lateral} = \begin{pmatrix} -0.6271 & 0.6271 & 0.2927 & -0.9877 \\ -515.7 & -41.99 & 0 & -4.3370 \\ 0 & 1 & 0 & 0 \\ -40.5906 & -6.381 & 0 & -3.4165 \end{pmatrix}$$

$$[B]_{Lateral} = \begin{pmatrix} 0.005473 & -0.1537 \\ -1208.1 & 151.85 \\ 0 & 0 \\ -182.15 & 45.54 \end{pmatrix}$$

**Longitudinal**($\alpha = 17.3°$)

$$[A]_{Longitudinal} = \begin{pmatrix} -0.2654 & -0.3430 & 0 & -0.6273 \\ -0.9633 & -1.4694 & 0.9099 & 0 \\ 0.9370 & -1.4075 & -4.4118 & 0 \\ 0 & 0 & 1 & 0 \end{pmatrix}$$

$$[B]_{Longitudinal} = \begin{pmatrix} -0.0356 & -0.1182 & -0.0180 \\ -0.1740 & -0.2153 & -0.0.00164 \\ -20.18 & -7.023 & 8.235 \\ 0 & 0 & 0 \end{pmatrix}$$

**Lateral**($\alpha = 17.3°$)

$$[A]_{Lateral} = \begin{pmatrix} 0.0574 & 0.00092 & 0.6273 & -0.9877 \\ -248.0 & -19.60 & 0 & -2.024 \\ 0 & 1 & 0 & 0 \\ -29.89 & -2.978 & 0 & -1.594 \end{pmatrix}$$

$$[B]_{Lateral} = \begin{pmatrix} 1.783 \times 10^{-5} & -0.0666 \\ 146.8.1 & 56.35 \\ 0 & 0 \\ 19.11 & 12.56 \end{pmatrix}$$

7.8.4.4. Analysis of the State Space Models at $\alpha = 3°$

Based on the state space model, analysis on the effect of the initial conditions were done. Initial conditions used were $\alpha = 1deg$ and $\beta = 1deg$ for longitudinal and lateral case.

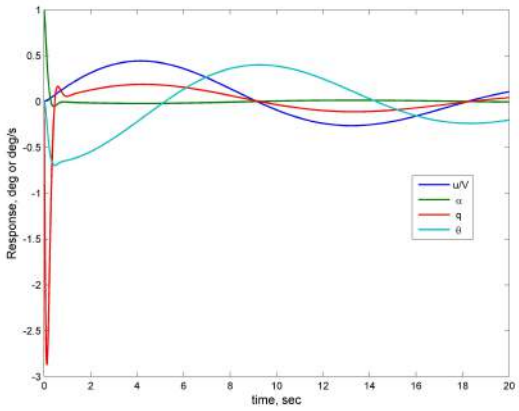


**(1)** Longitudinal Direction

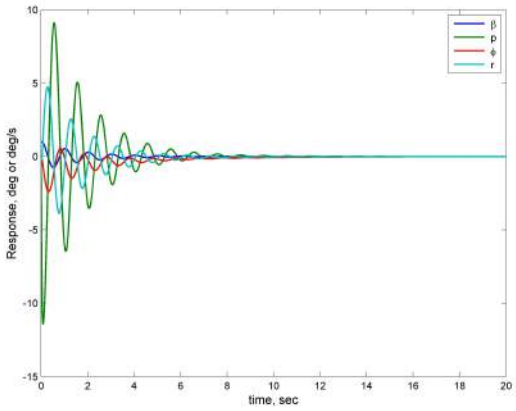


**(2)** Lateral Direction

**Figure 7.8.28:** Time Response of the System with Initial Conditions in Longitudinal and Lateral Directions at $\alpha = 3°$

Fig. 7.8.28 shows the time responses of the system subjected to initial conditions in longitudinal(Fig. 7.8.371) and lateral(Fig. 7.8.372) directions. The pole locations of the systems are listed in Table 7.8.11, and the root locus of them are shown in Fig. 7.8.31.

**Table 7.8.11:** Pole Locations for Lateral and Longitudinal Systems at $\alpha = 3°$

| Longitudinal | | Lateral | |
|---|---|---|---|
| Pole Locations | Damping Ratio | Pole Locations | Damping Ratio |
| $-6.5553 \pm 6.7124i$ | 0.6987 | $-44.58$ | 1.00 |
| $-0.0567 \pm 0.3464i$ | 0.1616 | $-0.594 \pm 6.269i$ | 0.0943 |
| | | $-0.2626$ | 1.00 |

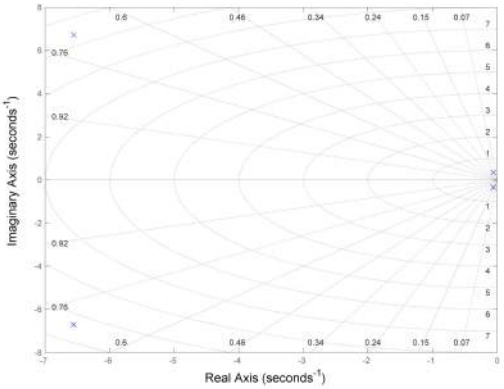


**(1)** Longitudinal

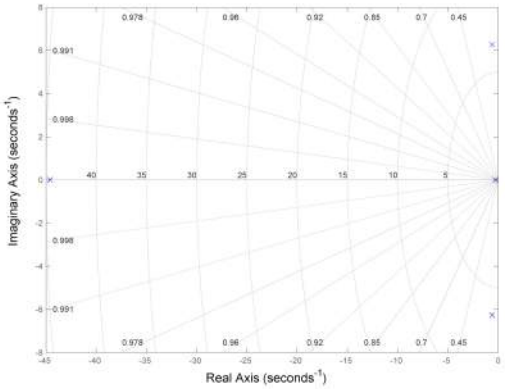


**(2)** Lateral

**Figure 7.8.29:** Root Locus of the Longitudinal and Lateral Systems at $\alpha = 3°$

7.8.4.5. Analysis of the State Space Models at $\alpha = 17.3°$ The same initial conditions applied for low angle of attack case($\alpha(0) = 1°$ and $\beta(0) = 1°$) were used for the high angle of attack. The responses in longitudinal and lateral directions are shown in Fig. 7.8.30.

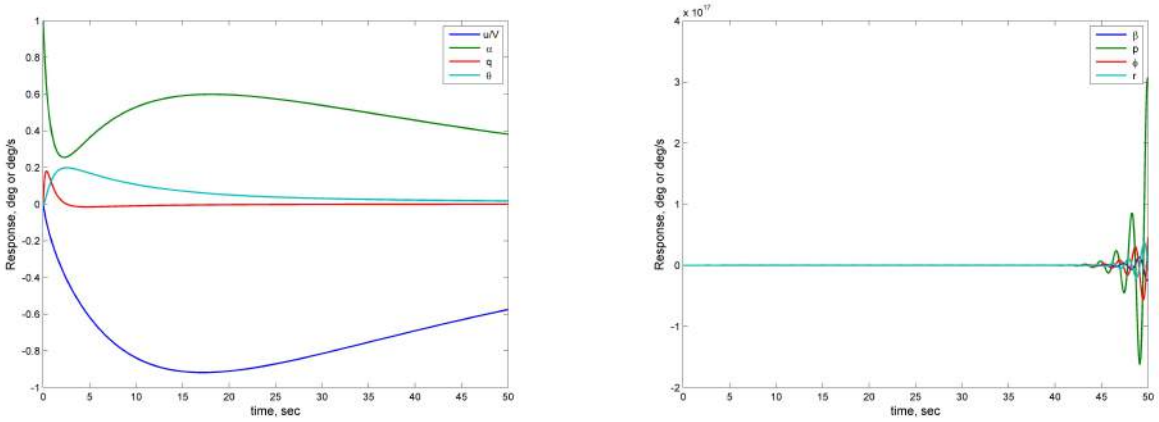


**(1)** Longitudinal Direction **(2)** Lateral Direction

**Figure 7.8.30:** Time Response of the System with Initial Conditions in Longitudinal and Lateral Directions with $\alpha = 17.3°$

It is clear that the airplane became less stable in longitudinal direction from the time the states take to converge to zero compared to the case with low angle of attack. For lateral direction, airplane became unstable. The pole locations of the systems are listed in Table 7.8.11, and the root locus of them are shown in Fig. 7.8.31.

**Table 7.8.12:** Pole Locations for Lateral and Longitudinal Systems at $\alpha = 3°$

| Longitudinal | | Lateral | |
|---|---|---|---|
| Pole Locations | Damping Ratio | Pole Locations | Damping Ratio |
| $-4.856$ | 1 | $-21.985$ | 1.00 |
| $-1.1494$ | 1 | $-0.757 \pm 3.725i$ | -0.1992 |
| $-0.1219$ | 1 | $-6613$ | 1.00 |
| $-0.0194$ | 1 | | |

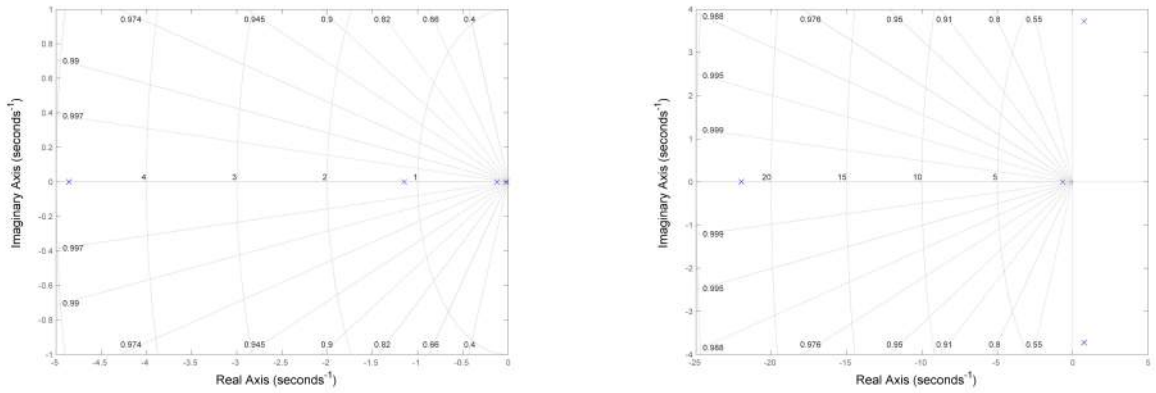


**(1)** Longitudinal **(2)** Lateral

**Figure 7.8.31:** Root Locus of the Longitudinal and Lateral Systems at $\alpha = 17.3°$

7.8.4.6. Yaw and Roll Damper for High Angle of Attack

From the time response and pole locations for lateral direction at high angle of attack, the system has instability. In order to stabilize the airplane, systems called yaw damper and roll damper need to be implemented. If an airplane has a gyroscope, roll rate and yaw rate can be easily measured. Yaw damper and roll damper are the systems that utilize the feed back gains to increase stability in lateral direction. Schematic of the roll damper and yaw dampers are shown in Fig. 7.8.32.

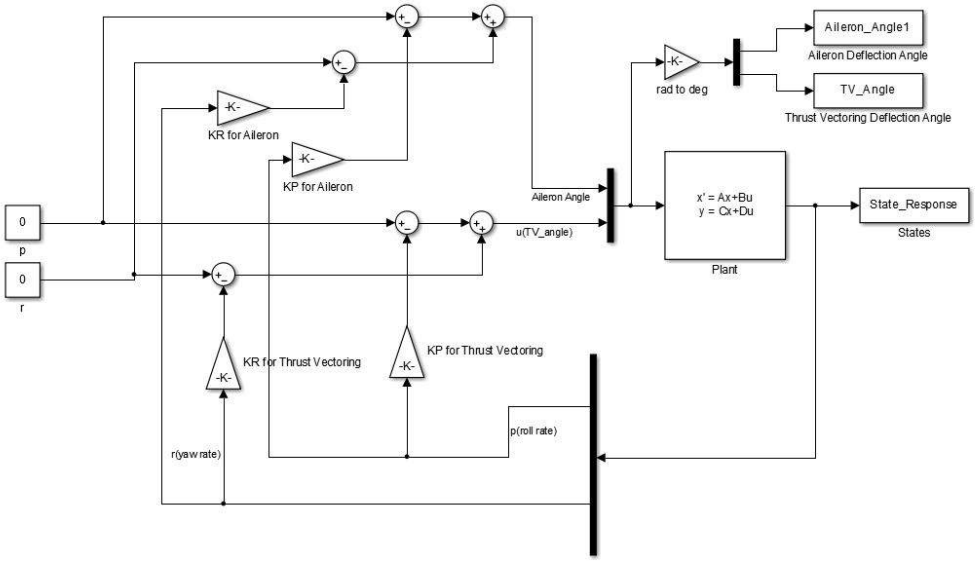


**Figure 7.8.32:** Schematic of the Yaw and Roll Dampers

As shown in Fig. 7.8.32, roll rate and yaw rate are fed back to the signal input with certain gains multiplied, $Kp$ and $Kr$. In this airplane, four gains need to be determined, $Kp_{Aileron}$, $Kr_{Aileron}$,$Kp_{T.V.}$, and $Kr_{T.V.}$. In order to determine these four gains, a manual iteration was done. With the dampers with the gains in Table. 7.8.13, the same initial condition analysis

**Table 7.8.13:** Damper Gains for High Angle of Attack

| | $K_p$ | $K_r$ |
|---|---|---|
| Aileron | 0.5 | -0.3 |
| Thrust Vectoring | 0.5 | 0.5 |

was done. Its responses are shown in Fig. 7.8.33.

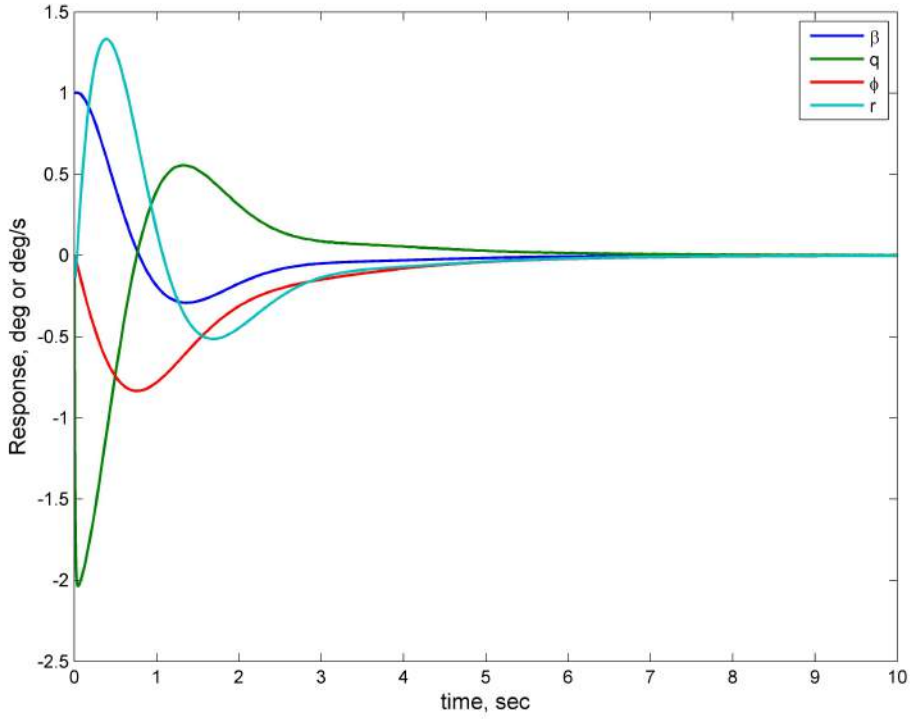


**Figure 7.8.33:** Responses of the Lateral Direction States with Dampers Implemented

With the dampers, the airplane shows stability in lateral direction. The new pole locations and damping ratio are shown in Table 7.8.14 and root locus is shown in Fig. 7.8.34.

**Table 7.8.14:** Pole Locations for Lateral System with yaw and roll dampers at $\alpha = 17.3°$

| Lateral | |
|---|---|
| Pole Locations | Damping Ratio |
| $-119.2$ | 1 |
| $-1.69 \pm 2.12i$ | 0.6225 |
| $-0.676$ | 1 |

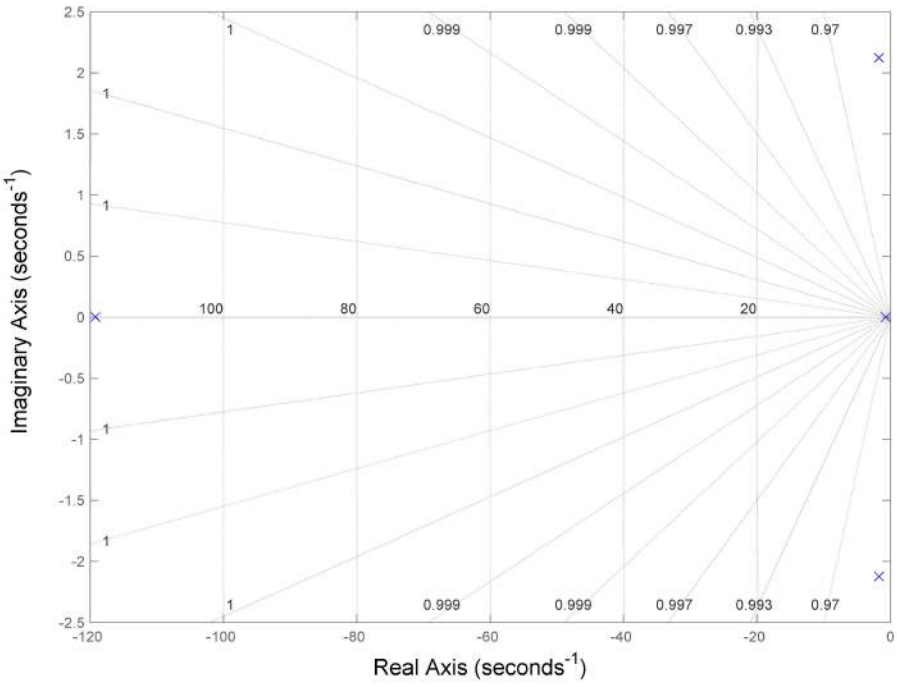


**Figure 7.8.34:** Pole locations of the lateral direction system with yaw and roll dampers

However, the behavior of the ailerons and thrust vectoring also need to be considered because they have limits for the deflection angles. Their responses are shown in Fig. 7.8.35.

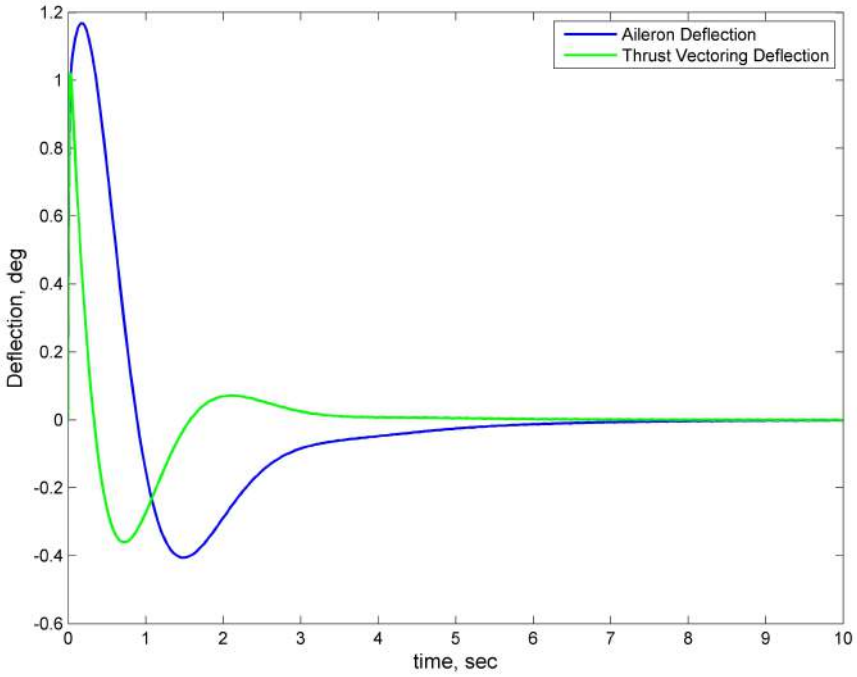


**Figure 7.8.35:** Deflections of the Aileron and Thrust Vectoring

Both the aileron and thrust vectoring do not deflect much. In fact, the maximum deflection is less than 1.2°. Because the responses are due to the initial condition with $\beta = 1°$, the deflection angles with different $\beta$ angles as initial conditions can be obtained by multiplying the responses with $\beta$ angle chosen. For example, if the initial $\beta$ angle was chosen to be 10°, the deflection angles would be ten times what is shown in Fig. 7.8.35. Since disturbances cannot be large, these dampers can be implemented to the airplane and stabilize the airplane.

7.8.4.7. Tailless Configuration One of the goals for the project was to control the airplane without vertical tail. In order to create a mathematical model of the airplane without vertical tail, the same process described in Section 7.8.4.1 were used. From the wind tunnel test, the effect of the vertical tail in both static and dynamic derivatives were calculated. By subtracting the effect of the vertical tail from the stability derivatives for the configuration with the vertical tail, the stability derivatives for the configuration without vertical tail were found. Here, the lateral stability was the interest of study thus only the lateral stability derivatives are shown in Table 7.8.15. Note that the deflection derivatives should not change.

**Table 7.8.15:** Non-Dimensional Derivatives for Lateral Directions with Tailless Configuration at $\alpha = 3°$

| Side-Force Derivatives | Value | Roll Derivatives | Value | Yaw Derivatives | Value |
|---|---|---|---|---|---|
| $C_{y_\beta}$ | -0.290 | $C_{l_\beta}$ | -0.0451 | $C_{n_\beta}$ | -0.006023 |
| $C_{y_p}$ | 0.03475 | $C_{l_p}$ | -0.2081 | $C_{n_p}$ | -0.01446 |
| $C_{y_r}$ | 0.2513 | $C_{l_r}$ | 0.0526 | $C_{n_r}$ | -0.2412 |
| $C_{y_a}$ | 0.0000305 | $C_{l_a}$ | 0.0767 | $C_{n_a}$ | -0.0348 |
| $C_{y_{T.V.}}$ | -0.114 | $C_{l_{T.V.}}$ | 0.0197 | $C_{n_{T.V.}}$ | 0.0516 |

The same process was done for the high angle of attack case.

**Table 7.8.16:** Non-Dimensional Derivatives for Lateral Directions with Tailless Configuration at $\alpha = 17.3°$

| Side-Force Derivatives | Value | Roll Derivatives | Value | Yaw Derivatives | Value |
|---|---|---|---|---|---|
| $C_{y_\beta}$ | 0.183 | $C_{l_\beta}$ | -0.117 | $C_{n_\beta}$ | 0.135 |
| $C_{y_p}$ | 0.03475 | $C_{l_p}$ | -0.2081 | $C_{n_p}$ | -0.01446 |
| $C_{y_r}$ | 0.2690 | $C_{l_r}$ | 0.0508 | $C_{n_r}$ | -0.251 |
| $C_{y_a}$ | 0.0000305 | $C_{l_a}$ | 0.0767 | $C_{n_a}$ | -0.0348 |
| $C_{y_{T.V.}}$ | -0.114 | $C_{l_{T.V.}}$ | 0.0197 | $C_{n_{T.V.}}$ | 0.0516 |

Based on these dimensionless derivatives, the state matrices for tailless configuration were found.

**Lateral**($\alpha = 3°$)

$$[A]_{Lateral} = \begin{pmatrix} -0.3742 & 8.382 \times 10^{-4} & 0.2583 & --0.9939 \\ -556.5 & -47.59 & 0 & -3.765 \\ 0 & 1 & 0 & 0 \\ -85.93 & -7.232 & 0 & -1.576 \end{pmatrix}$$

$$[B]_{Lateral} = \begin{pmatrix} 0.005473 & -0.1537 \\ -1208.1 & 151.85 \\ 0 & 0 \\ -182.15 & 45.54 \end{pmatrix}$$

**Lateral**($\alpha = 17.3°$)

$$[A]_{Lateral} = \begin{pmatrix} 0.2596 & 0.00092 & 0.2583 & -0.9929 \\ -1175.0 & -47.59 & 0 & -3.025 \\ 0 & 1 & 0 & 0 \\ -111.4 & -7.232 & 0 & -1.770 \end{pmatrix}$$

$$[B]_{Lateral} = \begin{pmatrix} 1.783 \times 10^{-5} & -0.0666 \\ 146.8.1 & 56.35 \\ 0 & 0 \\ 19.11 & 12.56 \end{pmatrix}$$

Initial condition analysis for tailless configuration were done for both low and high angle of attack.

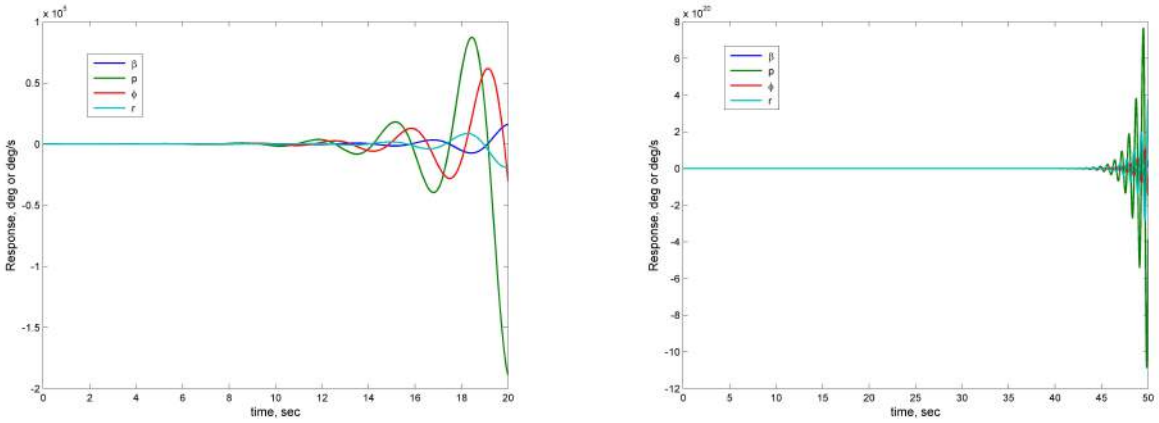


**(1)** $\alpha = 3°$ **(2)** $\alpha = 17.8°$

**Figure 7.8.36:** Lateral Responses of the Tailless Configuration at High and Low angle of Attack

Fig. 7.8.36 shows the responses of the airplane without vertical tail in lateral direction with high and low different angles of attack. Pole locations of each case were also found. They are shown in Fig. 7.8.37.

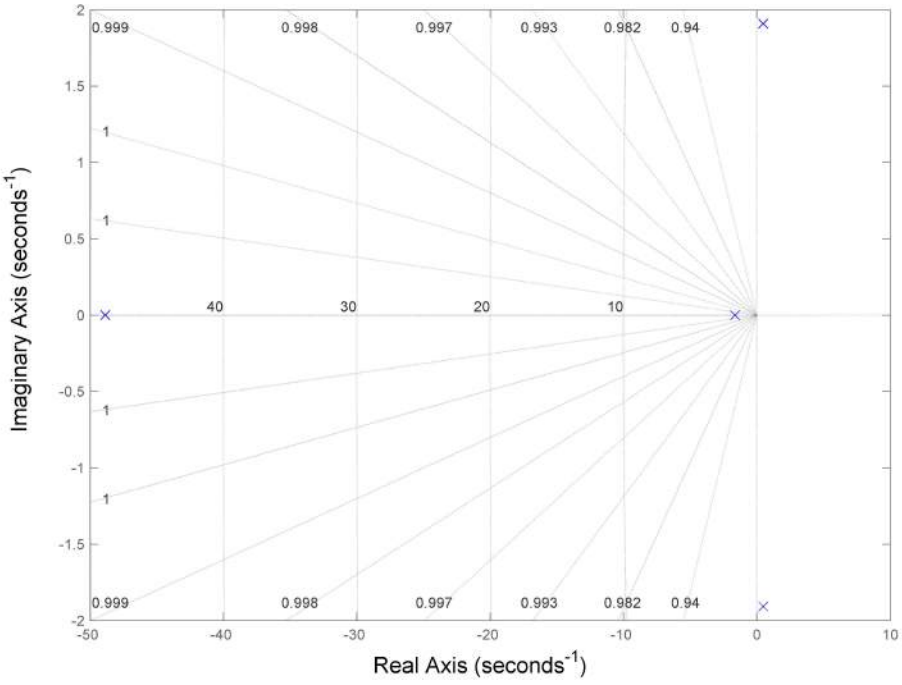


**(1)** $\alpha = 3°$

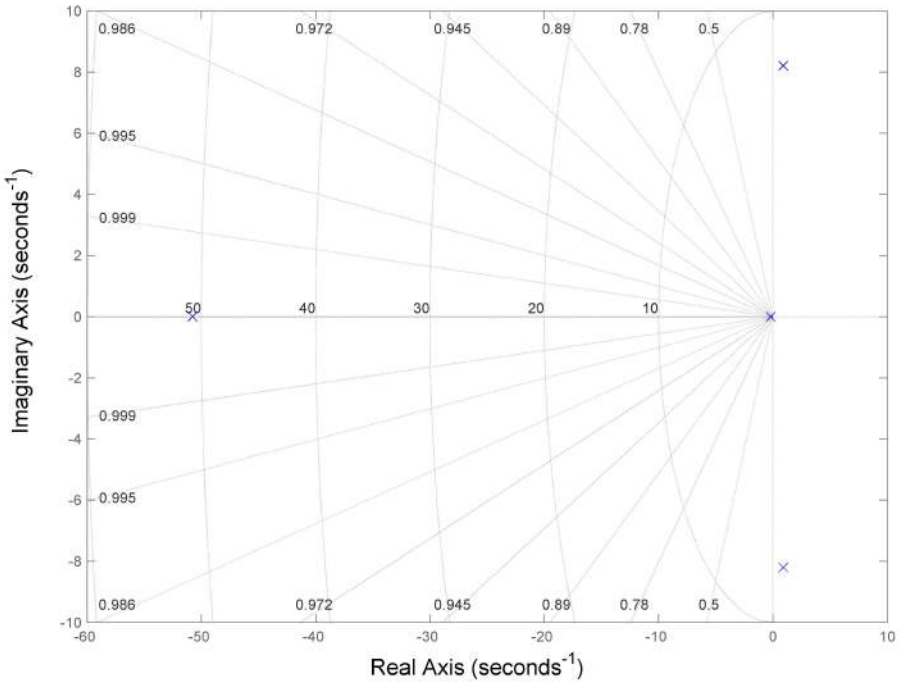


**(2)** $\alpha = 17.8°$

**Figure 7.8.37:** Pole Locations of the Systems at both High and Low angles of attack

Clearly, tailless configuration at both of the angles of attack are unstable so roll and yaw dampers shown in Fig. 7.8.32 need to be implemented.

With an iteration, necessary feedback gains for both low and high angle of attack cases were found. By implementing the dampers with the gains found above, the airplane became

**Table 7.8.17:** Damper Gains for Low Angle of Attack($\alpha = 3°$) with Tailless Configuration

| | $K_p$ | $K_r$ |
|---|---|---|
| Aileron | -0.08 | -0.003 |
| Thrust Vectoring | 0.08 | 0.08 |

stable. The response to the initial condition ($\beta = 1°$) is shown in Fig. 7.8.38.

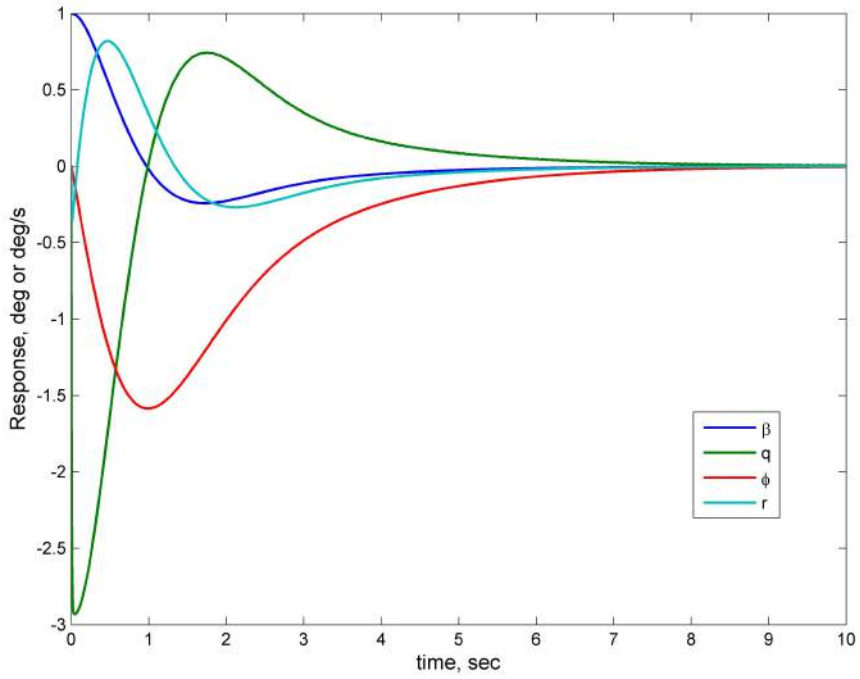


**Figure 7.8.38:** Response in lateral direction with dampers implemented at $\alpha = 3°$

The new pole locations with damping ratio and root locus are shown in Table 7.8.18 and Fig. 7.8.39.

**Table 7.8.18:** New locations of the poles with damping ratio with dampers at $\alpha = 3°$ for tailless configuration

| Lateral | |
|---|---|
| Pole Locations | Damping Ratio |
| $-190.54$ | 1 |
| $-1.74 \pm 1.45i$ | 0.7681 |
| $-0.648$ | 1 |

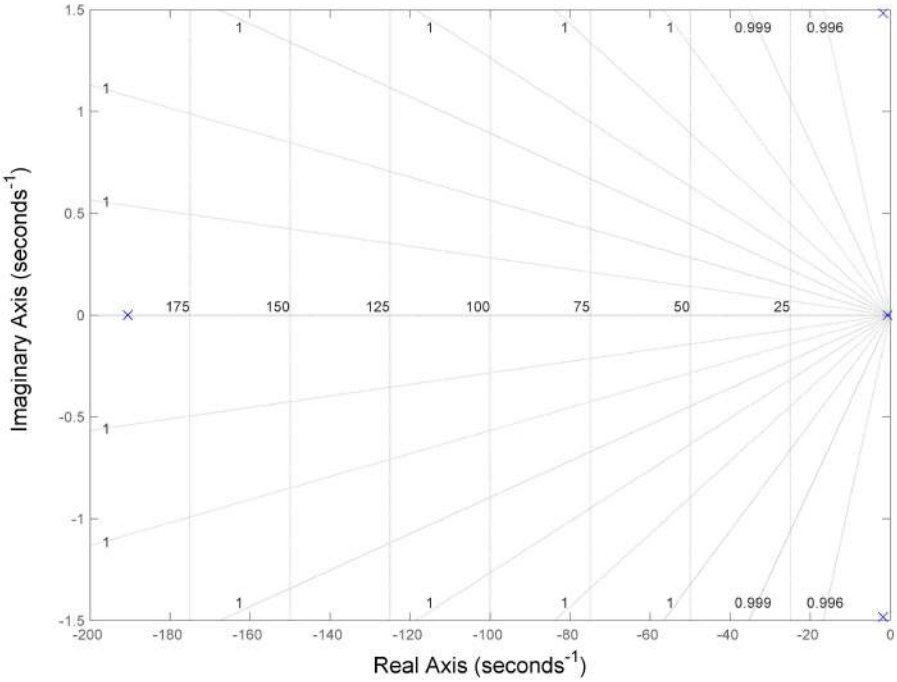


**Figure 7.8.39:** Pole locations of the lateral direction system with dampers with $\alpha = 3°$

The deflections of the ailerons and thrust vectoring are shown in Fig. 7.8.40.

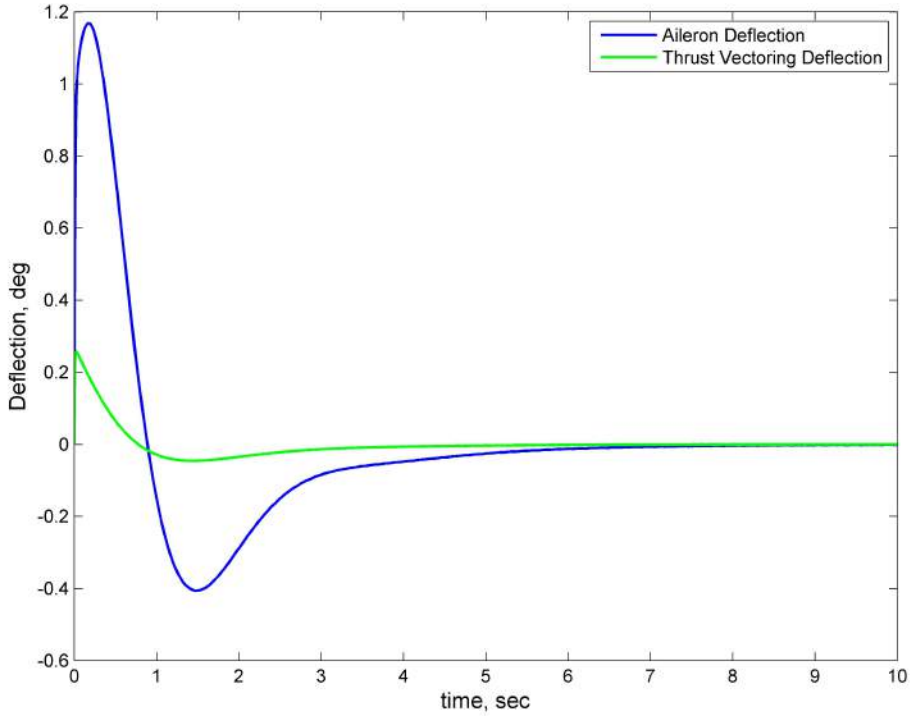


**Figure 7.8.40:** Deflections of the aileron and thrust vectoring for tailless configuration at $\alpha = 3°$

Both the thrust vectoring and aileron do not deflect more than 1.2° which allows themselves to deflect enough for larger initial yaw angle. Thus, the roll and yaw dampers with gains shown in Table 7.8.17 can be also implemented for this angle of attack without vertical tail.

For higher angle of attack case, different gains for the roll and yaw dampers were found. The gains and responses of the system with the dampers are shown in Table 7.8.19 and Fig. 7.8.41, respectively. By implementing the dampers with the gains found above, the

**Table 7.8.19:** Damper Gains for Low Angle of Attack($\alpha = 17.3°$) with Tailless Configuration

| | $K_p$ | $K_r$ |
|---|---|---|
| Aileron | 0.25 | -0.3 |
| Thrust Vectoring | 0.25 | 0.25 |

airplane became stable. The response to the initial condition ($\beta = 1°$) is shown in Fig. 7.8.41.

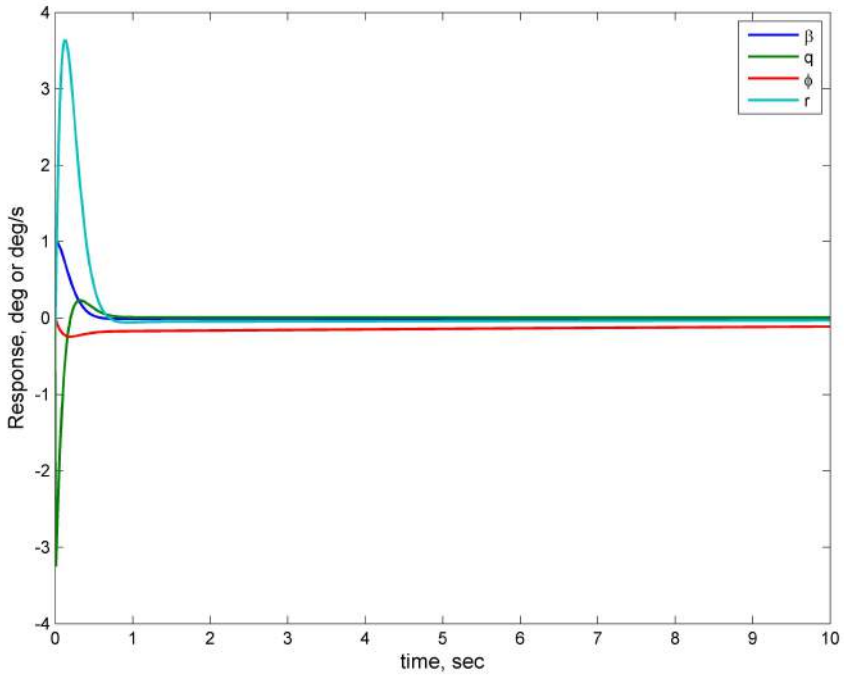


**Figure 7.8.41:** Response in lateral direction with dampers implemented at $\alpha = 17.3°$

Similar to the lower angle of attack case, the poles of of the system moved to new locations as dampers were implemented. The new locations of the poles and corresponding damping ratios are listed in Table 7.8.20.

**Table 7.8.20:** New locations of the poles with damping ratio with dampers at $\alpha = 17.3°$ for tailless configuration

| Lateral | |
|---|---|
| Pole Locations | Damping Ratio |
| $-318.34$ | 1 |
| $-7.49 \pm 3.89i$ | 0.7681 |
| $-0.047$ | 1 |

The root locus of the new system with dampers are shown in Fig. 7.8.42.

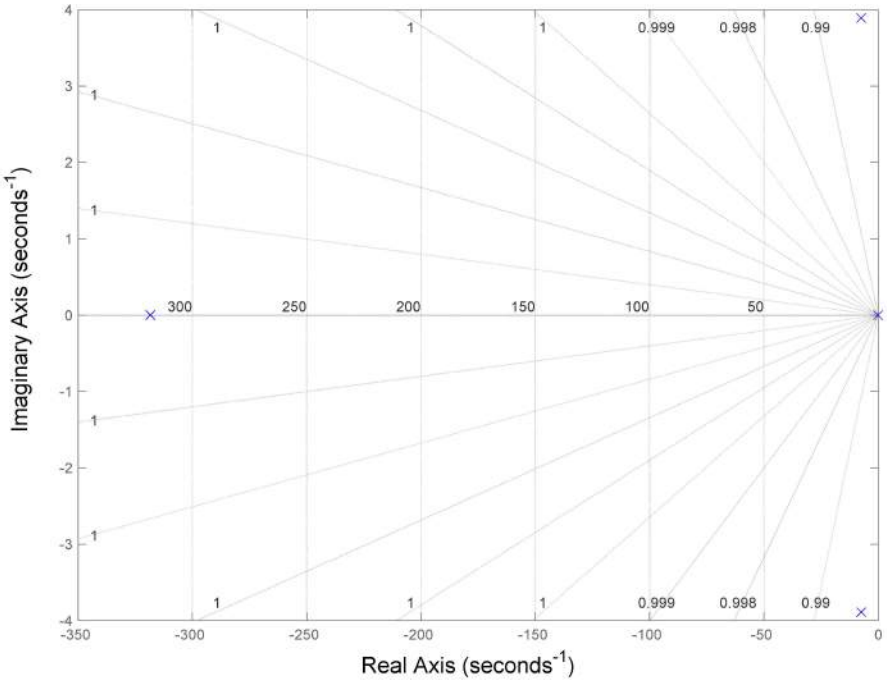


**Figure 7.8.42:** Pole locations of the lateral direction system with dampers with $\alpha = 173°$

The deflections of the ailerons and thrust vectoring are shown in Fig. 7.8.43.

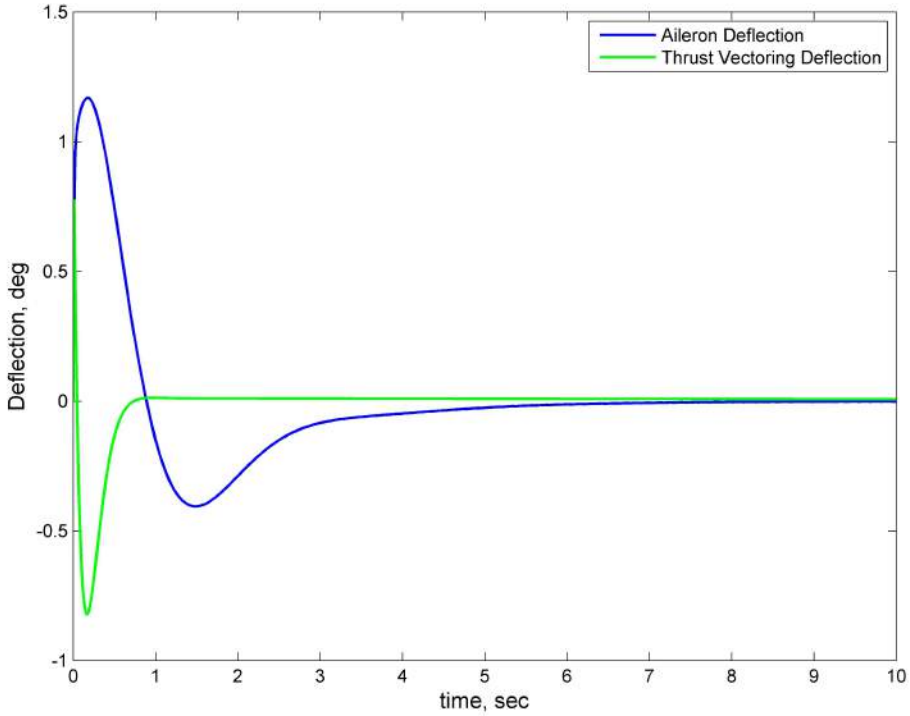


**Figure 7.8.43:** Deflections of the aileron and thrust vectoring for tailless configuration at $\alpha = 17.3°$

Even though ailerons deflect slightly larger than those did for lower angle of attack, the deflection angle is still less than 1.3°. There is not much deflection for the thrust vectoring as well. Thus, again, the yaw and roll dampers can be implemented to the actual airplane because the airplane is laterally stable and deflection of the ailerons and thrust vectoring are small enough.

### *7.8.5. Active Control*

To increase yaw stability and prevent sideslip an active control system was developed using thrust vectoring. A yaw wind vale is used as the sensor to provide feedback to the control system. A Hall effect sensor is used in combination with gain amplifier and analog to digital converter to measure the position of the vale. The physical controller is an Arduino MEGA. The controller runs a PID control scheme. The constants were chosen based off wind tunnel dynamics analysis and simulation to increase yaw stability. The set point for the PID controller is supplied from a pulse width modulation signal from the Pixhawk. The control system was chosen to run on the Arduino instead of directly on the Pixhawk to lower the risk involved while the system is being tested. From simulation it appeared that using vector thrust could stabilize the aircraft as well if not better than a vertical tail for conditions when the plane is producing thrust above 75% thrust. The required servo rotation rate for yaw stability was determined to be at least 1.5 rad/sec, which can be achievable using standard RC servos. The Arduino MEGA was tested and found to update at a rate of 400 Hz, which would be sufficient. It is unclear whether the wind vales will be accurate enough to provide

feedback for the control system because during testing the output range was around 30 mV and there was a significant amount of noise in the readings. A different selection of Hall effect sensors could greatly improve the accuracy of the readings.

### *7.8.6. X-Plane*

Commercial flight simulator software has long been used by the public to work on their flying skills. X-Plane is the first commercially available software that allows users to create aircraft and save mathematical flight data. This allows one to easily simulate a flight test on a computer. One main benefit to using flight simulator software are the time and cost savings compared to long Computational Fluid Dynamic (CFD) runs, wind tunnel testing or actual flight time. Another great benefit is the ability to quickly prototype aircraft features such as wing area, tail volume, CG locations, flight control deflection, landing gear, and many more.

The purpose of this section will be to use the X-Plane software to gain the following items: create an accurate model of the UAV; gain usable data on the performance and handling qualities; compare the flight test outputs to similar simulations using wind tunnel data.

7.8.6.1. X-Plane Software Package X-Plane is an affordable and commercially available flight simulator that can be used for pilot training and engineering. It is one of the first to use blade element theory for its flight dynamics modeling (FDM), versus other flight simulator software that use the coefficient build up method or stability derivatives to model flight characteristics. The use of blade element theory is the key reason why users can easily create and modify aircraft models within X-Plane's Plane Maker application.

Blade element theory divides the aircraft's lifting surfaces into multiple longitudinal strips and the calculated forces on each strip are added together. Once the airfoil is broken into strips the transverse and longitudinal local velocities are summed. This allows X-Plane to easily calculated the effect of sideslip on each lifting body. This method of calculation is used to determine lift, drag and moments on all lifting surfaces.

Plane Maker is the application used to create the aircraft's overall geometry. X-Plane differs from other readily available software in the sense that it uses the modeled geometry to determine flight modeling. The modules in Plane Maker allow the user to create the fuselage, wings, empennage, nacelles and landing gear.

Airfoil maker is an application that allows the user to set the characteristics of each lifting body airfoil. The program has access to hundreds of popular NACA airfoils, which speeds up the aircraft modeling. One useful feature is the freedom of having multiple wing sections with differing airfoils, or different root and tip airfoils.

7.8.6.2. UAV Modeling & Prototyping Once a general design was established by the class it was then modeled in X-Planes. The first step was modeling the fuselage and wing. The wing was one of the items that could not be varied later on due to our use of the Class of 2013's inboard wing.

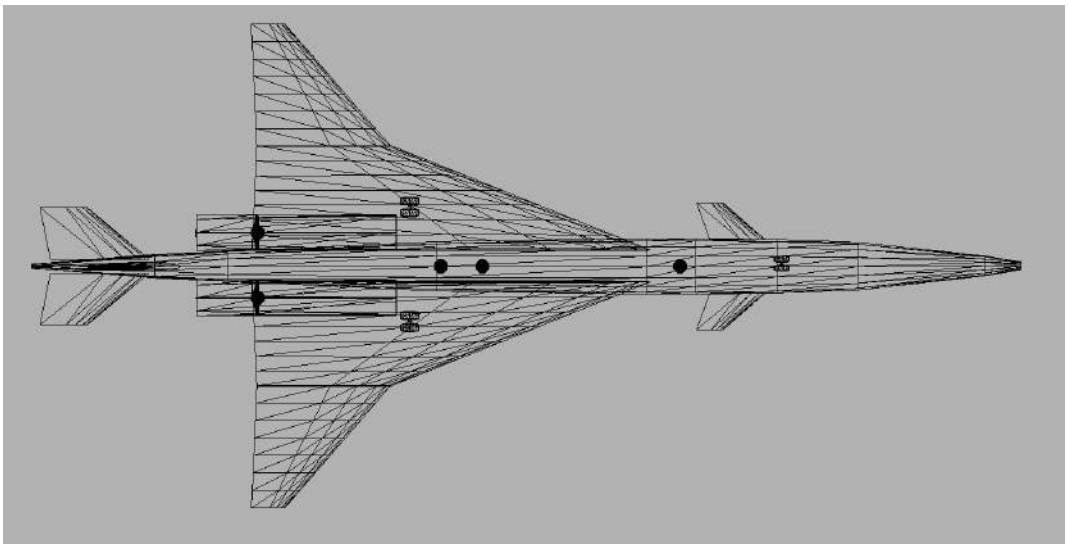

**Figure 7.8.44:** . UAV Modeled in X-Planes (Wireframe View)

The fuselage was created by loading a bitmap of the aircraft into Plane Maker and setting the number of cross sections. 12 cross-sections were used on the fuselage along with 9 nodes in each cross section, giving a very accurate model of the fuselage.

3 different airfoils were used to model the UAV's wings, canard, horizontal and vertical tail. The wing was broken into two sections, inboard and outboard. The inboard wing was of a subsonic design. The canards, horizontal, and vertical all used symmetrical airfoils. The method used to create the correct size of each lifting body is to set the airfoil thickness, then use the bitmap top view to set the lifting body's size. This was a very user-friendly way of creating lifting bodies, and allows for easy modification. Wing tip rudders were present in early designs, but later removed to expedite UAV fabrication.

The UAV's nacelles were modeled easily as a miscellaneous body, with an open center section. The EDFs were then modeled as propellers, with characteristics similar to EDFs, given by the propulsion team. Thrust, and run time were both set early in the design process and changed as the propulsion team perfected their thrust and run time calculations.

The flight controls modeled were ailerons, flaps, canards, stabilator, and rudder. The size and locations for these were again set by using the bitmap pasted into the Plane Maker GUI. Deflections were then set to initial values and tested in the program to determine effectiveness. Unfortunately X-Planes does not allow the use of flight control derivatives, and cannot accept these parameters when creating a aircraft model.

7.8.6.3. UAV Flight Testing The two types of flight tests done in using X-Plane were of the dynamic longitudinal stability variety. Both the short period and phugoid motions were investigated. Unfortunately, phugoid data was the only set of data that could be recorded. The short period mode could not be excited in X-Planes. Even after multiple attempts at different airspeeds, altitudes, and with different operators. Figure below shows the phugoid mode as compared to wind tunnel data.

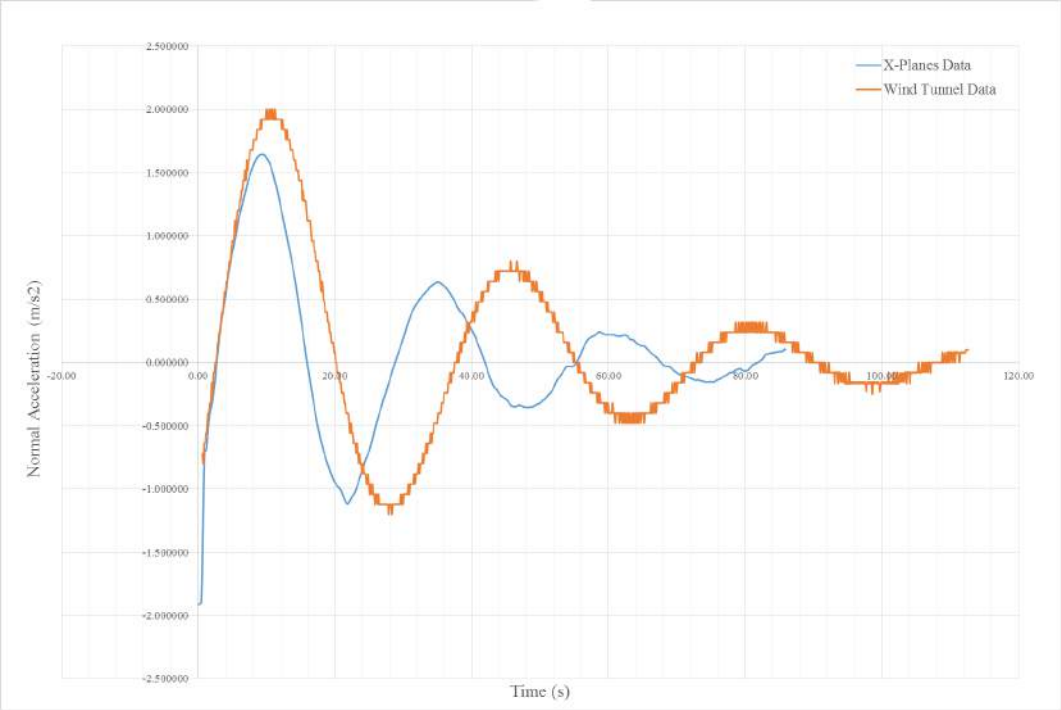


**Figure 7.8.45:** Phugoid mode response of X-plane and Wind tunnel flight simulator)

The period of the X-Plane data is about 25.4 sec., while the wind tunnel data shows a period of 35.2 sec. This error can most likely me attributed to a less than ideal model of the UAV in X-Planes. Commercially available models are able to represent aircraft very well.

### *7.8.7. Forebody Design*

One of the aerodynamic features that was investigated was the effect of fore-body shape on the stability and performance of the aircraft. Skow and Erickson [Reference 1] offers a large body of information on the subject and provided the foundation for this research. Although the majority of information was tailored towards military applications, the same patterns and lessons learned from their text were thought to be applicable towards a commercial, supersonic aircraft. Firstly, the forebody is defined by Skow and Erickson to be the geometric shape which extends from the tip of the nose, encompasses the cockpit and blends into the main wing-body. For this project, the boundary was defined as the plane at which the fuselage becomes a constant cross section, close to the leading edge of the inboard wing. The stability of an aircraft at high angles of attack is significantly dictated by the forebody shape. Supersonic-capable aircraft are designed within the mindset of overcoming large drag polars during the transonic regime and thus the nose of the aircraft come to a fine point along a sharp curve. The vortex patterns generated over the nose at low angles of attack are symmetric but are highly asymmetric due to turbulence at high angles of attack. This causes a yawing moment which leads to instability. One of the geometric factors which significantly affects the stability is the fineness ratio. This is the length of the fore-body divided by tis maximum diameter. Supersonic design uses high fineness ratios to mitigate sonic booms and also increase the percentage of the aircraft which is inside the Mach angle at cruise. The effect of the fineness ratio on the yawing moment coefficient is presented in Fig. 7.8.47. In

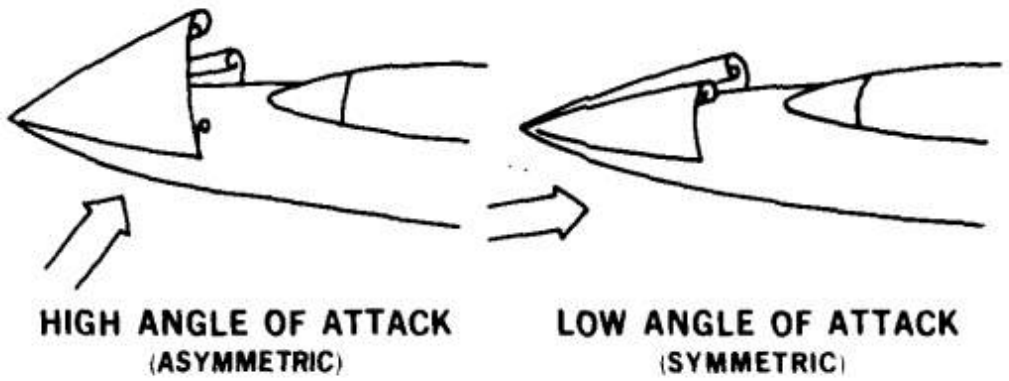


**Figure 7.8.46:** Vortex generated on the forebody of the aircraft at low and high angles of attack

general, the yaw coefficient increases with a larger fineness ratio. The yaw stability at a high angle of attack is also affected by the cross sectional geometry of the forebody. Defined by $\frac{h}{b}$ where $h$ is the height and $b$ is the maximum width of the elliptical cross section, the more "flat" the elliptical shape is to the horizontal x-y plane, the more stable it is directionally However, this also denotes a larger projected area in the pitch direction, which can result in undesired pitch-up tendencies during flight. On the other hand, a high ellipticity leads to directional instability due to sideslip. A version was created as a compromise between the "flat" and "skinny" elliptical cross section with a fineness ratio of 6.5. (Fig. 7.8.50 and Fig. 7.8.51. It should be noted that although this is quite large and could possibly result in higher yaw moment coefficients induced by vortices at high angles of attack, the application of the concept in a less performance-oriented commercial aircraft was thought to delay the onset of instability due to the assumed more inherently stable configuration as compared to military wing planforms.

The CAD geometry was based on several cross section geometry at different cut planes which were lofted together. This was named the "top-heavy" forebody due to the large distribution of mass towards the crown of the fuselage. This initial version was modified after consideration of the undesirable loft with the constant cross section at the aft end of the forebody and a "box-like" geometry which was not akin to commercial fuselages. Compare with the fuselage of the Concorde which is very smooth and more elliptical. The modified version of the bottom-heavy forebody is displayed below as a formal drawing. The cross section is also available.

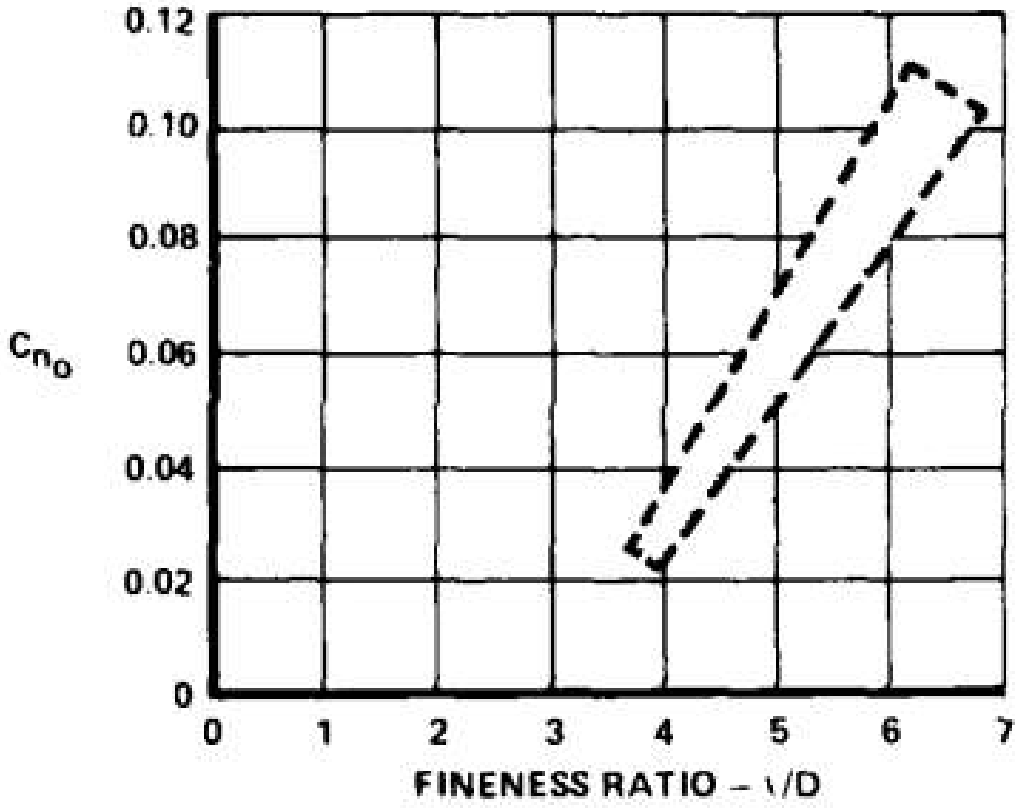


**Figure 7.8.47:** Relationship between the fineness ratio and the yawing moment coefficient

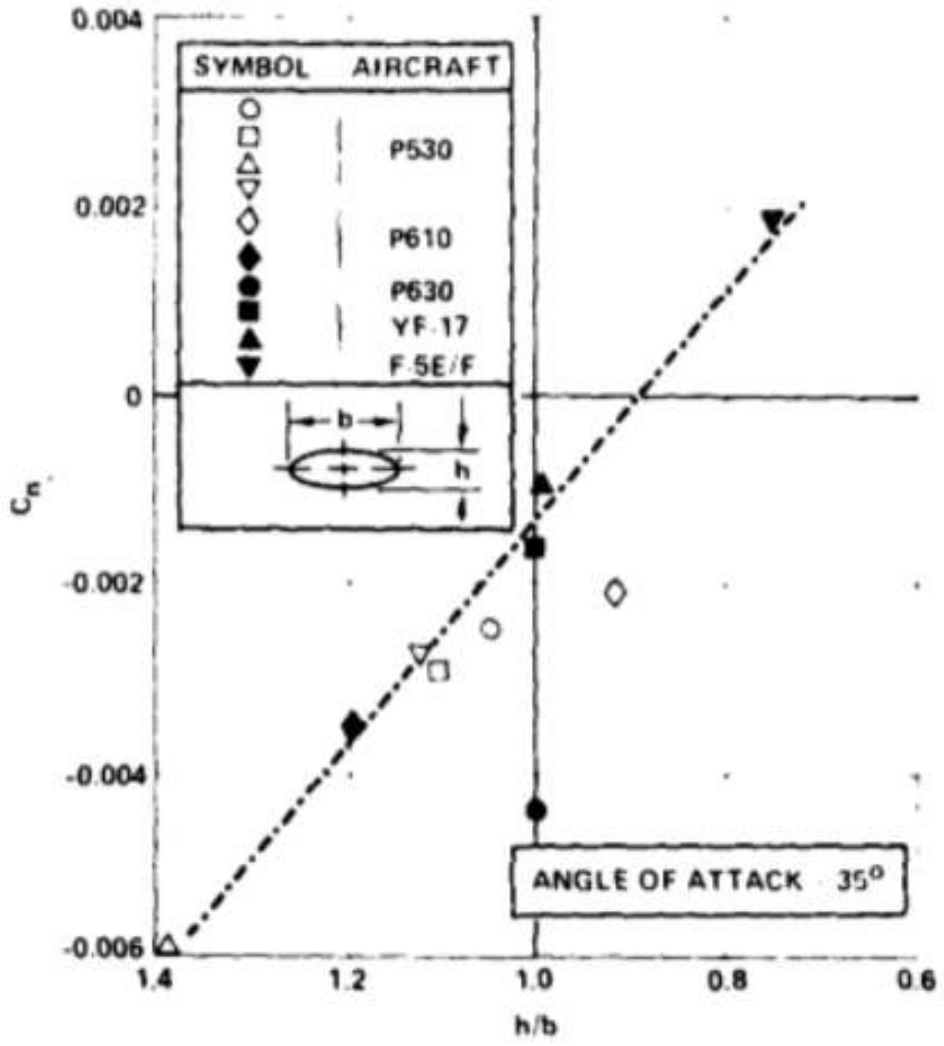


**Figure 7.8.48:** Relationship between the fineness ratio and the yawing moment coefficient

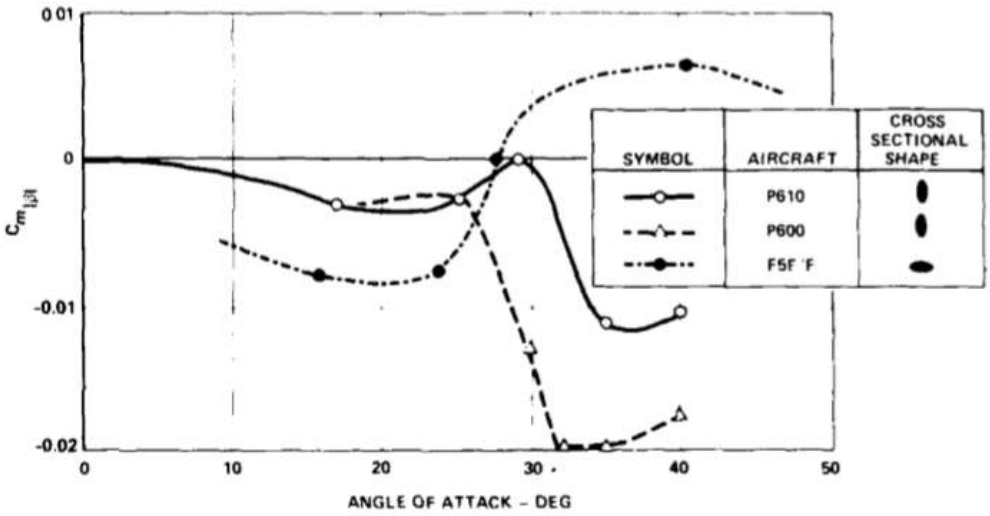


**Figure 7.8.49:** Relationship between the fineness ratio and the yawing moment coefficient

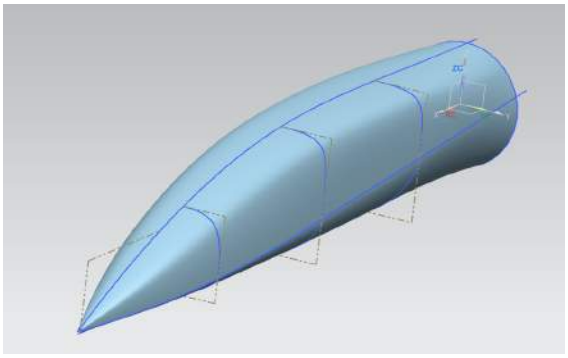

**Figure 7.8.50:** Drawing of the forebody

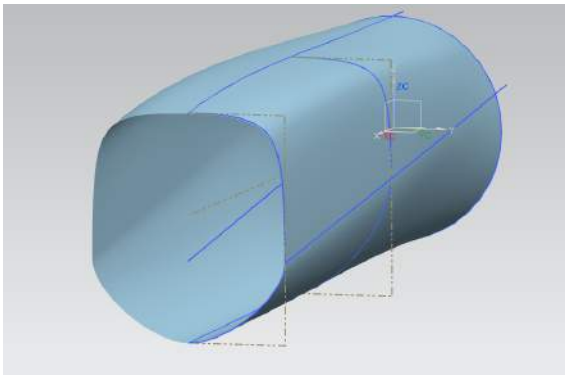

**Figure 7.8.51:** Cross section of the forebody

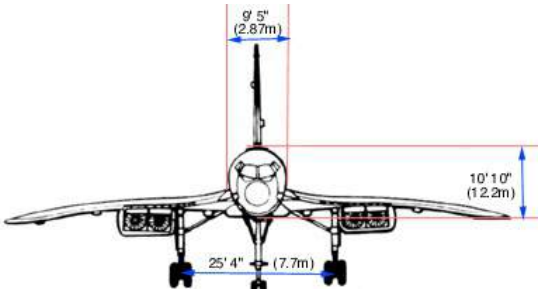


**Figure 7.8.52:** Fuselage of the Concorde

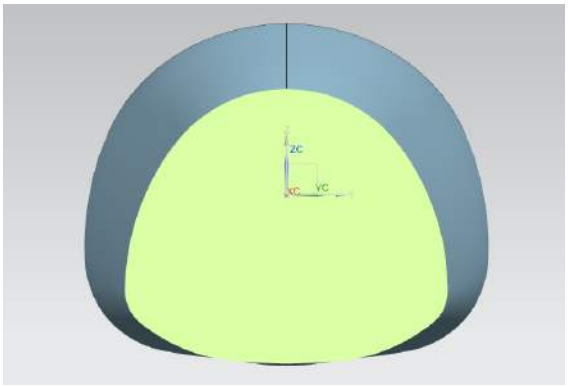


**Figure 7.8.53:** Final cross section

The top-heavy forebody is also available. The cross sections at 0, 10, 20 and 40 inches from the aft end of the forebody are available as different visualizations.

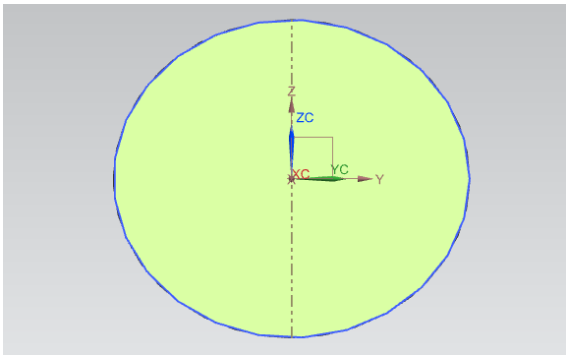


**(1)** Cross Section at 0 inch

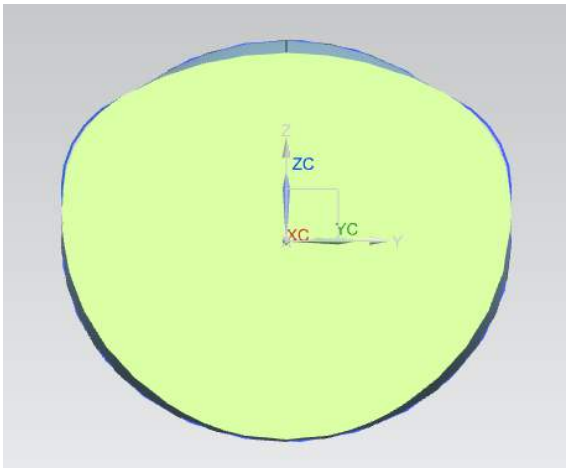


**(2)** Cross Section at 10 inch

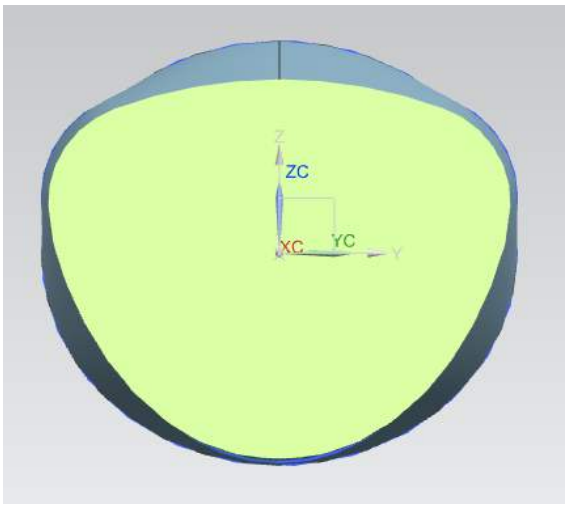


**(3)** Cross Section at 20 inch

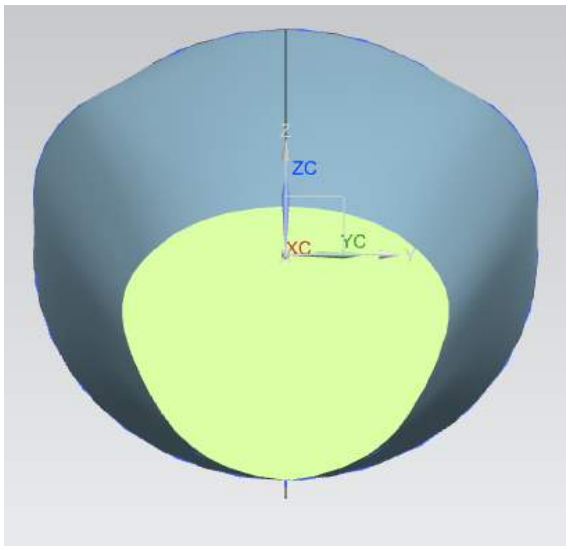


**(4)** Cross Section at 40 inch

**Figure 7.8.54:** Cross sections at different locations

### *7.8.8. NX*

NX was mostly used in the earlier stages of design for the R-UAV and Wind Tunnel Model because the company that machined the R-UAV molds as well as the wind tunnel model parts, Aerotec, uses NX for CNC. Later in the project SolidWorks was used for tasks such as the interior structural modeling, avionics placing, and weight calculations due to the familiarity with SolidWorks that most members had from previous courses. The fuselage was modeled similar to the 2014 aircraft, with a circular cross section. The general shape was that of a Sears-Haack body to minimize wave drag. The nose was designed with a duck bill shape, slowly extending out to the main section of the fuselage. The fuselage tapered in at the wing joint for area ruling. The decision was made to use a vertical fin tail, similar to that of a 777X as opposed to a pointed tail, or a horizontal deck, in hopes of improving yaw stability. The length of the fuselage was increased from the 2013 and 2014 aircraft at the

recommendation of the advisors for improved low boom characteristics. The fuselage was modeled in NX by creating top and bottom outer mold lines of the fuselage, then the line of maximum thickness from the top down. These outer mold lines were created using splines, which allowed for easy modification of the fuselage curves to produce more consistent area ruling. Finally fuselage cross section sketches were created at specific distances along the fuselage to dictate the shape of the body.

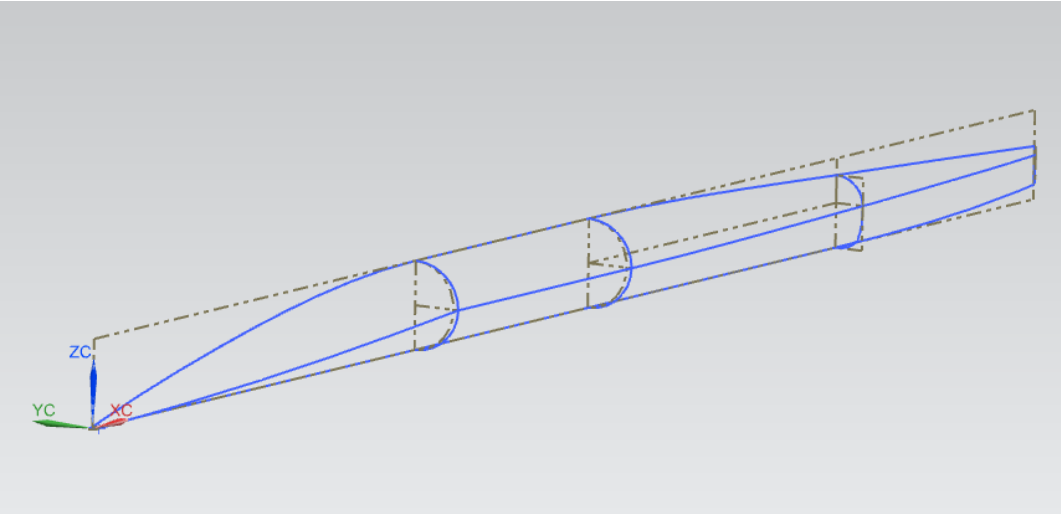


**Figure 7.8.55:** Sketch of the fuselage

Surfaces were then created by lofting between the cross sections using the outer mold lines as guide curves. It was later decided to modify the forward cross section from a perfect circle to slightly elliptical to accommodate a larger interior volume in the fuselage for construction of the R-UAV.

A modified 2013 wing planform with a significantly decreased notch area was attached to the fuselage. The airfoil and sweep angle remained constant from the 2013 wing, as did the span. The canard and horizontal tail sizes were created on the recommendation that the total projected area of the tail and canard should be roughly 1/6th the area of the wing area. Canard and tail areas were later changed upon sizing that was done in VLAERO. Apart from the wing all airfoil surfaces were created using a formula based wing file, which relied on formulas to dictate the span, chord length, sweep, incidence, and dihedral angle, allowing for rapid modification of control surfaces based on the results of CFD and VLAERO.

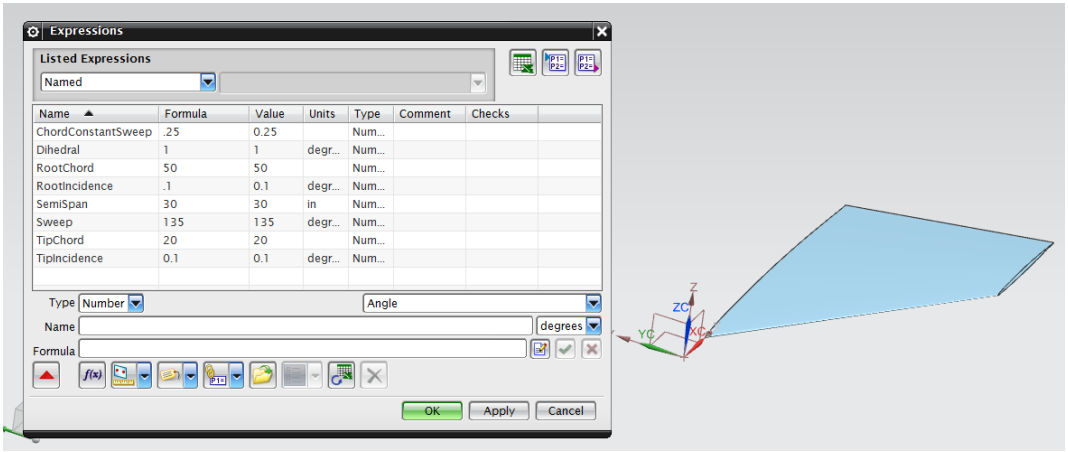


**Figure 7.8.56:** Parametric Wing

The wing planform was creating by using identical airfoils for the root and tip, then by increasing the size of the airfoil at the crank to minimize the notch area. The surfaces were then created by lofting between the airfoils. Because of the decision to use the 2013 wind tunnel wing planform, but using a reduced notch area, careful modeling had to be done. The geometry from the wind tunnel model was imported, and the surfaces were recreated using the Enlarge Surface feature. Modified airfoil shapes were created by extending the cutoff of the 2013 planform to the trailing edge of the 2015 planform.

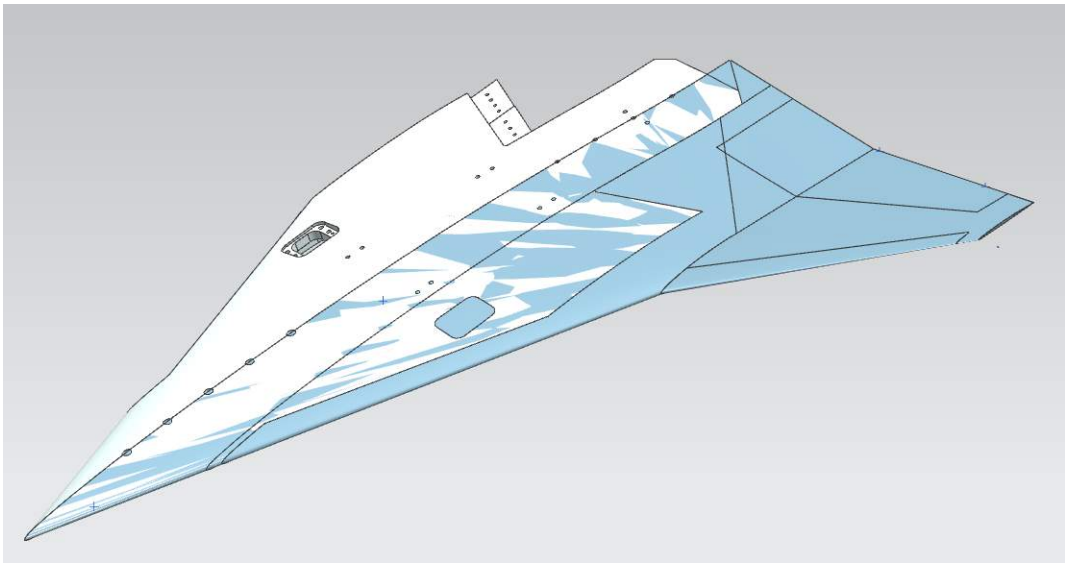

**Figure 7.8.57:** Wing of the wind tunnel model

This created minor breaks in the natural curvature of the inboard section of the wing, but was deemed minor and insignificant by the advisors.

**Figure 7.8.58:** Airfoild Section of the wind tunnel model

Using the geometry Aerotec was able to manufacture pieces for the wind tunnel that attached to the inboard wind tunnel mount from 2013.

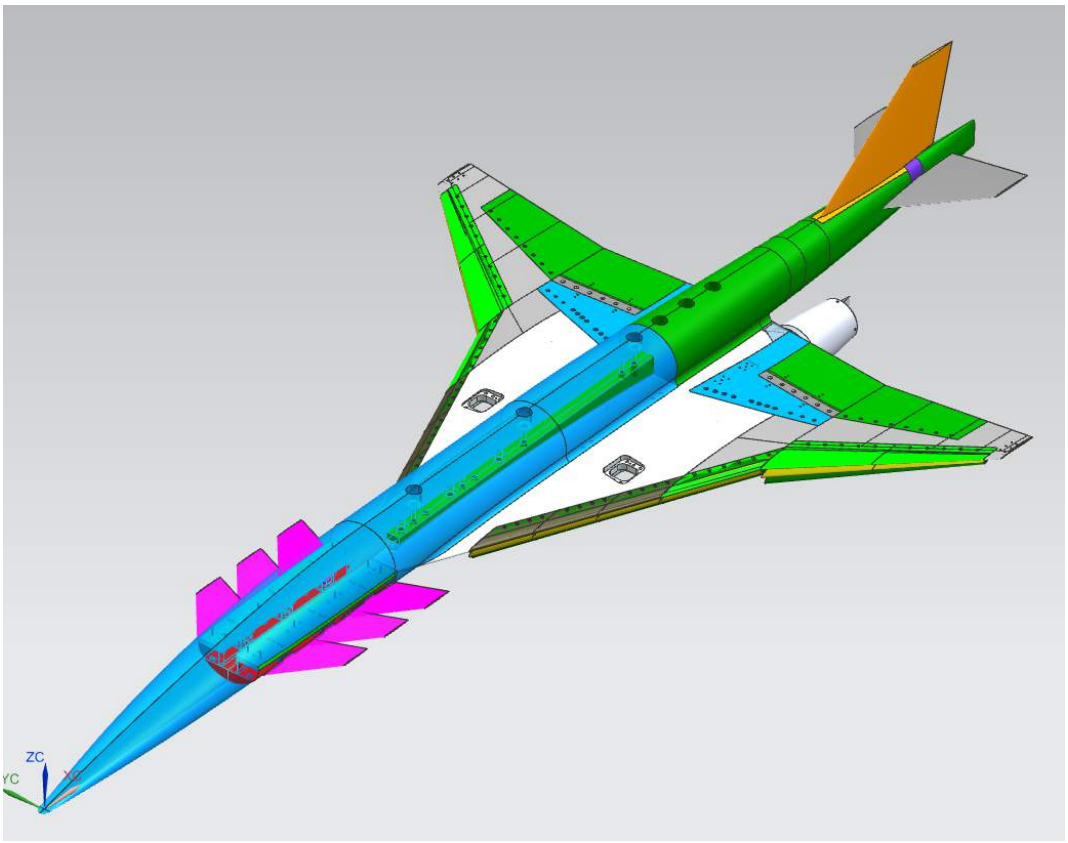


**Figure 7.8.59:** Drawing of the wind tunnel model

Additional canard positions were modeled to test three different positions along the fuselage. The leading edge of the model was trimmed to allow for varying degrees of leading edge droop. The ailerons and flaps were modeled using sizing obtained from VLAERO. Winglet and winglet rudders were sized via VLAERO and created by lofting the wing 90 degrees up and down.

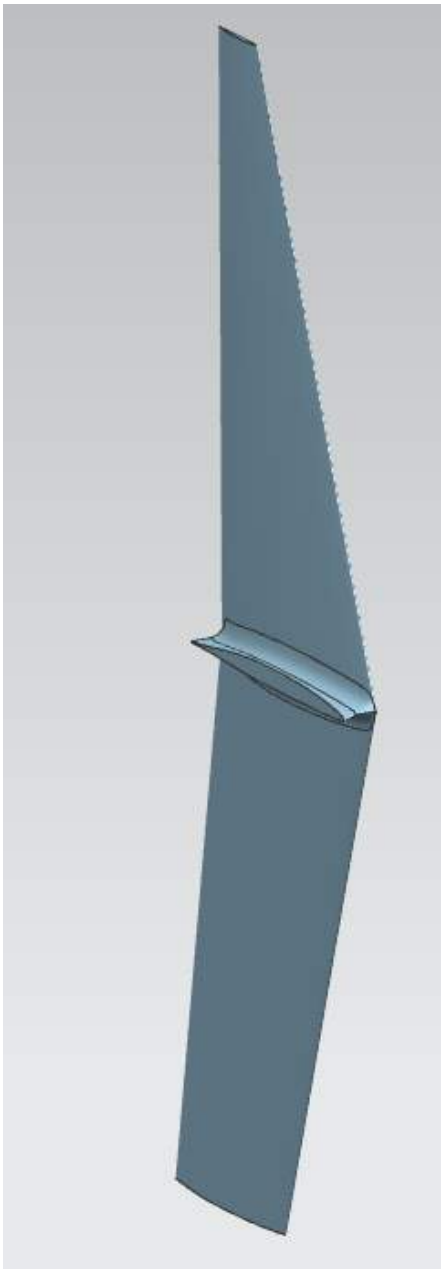

**Figure 7.8.60:** Sketch of the winglet

After wind tunnel tests the team decided to use the forward most canard position, 30 degree leading edge droops, no winglets or winglet rudders, as well as a slightly larger horizontal stabilizer. To substitute for the winglet rudders, a traditional vertical tail rudder was added. The larger horizontal stabilizer was modified using the formulas in the original part file. The size and shape of the fuselage and wing behaved well in the wind tunnel and required no changes.

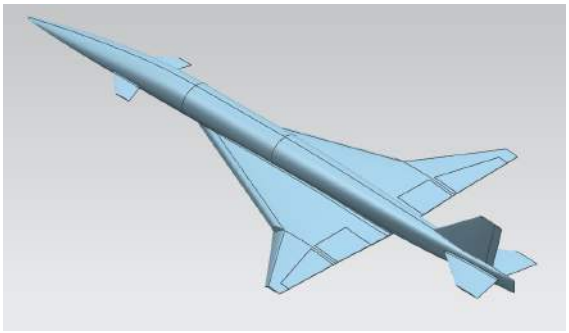

**(1)** Isometric view of R-UAV

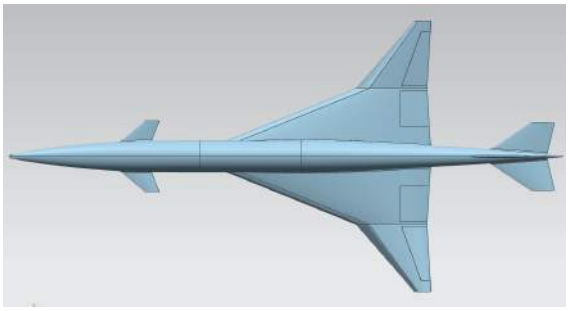

**(2)** Top view of R-UAV

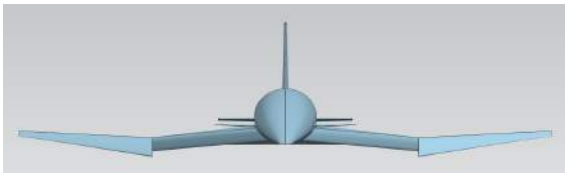

**(3)** Front view of R-UAV

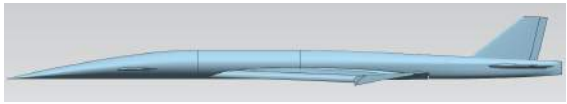

**(4)** Side view of R-UAV

**Figure 7.8.61:** Cross sections at different locations

For the R-UAV it was decided to thicken the airfoil at the crank and the tip to allow more room for internal structures such as servos and other control mechanisms for flaps and ailerons. Fuselage and wing molds were created and sent to Aerotec. The Wing was separated into lower and upper skin, and the fuselage was separated into a long bottom mold that spanned the entire fuselage, and three upper fuselage sections. These sections were then subtracted from an extruded block to create the molds.

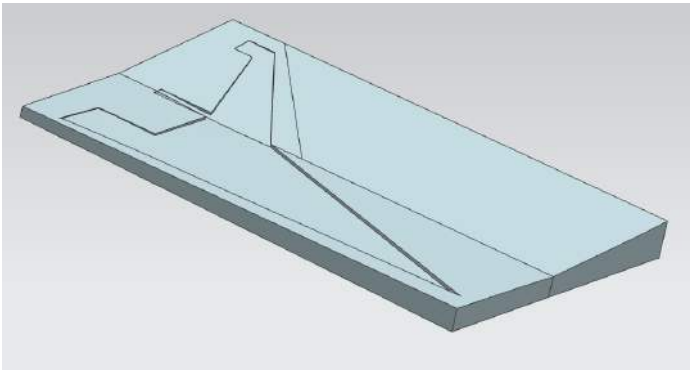

**Figure 7.8.62:** Mold of the wing

For construction hot wire cutting templates had to be created for several pieces such as the canards, vertical tail, horizontal tail, flaps, and ailerons. These were created by projecting the side curves onto a sketch, as well as a stand piece. An upper and lower template to guide the hot wire cutter were then created. These templates were inserted into a base that was modeled that housed both sides of the template to determine the length of the foam piece.

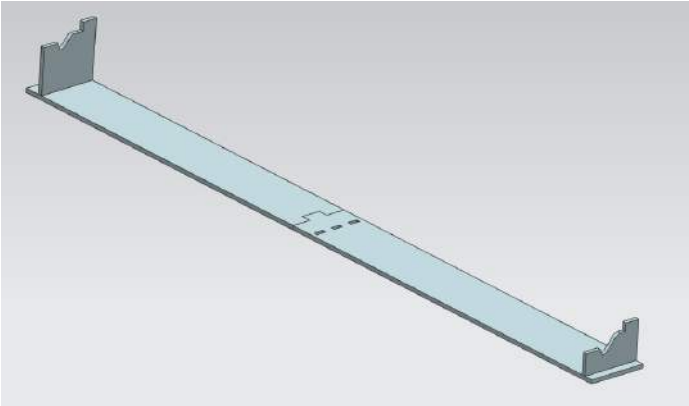

**Figure 7.8.63:** Template for the hot wire cutting

This format was also used to create a jig for the lay ups to ensure a good, accurately positioned bond for the wing and fuselage, as well as a secure base for placing internal structures and avionics.

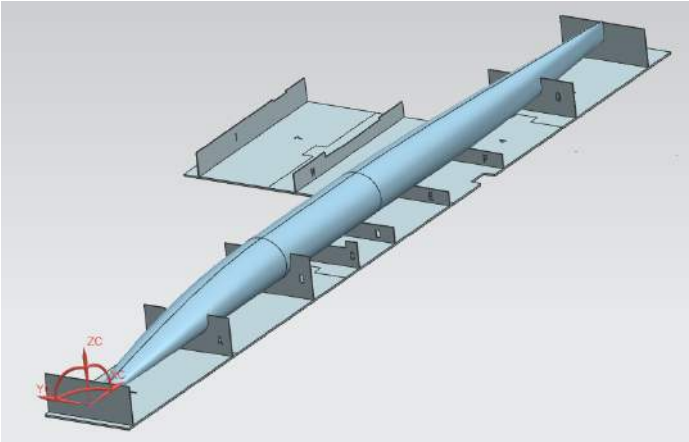

**Figure 7.8.64:** Sketch of the jig

For the design of the nacelle, the initial design was based on the 2014 model and was re-created in Solidworks 2014. Using Solidworks, knitted surfaces were used to create the geometry of the nacelle. The nacelle was initially split into 4 main parts. The inlet, duct, cowl, and nozzle. The lips of the inlet were created using surface sweeps and surface lofts. The circular shape of the cowl was used as a guide curve which allowed the inlet and nozzle to evenly converge to the shape of the cowl. It was also difficult to create the inlet corner lofts, and two guide curves were eventually used to solve this problem. From here, the inside of the nacelle and the outside of the nacelle up to the circular cross section of the cowl were created using two separate surface lofts. Surfaces were then used to create the constant cross section cowl and were also used to create the converging nozzle. This design is shown in Fig. 7.8.65. From here, various adaptations were created using the 2014 as a base design. As the design progressed, the inlet and nozzle areas were increased, the nozzle lip thickness was decreased, and the inlet lip was thickened on the exterior faces of the nacelle. A full description of the nacelle design progression can be found in the propulsion section of this document. The larger lip was created the same way as the initial lip and was constrained

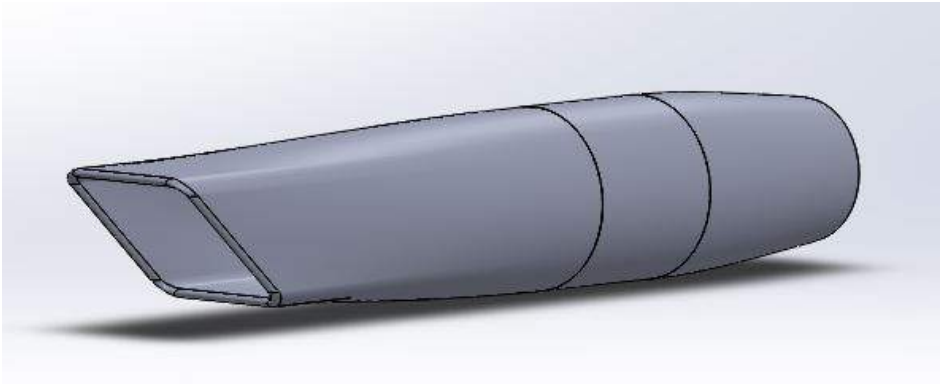

**Figure 7.8.65:** Initial Design of the Nacelle

to be tangent to the inside face of the duct, making a smooth surface for air to flow. This final configuration is shown in Fig. 7.8.66. After the base nacelle geometry was determined,

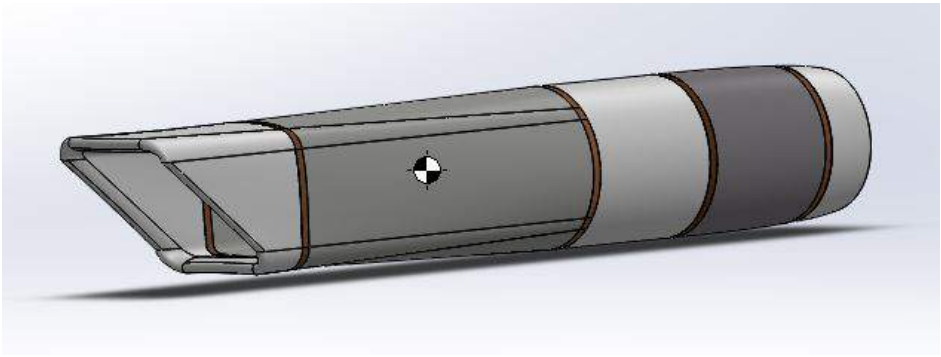

**Figure 7.8.66:** Final Design of the Nacelle

the nacelle was split into 10 parts. An inlet, duct, cowl front, cowl back, nozzle base, and nozzle end were created. Between each of these parts is a bulkhead. At this point, the mass properties of the different materials were input and the estimated center of gravity was determined. Next, the nozzle end was modified to hold the thrust vectoring vane, and to be printed as an assembly. The vane was created by splining points of a NACA 0015 airfoil and then resizing the resulting sketch. A rod was then built into the vane and was mated symmetrically to two vertically aligned holes in the nozzle end. Finally, a stopper was added to the rod to keep the vane from sliding up and down within the nozzle end. After this, a ramp was added to the upper lip of the inlet to create a smooth transition from the underside of the wing to the inlet of the nacelle. The ramp was designed as a shallow "S" curve shape so that it would be tangent to both the inside of the lip of the nacelle as well as the underside of the wing.

### *7.8.9. R-UAV geometry*

A decision was made by the team to convert to Solidworks 2014 for designing the interior structure as well as integrating all the elements of the R-UAV. As a management decision, this was beneficial for all teams for many reasons. First, the Propulsion team had designed

their entire nacelles in Solidworks 2014. Second, editing the weights and mass information for tracking the weight and moment of inertia proved to be much easier in Solidworks than in NX. Third, there was much more open access for Solidworks 2014 (20+) than for NX (3 computers) which enabled many teams to access the model and acquire information more efficiently. Fourth, many students underwent a class specifically designed to prepare them to use the Solidworks platform which meant the potential workforce was an order of magnitude greater. Although the Solidworks program was, in hindsight, a little less powerful than NX in creating complex shapes and in its compatibility to works with multiple formats (Parasolids, IGES, etc.), the benefits outnumbered the potential losses from switching to the Solidworks platform from NX.

First, a shell was created from the NX model to simulate just the skin of the aircraft. Assuming a 0.020" thickness, the shell was imported into NX. Second, the bulkheads were placed at locations suggested by the Structures group. The ribs were added, then the ESDU wing was formalized. Finally, all finalized files were integrated into the final configuration. The faces of each bulkhead and rib were used to outsource water-jet parts to West Coast Inc.

### 7.9. R-UAV Construction

The skin of the R-UAV was constructed using molds of the fuselage and wings manufactured by AeroTEC, as shown in Fig. 7.9.1. The lower surface of the fuselage was made using a single mold, while the upper surface was created in 3 sections. This was done to use the large, center mold as a main hatch on the R-UAV for accessibility.

**(1)** R-UAV fuselage molds

**(2)** R-UAV wing molds

**Figure 7.9.1:** Molds used to create skin of the R-UAV

Layups were performed on the molds using vacuum bagging techniques, as shown in Fig. 7.9.2. The exact materials used for the skin can be found in Table 7.0.4, in the Weights section.

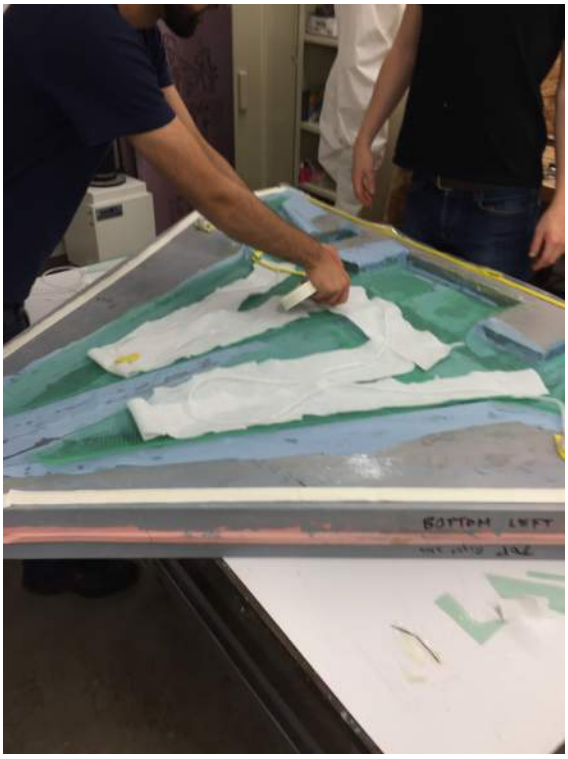


**(1)** Fiberglass layups on the wing skin

**(2)** Process of securing the vacuum

**Figure 7.9.2:** Process of vacuum bagging the wing skin

The keel beam along the lower surface was divided into two main beams, using balsa wood and reinforced with 3.7 $\frac{oz}{yd^2}$ carbon fiber tape.

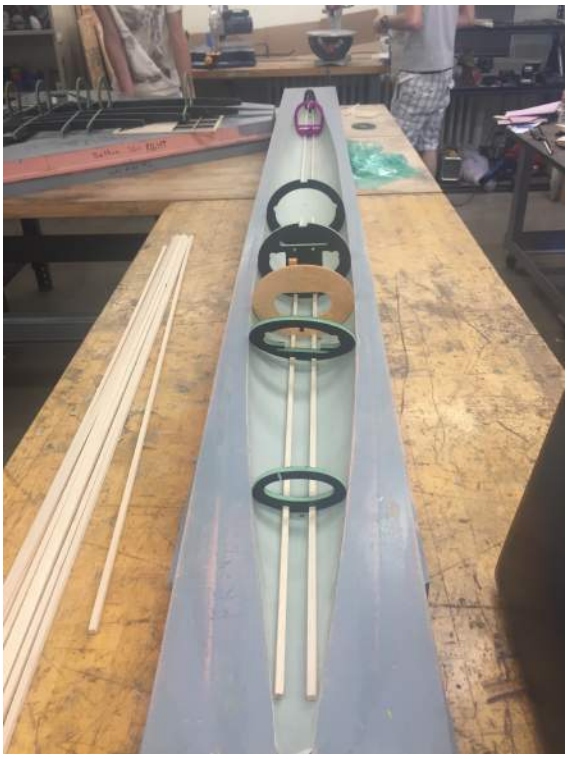

**(1)** Keel Beam of the Fuselage

**(2)** Keel Beams of the fuselage reinforcement

**Figure 7.9.3:** Keel Beam of the R-UAV

The wing skin was manufactured in a similar way, but reinforced with carbon fiber along the leading edge and span wise along the locations of the spars to increase the moments of inertia, as shown in Fig. 7.9.4.

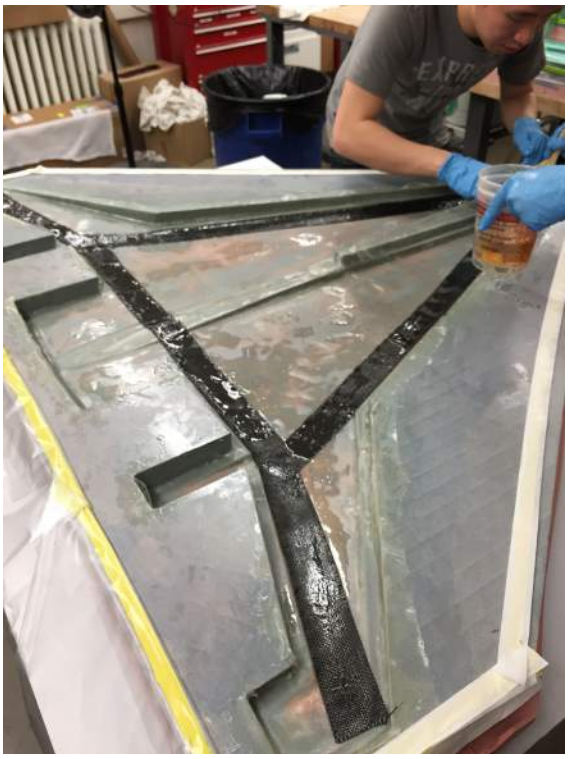

**(1)** A layup with carbon fiber on the wings

**(2)** Final carbon fiber arrangement along the wings

**Figure 7.9.4:** Keel Beam of the R-UAV

The control surfaces of the R-UAV were created using balsa wood blocks made from multiple plies glued together. Templates of their profiles were laser cut for the top view, inboard and outboard airfoils, as well as hinge line templates to connect them to the R-UAV.They were sanded to the proper shape using the templates as guides, as shown in Fig. 7.9.5. They were finished by laminating them with a single ply of $\frac{3}{4}$ oz/$yd^2$ fiberglass.

**Figure 7.9.5:** Balsa wood with templates used to shape them.

The canards and horizontal stabilator were manufactured in the same way as the control surfaces, with additional parts made for the rods used to mount them to the internal structure of the fuselage. A plate with an extruded rod were 3D printed, which an additional carbon fiber reinforcement, for the canards, which was then embedded into the balsa wood to provide a mechanical joint between the control surface and the shaft coupler. The parts for this can be seen in Fig. 7.9.6. For the horizontal stabilator, a pure carbon fiber rod was used for the extra strength.

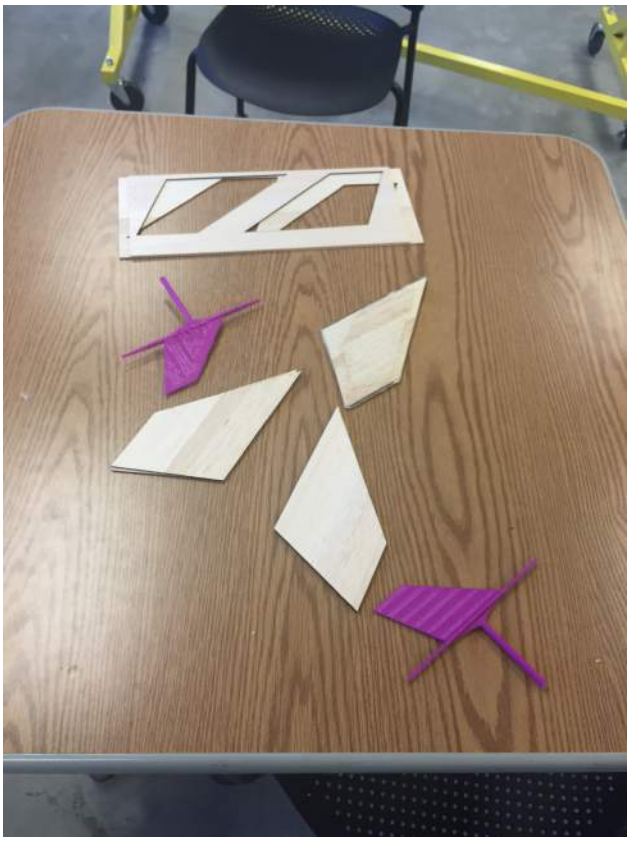

**Figure 7.9.6:** Balsa wood canards with 3D printed rods

The vertical tail, as well as its rudder, were created using a combination of foam, plywood, and PLA. The airfoil itself was hot wire cut and the rudder hinge line template was laser cut, for added accuracy when joining the rudder and vertical tail with hinges. The airfoil was reinforced with a $\frac{3}{4}$ oz/$yd^2$ fiberglass layup. The PLA was used to make a mount for the vertical tail so that it could mount to the fuselage, with the stress distributing accordingly, as shown in Fig. 7.9.7.


**Figure 7.9.7:** Foam vertical tail, with the fuselage mount

The nacelles were created using 3D printed parts for the inlets, exits, and vectored thrust flaps, foam cut with a hot wire cutter, and plywood bulkheads. They were finished by laminating the pieces with 2 plies of $\frac{3}{4}$ oz/$yd^2$ fiberglass.

**Figure 7.9.8:** Laser cut nacelle bulkheads

**Figure 7.9.9:** Full nacelle with various parts

Once the skins and main surfaces were constructed, the internal structure of the R-UAV was built. The ribs, bulkheads, and spars were manufactured out of a sandwich structure

fabricated from 3.7 oz/$yd^2$ carbon fiber cloth and PVC foam. The parts were modeled in SolidWorks and sent off to be waterjet by West Coast Waterjet.

Full integration of the R-UAV took time and precision. The fuselage and wings were integrated using a jig built of foam and plywood. The individual parts were modeled in NX, as explained in the Vehicle Integration portion of this report. Templates of t-sections of the lower surface of the R-UAV were laser cut and later glued together. In addition, the gaps between the templates were filled with foam, which was hot wire cut to match the entire lower surface completely. This ensured 100% alignment between the fuselage and wings. This ensured the integration between the waterline of the fuselage and the dihedral of the wings was correct. The final jig can be seen in Fig. 7.9.10.

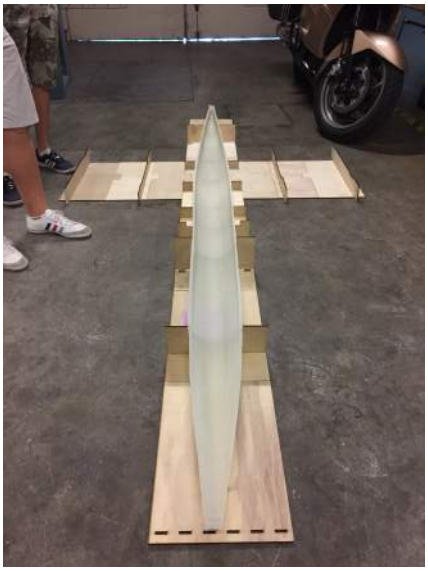

**(1)** Keel Beam of the Fuselage

**(2)** Keel Beams of the fuselage reinforcement

**Figure 7.9.10:** Jig used to integrate the skins and internal structure

The ribs in the wing skin were epoxied onto the wings while the skin sat in the mold to ensure the positioning as well as prevent any deformation during curing. The epoxy was a combination of epoxy and carbon fibers.

The sparks, bulkheads and wing alignment were all done in one step because the bulkheads and spars were designed as one piece, as shown in Fig. **??**.

**Figure 7.9.11:** The interal structure of the R-UAV

The main landing gears were mounted to the R-UAV using a platform fabricated out of balsa wood and aluminum sheet metal, as shown in Fig. 7.9.12

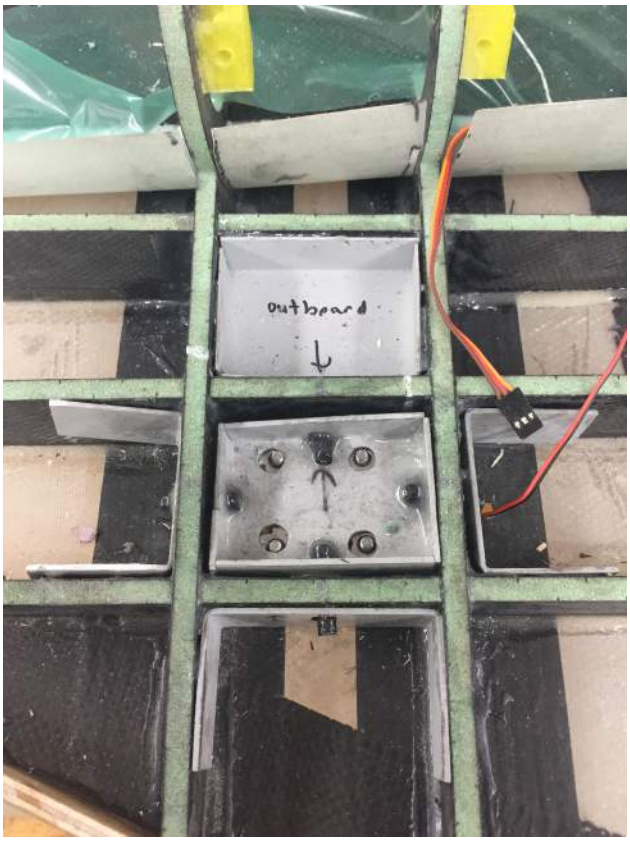


**Figure 7.9.12:** Metal mounts used for mounting the main landing gears

The nose gear is controlled using a servo, thus the mount was designed and built out of PLA to combine these components, as shown in Fig. 7.9.13.

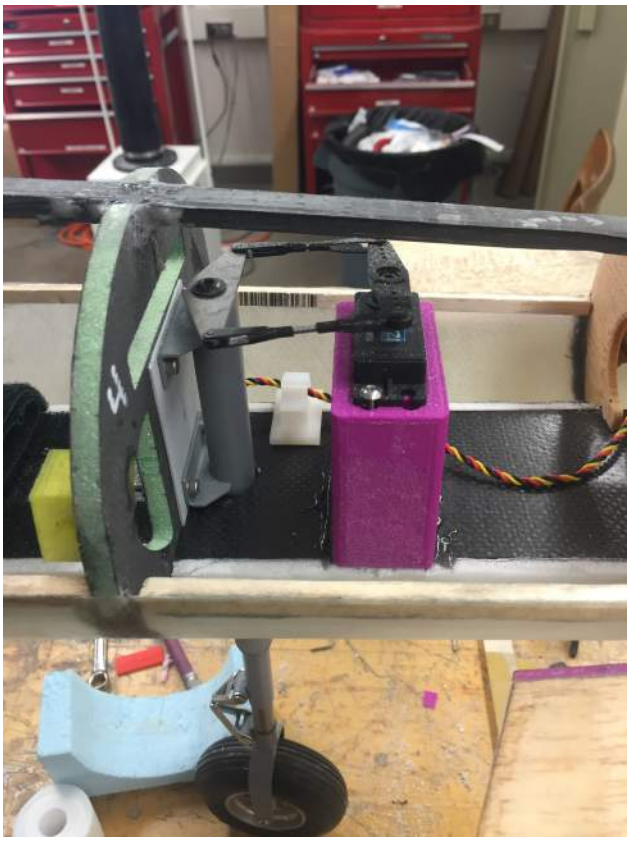

**Figure 7.9.13:** The 3D printed mount for the landing gear and servo

One of the most important aspects of the design of the R-UAV this year was accessibility. To do this, the middle portion of the upper fuselage skin was designed and constructed to be entirely removable. 3D printed fasteners were designed and mounted to the bulkheads and upper fuselage skin, making it removable with metal pins.

Lastly, the wings were bonded to the fuselage using a lapjoint along the edges. Future work to be completed at the time of this report include cleaning up the edges of the lap joint, priming, spackling, and finally painting the R-UAV.

Overall, 3D printing was a highly utilized tool in the construction process this year, however due to the time constraints of this type of project, it is highly advised that this is experimented with early on in the course to understand more about the structural integrity and the tolerances that can be expected from the parts. Based on the quantity of parts produced this year, it is advisable to buy a 3D printer for accessibility and time constraints that services on campus cannot meet. A flash forge 3D printer will produce much better parts than a makerbot, if one is purchased. Although this would minimize the amount of on-campus services that would be required, Makerspace was incredibly useful to this project. Having a large number of students acquainted with the computing tools and manufacturing hardware available is highly advised. Lastly, the jig was imperative in aligning the R-UAV body and useful for future years, however, if budget permits, it would be helpful to have AeroTEC create one solid mold for the entire lower surface to save time.

## 7.10. Performance

The main limiting factor with Performance is the weight of the aircraft. In order for the aircraft to perform with in the flight envelope the aircraft needed to be light enough. If the plane was not within the flight envelope it would be required that the plane be downsized.

### *7.10.1. Design Performance Requirements*

The design envelope of an aircraft is constrained by performance. Design requirements for stability and control of the R-UAV are outlined in the Requirements for Performance (RFP) APPENDIX REFERENCE. These include the following:

- The R-UAV must be able to hold a crab (sideslip) angle of $\beta \approx 10\,\text{deg}$ for trimmed airspeeds up to $1.3V_s1g$.
- The lateral-directional authority must be sufficient to trim out unbalanced yaw forces due to failure of a single engine (windmilling) down to $v_2 = 1.15v_s1g$.
- Nose-down pitch-control authority at high angles of attack must be sufficient to produce a rotational acceleration of $8\frac{\text{deg}}{S^2}$.
- A minimum center-of-gravity range of 6%MAC must be accommodated.
- Pitch-control authority must be sufficient to trim at $v_s1g$ at maximum flap deflection.
- Maximum roll-control authority must be sufficient to bank in one second to 45deg at $v_appr$ and to 70 deg at $v_cruise$.
- Minimum approach speed should be $v_appr = 1.23v_s1g$ and minimum initial takeoff climb speed should be $v_2 = 1.15v_s1g$. Maximum zero-wind liftoff speed must be less than $45mph$ unless the tire/wheel combination of the landing gear has been sufficiently tested at a higher speed.
- In a missed-approach situation, the aircraft must be capable of going from 3deg glide slope at $0.95v_appr$ to +3 deg climb in approach configuration in less than 2.5 seconds.

### *7.10.2. Summary of Minimum, Maximum and Reference Airspeeds*

In order to meet the required performance values for takeoff velocity and climb speed they were calculated based off of weight and maximum usable coefficient of lift. The maximum coefficient of lift value used was 1.1. This was found from the maximum usable angle of attack. The angle of attack was limited to due to an increase in pitching instability and yawing that occurred at 26 degrees alpha. The weight of the aircraft was then assumed to be 32 pounds. The approach speed, initial takeoff climb speed, and take off speed are based off of the stall speed and are respectively 1.23 Vstall, 1.15 Vstall, and 1.2 Vstall. The Vstall velocity was found from the following equation, Equation 7.10.1.

$$V_{stall} = \sqrt{(\frac{(2W)}{\rho * C_l * S} \tag{7.10.1}$$

The density was assumed to be at sea level and the wetted area used was 8.22 feet. The climb gradient equations are as seen below in Equation 7.10.2. The estimated rate of climb value, (for more detailed values see Takeoff Climb section), was found using the take off velocity and the sin of the climb gradient.

$$ClimbGradient = \frac{D}{L} - \frac{T}{W} \tag{7.10.2}$$

**Table 7.10.1:** Important Maximum and Minimum Performance Data

| Items | Values |
|---|---|
| Stall Speed, mph | 36.012 |
| Approach Speed, mph | 44.304 |
| Min Initial Takeoff Climb Speed, mph | 41.422 |
| Takeoff Speed, mph | 43.224 |
| T/W assuming 11 lb from engines | 0.7333 |
| D/L at 0.6 $C_l$ fully pitch up | 0.2902 |
| G Climb Gradient | 0.4431 |
| Climb gradient, deg | 26.305 |
| Rate of Climb, mph | 19.941 |

### *7.10.3. Summary of Trim Conditions*

In order to obtain expected trimmed force and moment coefficients for each canard configuration, the coefficients from the stabilator H2 runs were interpolated of a range of stabilator deflections and angles of attack, and the zero-deflection coefficients were subtracted. A MATLAB script was written to add the effects of all possible stabilator deflections to the C4 ($\delta_C = 0°$ and $\delta_C = 15°$) run data. The code would then specify, for each input airspeed, which $\alpha - \delta_H$ combinations would result in vertical force balance, and then which (of those) would also result in pitching moment equilibrium. This script is included in Appendix (APPENDIX NUMBER).

The lift-to-drag ratio versus airspeed for clean-configuration trimmed flight is shown in Fig. **??**. The maximum efficiency is achieved while cruising at 60mph, corresponding to an angle of attack of about $\alpha = 7.5$. The lift-to-drag ratio decreases noticeably with canard deflection, likely due to a combination of downwash on the main wing from the canard, more negative lift on the stabilator, and lower efficiency of the canard at higher deflections. The maximum efficiency shifts to slightly greater angles of attack with increasing canard deflection. The lift-to-drag ratio suffers a decrease of approximately 1 due to trimming with just the stabilator deflected, ($\delta_C = 0$) over this range of angles of attack compared to the untrimmed case with zero control deflections. (REFERENCE TO WT RUN212 LODvsALPHA)

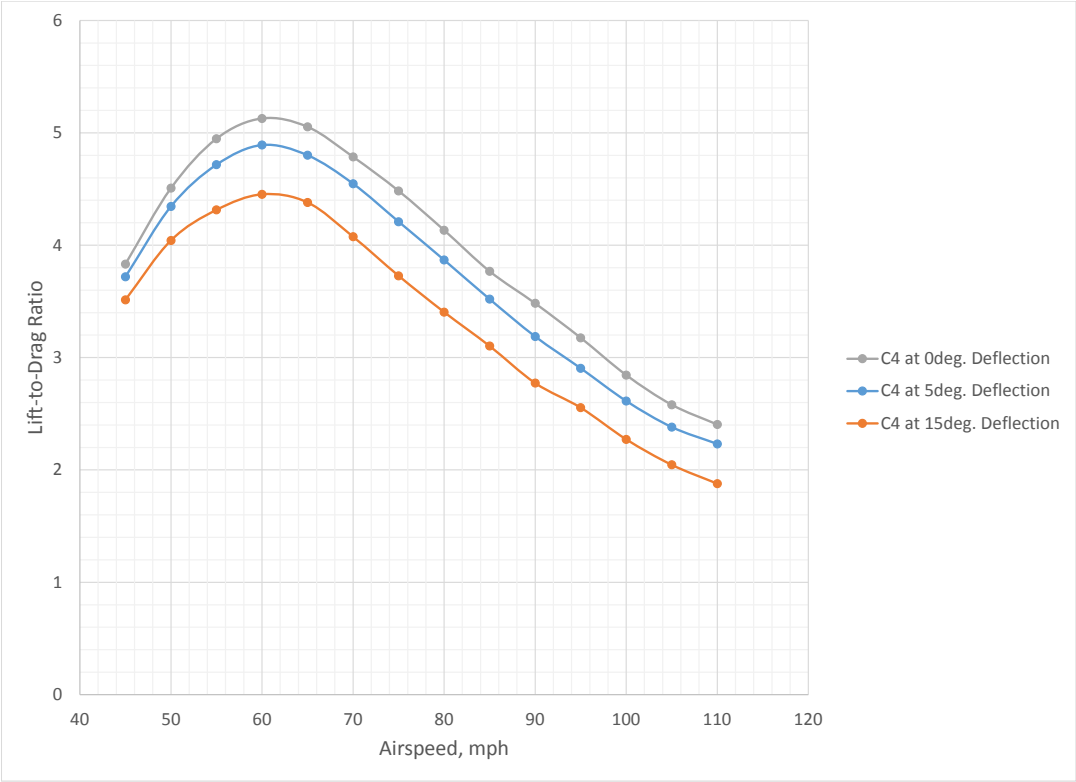


**Figure 7.10.1:** Trimmed lift-to-drag ratio versus airspeed for a clean configuration at various canard deflection angles.

The trimmed drag polar for clean-configuration trimmed flight is shown in Fig. **??**. These values are given over the same range of trimmed airspeeds (45mph $< v <$ 110mph) as the previous $L/D$ charts. The trimmed drag polar with the flaps deployed at $\delta = 10°$ is shown in Fig. 7.10.2. The flaps-down configuration shows a much lesser dependency of drag on lift coefficient.

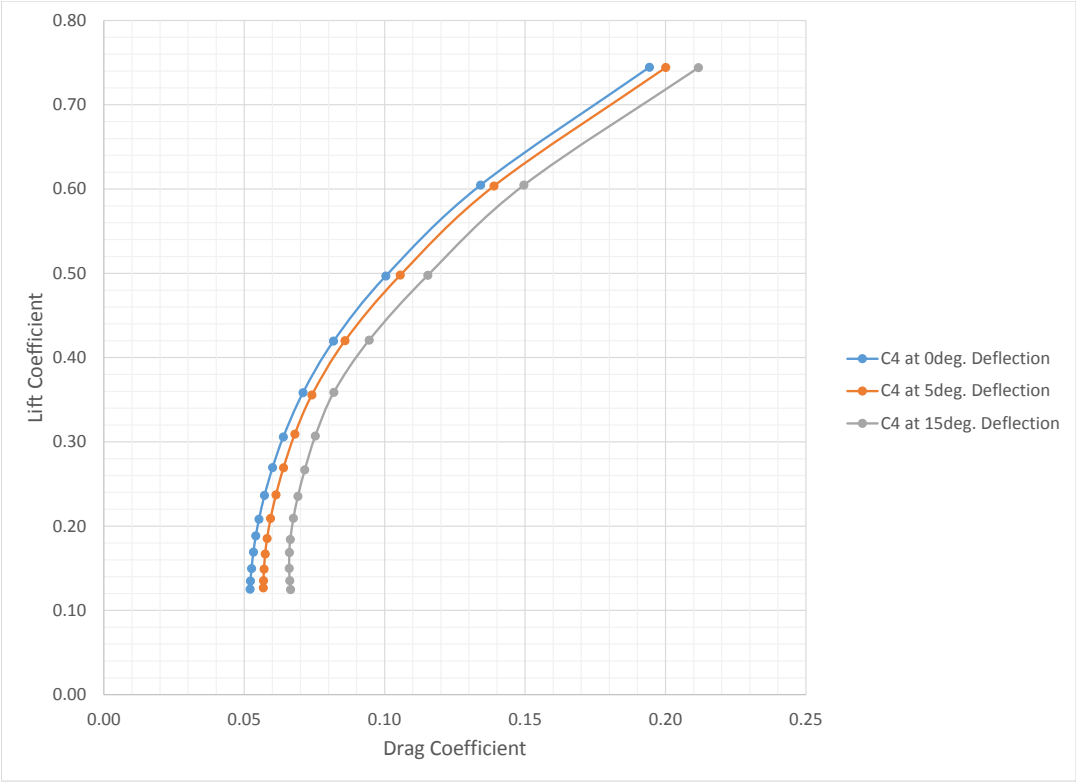


**Figure 7.10.2:** Trimmed drag polar for a clean configuration.

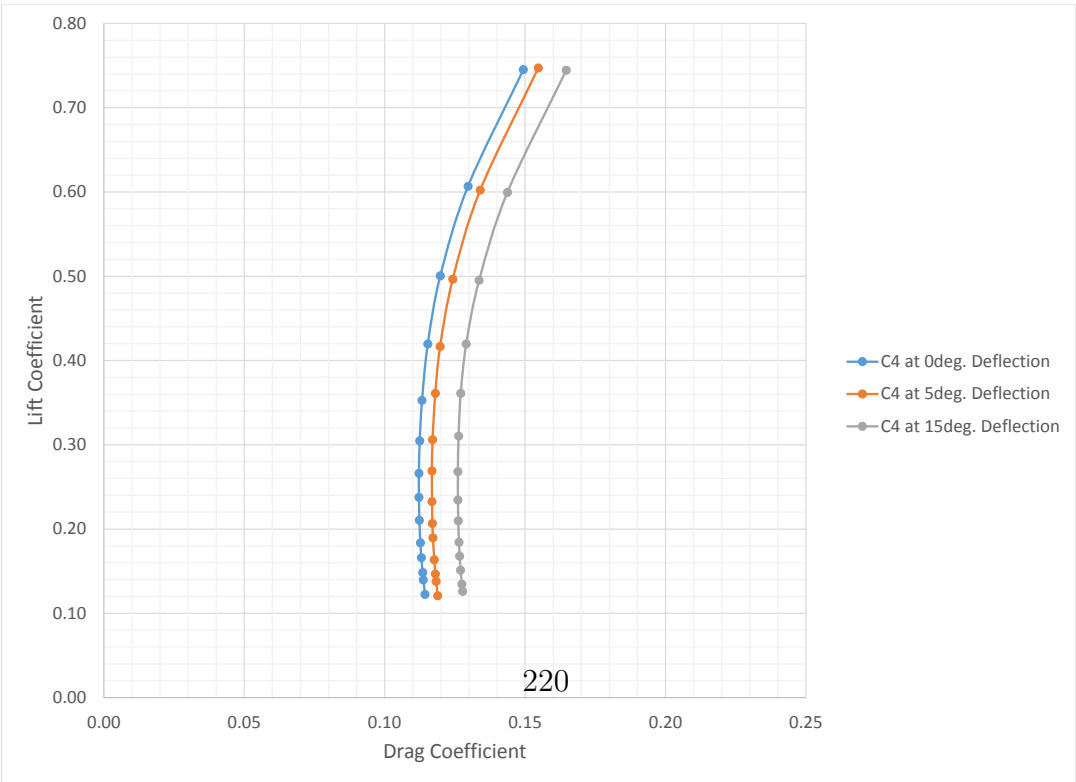

The interpolated stabilator deflection angles necessary for trimmed flight (given canard deflection and airspeed) are shown in Fig. **??** for a clean configuration. For higher airspeeds, the stabilator has the advantage of being deflected downward (positively) and thus generating positive lift; this point is however, delayed by positive canard deflection. The trim points of maximum efficiency do correspond to a negative stabilator deflection of a few degrees, and, at most cruise speeds of interest (above about 70mph), do result in positive lift on both longitudinal stabilizing surfaces as well as an acceptable lift-to-drag ratio. It is in the interest of efficient cruise to deflect the canard minimally; the canard's primary purpose on the aircraft will not be to improve efficiency but rather to increase rotational authority, prevent onset of deep stall on the main wing. As seen in the plot, the stabilator has plenty of authority to trim out unbalanced pitching moment from the main wing with the canard undeflected in a clean configuration, and does not need to be deflected more than -10°to trim the aircraft even at airspeeds close to those at takeoff. This is also true with the flaps deflected as long as the canard is not deflected too dramatically, although with the extra pitch-down moment contribution from the flaps, trim cannot be achieved with a positive-lifting stabilator deflection.

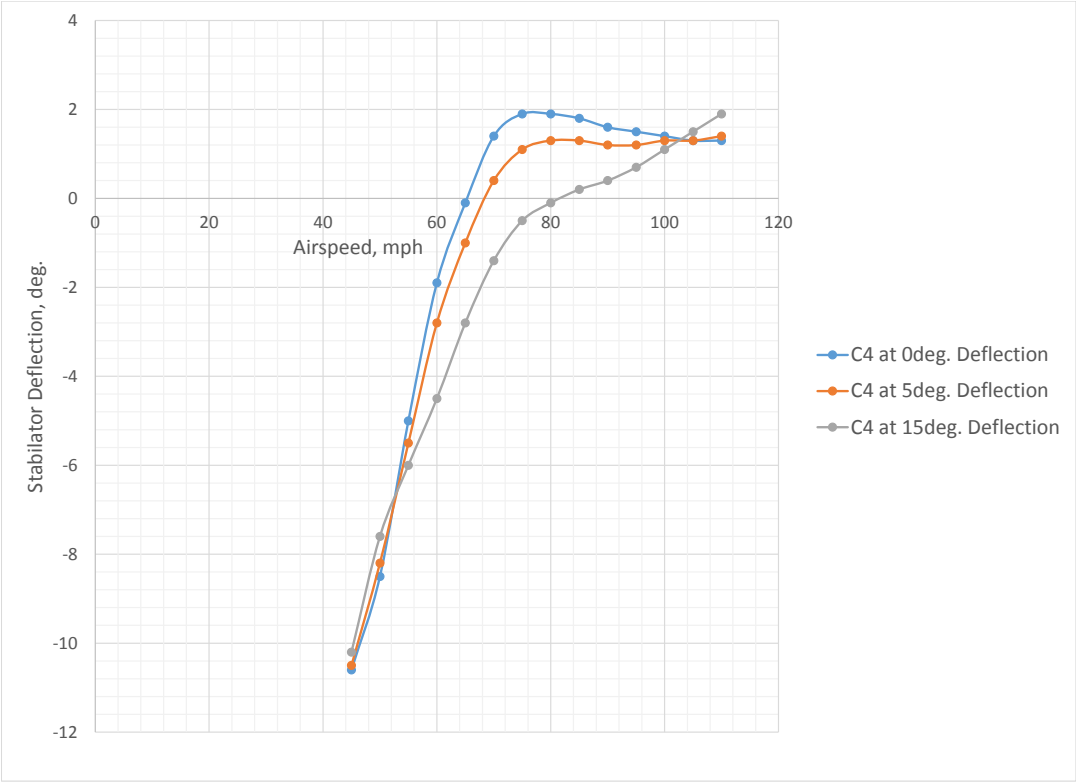


**Figure 7.10.4:** Stabilator deflections necessary to for trimmed flight in clean configuration.

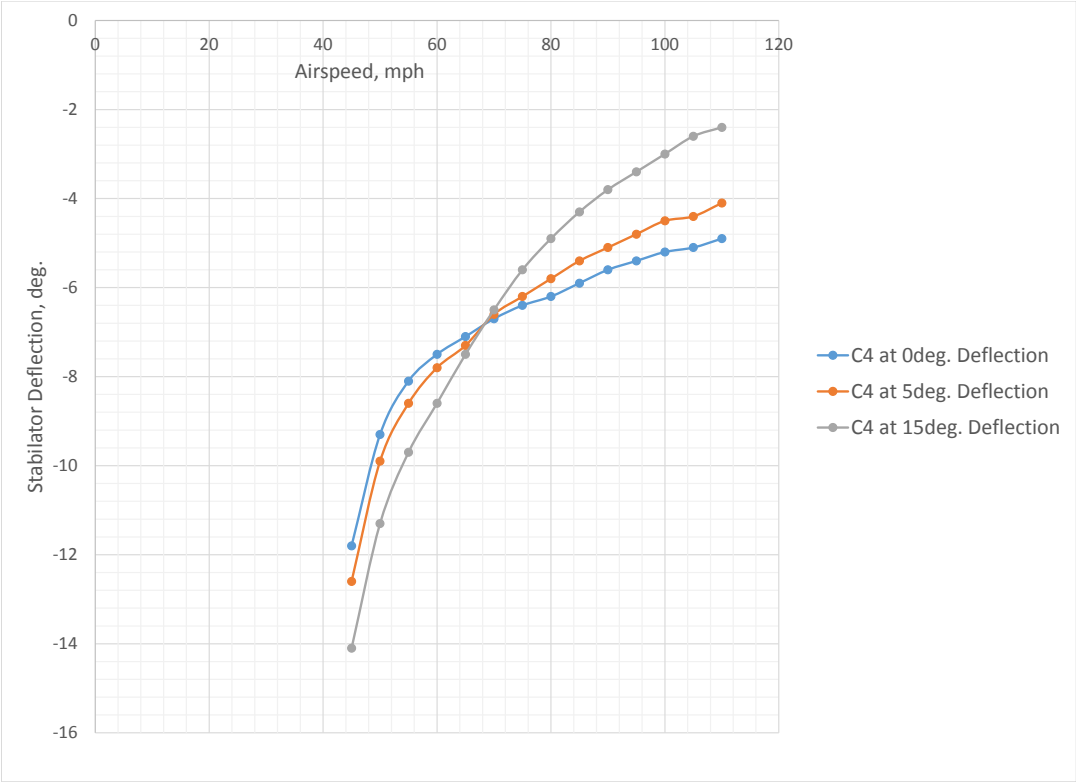


**Figure 7.10.5:** Stabilator deflections necessary to for trimmed flight with the flaps down.

Further aerodynamic data on the trim points of both clean and flaps-down configurations can be found in Appendix (REFERENCE).

### *7.10.4. Takeoff Climb*

Figure 7.10.6 shows the trimmed flight-path angles possible for both canard configurations at maximum thrust. At airspeeds below about 65mph the climb angle can exceed $\gamma = 20°$ with the flaps deflected at 10°. This data was generated by adding the interpolated 10°-flap force and moment contribution to the configurations with both the stabilator and canard deflected; a MATLAB script was used to search for the combination of deflections and angle of attack that would trim the aircraft for a given airspeed (see Appendix 8.1.3.2. Since the design takeoff airspeed is less than 50mph, the configuration meets the requirement that the climb angle $\gamma$ must be at least 20° with reasonable control surface deflections.

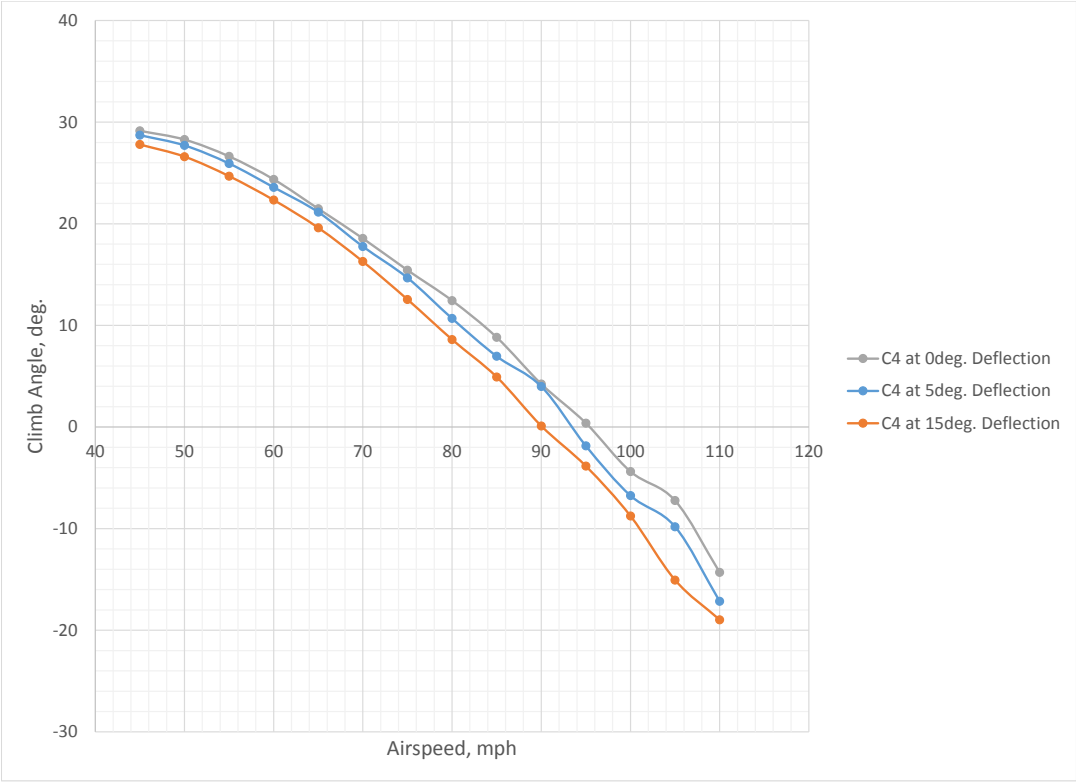


**Figure 7.10.6:** Maximum climb angle as a function of trimmed airspeed.

The flight-path angle was calculated using the premise that excess thrust beyond what is required for steady, level flight contributes to the retainment of vertical velocity. This is expressed in Eq. 7.10.3:

$$sin\gamma = \frac{T}{W} - \frac{1}{L/D} \tag{7.10.3}$$

The throttle setting necessary to climb at a certain angle or rate at a given airspeed is shown in Figs. **??** and **??** for a flaps-down configuration. Climbing at $\gamma = 20°$ at any airspeed requires close to maximum throttle but is possible up to approximately 68mph.

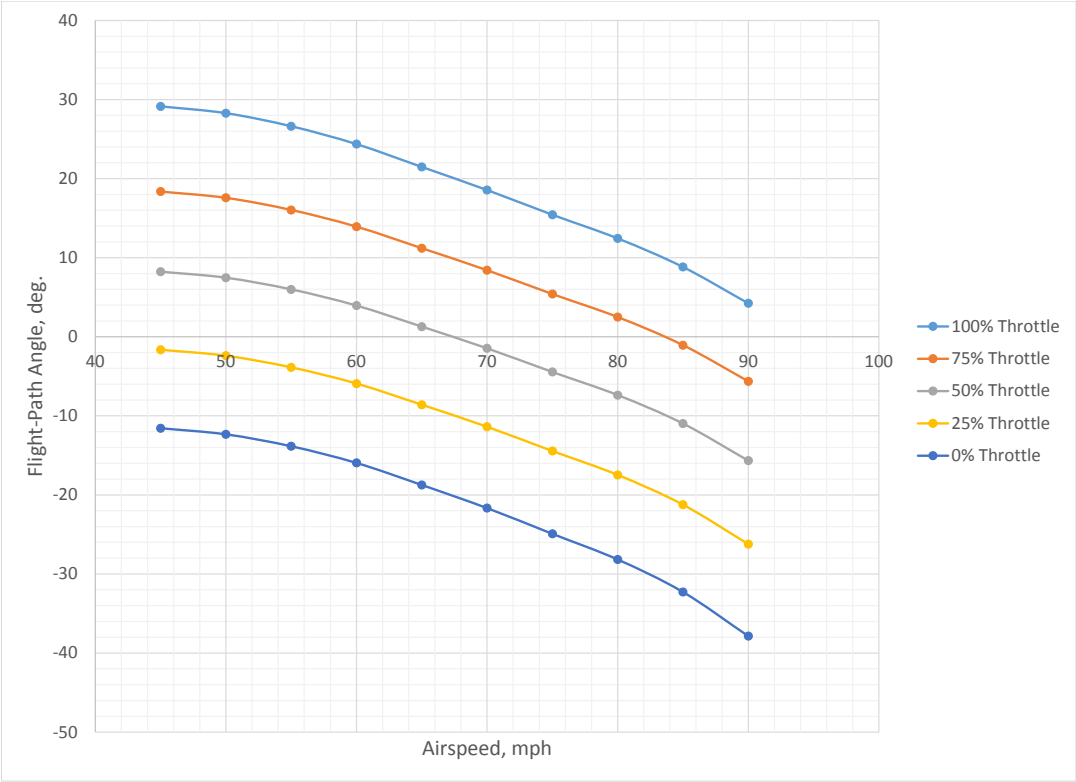


**Figure 7.10.7:** Flight-path angle $\gamma$ as a function of trimmed airspeed for various throttle settings.

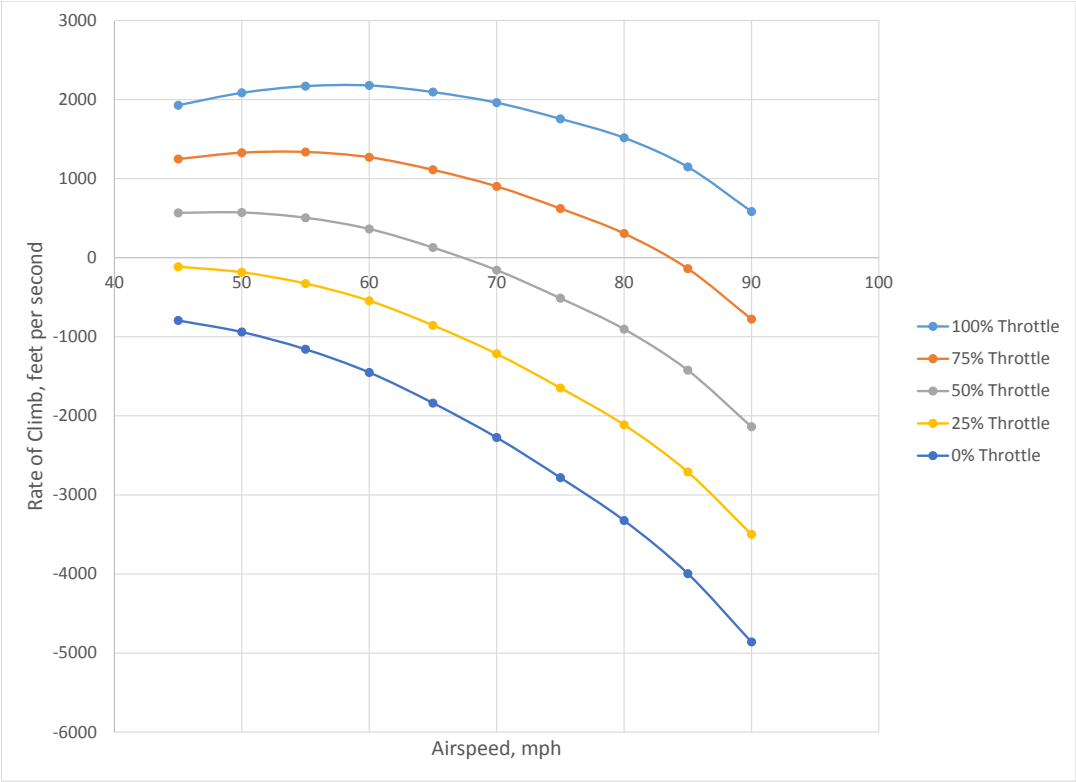


**Figure 7.10.8:** Rate-of-climb as a function of trimmed airspeed for various throttle settings.

The maximum-climb-angle airspeed is estimated to be 44mph, close to the maximum takeoff airspeed. The maximum-climb-rate airspeed at 100% throttle is estimated to be 55mph.

### *7.10.5. Takeoff Rotation*

Ground rotation upon takeoff is one of the more stringent requirements for pitching moment control authority. This is assessed by a summation of moments about the location of the rear landing gear strut at high canard and stabilator deflections with the flaps down. The aerodynamic moment about the center of gravity (designed to be 18% MAC) is translated to this alternative moment center using Eq. 7.10.4. This value, which should be positive with significant control surface deflections, is summed with the moment from the weight of the aircraft, offset by the distance between the C.G. and the rear gear strut, normalized by the mean aerodynamic chord. In order for the aircraft to rotate at takeoff, this net moment must be positive as per Eq. 7.10.5. When this value becomes positive, the reaction force from the nose strut should also be zero and the aircraft should begin to pitch upward.

$$c_{M,gear} = c_{M,18\%} + c_{L,B}(\frac{x_{gear} - x_{18\%}}{MAC}) \tag{7.10.4}$$

$$c_{M,18\%} + (c_{L,B} - \frac{W}{sq})(\frac{x_{gear} - x_{18\%}}{MAC}) > 0 \tag{7.10.5}$$

The net pitching moment about the rear gear strut is shown in Fig. **??** for $\alpha = 3°$, which is equal to the ground attitude angle of the aircraft. At 15°canard deflection the stabilator must also be deflected at close to -15°in order to rotate at the specified takeoff speed of 45mph. The canard should likely not be deflected more than this due to the possible onset of stall as the angle of attack increases subsequent to the onset of rotation. The stabilator could be deflected somewhat more than this if necessary since it should not be in danger of stalling with increasing angle of attack (the stabilator angle of incidence should increase from a negative value). The control surfaces should indeed be sufficient to rotate the aircraft upon takeoff, but this does appear to be one of the most demanding situations for pitch control.

It should be noted that the operative value is the pitching moment about the actual gear wheel rather than the intersection of the strut and the body axis. These values should however be very similar as long as the net longitudinal force is small and the aircraft is not significantly accelerating forward at this point during takeoff.

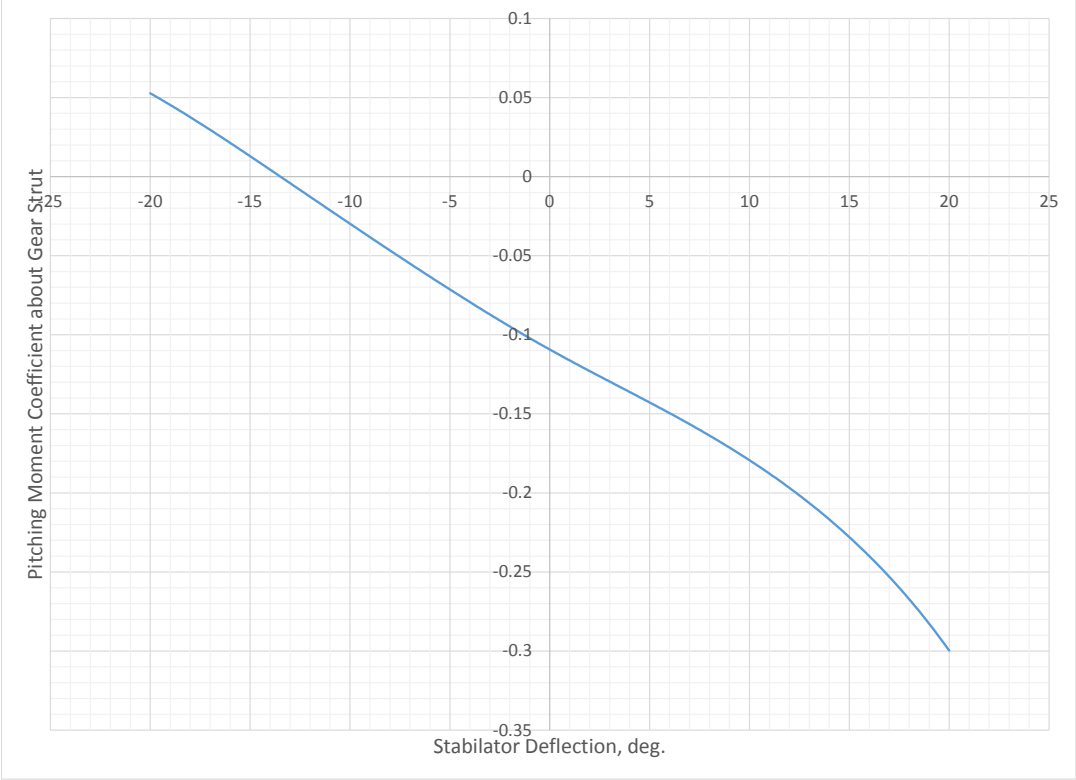


**Figure 7.10.9:** Pitching moment coefficient about main gear strut from aerodynamic forces and weight as a function of stabilator deflection angle at 15°canard deflection.

### *7.10.6. Takeoff and Landing Distances*

The takeoff ground-roll distance was predicted to be approximately 198 ft for the final configuration. This was calculated numerically via summation of forces during the takeoff acceleration phase B. The expanded equations of motion are shown below.

$$V_{t+\Delta * t} = Vt + a_t \Delta * t \tag{7.10.6}$$

$$s_{t+\Delta * t} = s_t + V_t \Delta * t + a_t \Delta * t_2 * 2/2 \tag{7.10.7}$$

Thrust data was taken from 3x3 wind tunnel tests. A best fit approximation was then used in the MATLAB simulation to vary thrust with wind speed. Ground effect was taken into account using the equation shown below. Ground effect is dependent on the ratio between

height of the wing and span. This equation becomes less accurate as the ratio decreases but was found to be acceptable for the height and span of the R-UAV.

### *7.10.7. Pitch-Down Acceleration*

A requirement for pitch authority at high angles of attack is that the aircraft's longitudinal control surfaces should suffice to produce a pitch-down acceleration of at least $8°/s^2$. The pitch-down capabilities of the The interpolation MATLAB script (see Appendix 8.1.3.2) used to find trim conditions also calculates a range of untrimmed (with nonzero pitching moment at a specified value of $c_L$) cases. Running the script with the flaps down, these cases can be surveyed at a given level-flight angle of attack, canard deflection and stabilator deflection to retrieve the resultant pitching moment coefficient. This value can then be re-dimensionalized and divided by the appropriate moment of inertia to return a thershoold value for pitch-down moment. The values used for this calculation are $\alpha = 18°$, $\delta_C = -30°$ and $\delta_H = 15°$. The combination of the canard angle and angle of attack result in a (presumably) non-stalling canard angle of incidence, while the stabilator is closer to stall conditions. Its angle of incidence should be some value less than 33°(sum of angle of attack and deflection angle less the downwash). Since the main wing does not actually stall until beyond this angle and uses a similar airfoil, it is assumed that the stabilator should not lose effectiveness at this angle of incidence. The resultant pitch-down moment and acceleration is displayed in Table **??**.

**Table 7.10.2:** Data pertaining to threshold nose-down control authority case.

| | |
|---|---|
| $\alpha$ | 18.0° |
| $\delta_C$ | -30° |
| $\delta_H$ | 15° |
| $c_{M18\%}$ | -0.2780 |
| $M_{18\%}$ | |
| $\frac{\partial^2 \alpha}{\partial t^2}$ | |

### *7.10.8. Nullification of Adverse Roll-Yaw Coupling*

When the ailerons are deflected they produce not only a rolling moment on the R-UAV, they also produce a yawing moment due to the asymmetric drag on each wing produced by the asymmetric lift. Thus the rudder needs to be used to null-out the yawing moment from the ailerons, and the ailerons need to be deflected to null-out the roll produced by deflecting the rudder. These deflections due to adverse yaw and roll need to be kept under 15% of total control surface deflection to maintain controllability of the aircraft while deflecting the other control surface to its maximum, as per the airworthiness requirements (see Appendix 8.1.1). It was assumed that the ailerons would have a maximum deflection of 20°, and the rudder would have a maximum deflection of 25°.

As shown in Fig. 7.10.10, the necessary deflections of the rudder to null-out adverse yaw from the ailerons is within acceptable limits up to $\alpha = 10°$, and goes up to $\alpha = 15°$ for the

necessary deflections of the ailerons to null-out adverse roll from the rudder. Above these angles of attack, the necessary deflections take up a considerable percentage of the total deflections of each control surface.

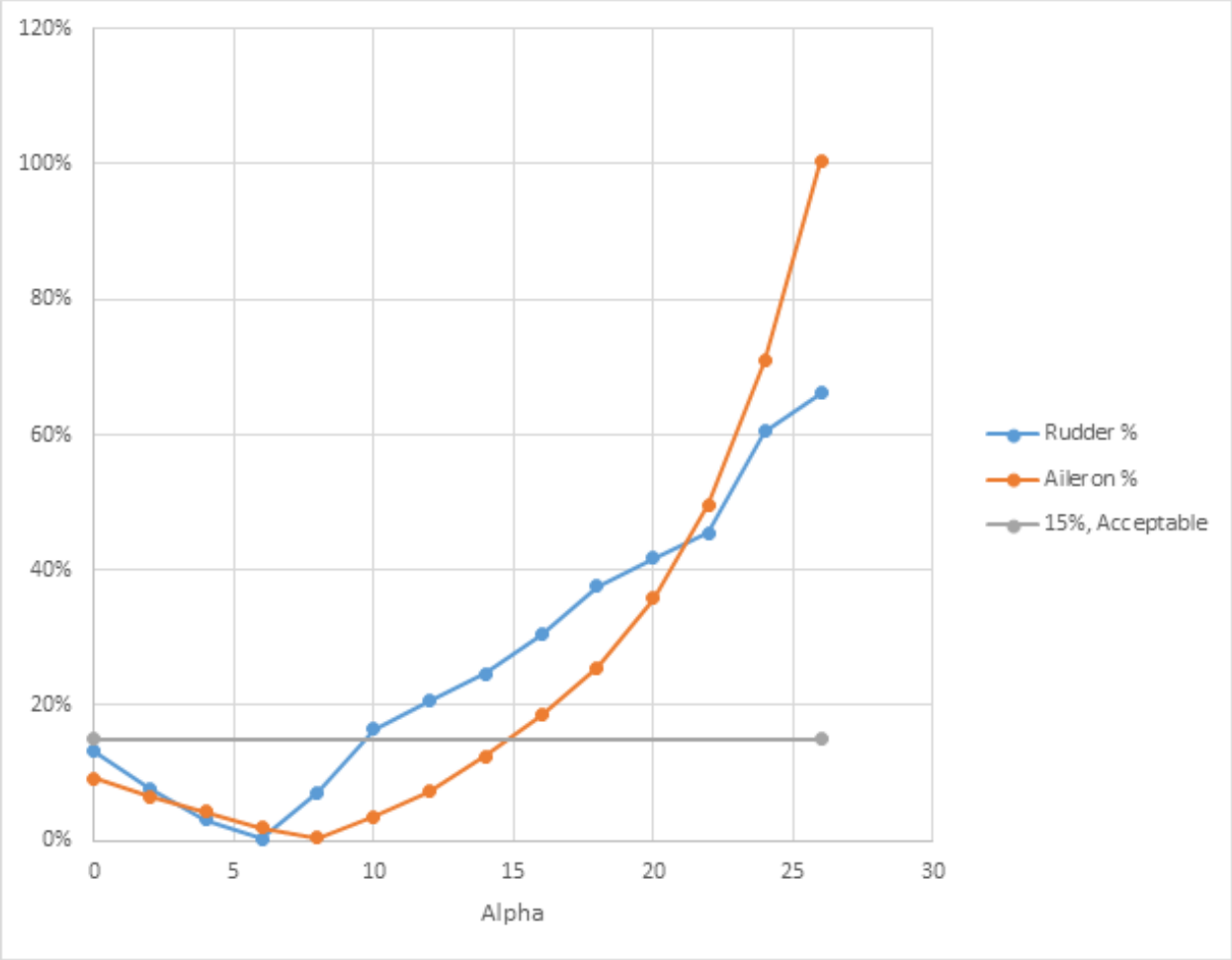


**Figure 7.10.10:** Required deflection to null-out adverse rolling and yawing moment.

### *7.10.9. Roll Control Authority*

The R-UAV is required to in one second roll 45°at approach velocity and 70°at cruise velocity with full aileron deflection. The roll damping derivative is the dimensional derivative of the coefficient of roll rate due to roll rate as shown in Equation7.10.8

$$L_p = \frac{QSb}{I_x}\frac{b}{2V}C_{l,p} \tag{7.10.8}$$

The roll control derivative is shown in Equation7.10.9

$$L_\delta = \frac{QSb}{I_x}C_{l,\delta} \tag{7.10.9}$$

The steady state roll rate of the aircraft is a function of the aileron deflection and the inertial and aerodynamic resistance of the aircraft to rolling as shown in Equation7.10.10

$$P_{ss} = -\frac{L_\delta}{L_p}\delta \tag{7.10.10}$$

The time response roll rate ignoring any transient responses is given by Equation7.10.11

$$P(t) = P_{ss}1 - e^{L_p t} \tag{7.10.11}$$

The roll rate of the aircraft quickly hits its steady state rate of close to 90°of roll per second as shown in Fig. 7.10.11. With this response the R-UAV is easily capable of meeting the requirement of 45°and 70°of roll in a second at approach and cruise. The necessary aileron deflection to achieve this was only 5°at both conditions.

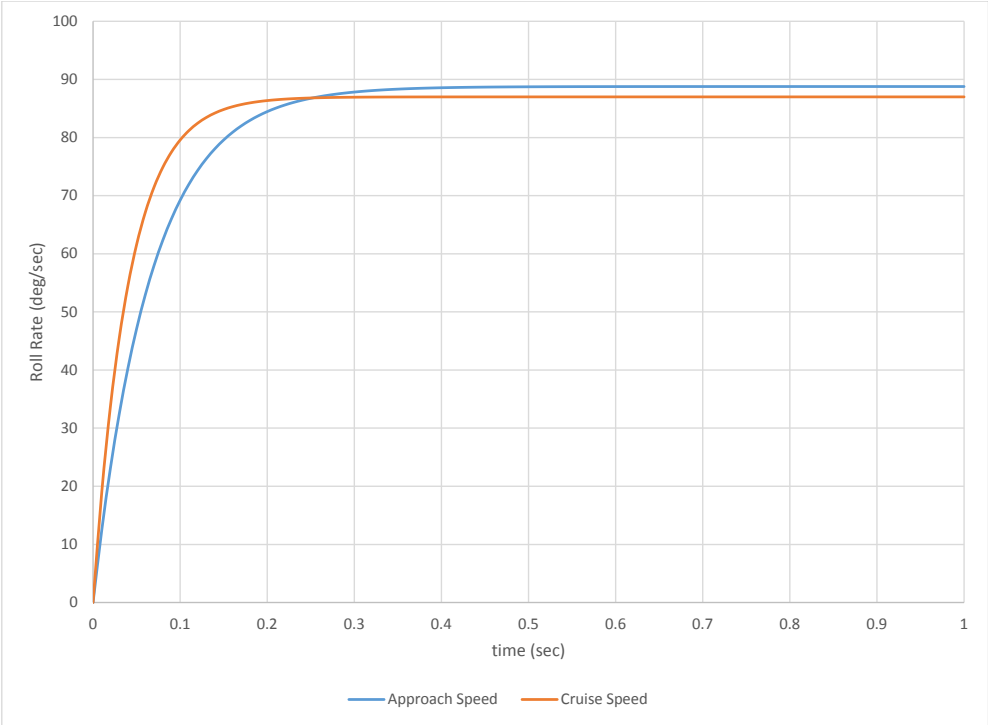


**Figure 7.10.11:** Roll Rate due to Aileron Deflection of 5 degrees

### *7.10.10. Missed Approach*

For a missed landing approach, or "wave-off", the aircraft must be capable of transitioning from a 3°glideslope at $0.95v_{appr}$ to a (positive) 3°climb in approach and landing configurations at the most adverse C.G. location in 2.5 seconds or less. This requirement can be translated to a change in vertical velocity $\Delta v_v$ which, when divided by the maximum maneuver duration, yields the average acceleration required for this change in climb angle. Summing forces and incorporating a non-negligible flight-path angle $\gamma$ yields the following:

$$\frac{g}{W}[(T - \frac{1}{2}c_D\rho s v^2)sin\gamma + \frac{1}{2}c_L\rho s v^2 cos\gamma - W] = \frac{d}{dt}(vsin\gamma) \tag{7.10.12}$$

Rearranging and expanding the time derivative:

$$\dot{\gamma} = \frac{g}{W}[\frac{T}{v}tan\gamma - \frac{W}{v}sec\gamma + \frac{1}{2}\rho s v(c_L - c_D tan\gamma)] \tag{7.10.13}$$

This was numerically integrated using a Runge-Kutta solver, using inputs of $v = 0.95v_appr = 59.1$mph and sea-level density. The approach speed used is equal to 123% of the minimum trimmed speed (which is not the 'stall speed' per se due to pitch-up being the limiting factor rather than stall). This corresponds to $c_L = 0.65$, the $c_L$ value at pitch-up at the most adverse CG (25% MAC at approximately 6% static margin). The drag coefficient is assumed to be constant throughout the maneuver with the drag force equal to the thrust. A time-history plot of flight-path angle $\gamma$ is shown for various lift coefficients.

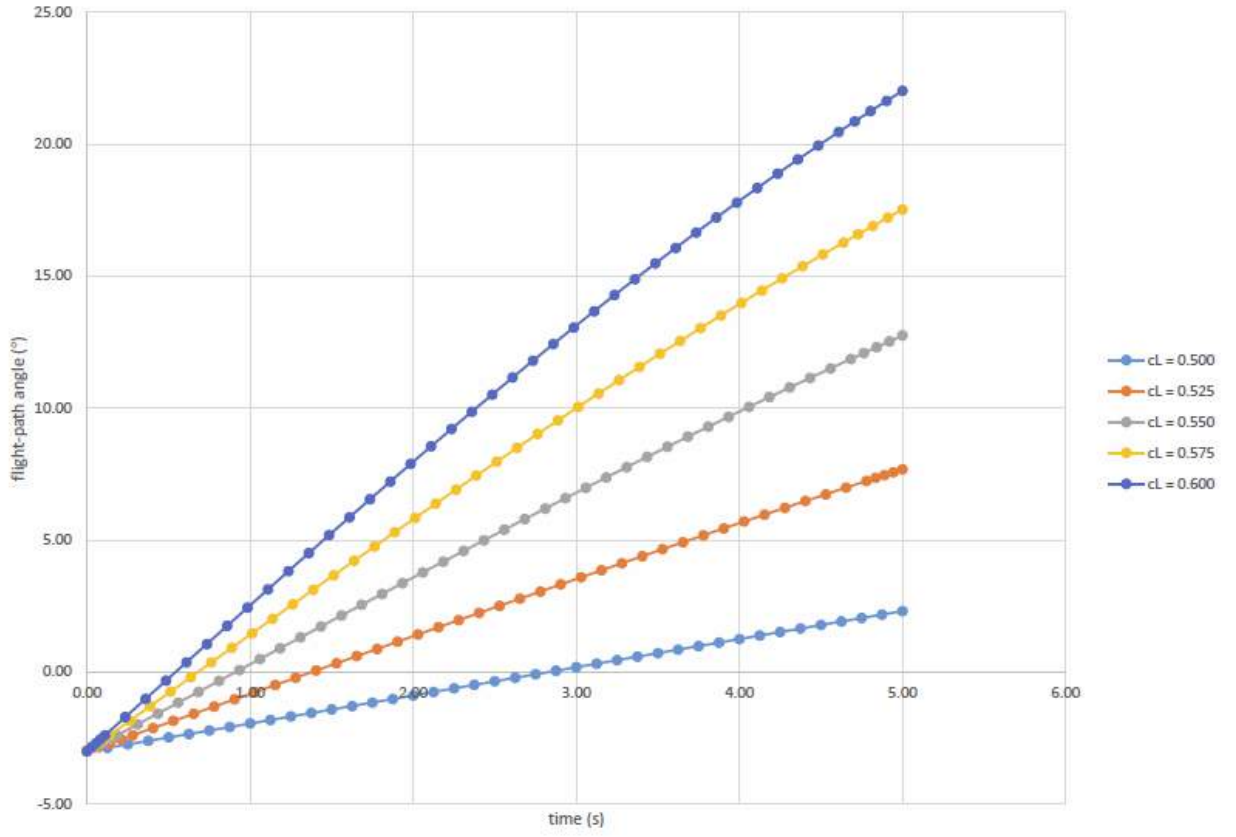

### *7.10.11. Return-to-Land Maneuver*

The return-to-land maneuver, applicable if the aircraft experiences flight-inhibiting issues after the commit-to-stop point ("point of no return") and has to take off anyway due to lack of remaining runway, is to be performed as follows: the aircraft should continue straight for two seconds after cleared liftoff, reduce thrust to 20%, turn 180°at a shallow bank angle, gaining at least 25ft in altitude during the turn. This is generally a restraint on thrust, since the climb requirement is essentially a normal takeoff climb requirement with decreased thrust due to throttle setting and decreased lift due to a component of the lift providing the centripetal acceleration in the turn.

$$a_c = \frac{Lg \sin \phi}{W} = \frac{V^2}{r} \tag{7.10.14}$$

The horizontal distance traveled by the aircraft during the turn (the length of the semicircular arc) can be multiplied by the tangent of a constant climb angle $\gamma$ to obtain the actual vertical distance traveled. Substituting this result yields Eq. 7.10.15.

$$g \sin \phi = \frac{\pi V^2 \tan \gamma}{\Delta h} \tag{7.10.15}$$

From here, the actual required constant flight-path angle $\gamma$ can be calculated for this maneuver, as in Eq. 7.10.16.

$$\gamma = \arctan \frac{g \Delta h \sin \phi}{\pi V^2} \tag{7.10.16}$$

The airspeed chosen here was a very conservatively low 35mph, requiring a $c_L$ of 1.233. Substituting these values into Eq. 7.10.16 and using a bank angle of $\phi = 15°$ yields a required flight-path angle of $\gamma = 1.44°$, corresponding to a turn radius of 316ft. With both engines operational and reduced to 80% throttle, the aircraft can still maintain a climb angle of nearly 20°. If the return-to-land maneuver were necessary in the case of a single engine loss, the aircraft can sustain a climb angle of 3.5°with the single operational engine reduced to 80% throttle, hereby meeting this requirement.

### *7.10.12. Non-zero Crab-Angle Trim*

The RUAV is required to be able to trim at sideslip angles up to $\beta = \pm 10\,\text{deg}$ at $c_L$ values up to that of 1.3vs1g. This requires the lateral control surfaces (in this case just the tail rudder, since the winglets are fixed) to have enough authority to trim out the restoring yawing moment provided by the stability of (primarily) the vertical stabilizer and winglets. As discussed, this stability derivative has to be at least $\frac{\partial c_N}{\partial \beta} \geq 0.002 \frac{1}{\circ}$ for small sideslip angles $\beta$. The trim requirement can be expressed as follows, where $\delta_V$ is the rudder deflection necessary.

$$c_N + \frac{\partial c_N}{\partial \delta_V} \delta = 0 \tag{7.10.17}$$

If a vertical tail rudder had been tested in the wind tunnel, this capability could easily be confirmed by showing a zero-yawing moment intercept at some tested rudder deflection $\delta_V$ (or between two tested deflections). The wingtip rudders were not shown to have enough yawing moment authority to trim the aircraft at such a sideslip angle; at small angles of

attack the rudders could only trim out up to 5°sideslip (REFER TO WINGTIP RUDDER CHART). Yawing moment data for the final (undeflected) control surface configuration is shown below in Fig. **??**. This indicates, at various angles of attack, the yawing moment that needs to be trimmed out at a given sideslip angle.

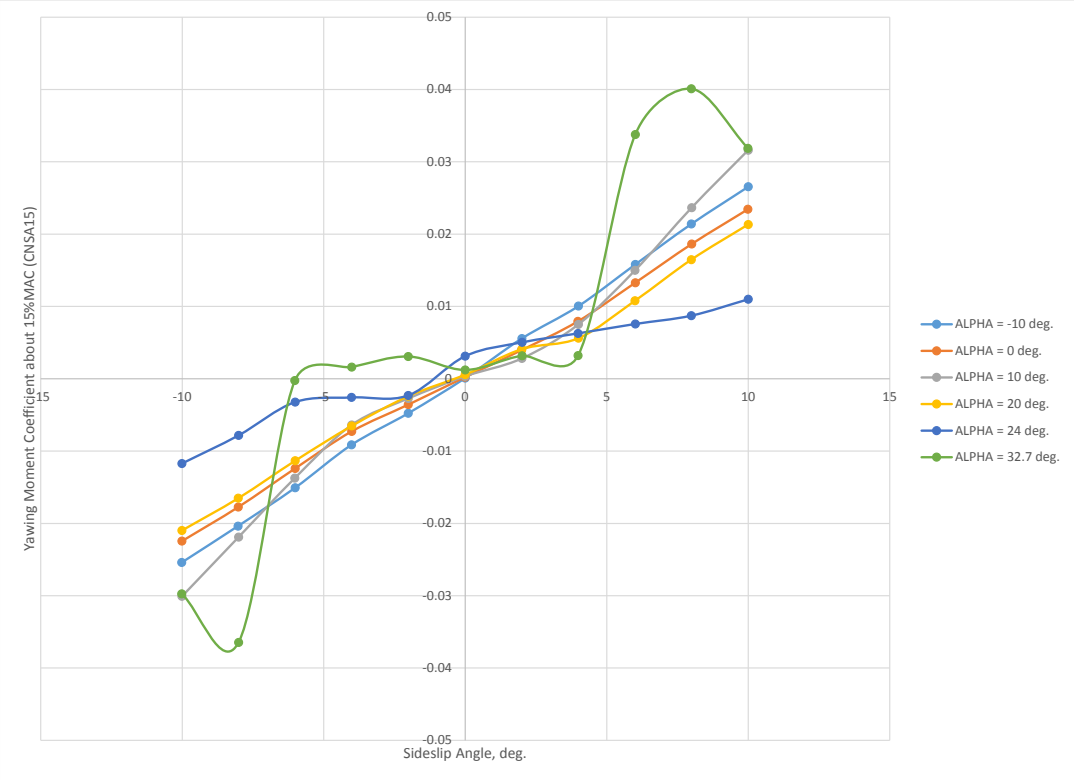


**Figure 7.10.12:** Yawing moment coefficient as a function of sideslip angle $\beta$ at various angles of attack.

According to the wind tunnel data, the aircraft is most stable in yaw at moderately low-airspeed angles of attack; the greatest restoring yawing moment for $\beta = 10°$ occurs at about $\alpha = 10°$, which requires the lateral control surfaces to provide about $c_n = 0.032$. WHAT IS ALPHA AT VS1G TRIM?

### *7.10.13. Trim at Engine-Out Conditions*

As with most twin-engine aircraft, the RUAV is required to be able to trim in yaw at relatively low airspeeds if an engine is lost during takeoff. The moment from the engine is the product of the thrust at full-throttle and the distance between the engine and the longitudinal axis of the aircraft, which must be trimmed out by the inherent lateral stability of the configuration and the lateral control authority. The single-engine moment can be expressed

as a coefficient (normalized by the same parameters as $c_N$) and compared directly to the yawing moment coefficients of the configuration (with the rudder deflected) to determine the sideslip angle necessary to trim the aircraft.

#### *7.10.14. Gust Tolerance*

The aircraft must be able to withstand 15mph gusts at cruise conditions.

### 7.11. Flight Test

The Flight test team was responsible for completing all of the necessary tasks for flying the airplane. This included developing a systems check plan, flight test equipment plan and flight test maneuvers for the airplane.

#### *7.11.1. Control Systems Check*

- Ensure that all of the controls power-up properly.
- Check all control linkages and horns for solid attachment.
- Verify the location and orientation of all of the antennas.
- Make sure the telemetry, EDF power and data logger do not interfere with one another.
- Exercise each control surface back and forth and check for binding.
- Check each surface for zero position and throw limits.
- Verify intended pitch control and C.G. match the analysis.
- Verify brakes works.
- Check mixing control for each function, including flaperons up/down.
- Check what is set up for gyros and what the gains are (deflection movement vs pitch/yaw/roll rates).
- Make sure the exponential rates are adjusted for all control commands to avoid over-sensitivity but still give adequate control authority at low "q" conditions.

#### *7.11.2. Flight Test Equipment*

- 2 laptops preinstalled Eagle Tree software fully charged
- 2 video cameras fully charged
- 8 6-cell batteries fully charged and functional
- 3 scales for measuring C.G with 4-9 volt batteries
- 4 car batteries with clips and air compressor for charging brakes

- 2 Arduino Batteries
- 2 Receiver Batteries
- STORM and 2015 Foamie
- DX-18 controller fully charged
- Portable DC power source for DX-18
- Tarp
- Laptop with Pixhawk software fully charged
- Plastic bolts and battery tray
- 2 Y-connectors for batteries
- Voltmeter and 6 cell voltmeter
- C.G Stand
- Card table
- Seagull Box including 2 seagulls, 2 seagull to USB cables and 4 volt
- New battery charger, power supply and battery hookup
- New battery charger, power supply and battery hookup
- 2 Power supply to car battery hookup
- Screwdriver for nylon screws
- Forceps
- Speed tape, Painters tape, duct tape
- One set of directions per car

#### *7.11.3. Important Test Day Information*

The flight test for the 2015 R-UAV will occur at the Coupeville naval base on Whidbey Island. Directions and important travel information are found below.
*Directions*
*Ferry Schedule*
*Ferry Fare*

### *7.11.4. Flight Test Plan*

1. Ground Test

    - Ensure that a full systems check has been performed on the aircraft before beginning any flight test.
    - Perform a low and high speed taxi test and use the high speed taxi test to check the ground systems including ground steering, braking, turn radius and stability on the gear.
    - Audio and video coverage of the ground test from two vantage points and use radio to communicate between pilot location observers, video recorders and telemetry station.
    - Check the air data system including alpha-beta sensor, pressure altitude and pitot-static airspeed.
    - Check the pitch control for takeoff by applying a pulse of 50-70% takeoff speed to see if the nose is lifted.
    - Check radio holds/fades.
    - **Ensure that all the points are addressed and all issues are resolved before moving on to the flight test.**

2. Flight Test

    - Continuously monitor and call out the readings for air speed, less frequently for altitude and monitor the flight time and battery power.
    - Rotate and liftoff the plane when at the target takeoff speed.
    - Use a straight and shallow climb angle.
    - Turn the aircraft at a shallow to moderate bank angle.
    - Monitor speed, clean up flaps and reduce throttle to level cruise flight.
    - Complete one or two circuits at medium to high altitude, check general handling control and trim.
    - **Return to land if any issues arise.**

3. Performance Test

    - Perform a pitch command pulse and observe the response and return to stable position.
    - Perform a yaw command pulse and observe the response and return to stable position.
    - Perform a roll command pulse and observe the response and return to stable position.
    - Perform a 5-turn on upwind or downwind leg of the racetrack to check roll and heading control in the right and left bank.

- Decelerate the plane and set landing flap, perform a practice approach and go around at safe altitude to check handling, glide-slope and target approach speed.
- **If time remaining**, fly a circuit at safe speed in the landing configuration to perform a shallow roller coaster maneuver at constant throttle to obtain in flight lift and drag information.
- Fly normal approach, landing and rollout.

4. Post Flight Check

   - Check the motor, battery, ESC temperatures, radio signal holds and fades.
   - Perform an airframe inspection.
   - Note any handling, performance or systems comments, pilot impressions and ground crew/telemetry issues.

## 8. Summary and Conclusions

The project's objective was to design a tailless supersonic airplane from preliminary concept to the detailed design of the R-UAV. There were several unique features about this year's design like implementation of thrust vectoring. Through the process of designing and building the airplane, students obtained the skills to use industry-level tools as well as the management skills required to propel a large and complex project with strict time constraints. This invaluable learning experience provided an opportunity for the students to understand the aerospace materials very deeply and what it is to be a professional.

# Appendix

## 8.1. Stability and Control

### *8.1.1. Airworthiness Requirements*

The following are the comprehensive airworthiness requirements dcumented toward the beginning of the design process.

#### 8.1.1.1. Geometric Guidelines

- Wing airfoil $t/c \geq 2.4\%$, outboard panel $t/c \geq 3.2\%$, inboard panel $t/c \leq 4.5\%$.
- Rear spar depth $\geq$ 2.75" full-scale or 1/10 of trailing-edge control surface chord.
- For canard and/or tail surface: $3.2\% < t/c < 4.5\%$ except at root which can be thicker or have a "fillet"
- 1°nose down < ground-roll pitch attitude < 3°nose up.
- Pitch- and roll- angle ground clearance $\geq 10°$, but must be sufficient to avoid frequent nacelle/wingtip damage or dragging the tail upon takeoff rotation.
- Nose gear position relative to airplane CG $\geq$ nose load ¿ 10% taxi gross weight for ground steering side-force (minimum of 5% if steering authority is verified by taxi tests), but must not exceed pitch-control limits for nosewheel liftoff at takeoff rotation.
- Fineness ratios: Minimum overall vehicle length $> 1.35 b_{wing}$ for reasonable supersonic drag, unless otherwise proven by analysis. Optimum is approximately 1.6-1.8 (and up to 3.0 for minimum sonic boom). Forebody fineness guideline as follows: length ahead of wing > 4 times maximum body diameter with max diameter near wing apex. Optimum is approximately 6-7 (much longer for minimum-sonic-boom designs).
- Wing loading: approximate full scale aircraft wing loading $\quad 50 \text{ psf} < W/S < 80 \text{ psf}$
- Wing sections having a leading-edge sweep more than 4°inside the Mach cone can use blunt leading-edged "supercritical" type subsonic airfoil shapes; wing sections having less sweep must use fighter type airfoils (F-16, etc.) scaled in $t/c$, with essentially sharp leading edges.
- If no other data is available to confirm a particular installation, assume a representative engine nozzle length for Mach 1.6-1.8 cruise is about 1.5 times the engine diameter. Assume a representative engine inlet length for Mach 1.6-1.8 cruise is about 2.5 times the engine diameter. S-duct inlets may need to have longer subsonic diffuser sections.

#### 8.1.1.2. V-N and Design Loads

- Design speeds and 'g' limits should be shown on a V-N diagram.
- Use at least one level more stringent in limit maneuver loads for the R-UAV than for the corresponding full-scale aircraft's mission (and not less than +3.8g/-1.5g ).

- For an R-UAV representing a bizjet/Mil Handling Qualities Class 2 aircraft, design to FAR "Utility Category" as a minumum, or 25.337(b) maneuver loads (without applying 3.8g maximum). E.g. use limit loads of +4.5g/ -2g.
- For representing 'fighter' or aerobatic full-scale aircraft types, design R-UAV to a limit load of 1.75 times FAR/Mil Spec full-scale aircraft and mission limit loads.
- Design to an ultimate load of 1.5 times the limit load if static proof article is tested to breaking. Design to an ultimate load of 1.7 times the limit load if the flight vehicle itself is static-test verified to 1.5g load. Design to an ultimate load of 2.25 times the limit load if no static test is conducted.
- Design to withstand a $15^{ft}/_{s}$ wind gust load at $V_{cruise}$.
- Assume $v_{dive}$ to be greater than 1.25 times the maxiumum level-flight speed.
- Confirm aircraft to be flutter-free up to $1.2v_{dive}$ using FEM analysis or simplified PD approximations.
- Design airframe to a 3g-limit-load vertical impact on landing gear.
- Design to 1g x MTOGW sideward and aft limit load on each main gear leg with a safety factor of 1.5.
- Design battery compartments and other safety critical items to at least a 9g longitudinal "crash landing" load without hazard (e.g. LiPo packs breaking free and being ejected from or pierced by structure).
- Key fittings, wing bolts, et cetera (non-break-away components) must be designed to safety factor of 5 on expected limit loads. Attachment of components to outboard wings/tips, or on extreme ends of the fuselage subject vibration, centrifugal loads, et cetera should be designed to local instantaneous loads of 14g (i.e. local surface/ attachments load is 14 times the winglet or other component's weight).

#### 8.1.1.3. Performance Requirements

- The critical conditions for R-UAV sizing will generally be endurance, climb gradient, approach speed, landing and takeoff distance, maximum liftoff speed, maximum level-flight speed, climbing turns, speed "undershoot" margin between takeoff or approach target speed and stall or loss of control.
- Define $V_{S1g}$ (effective 1g level-flight 'stall' speed) for airplane performance as based on maximum usable trimmed $c_L$ for each nominal flap/gear/C.G./weight combination. (By analysis this may be shown equivalent to one set of reference flight conditions at max takeoff, cruise and landing configurations if desired).
- Maximum usable $c_L$ is that for which pitching moment shows sustained pitch-up (unstable $\frac{\mathrm{d}c_M}{\mathrm{d}c_L}$ over a $c_L$ range greater than 10%), or when nose-down control is insufficient to produce rapid nose-down pitch recovery, or when yaw "nose slice", wing rock/roll-off lateraldirectional instability prevents controllable flight, orthe LCSP number indicates high-spin susceptibility with lateral control input.

- Minimum approach speed $V_{appr}$ = 1.23 $V_{S1g}$ (or minimum 5°$\alpha$ margin if pitch-up is severe and/or no $\alpha$-limiting/stick pusher, whichever is the more conservative for flight safety). Minimum operational approach speed is the sum of $V_{appr}$ and the expected wind-gust velocity.

- Minimum initial takeoff climb speed just after liftoff ($V_2$) is equal to1.15 $V_{S1g}$ (normal takeoff climb speed is faster than this: apprximately 1.35$V_{S1g}$).

- Landing distance (from 5 ft above runway) and takeoff distance (to 5 ft above runway) should be less than 400ft (subject to approval by the project pilot).

- Assume takeoff maximum zero-wind liftoff speed must be less than 45mph unless the tire/wheel speed limit tests indicate a higher value can be safely used.

- If $V_{appr}$ is less than 90% of the minimum-thrust-required velocity less than the mimimum-power-required velocity, then additional analysis or simulation should be done to show satisfactory "back-side" approach characteristics.

- Missed approach or "wave-off"; aircraft must be capable of going from 3°glideslope ($\gamma = -3°$) at 0.95$V_{appr}$ to 3°climb in approach or landing configuration at most adverse C.G. in less than 2.5 seconds (based on scaling of AFFDL-TR-78-154 handling qualities guidelines).

- Required design endurance is 7 minutes (normal mixed-throttle use "takeoff/climb/mild test maneuvers/descent/missed approach/land" mission profile). Check minimum endurance of 4.5 minutes for maximum overweight/high-drag/low-thrust situation. EDF battery weight versus capacity and power demand versus thrust setting can be used to define a virtual TSFC curve for EDF motors for sizing purposes, provided that range and endurance equations hold for $W_{initial} = W_{final}$.

- Installed net thrust (including duct losses and forward velocity-thrust 'lapse') must be sufficient to simulate the full-scale aircraft's climb gradient performance (SSBJ at MTOGW and normal thrust, gear-up, 18-20°climb gradient after takeoff)

- Minimum installed R-UAV static $\frac{T}{W}$ should be 1.1 times the static $\frac{T}{W}$ of full-scale aircraft MTOGW (assume a full-scale SSBJ maximum static $\frac{T}{W}$ of about 0.55 with no noise de-rate )

- Minimum idle thrust at $V_{appr}$ must provide a steady glide slope of 5°or steeper in landing configuration unless otherwise demonstrated as satisfactory by analysis or simulation.

- Thrust must be sufficient to maintain level flight at 1.2$V_{S1g}$ in gear-down landing flaps configuration with one engine shut down and windmilling.

- Thrust must be sufficient for a return-to-land maneuver immediately following takeoff: reduce thrust 20% and continue straight for 2 seconds after liftoff, then (still in takeoff configuration) initiate a 180°turn at a shallow (10-15°) bank angle, gaining a minimum of 25 ft altitude by a point abeam the point of takeoff rotation.

#### 8.1.1.4. Stability and Controls Requirements

- Adverse roll due to yaw control, or adverse yaw due to roll control, should be limited and able to be nulled-out by less than 15% deflection of the 'rudder' or 'aileron' command.
- The R-UAV must be able to hold a steady-state 'crab angle' of about 10°sideslip at alphas up to $c_L$ for $1.3V_{S1g}$ (assuming that operational approach and takeoff speeds for cross-wind conditions would be slightly higher than for zero-wind conditions), or by analysis sufficient for takeoff and approach in an 8mph direct 90°cross-wind (or 8mph vector component).
- Lateral-direction control authority must be sufficient to trim out imbalanced yaw forces due to a failed, windmilling engine on one side and maximum thrust on the opposite side at all speeds down to $V_2 = 1.15V_{S1g}$. If not, a loss-of-control speed floor must be declared for engine out conditions.
- Nose-down pitch-control authority at high angles of attack must be sufficient to produce a rotational acceleration of $8^{\circ}/s^2$ unless otherwise proven sufficient by simulation or analysis.
- Unless otherwise proven to be sufficient through analysis and simulation, nose-up pitch-control authority should be sufficient to:
  1. Rotate for takeoff using 2/3 of full stick/yoke travel at forward-limit C.G.
  2. Hold the nosewheel off the runway using full-aft stick/yoke on landing rollout until a speed equal to 50% of the approach speed.
  3. Quickly initiate a wave-off/ go-around maneuver on landing approach at minimum approach speed, full flap and most forward C.G.
- A minimum C.G. range of 6%MAC must be accomodated. Pitch-control authority must be sufficient to trim to $V_{S1g}$ in all flap/gear configurations, including thrust line effects, and using the preferred combination of pitch control effectors (elevator, elevons, canard, et cetera).
- Maximum roll-control authority shouldl be sufficient to bank in one second to 45°at $V_{appr}$ and to 70°at $V_{cruise}$. Alternatively, if all aspects of the R-UAV are "dynamically scaled" and operated at dynamically-similar inertias, then dynamic-scaling of the Mil Spec handling qualities' roll rates for Class-II aircraft types may be used.
- Static yaw stability of $\frac{\mathrm{d}c_n}{\mathrm{d}\beta} = 0.002^{1}/_{\circ}$ yaw is desired for small sideslip angles at values of $c_L$ up to $0.8V_{cruise}$, $\frac{\mathrm{d}c_n}{\mathrm{d}\beta}$ as low as 0.001 is acceptable if a yaw-damper (verified by testing and simulation) is also used. $\frac{\mathrm{d}c_n}{\mathrm{d}\beta}$ should be stable out to at least 10°sideslip up to at least $c_L$ up to that corresponding to $1.15V_{S1g}$ in takeoff configuration.
- Control surface motion commanded by yaw/pitch/roll dampers to aid dynamic stability should not exceed 15% of available throw in order to avoid 'saturation' in maneuver control situations unless additional testing or analysis proves otherwise.

- Minimum pitch-stability static margin of 6% should be maintained at speeds down to $1.15V_{S1g}$. Static margins as low as 1% may be permitted with artificially added pitch damping (pitch gyro) with sufficient confirmation from simulation or analysis. Zero and negative margins are not advised without a full-authority closed-loop control law and extensive simulation, analysis and testing. Aft-limit centers of gravity with 0% to -10% static margin may be assumed for the full-scale aircraft, which impacts gear location, et cetera.
- Analysis of classical short-period pitch, phugoid, Dutch roll, and spiral stability modes must be provided for selected angles of attack and operating configurations, with and without added damping/augmentation to ensure safety of flight.

### *8.1.2. Additional Trim Conditions*

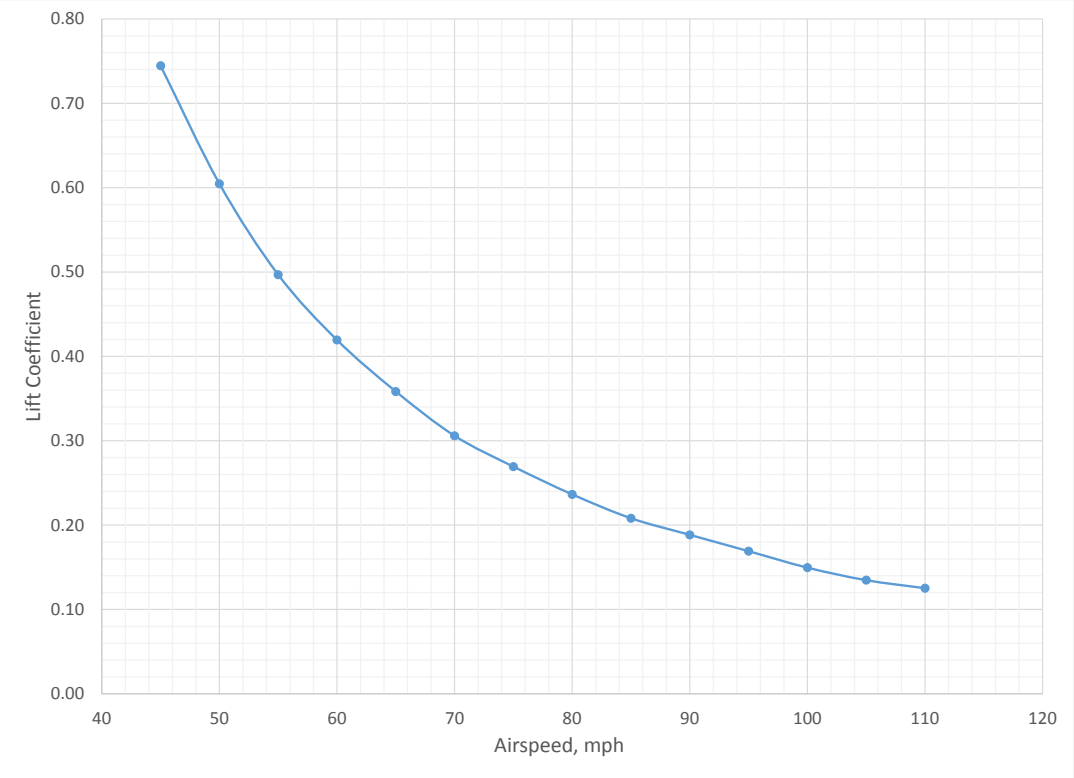


**Figure 8.1.1:** Trimmed lift coefficient versus airspeed.

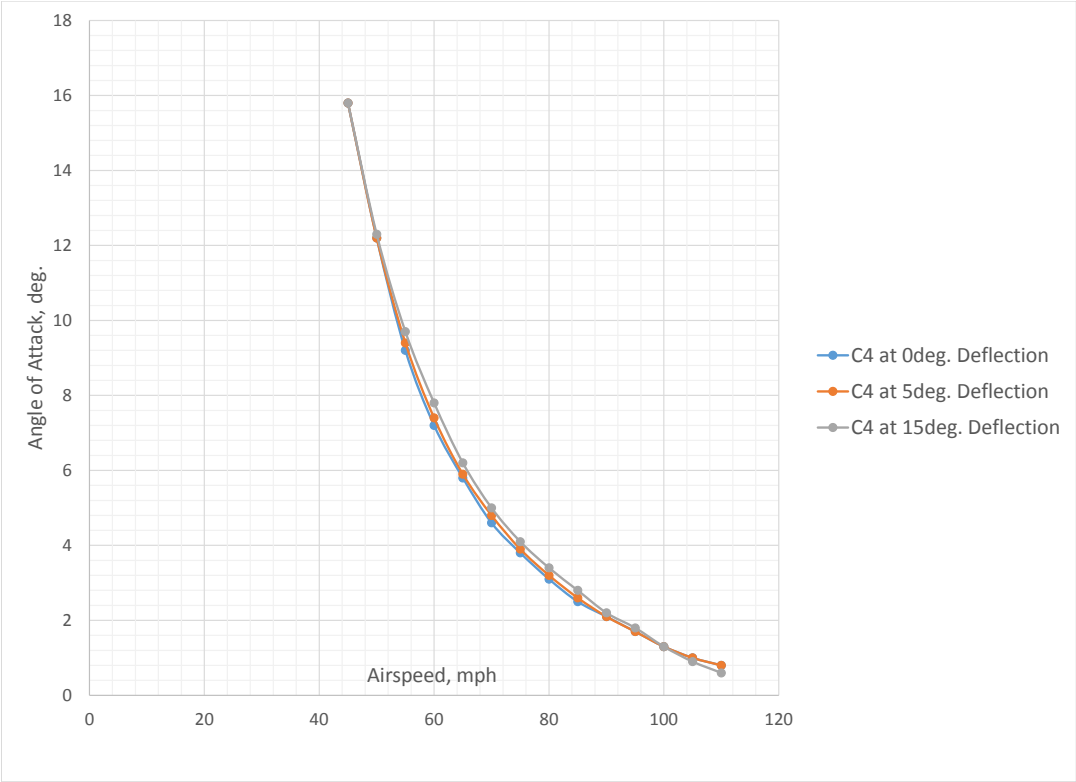


**Figure 8.1.2:** Trimmed angle of attack versus airspeed in a clean configuration.

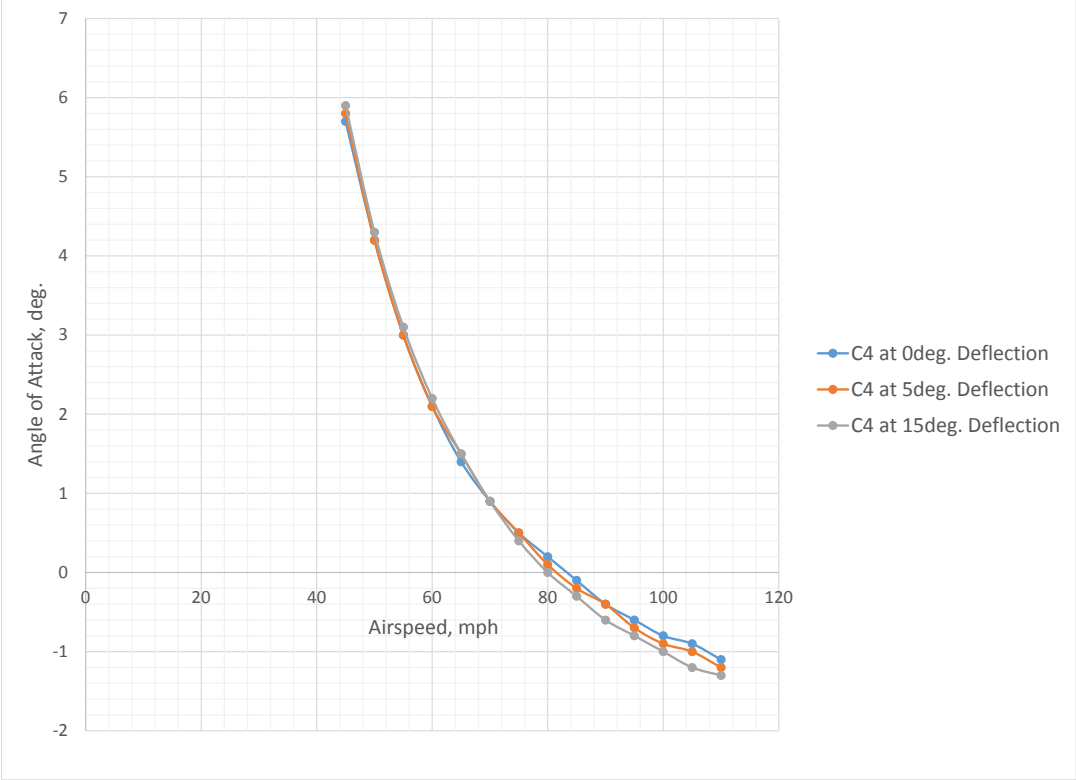


**Figure 8.1.3:** Trimmed angle of attack versus airspeed in a flaps-down configuration.

### *8.1.3. MATLAB Scripts*

```
function [ X, Z, M, Y, L, N] = DimensionalStabilityDerivative_Ver2...
    (c,b,S, m,  Q,Mach, V,Ix,Iy,Iz, ...
    CDset, CLset, Cmset, Clset, Cyset, Cnset,NumofLongCtrlSurface,...
    NumofLatCtrlSurface )
% This function takes the aircraft information, flight conditions, and
% demensionless stability derivatives and returns the dimensional stability
% derivatives

%% %%%%%%%%%%%%%% Detail of inputs %%%%%%%%%%%%%%%%%%%%%%%

% c----    chord length(ft)
% b----    wing span(ft)
% Q----    dynamic pressure(psf)
% Mach-    Mach Number
% S----    Wing Area(ft^2)
% m----    mass of the aircraft(slug)
% V----    speed(ft/s)
% Ix---    Moment of inertia about x-axis(slug-ft^2)
% Iy---    Moment of inertia about y-axis(slug-ft^2)
% Iz---    Moment of inertia about z-axis(slug-ft^2)
%
```

```
22 % CDset-  A vector containing CD derivatives (at least 5 by 1)
23 %           --          --
24 %          |CD;           |
25 %          |CD_M;         |
26 %          |CD_alpha;     |
27 %          |CD_alphadot;  |
28 %          |CD_q;         |
29 %          |CD_delta1;    |
30 %          |CD_delta2;    |
31 %          |CD_delta n;   |
32 %           --          --
33 % CLset-  A vector containing CL derivatives (at least 5 by 1)
34 %           --          --
35 %          |CL;           |
36 %          |CL_M;         |
37 %          |CL_alpha;     |
38 %          |CL_alphadot;  |
39 %          |CL_q;         |
40 %          |CL_delta1;    |
41 %          |CL_delta2;    |
42 %          |CL_delta n;   |
43 %           --          --
44 % Cmset-  A vector containing Cm derivatives (at least 4 by 1)
45 %           --          --
46 %          |Cm_M;         |
47 %          |Cm_alpha;     |
48 %          |Cm_alphadot;  |
49 %          |Cm_q;         |
50 %          |Cm_delta1;    |
51 %          |Cm_delta2;    |
52 %          |Cm_delta n;   |
53 %           --          --
54 % Clset-  A vector containing Cm derivatives (at least 3 by 1)
55 %           --          --
56 %          |Cl_beta;      |
57 %          |Cl_p;         |
58 %          |Cl_r;         |
59 %          |Cl_delta1;    |
60 %          |Cl_delta2;    |
61 %          |Cl_deltan;    |
62 %           --          --
63 % Cyset-  A vector containing Cm derivatives (at least 3 by 1)
64 %           --          --
65 %          |Cy_beta;      |
66 %          |Cy_p;         |
67 %          |Cy_r;         |
68 %          |Cy_delta1;    |
69 %          |Cy_delta2;    |
70 %          |Cy_deltan;    |
71 %           --          --
72 % Cnset-  A vector containing Cm derivatives (at least 3 by 1)
73 %           --          --
74 %          |Cn_beta;      |
75 %          |Cn_p;         |
76 %          |Cn_r;         |
77 %          |Cn_delta1;    |
78 %          |Cn_delta2;    |
79 %          |Cn_deltan;    |
80 %           --          --
81
82
83 % NumofLongCtrlSurface ---   Number of Longitudinal control surfaces
84 % NumofLatCtrlSurface  ---   Number of lateral control surfaces
85 %% %%%%%%%%%%%%%% Asserting input elements %%%%%%%%%%%%%%%%%%%%%%%%
86 assert(c>0,     'Chord length cannot be less than zero!')
87 assert(b>0,     'Span length cannot be less than zero!')
88 assert(S>0,     'Wing Area cannot be less than zero!')
89 assert(m>0,     'Mass cannot be less than zero!')
90 assert(Q>0,     'Dynamic Pressure cannot be less than zero!')
91 assert(Mach>=0, 'Mach Number cannot be less than zero!')
```

```
92  assert(V>0,     'Flight speed cannot be less than zero!')
93  assert(length(CDset)==5+NumofLongCtrlSurface,...
94      'CD set does not have the right number of inputs. It must be 5+Num of Long Ctrl Surface'
            )
95  assert(length(CLset)==5+NumofLongCtrlSurface,...
96      'CL set does not have the right number of inputs. It must be 5+Num of Long Ctrl Surface'
            )
97  assert(length(Cmset)==4+NumofLongCtrlSurface,...
98      'Cm set does not have the right number of inputs. It must be 4+Num of Long Ctrl Surface'
            )
99  assert(length(Clset)==3+NumofLatCtrlSurface,...
100     'Cl set does not have the right number of inputs. It must be 3+Num of Long Ctrl Surface'
            )
101 assert(length(Cyset)==3+NumofLatCtrlSurface,...
102     'Cy set does not have the right number of inputs. It must be 3+Num of Long Ctrl Surface'
            )
103 assert(length(Cnset)==3+NumofLatCtrlSurface,...
104     'Cn set does not have the right number of inputs. It must be 3+Num of Long Ctrl Surface'
            )
105 %% %%%%%%%%%%%%% Extracting variables from input matrix%%%%%%%%%
106
107 % CD(Coeff of drag) derivatives.
108 CD = CDset(1);
109 CD_M = CDset(2);
110 CD_alpha = CDset(3);
111 CD_alphadot = CDset(4);
112 CD_q = CDset(5);
113 CD_delta = zeros(NumofLongCtrlSurface,1); % Initialize ctrl surface derivatives
114 for n = 1:NumofLongCtrlSurface
115     CD_delta(n) = CDset(n+5);
116 end
117
118 % CL(Coeff of lift) derivatives.
119 CL = CLset(1);
120 CL_M = CLset(2);
121 CL_alpha = CLset(3);
122 CL_alphadot = CLset(4);
123 CL_q = CLset(5);
124 CL_delta = zeros(NumofLongCtrlSurface,1);
125 for n = 1:NumofLongCtrlSurface
126     CL_delta(n) = CLset(n+5);
127 end
128
129 % Cm(Coeff of moment) derivatives.
130 Cm_M = Cmset(1);
131 Cm_alpha = Cmset(2);
132 Cm_alphadot = Cmset(3);
133 Cm_q = Cmset(4);
134 Cm_delta = zeros(NumofLongCtrlSurface,1);
135 for n = 1:NumofLongCtrlSurface
136     Cm_delta(n) = Cmset(n+4);
137 end
138
139 % Cl(roll) derivatives.
140 Cl_beta = Clset(1);
141 Cl_p = Clset(2);
142 Cl_r = Clset(3);
143 Cl_delta = zeros(NumofLatCtrlSurface,1);
144 for n = 1:NumofLatCtrlSurface
145     Cl_delta(n) = Clset(n+3);
146 end
147
148 % Cn(yaw) derivatives.
149 Cn_beta = Cnset(1);
150 Cn_p = Cnset(2);
151 Cn_r = Cnset(3);
152 Cn_delta = zeros(NumofLatCtrlSurface,1);
153 for n = 1:NumofLatCtrlSurface
154     Cn_delta(n) = Cnset(n+3);
155 end
```

```
156
157 % Cy(side force) derivatives.
158 Cy_beta = Cyset(1);
159 Cy_p = Cyset(2);
160 Cy_r = Cyset(3);
161 Cy_delta = zeros(NumofLatCtrlSurface,1);
162 for n = 1:NumofLatCtrlSurface
163     Cy_delta(n) = Cyset(n+3);
164 end
165 %% %%%%%%%%%%%%% Calculating the dimensional stability derivatives%%%%%%%
166
167 % X directional
168 X.u = -Q*S/(m*V)*(2*CD + Mach * CD_M);
169 X.alpha = Q*S/m*(CL - CD_alpha);
170 X.alphadot = -Q*S/m*(c/(2*V))*CD_alphadot;
171 X.q = -Q*S*c/(m*2*V) * CD_q;
172 % for the control surfaces
173 for n = 1: NumofLongCtrlSurface;
174     X.delta(n) = -Q*S/m*CD_delta(n);
175 end
176
177 % Z directional
178 Z.u = -Q*S/(m*V)*(2*CL + Mach * CL_M);
179 Z.alpha = -Q*S/m*(CD + CL_alpha);
180 Z.alphadot = -Q*S/m*(c/(2*V))*CL_alphadot;
181 Z.q = -Q*S*c/(m*2*V) * CL_q;
182 for n = 1: NumofLongCtrlSurface;
183     Z.delta(n) = -Q*S/m*CL_delta(n);
184 end
185
186 % Pitch
187 M.u = Q*S*c/Iy/V*Mach*Cm_M;
188 M.alpha = Q*S*c/Iy*Cm_alpha;
189 M.alphadot = Q*S*c/Iy*c/(2*V)*Cm_alphadot;
190 M.q = Q*S*c/Iy*c/(2*V)*Cm_q;
191 for n = 1: NumofLongCtrlSurface;
192     M.delta(n) = Q*S*c/Iy*Cm_delta(n);
193 end
194
195 % Y directional
196 Y.beta = Q*S/m*Cy_beta;
197 Y.p = Q*S/m*b/(2*V)*Cy_p;
198 Y.r = Q*S*b/m/(2*V)*Cy_r;
199 for n = 1: NumofLatCtrlSurface;
200     Y.delta(n) = Q*S/m*Cy_delta(n);
201 end
202
203 % Roll
204 L.beta = Q*S*b/Ix*Cl_beta;
205 L.p = Q*S*b/Ix*b/(2*V)*Cl_p;
206 L.r = Q*S*b/Ix*b/(2*V)*Cl_r;
207 for n = 1: NumofLatCtrlSurface;
208     L.delta(n) = Q*S*b/Ix*Cl_delta(n);
209 end
210
211 % Yaw
212 N.beta = Q*S*b/Iz*Cn_beta;
213 N.p = Q*S*b/Iz*b/(2*V)*Cn_p;
214 N.r = Q*S*b/Iz*b/(2*V)*Cn_r;
215 for n = 1: NumofLatCtrlSurface;
216     N.delta(n) = Q*S*b/Iz*Cn_delta(n);
217 end
218
219 end
```

```
1 function [ An, In, Bn, A, B] = FindLongitudinalStateMatrix_Ver2...
2     ( V,theta , X, Z, M )
3 % This function takes flight velocity, flight path angle, and dimensional
4 % stability derivatives(X, Z, M) which are in structure form. This function
5 % returns the raw state space matrix and the right state space derivatives.
```

```
6
7  %% Deltai of Inputs:
8  %           V---    Velocity
9  %           X---    X direction derivatives in structure form
10 %           Z---    Z direction derivatives in structure form
11 %           M---    Moment derivatives in structure form
12 %           theta-  Flight path angle
13
14 %% Asserting inputs.
15 if size(X.delta)~=size(Z.delta)
16     display('There is discrepancies in number of control surfaces')
17 elseif size(X.delta)~=size(M.delta)
18     display('There is discrepancies in number of control surfaces')
19 elseif size(M.delta)~=size(Z.delta)
20     display('There is discrepancies in number of control surfaces')
21 else
22 % Gravitational Acceleration
23 g = 32.2; %(ft/s^2)
24
25 % Defining In matrix
26 In = [V          0          0          0;
27       0      V-Z.alphadot   0          0;
28       0      -M.alphadot    1          0;
29       0          0          0          1;];
30
31 % Defining An matrix
32 An = [V*X.u      X.alpha      0       -g*cos(theta);
33     V*Z.u        Z.alpha    (V+Z.q)       -g*sin(theta);
34     V*M.u        M.alpha     M.q           0;
35     0            0           1             0];
36
37 % Defining Bn matrix
38 NumofCtrlSurface = length(X.delta);
39 Bn = zeros(4,NumofCtrlSurface); % Initialize Bn
40 for n = 1:NumofCtrlSurface;
41     Bn(1,n) = X.delta(n);
42     Bn(2,n) = Z.delta(n);
43     Bn(3,n) = M.delta(n);
44     Bn(4,n) = 0;
45 end
46
47 % Calculating the state matrices, A and B.
48 A = In\An;
49 B = In\Bn;
50 end
51
52 end
```

```
1  function [  An, Bn,In, A, B] = FindLateralStateMatrix_Ver2...
2      ( V, theta, Ixx, Izz, Ixz, Y, L, N)
3  % This function takes flight velocity, flight path angle, moment of inertia
4  % about x axis, moment of symmetry about xz, and lateral dimensional
5  % derivatives(Y,L,N). This function returns the raw state space matrices
6  % An, Bn, and Im, and the modified state space matirces A and B.
7
8  %% Detail of Inputs:
9  %           V---    Flight velocity
10 %           theta-- Flight path angle
11 %           Ixx-    Moment of inertia about x axis
12 %           Ixz-    Inertia of Symmetry
13 %           Y---    Y direction derivatives in structure form
14 %           L---    L(lift) derivatives in structure form
15 %           N---    N derivatives in structure form
16
17 %% asserting input elements
18 if size(Y.delta)~=size(L.delta)
19     display('There is discrepancy in number of control surfaces')
20 elseif size(Y.delta)~=size(N.delta)
21     display('There is discrepancy in number of control surfaces')
22 elseif size(L.delta)~=size(N.delta)
```

```
    display('There is discrepancy in number of control surfaces')
else
g = 32.2;
% Defining In matrix
In = [V      0        0        0;
      0      1        0   (-Ixz/Ixx);
      0      0        1        0;
      0  (-Ixz/Izz)  0        1;];

% Defining An matrix
An = [Y.beta     Y.p      g*cos(theta)     (Y.r-V);
      L.beta     L.p          0              L.r;
      0          1            0               0;
      N.beta     N.p          0              N.r];


NumofCtrlSurface = length(Y.delta);
% Defining Bn matrix
Bn = zeros(4,NumofCtrlSurface); % Initialize Bn
for n = 1:NumofCtrlSurface;
    Bn(1,n) = Y.delta(n);
    Bn(2,n) = L.delta(n);
    Bn(3,n) = 0;
    Bn(4,n) = N.delta(n);
end

A = In\An;
B = In\Bn;

end
end
```

```
function [CD_Dynamic, CL_Dynamic, Cm_Dynamic, Cy_Dynamic,Cl_Dynamic,Cn_Dynamic] =
    Dynamic_Derivative_Generator_Tailess(S, Weight, MAC, b,I_x,I_y,I_z,I_xy, v,UseWinglets,
    Angle)
% Calculate the Lateral Dynamic Derivatives Based Off Of Schmidt Equations.
% Basic Approximations
% need to update moments of inertia with more accurate numbers
%% Variable Definitions
% q: Dynamic Pressure (psf)
% S: Reference Area (ft^2)
% v: Freestream (infinity) velocity (ft/s)
% m: Mass (slugs)
% b: Wing Total Span (ft)
% z_v: Vertical distance of center of pressure of vertical tail from the x-axis
% l_v: Distance from Aircraft C.G. to Vertical Tail C.G. (ft)
% l_h: Distance from Aircraft C.G. to Horizontal Tail C.G. (ft)
% delta_c_l: Wing Sectional Lift Coefficient Spanwise Variation Due to Differences in Angle
    of Attack with Lateral Location on Wing
% eta: Dimensinoless Lateral Dimension, (2y/b)
% c: Wing Chord Length (ft)
% I_x: Moment of Inertia About the x-axis (slug*ft^2)
% I_y: Moment of Inertia About the y-axis (slug*ft^2)
% I_z: Moment of Inertia About the z-axis (slug*ft^2)
% C_L: Wing lift coefficient
% epsilon_alpha: Downwash angle on the horizontal tail
%% Inputs

    % Leave as 'true' if you want the calculation to use winglets,
                            % change to 'false' if you don't
q = 1/2*0.0023769*v^2;
m = Weight/32.2;
z_v = 5.7/12;               % assuming cg located 1" up from origin
l_v = 30/12;
l_h = 33/12;
l_c = -46/12;               % may need to update (based on Canard 2?)
l_w = 21/12;
S_Htail = 106/144;
S_Canard = 20/144;          % may need to update (based on Canard 2?)
S_Vtail = 0;
```

```
S_Winglet = 12/144;          % may need to update
I_xz = 0         *0.0685217659*3.28084^2; % assumed to be zero?
% Wing Dimensions
root_chord = 51/12;
crank_chord = 15/12;
tip_chord = 4/12;
inboard_span = 13.9/12;
outboard_span = 14.1/12;

switch Angle
%% Given Inputs at Alpha = 3 degrees, using CG = 20% MAC
    case 3
% Derivatives from wind tunnel
C_y_beta = -0.28993634;              % From General Derivatives
C_l_beta = -0.045064921;         % From General Derivatives
C_n_beta =  -0.006023219;        % From General Derivatives
C_L_alpha_vtail =0;  % Lift slope of vertical tail
% Roll Derivative of tail and winglet
%C_L_alpha_vtail = 0.19623*S/S_Vtail;   % Lift slope of vertical tail, normalized to the
    tail area,
%C_L_alpha_winglets =  0.121878553428090*S/4/S_Winglet; %Based on run 144 and 169,
    normalized to the winglet area

% Lift coefficient and lift Slope
C_L          = 0.2289;               % From General Derivatives
CL_alpha     = 2.8781;

% lateral control
C_y_delta =  0.07793;        % From General Derivatives
C_l_delta = -0.00509;        % From General Derivatives
C_n_delta = -0.02362;        % From General Derivatives

% longitudinal control
V_Htail = (S_Htail/S)*(l_h/MAC);
C_L_Htail = 0.35347*S/S_Htail;       % From General Derivatives
C_D_Htail = 0.03093*S/S_Htail;       % From htail derivatives
V_Canard = (S_Canard/S)*(l_c/MAC);
C_L_Canard = -0.03777*S/S_Canard;    % From General Derivatives
C_D_Canard = 0.01997*S/S_Canard;     % From General Derivatives


epsilon_alpha = 0.522842*pi/180;         % Downwash angle on the horizontal tail

if UseWinglets == false
    C_L_alpha_winglets = 0;
end


%% Given Inputs at Alpha = 12 degrees, using CG = 20% MAC
    case 17.3
% Derivatives from wind tunnel
C_y_beta = 0.182858943;          % From General Derivatives
C_l_beta = -0.117151427;         % From General Derivatives
C_n_beta =  0.134857792;         % From General Derivatives

% Roll Derivative of tail
C_L_alpha_vtail = 0.19623;  % Lift slope of vertical tail
C_L_alpha_winglets = -0.00989*S/(4*S_Winglet);

% Lift Slope
C_L = 0.8479;
CL_alpha = 2.24330;              % From General Derivatives

% lateral control (winglets)
C_y_delta =  0.05147;        % From General Derivatives
C_l_delta =  0.00782;        % From General Derivatives
C_n_delta = -0.00989;        % From General Derivatives

% longitudinal control
V_Htail = (S_Htail/S)*(l_h/MAC);
```

```
104 C_L_Htail = 0.32972*S/S_Htail;       % From htail derivatives
105 C_D_Htail = -0.02700*S/S_Htail;      % From General Derivatives
106 V_Canard = (S_Canard/S)*(l_c/MAC);
107 C_L_Canard = -0.00067*S/S_Canard;    % From General Derivatives
108 C_D_Canard = 0.03342*S/S_Canard;     % From General Derivatives
109
110 epsilon_alpha = -2.14867*pi/180;        % Downwash angle on the horizontal tail
111
112 if UseWinglets == false
113     C_L_alpha_winglets = 0;
114 end
115
116 %
117     otherwise
118         display('Angle is not recognized')
119 end
120 %% Derivatives Due to Beta (side-slip)
121
122 % Dimensionless Lateral Control Derivatives
123 % Given from Wind Tunnel Test Data
124
125 % Dimensional Derivatives
126 Y_beta = ((q*S)/m)*C_y_beta;                          % Dimensional Side Force Coeff. Due to
        Side-slip Angle, Beta
127 L_beta = ((q*S*b)/I_x)*C_l_beta;                      % Dimensional Roll Moment Coeff. Due to
        Side-slip Angle, Beta
128 N_beta = ((q*S*b)/I_z)*C_n_beta;                      % Dimensional Yaw Moment Coeff. Due to
        Side-slip Angle, Beta
129
130 %% Dimensional Roll Derivatives Due to Yaw Rate r
131
132 % Dimensionless Yaw Damping Derivatives
133 C_y_r = 2*l_v/b*C_L_alpha_vtail*S_Vtail/S + 2*l_w/b*C_L_alpha_winglets*4*S_Winglet/S %
        Dimensionless Coefficient, Side Force wrt Yaw Rate, ignoring negligible wing
        contribution
134
135
136 C_l_r = -((z_v)/b)*C_y_r + (C_L/4)                   % Dimensionless Coefficient, Roll Moment
        wrt Yaw Rate
137 C_n_r = -(l_v/b)*(C_y_r)                             % Dimensionless Coefficient, Yaw Damping
        Term wrt Yaw Rate, ignoring negligible wing contribution
138
139 % Dimensional Roll Damping Stability Derivatives Due to Yaw Rate, r
140 Y_r = ((q*S)/m)*(b/(2*v))*C_y_r                       % Dimensional Side Force Coeff. Due to
        Yaw Rate, r
141 L_r = ((q*S*b)/I_x)*(b/(2*v))*C_l_r                  % Dimensional Roll Moment Coeff. Due to
        Yaw Rate, r
142 N_r = ((q*S*b)/I_z)*(b/(2*v))*C_n_r                  % Dimensional Yaw Moment Coeff. Due to
        Yaw Rate, r
143
144
145 %% Dimensional Roll Derivatives Due to Roll Rate p
146
147 % equations for estimation of roll damping derivative using elementary wing strip theory
148 % eta_1 = 0:(inboard_span/(b/2))/100:inboard_span/(b/2);
149 % eta_2 = inboard_span/(b/2):(1-inboard_span/(b/2))/100:1;
150 % integrand_1 = zeros(1,101);
151 % integrand_2 = zeros(1,101);
152 % for i=1:101
153 %     integrand_1(i) = 2*C_L*(root_chord - crank_chord/root_chord*inboard_span*eta_1(i)/2)*
        eta_1(i)^2;
154 %     integrand_2(i) = 2*C_L*(crank_chord - tip_chord/crank_chord*outboard_span*eta_2(i)/2)*
        eta_2(i)^2;
155 % end
156 % int_1 = trapz(eta_1,integrand_1);
157 % int_2 = trapz(eta_2,integrand_2);
158
159 eta_1 = 0:(inboard_span/(b/2))/100:inboard_span/(b/2); % inboard section, into 100 pieces
160 eta_2 = inboard_span/(b/2):(1-inboard_span/(b/2))/100:1;% outboard section, into 100 pieces
161
```

```
Inboard_Y   = (crank_chord - root_chord);
Inboard_X   = (inboard_span)/(0.5*b);
Inboard_Slope = Inboard_Y/Inboard_X;

Outboard_Y  = (tip_chord - crank_chord);
Outboard_X  = 1-(inboard_span)/(0.5*b);
Outboard_Slope = Outboard_Y/Outboard_X;

for i = 1:101;
        chord_in(i)    = Inboard_Slope*eta_1(i) + root_chord;
        chord_out(i)   = Outboard_Slope*(eta_2(i)-inboard_span/(b*0.5))+crank_chord;
        integrand_1(i) = CL_alpha*chord_in(i)*(eta_1(i))^2;
        integrand_2(i) = CL_alpha*chord_out(i)*(eta_2(i))^2;
end
int_1 = trapz(eta_1,integrand_1);
int_2 = trapz(eta_2,integrand_2);

% Dimensionless Roll Damping Derivatives
C_y_p = 0;                                          % Value of zero by assumption
C_l_p = -b/2/S*(int_1 + int_2);                     % Dimensionless Coefficient, Roll Moment wrt Roll Rate (This uses elementary wing strip theory)
C_n_p = -(C_L/8);                                   % Dimensionless Coefficient, Yaw Damping Term wrt Roll Rate, ignoring negligible wing contribution

% Dimensional Roll Damping Stability Derivatives Due to Roll Rate, p
Y_p = 0;                                            % Dimensional Side Force Coeff. Due to Roll Rate, p
L_p = ((q*S*b)/I_x)*(b/(2*v))*C_l_p;                % Dimensional Roll Moment Coeff. Due to Roll Rate, p
N_p = ((q*S*b)/I_z)*(b/(2*v))*C_n_p;                % Dimensional Yaw Moment Coeff. Due to Roll Rate, p


%% Derivatives Due to Lateral Control

% Dimensionless Lateral Control Derivatives
% Given from Wind Tunnel Test Data

% Dimensional Derivatives Due to Lateral Control
Y_delta = ((q*S)/m)*C_y_delta;                      % Dimensional Side Force Coeff. Due to Control Surface Deflection
L_delta = ((q*S*b)/I_x)*C_l_delta;                  % Dimensional Roll Moment Coeff. Due to Control Surface Deflection
N_delta = ((q*S*b)/I_z)*C_n_delta;                  % Dimensional Yaw Moment Coeff. Due to Control Surface Deflection


%% Derivative due to Pitch Rate, q

C_D_q = 2.20*(V_Htail*C_D_Htail-V_Canard*C_D_Canard);          % Dimensionless Drag Force Coeff. Due to Horizontal Tail
C_L_q = 2.20*(V_Htail*C_L_Htail-V_Canard*C_L_Canard);          % Dimensionless Lift Force Coeff. Due to Horizontal Tail
C_m_q = -2.20*(V_Htail*l_h*C_L_Htail+V_Canard*l_c*C_L_Canard); % Dimensionless Pitch moment Coeff. Due to Horizontal Tail

X_q = -q*S/m*(MAC/(2*v))*C_D_q;                                % Dimensional Drag Coeff. Due to Pitch Rate
Z_q = -q*S/m*(MAC/(2*v))*C_L_q;                                % Dimensional Lift Coeff. Due to Pitch Rate
M_q = q*S*MAC/I_y*(MAC/(2*v))*C_m_q;                           % Dimensional Pitch Moment Coeff. Due to Pitch Rate

%% Derivatives due to alpha dot

C_D_alpha_dot = 2.20*(V_Htail*epsilon_alpha*C_D_Htail-V_Canard*C_D_Canard);          % Dimensionless Drag Force Coeff. Due to Horizontal Tail
C_L_alpha_dot = 2.20*(V_Htail*epsilon_alpha*C_L_Htail-V_Canard*C_L_Canard);          % Dimensionless Lift Force Coeff. Due to Horizontal Tail
```

```
C_m_alpha_dot = -2.20*(V_Htail*epsilon_alpha*l_h*C_L_Htail+V_Canard*l_c*C_L_Canard);    % Dimensionless Pitch Moment Coeff. Due to Horizontal Tail

X_alpha_dot = -q*S/m*(MAC/(2*v))*C_D_alpha_dot;              % Dimensional Drag Force Coeff. Due to AoA Rate
Z_alpha_dot = -q*S/m*(MAC/(2*v))*C_L_alpha_dot;              % Dimensional Lift Force Coeff. Due to AoA Rate
M_alpha_dot = q*S*MAC/I_y*(MAC/(2*v))*C_m_alpha_dot;         % Dimensional Pitch Moment Coeff. Due to AoA Rate

CD_Dynamic.q             = C_D_q;
CD_Dynamic.alpha_dot     = C_D_alpha_dot;

CL_Dynamic.q             = C_L_q;
CL_Dynamic.alpha_dot     = C_L_alpha_dot;

Cm_Dynamic.q             = C_m_q;
Cm_Dynamic.alpha_dot     = C_m_alpha_dot;

Cy_Dynamic.p = C_y_p;
Cy_Dynamic.r = C_y_r;

Cl_Dynamic.p = C_l_p;
Cl_Dynamic.r = C_l_r;

Cn_Dynamic.p = C_n_p;
Cn_Dynamic.r = C_n_r;
end
```

#### 8.1.3.1. Files related to state space model

#### 8.1.3.2. Trim Condition Interpolator

```
clear all

% For both canard configurations and either 0deg. or 15deg. deflection (specified), this code calculates all of the trim
% coefficients and necessary stabilator deflection for a handful of
% airspeeds.

tic

% TRIM INPUTS ("TRIMPUTS")


%for vmph = 45:5:110
for vmph=80

C = 4; % canard configuration (either 2 or 4)
v = vmph/0.681818; % airspeed, ft/s
deltaC = 15; % canard deflection, enter either 15 or 0
flaps = 0; % 1 for flaps-down config.; 0 for clean config.

% GEOMETRY

W = 32; % weight, lbs
T = 22; % thrust, lbs
s = 8.296; % wing area, ft^2
rho = 0.0023769; % slug/ft^3

% take the H data for different deflections, interpolate over a range of
% deflection angles, interpolate over a range of alpha
dataH(:,:,1) = csvread('run_0094.csv',1,0);
dataH(:,:,2) = csvread('run_0097.csv',1,0);
dataH(:,:,3) = csvread('run_0091.csv',1,0);
dataH(:,:,4) = csvread('run_0100.csv',1,0);
dataH(:,:,5) = csvread('run_0103.csv',1,0);
% 1st index AOA, 2nd index data type, 3rd index deflection
delta_test = [-15 -5 0 5 15]';
delta_range = [-20:0.1:20]';
for i = 1:23
```

```
38      for j = 1:49
39          data_per_delta = dataH(i,j,:);
40          data_over_range = spline(delta_test,data_per_delta,delta_range);
41          dataHdeltainterp(i,j,:) = data_over_range;
42      end
43  end
44
45
46  % interpolate over alpha
47
48  alpha_range = [-10:0.1:35]';
49
50  for k = 1:length(delta_range)
51   alpha_test = dataHdeltainterp(:,4,k);
52      for j = 1:49
53          data_per_alpha = dataHdeltainterp(:,j,k);
54          data_over_range = spline(alpha_test,data_per_alpha,alpha_range);
55          dataHinterp(:,j,k) = data_over_range;
56          dataHinterp(:,1,k) = alpha_range;
57      end
58  end
59
60  % subtract zero-deflection values
61
62  zero_deflection_dataH(:,:,1) = dataHinterp(:,:,find(delta_range==0));
63  for k = 1:length(delta_range)
64      dataHinterp(:,5:43,k) = dataHinterp(:,5:43,k)-zero_deflection_dataH(:,5:43,1);
65  end
66
67
68  %-------------------------------------------------------------------------
69  % Add flap contribution (does not take into consideration flap effect on
70  % effective stabilator deflection
71
72  flaps_data = csvread('flaps_down10.csv',1,0);
73  % FLAPS Columns: AOA | CDSA | CLSA |CLBA | CMSA15 | CMSA20 | CNSA15 | CNSA20
74
75  % interpolate over alpha
76
77   alpha_test = flaps_data(:,1);
78      for i = 2:size(flaps_data,2)
79          data_per_alpha = flaps_data(:,i);
80          data_over_range = spline(alpha_test,data_per_alpha,alpha_range);
81          flaps_data_interp(:,i) = data_over_range;
82      end
83      flaps_data_interp(:,1) = alpha_range;
84
85  % Add
86
87  if flaps == 1
88
89  for i = 1:size(dataHinterp,3)
90  dataHinterp(:,9,i) = dataHinterp(:,9,i)+flaps_data_interp(:,2); % CDSA
91  dataHinterp(:,11,i) = dataHinterp(:,11,i)+flaps_data_interp(:,3); % CLSA
92  dataHinterp(:,12,i) = dataHinterp(:,12,i)+flaps_data_interp(:,4); % CLBA
93  dataHinterp(:,15,i) = dataHinterp(:,15,i)+flaps_data_interp(:,5); % CMSA15
94  dataHinterp(:,17,i) = dataHinterp(:,17,i)+flaps_data_interp(:,6); % CMSA20
95  end
96
97  end
98  %-------------------------------------------------------------------------
99
100 if C == 4
101
102 dataC(:,:,1) = csvread('run_0116.csv',1,0); % 0 deg. Deflection
103 %dataC(:,:,2) = csvread('canardC4_5.csv',1,0); % 5 deg. Deflection
104 %dataC(:,:,2) = csvread('run_0119.csv',1,0); % 15 deg. Deflection
105 dataC(:,:,2) = csvread('run_0107.csv',1,0); % -30 deg. Deflection
106
107 elseif C == 2
```

```
108
109 dataC(:,:,1) = csvread('run_0212.csv',1,0);
110 dataC(:,:,2) = csvread('canardC2_15.csv',1,0);
111
112 end
113
114 for k = 1:2
115  alpha_test = dataC(:,4,k);
116     for j = 1:49
117         data_per_alpha = dataC(:,j,k);
118         data_over_range = spline(alpha_test,data_per_alpha,alpha_range);
119         dataCinterp(:,j,k) = data_over_range;
120         dataCinterp(:,1,k) = alpha_range;
121     end
122 end
123
124 dataC_0 = repmat(dataCinterp(:,:,1),1,1,length(delta_range));
125 dataC_15 = repmat(dataCinterp(:,:,2),1,1,length(delta_range));
126 data_H2_C_0 = dataC_0;
127 data_H2_C_0(:,5:43,:) = data_H2_C_0(:,5:43,:) + dataHinterp(:,5:43,:);
128 data_H2_C_15 = dataC_15;
129 data_H2_C_15(:,5:43,:) = data_H2_C_15(:,5:43,:) + dataHinterp(:,5:43,:);
130 Fdata_H2_C_15_CMSA18 = squeeze(data_H2_C_15(:,17,:)-0.02*data_H2_C_15(:,12,:));
131
132
133 % Find which data (per 3rd index) is trimmed (cM=0), for a given cL
134 % For each deflection (index 3), find the cL that is closest to the
135 % prescribed trimmed cL. Retain the row corresponding to that cL (eliminate
136 % the 1st dimension).
137
138 cL = 2*W/(rho*s*v^2); % required cL for trim
139
140 if deltaC == 15
141
142 for i = 1:length(delta_range)
143
144 cLindex = find(abs(squeeze(data_H2_C_15(:,11,i))-cL)==min(abs(squeeze(data_H2_C_15(:,11,i))-
        cL))); % find the index of the CLSA that is closest to the needed cL
145 ForceEq_data(:,i) = squeeze(data_H2_C_15(cLindex,:,i));
146
147 end
148
149 else
150
151 for i = 1:length(delta_range)
152
153 cLindex = find(abs(squeeze(data_H2_C_0(:,11,i))-cL)==min(abs(squeeze(data_H2_C_0(:,11,i))-cL
        )));
154 ForceEq_data(:,i) = squeeze(data_H2_C_0(cLindex,:,i));
155
156 end
157
158 end
159
160 ForceEq_data=ForceEq_data';
161
162 % 1st index is data type, 2nd index is deflection
163 % Pull out the deflection for which CMSA15 is closest to 0
164 ForceEq_data_CMSA18 = ForceEq_data(:,17)-0.02*ForceEq_data(:,12);
165 trimdex = find(abs(ForceEq_data_CMSA18)==min(abs(ForceEq_data_CMSA18)));
166 if length(trimdex)>1
167   trimdex = trimdex(end); % If there's more than one stabilator deflection that works, use
        the last one
168 end
169 deltaH = delta_range(trimdex);
170 trimconditions = ForceEq_data(trimdex,:);
171 ALPHA = trimconditions(4);
172 CLSA = trimconditions(11);
173 CDSA = trimconditions(9);
174 CMSA18 = trimconditions(17)-0.02*trimconditions(12);
```

```
LOD = CLSA/CDSA;
gamma = real(asind(T/W-1/LOD));
table(C,vmph,cL,deltaH,deltaC,ALPHA,CLSA,CDSA,CMSA18,LOD,gamma)
trimpoints((vmph-35)/5,:) = [C vmph cL deltaH deltaC ALPHA CLSA CDSA CMSA18 LOD gamma];
%clearvars -except trimpoints Fdata_H2_C_15_CMSA18

toc

end

toc
```

### *8.1.4. Appendix: Wind Tunnel Data*

#### 8.1.4.1. Dynamic Pressure Runs

Runs were done with the wing-body combination at different dynamic pressures to confirm that the aerodynamics around the aircraft do not display a significant dependency on dynamic pressure and, by extension, Reynolds number.

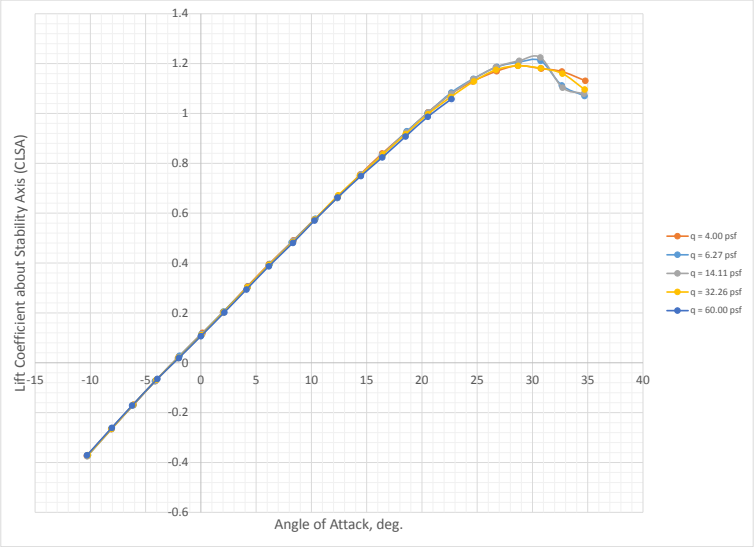


**Figure 8.1.4:** Lift coefficient as a function of angle of attack $\alpha$.

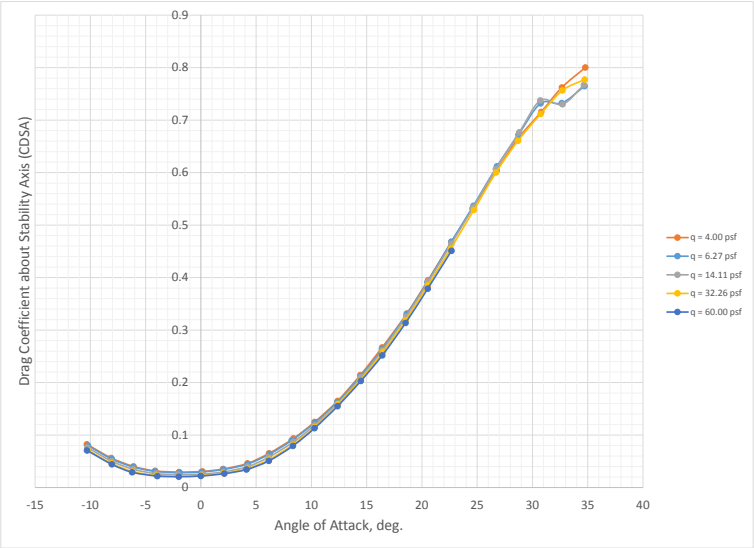


**Figure 8.1.5:** Drag coefficient as a function of angle of attack $\alpha$.

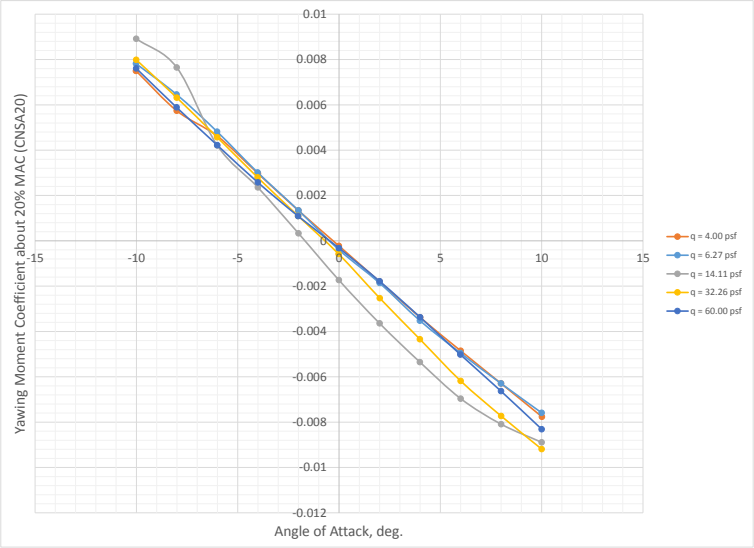


**Figure 8.1.6:** Yawing moment coefficient as a function of sideslip angle $\beta$.

#### 8.1.4.2. Final Configuration Pitch Runs

The following are $\alpha$-sweep runs for the final configuration with zero control deflections.

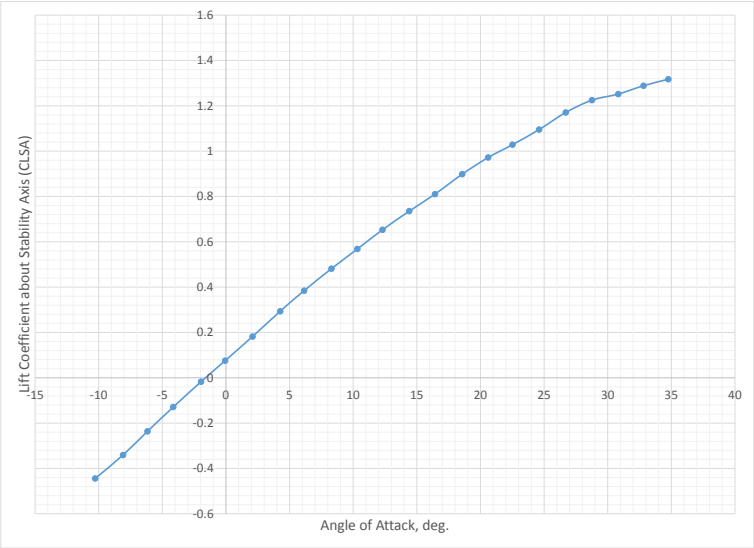


**Figure 8.1.7:** Lift coefficient about the stability axis as a function of angle of attack $\alpha$.

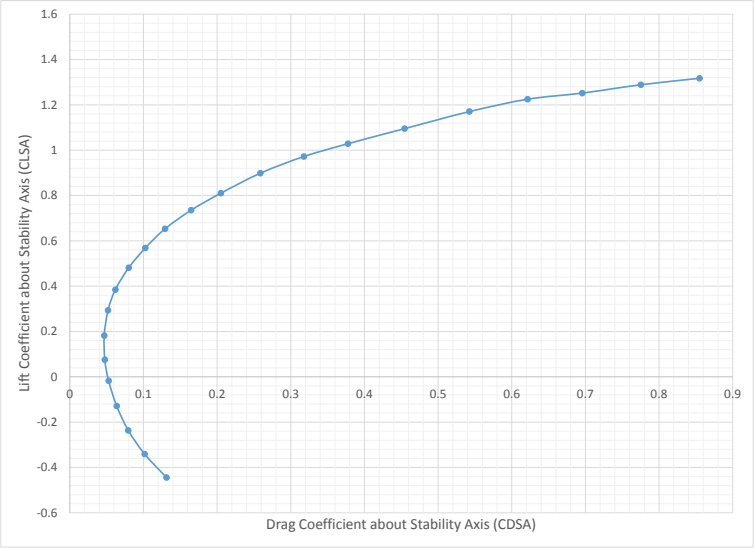


**Figure 8.1.8:** Drag polar about the stability axis.

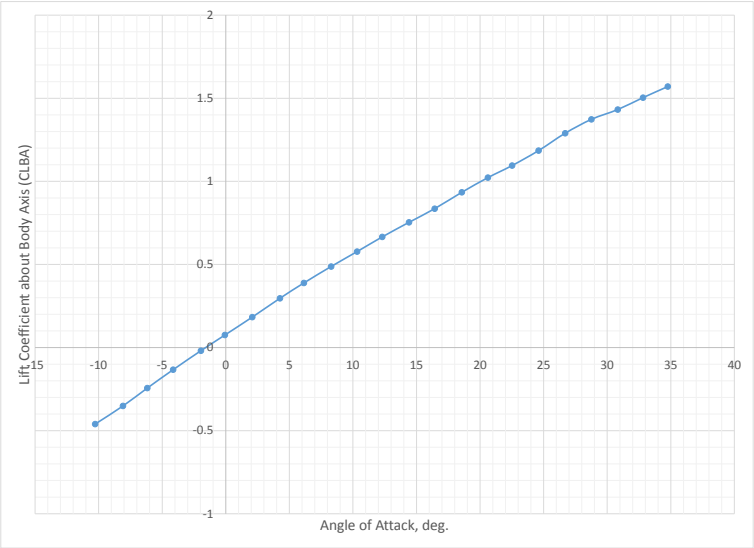


**Figure 8.1.9:** Lift coefficient about the body axis as a function of angle of attack $\alpha$.

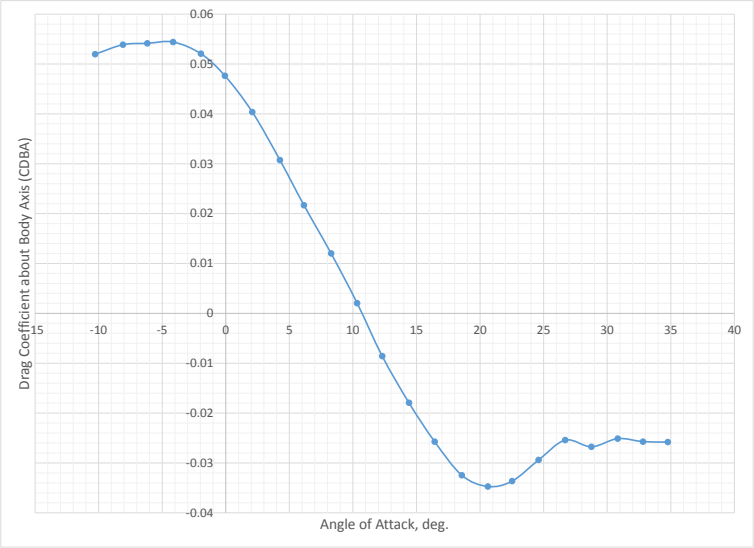


**Figure 8.1.10:** Drag coefficient about the body axis as a function of angle of attack $\alpha$.

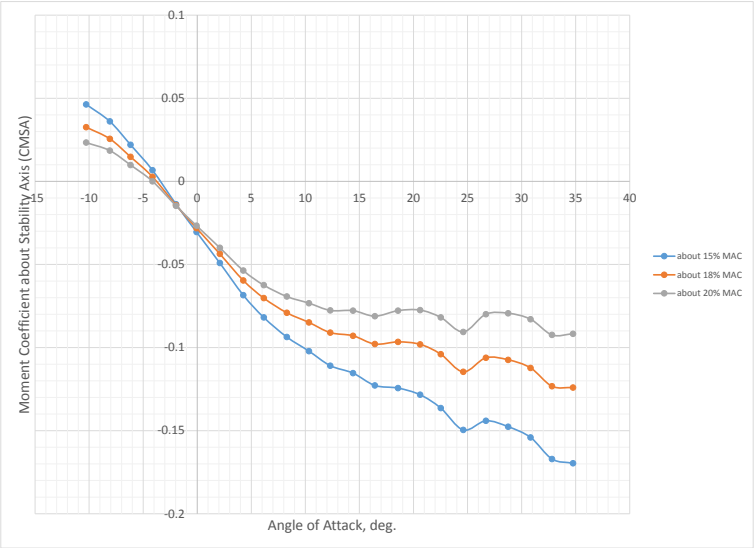


**Figure 8.1.11:** Pitching moment coefficient as a function of angle of attack $\alpha$.

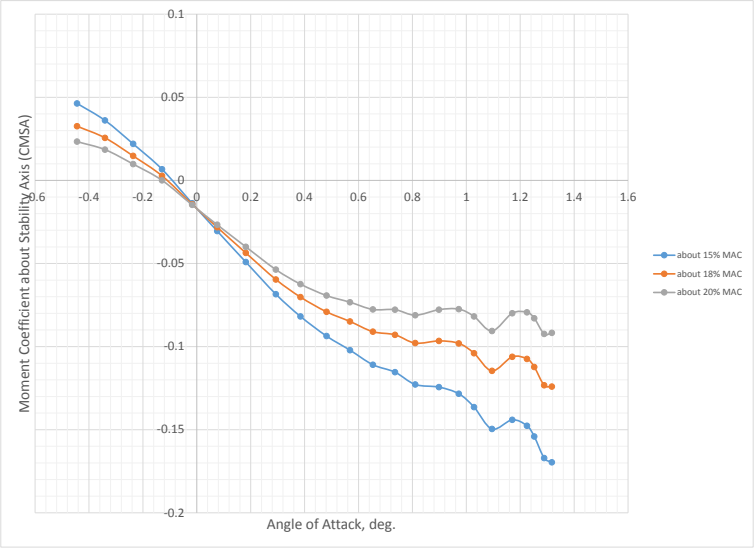


**Figure 8.1.12:** Pitching moment coefficient as a function of lift coefficient.

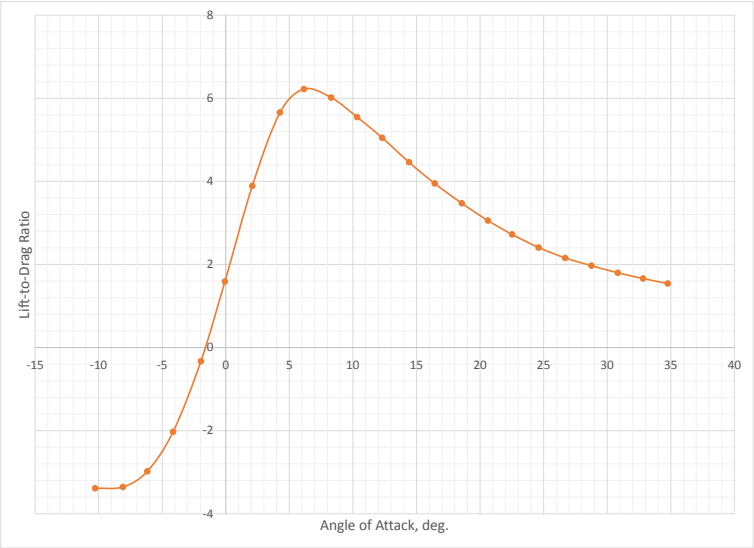


**Figure 8.1.13:** Lift-to-drag ratio as a function of angle of attack $\alpha$.

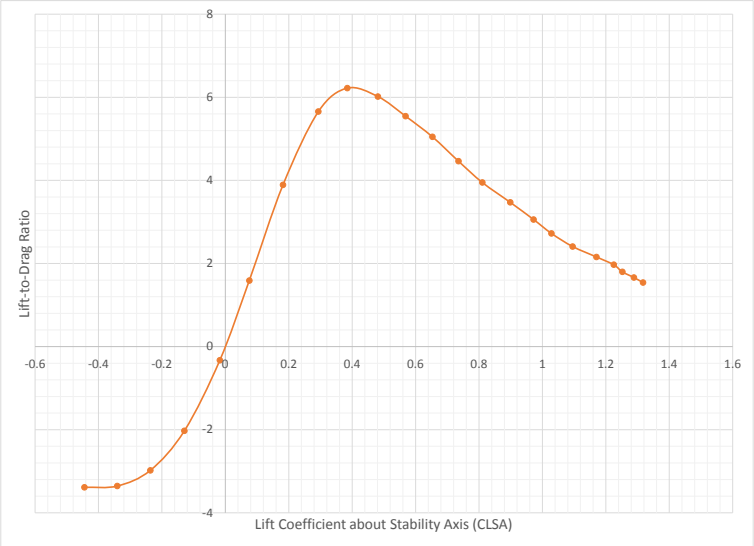


**Figure 8.1.14:** Lift-to-drag ratio as a function of lift coefficient.

#### 8.1.4.3. Final Configuration Yaw Runs

The following are $\beta$-sweep runs for the final configuration with zero control deflections.

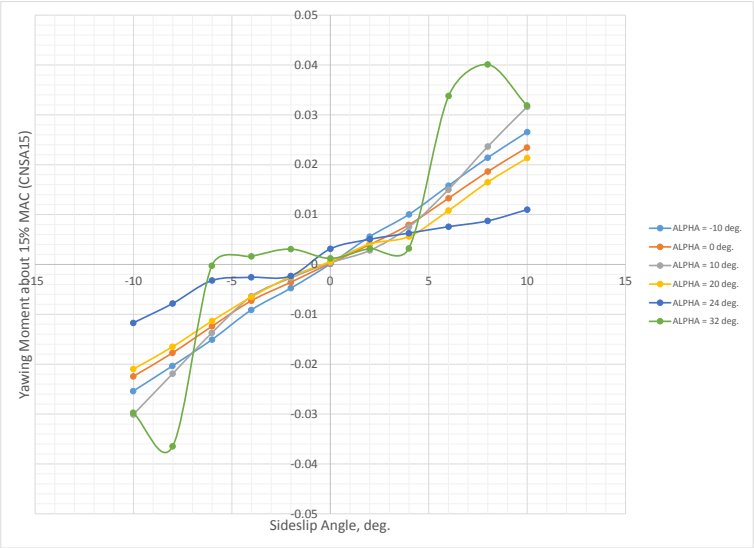


**Figure 8.1.15:** Yawing moment coefficient about 15% MAC as a function of sideslip angle $\beta$.

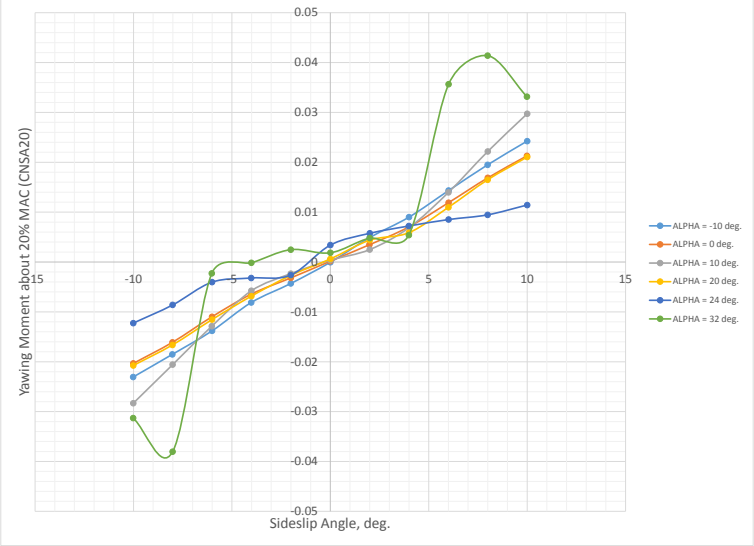


**Figure 8.1.16:** Yawing moment coefficient about 20% MAC as a function of sideslip angle $\beta$.

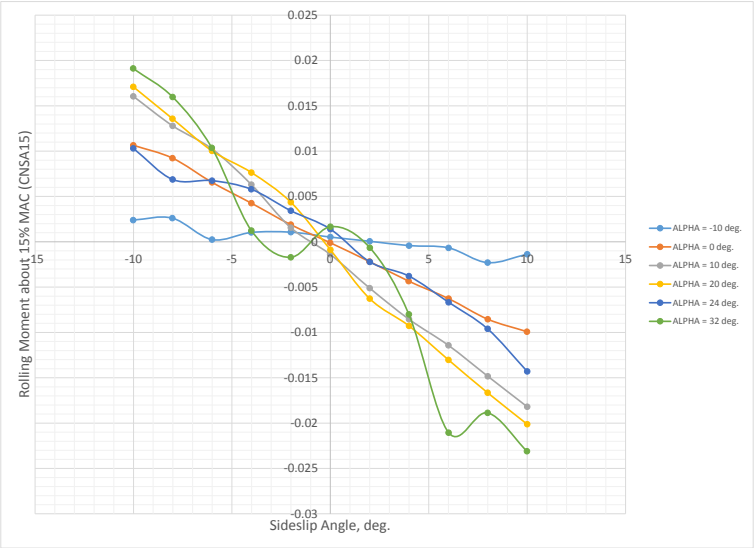


**Figure 8.1.17:** Rolling moment coefficient about 15% MAC as a function of sideslip angle $\beta$.

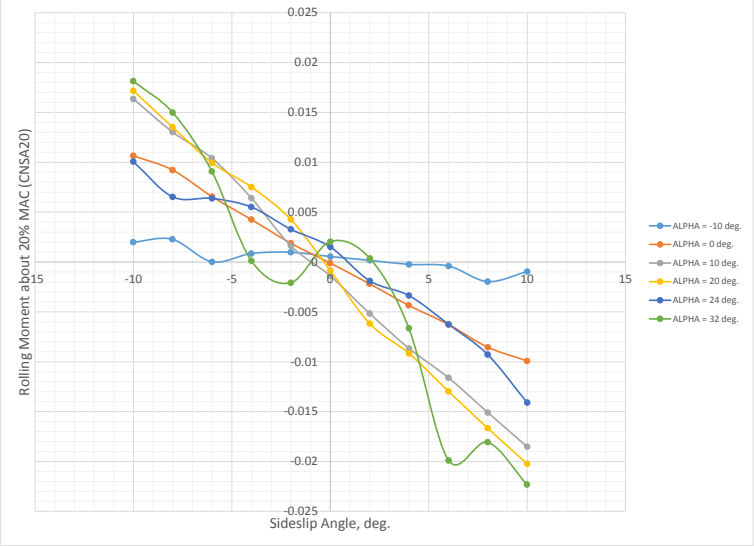


**Figure 8.1.18:** Rolling moment coefficient about 20% MAC as a function of sideslip angle $\beta$.

## 8.2. Flight Test

### *8.2.1. Gyro Bench Test*

To properly prepare the 2014 R-UAV for flight it was necessary to bench-test the gyros and determine the proper gain setting. This was done using the DC motor set-up in Guggenheim 205.

### *8.2.2. Set-Up*

The figures below show the Simulink model necessary to run this experiment.

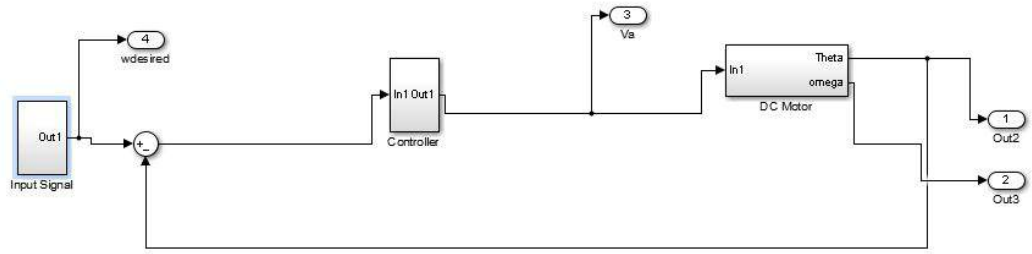


**Figure 8.2.1:** Full Simulink Model

This figure shows the main Simulink model used for running the bench gyro test. It contains a plant model for the DC motor, input signal and a PID controller. The figure below shows the signal sent to the motor.

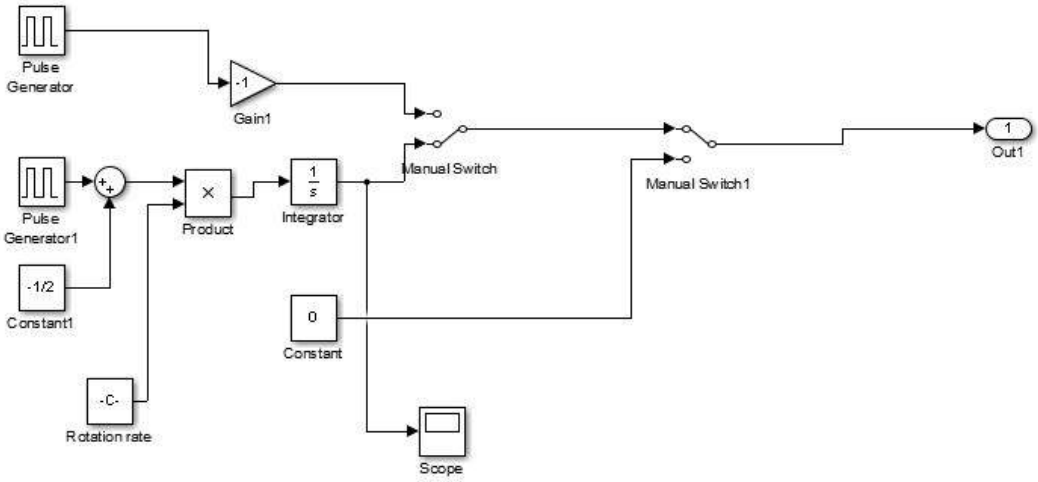


**Figure 8.2.2:** DC Motor Input Signal

The rotation rate of the DC motor can be set by changing the rotation rate block in this model. This produces a triangle wave with a slope equal to the rotation rate in radians per second.

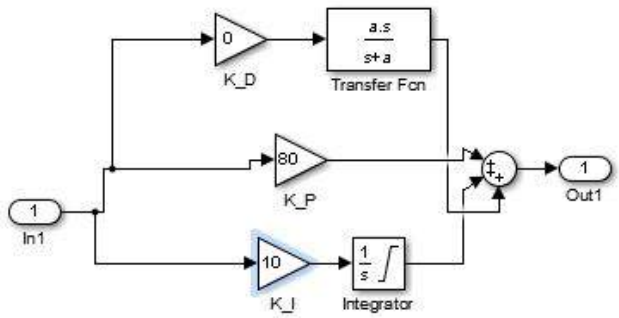


**Figure 8.2.3:** DC Motor Controller

The controller for the system allows the user to ensure that he DC motor runs smoothly. The gains were adjusted until the output from the motor was ideal.

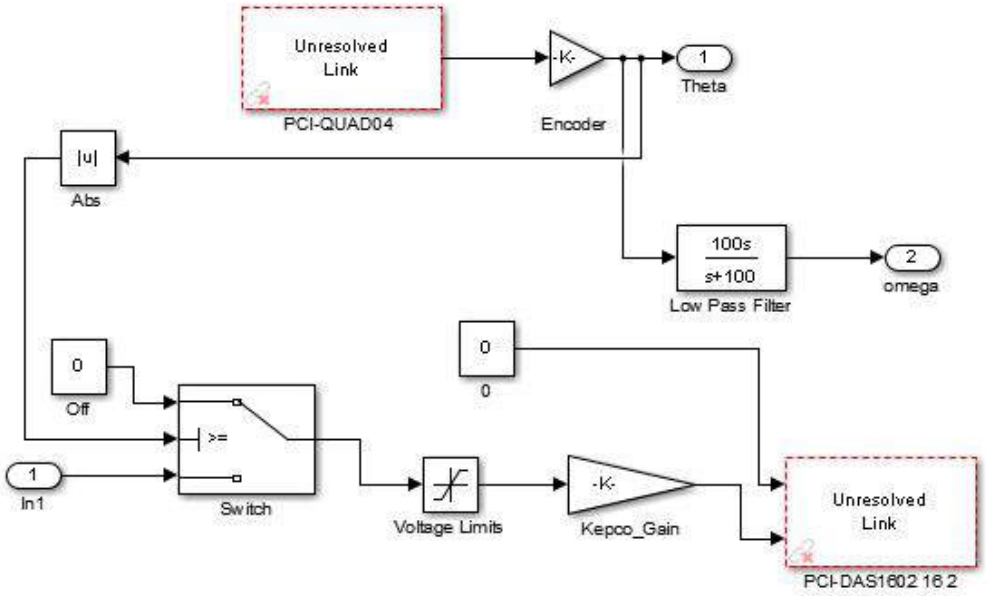


**Figure 8.2.4:** DC Motor Subsystem

The DC motor plant model represents the physical hardware in the simulation and is necessary for running the motor. The PCI blocks require installing the xPC target package in Simulink to use.

### *8.2.3. Procedure*

1. Ensure that the target PC is on and run xPC target on the host PC on MATLAB.
2. Load the Simulink models shown in the figures shown in the figures below.
3. Attach the analog output to the Kepco amplifier.
4. Attach the output of the Kepco amplifier to the motor position inputs on the DC motor.
5. Attach the DC motor encoder to the target PC.
6. Build the Simulink model and run the system. Make sure that the motor is rotating smoothly and at the desired rate before attaching the gyro.
7. Turn off the simulation.

8. Attach the gyro to the motor and the servo to the gyro.
9. Run the simulation again.
10. Record the positive and negative deflection of the servo for many different gain settings.
11. Repeat the previous steps with different motor rotation rates until the desired data is recorded.
12. Record the maximum deflection of the servo and write the gyro deflections as a percentage of the max deflection.

**Results**

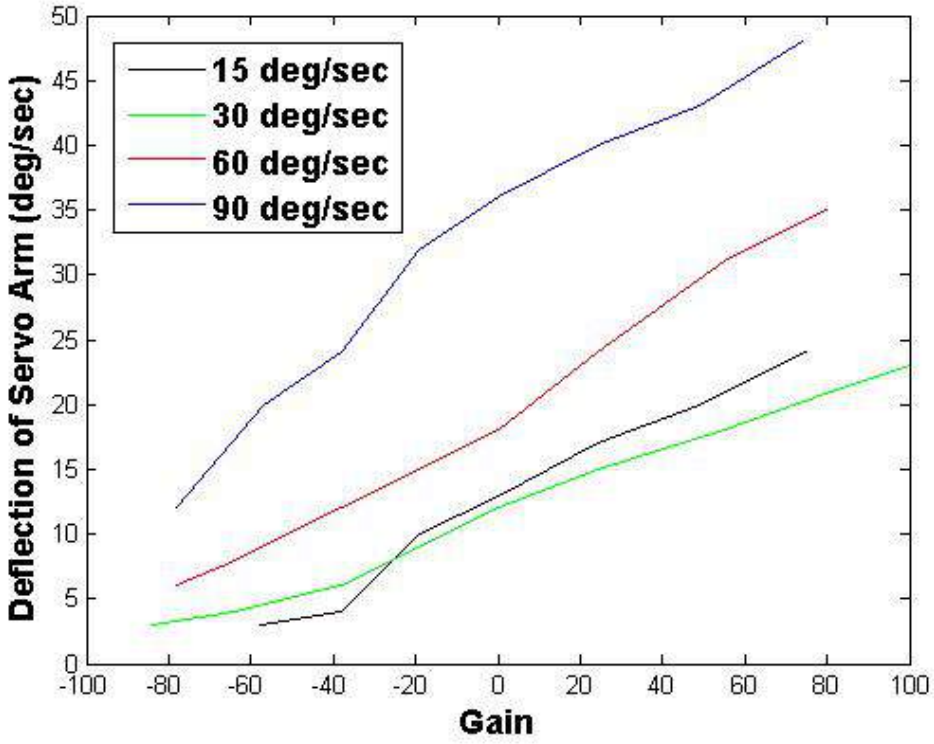


**Figure 8.2.5:** Gyro gain versus servo arm deflection for several rotation rates used.

The Fig. 8.2.5 shows the output of the G370a gyro measured using several different rotation rates. The results from the gyro bench testing show a clear correlation between the rotation rates of the gyro and the servo arm deflection. This is especially clear for the higher rotation rates used, as the 30 degree per second and 15 degree per second rotation rates seem to be close in the output. All servos produced no deflection when the gain setting on the DX18 was set to -100. More testing can be done using additional servos and or gyros to establish a clear connection between the receiver gain setting and the output produced when rotated.

## 8.3. Weights Appendix

**Table 8.3.1: 2006 Weights Information**

| Category | Component | Quantity | Total Weight |
|---|---|---|---|
| Structure | Fuselage | 1 | 3.897 |
| Structure | Wings | 1 | 5.286 |
| Structure | Canards | 1 | 0.612 |
| Structure | Horizontal Stabilator | 2 | 0.462 |
| Structure | Vertical Tail | 1 | 1.011 |
| **Total** | | | **14.754** |
| **Total without H. Stab or Nacelles** | | | **10.806** |
| Propulsion | Overall System | 1 | 7.4 |
| Systems | Servo Batteries & Receiver | 1 | 0.871 |
| Systems | Nose Gear | 1 | 0.63 |
| Systems | Main Gear | 1 | 1.88 |
| Systems | Servos for Stabilators | 2 | 0.38 |
| Systems | Telemetry/Transmitter | 1 | 0.132 |
| **Total** | | | **26.26** |

**Table 8.3.2: 2006 Structural Weight Percentage Breakdown**

| Component | Percentage |
|---|---|
| Fuselage | 26.41 |
| Wings | 35.82 |
| Canards | 4.148 |
| Nacelles | 23.62 |
| Horizontal Stabilator | 3.131 |
| Vertical Tail | 6.852 |

**Table 8.3.3: 2014 Projected Weight Breakdown**

| Component | Projected Weight (lbf) |
|---|---|
| Fuselage | 4.322 |
| Wings | 5.863 |
| Canards | 0.6788 |
| Nacelles | 0.8818 |
| Stabilator | N/A |
| Vertical Tail | 1.121 |

**Table 8.3.4: 2015 Component Sizes**

| Component | Surface Area $ft^2$) | Volume ($ft^3$) |
|---|---|---|
| Fuselage | 11.67 | N/A |
| Wings | 16.56 | N/A |
| Canards | 0.698 | 3.36 x $10^{-3}$ |
| Stabilator | 1.83 | 1.57 x $10^{-2}$ |
| Vertical Tail | 1.194 | 1.73 x $10^{-2}$ |

**Table 8.3.5: Fuselage Weight Breakdown**

| Component | Material | Weight (lbf) |
|---|---|---|
| Skin | 4 plies of 2.0 $\frac{oz}{yd^2}$ fiberglass | 1.775 |
| Bulkheads/Spars | Carbon Fiber Foam Sandwich | 0.2989 |
| Bulkheads # 3 & #11 | PLA | 0.242 |
| Rig Frame | Plywood | 0.0375 |
| Floor | Carbon Fiber Honeycomb Sandwich | 0.4856 |
| Hatch Fasteners | PLA + metal | 0.1625 |
| Landing Gear Mount | PLA | 0.1 |
| **Total** | | **3.064** |
| **Total w/ 10% Correction Factor** | | **3.3704** |

**Table 8.3.6: Wing Weight Breakdown**

| Component | Material | Weight (lbf) |
|---|---|---|
| Top Skin | 1 ply of 2.0 $\frac{oz}{yd^2}$ fiberglass + 2 plies of 3.7 $\frac{oz}{yd^2}$ fiberglass w/ CF reinforcement | 1.2375 |
| Bottom Skin | 1 ply of 2.3 $\frac{oz}{yd^2}$ fiberglass + 2 plies of 3.7 $\frac{oz}{yd^2}$ fiberglass w/ CF reinforcement | 1.9671 |
| Spars | Carbon Fiber Foam Sandwich | 0.1351 |
| Ribs | Carbon Fiber Foam Sandwich | 0.604 |
| Servo Mounts | Plywood | |
| Aileron Supports | Pink Insulator Foam | 0.036 |
| LE Droops | Pink Insulator Foam | 0.1587 |
| Nacelle Mounts | Sheet Metal | |
| **Total** | | **4.1384** |
| **Total w/ 10% Correction Factor** | | **4.552** |

**Table 8.3.7: Moments of Inertia of R-UAV Components: Structural Part 1**

| **Category** | **Component** | **mass** (in) | **x position** (slugs) | **y position** (in) | **z position** (in) | $I_{xx}$ (slugs-$in^2$) | $I_{yy}$ (slugs-$in^2$) | $I_{zz}$ (slugs-$in^2$) | $I_{xz}$ (slugs-$in^2$) |
|---|---|---|---|---|---|---|---|---|---|
| Structure | Fuselage Skin | 0.0551 | 53.7 | 0 | 2.51 | 0 | 6.89 | 6. 89 | 6.89 |
| Structure | Wing Skin (Right) | 0.0414 | 66.3 | 5.99 | 0.859 | 1.48 | 0.0835 | 1.57 | -0.362 |
| Structure | Wing Skin (Left) | 0.0414 | 66.3 | 5.99 | 0.859 | 1.48 | 0.0835 | 1.57 | -0.362 |
| Structure | LE Droop (Right) | 0.00246 | 66.3 | 5.99 | 8.59 | 0.0884 | 0.00497 | 0.0934 | -0.0215 |
| Structure | LE Droop (Left) | 0.00246 | 66.3 | -5.99 | 8.59 | 0.0884 | 0.00497 | 0.0934 | -0.0215 |
| Structure | Canard (Right) | 0.00161 | 26.5 | 5.3 | 2 | 0.0452 | 2.37 | 2.42 | 2.39 |
| Structure | Canard (Right) | 0.00161 | 26.5 | -5.3 | 2 | 0.0452 | 2.37 | 2.42 | 2.39 |
| Structure | Vertical Tail | 0.00149 | 103.9 | 0 | 7.13 | 0 | 2.27 | 2.27 | -2.27 |
| Structure | Stabilator (Right) | 0.00807 | 106.5 | 2.51 | 2.51 | 0.0508 | 14.0 | 14.0 | -14.0 |
| Structure | Stabilator (Left) | 0.00807 | 106.5 | -2.51 | 2.51 | 0.0508 | 14.0 | 14.0 | -14.0 |
| Structure | Bulkhead # 1 | 0.000248 | 10.1 | 0 | 1.2 | 0 | 0.746 | 0.746 | 0.746 |
| Structure | Bulkhead # 2 | 0.000870 | 22.0 | 0 | 2.2 | 0 | 1.60 | 1.60 | 1.60 |
| Structure | Bulkhead # 3 | 0.00366 | 29.1 | 0 | 4.2 | 0 | 4.69 | 4.69 | 4.69 |
| Structure | Bulkhead # 4 | 0.00174 | 37.4 | 0 | 4.7 | 0 | 1.31 | 1.31 | 1.31 |
| Structure | Bulkhead #5 | 0.000932 | 42.5 | 0 | 2.8 | 0 | 0.467 | 0.467 | 0.467 |
| Structure | Bulkhead #6 | 0.00180 | 55.1 | 0 | 2.0 | 0 | 0.172 | 0.172 | 0.172 |
| Structure | Bulkhead # 7 | 0.00292 | 67.1 | 0 | 1.5 | 0 | 0.0144 | 0.0144 | 0.0144 |
| Structure | Bulkhead # 8 | 0.00298 | 70.0 | 0 | 1.3 | 0 | 0.0782 | 0.0782 | 0.0782 |
| Structure | Bulkhead # 9 | 0.00280 | 75.9 | 0 | 1.2 | 0 | 0.339 | 0.339 | 0.339 |
| Structure | Bulkhead #10 | 0.00180 | 80.3 | 0 | 1.2 | 0 | 0.428 | 0.428 | 0.428 |
| Structure | Bulkhead #11 | 0.00205 | 59.0 | -0.055 | 2.2 | 0.0000052 | 1.19 | 1.19 | 1.19 |
| Structure | Bulkhead #12 | 0.000435 | 97.3 | 0 | 2.0 | 0 | 0.457 | 0.457 | 0.457 |
| Structure | Bulkhead #13 | 0.000248 | 106.1 | 0 | 2.3 | 0 | 0.422 | 0.422 | 0.422 |
| Structure | Rig Frame # 1 | 0.000233 | 29.1 | 0 | 4.2 | 0 | 0.298 | 0.298 | 0.298 |
| Structure | Rig Frame # 2 | 0.000233 | 37.4 | 0 | 4.7 | 0 | 0.1756 | 0.176 | 0.176 |
| Structure | Rig Frame # 3 | 0.000233 | 48.9 | 0 | 4.7 | 0 | 0.0595 | 0.0595 | 0.0595 |
| Structure | Rig Frame # 4 | 0.000233 | 62.7 | 0 | 4.7 | 0 | 0.00111 | 0.00111 | 0.00111 |
| Structure | Rig Frame # 5 | 0.000233 | 84.7 | 0 | 4.2 | 0 | 0.0915 | 0.0915 | 0.0915 |

**Table 8.3.8: Moments of Inertia of R-UAV Components: Structural Part 2**

| **Category** | **Component** | **mass** (in) | **x position** (slugs) | **y position** (in) | **z position** (in) | $I_{xx}$ (slugs-$in^2$) | $I_{yy}$ (slugs-$in^2$) | $I_{zz}$ (slugs-$in^2$) | $I_{xz}$ (slugs-$in^2$) |
|---|---|---|---|---|---|---|---|---|---|
| Structure | Rib 0.5 (Right) | 0.00348 | 64.4 | 3.6 | 1.0 | 0.0451 | 0.000801 | 0.0459 | 0.00606 |
| Structure | Rib 0.5 (Left) | 0.00348 | 64.4 | -3.6 | 1.0 | 0.0451 | 0.000801 | 0.0459 | 0.00606 |
| Structure | Rib 1 (Right) | 0.00248 | 67.7 | 6.0 | 0.8 | 0.0894 | 0.0198 | 0.109 | -0.0464 |
| Structure | Rib 1 (Left) | 0.00248 | 67.7 | -6.0 | 0.8 | 0.0894 | 0.0198 | 0.109 | -0.0464 |
| Structure | Rib 2 (Right) | 0.00155 | 69.9 | 8.4 | 0.6 | 0.110 | 0.0391 | 0.149 | -0.0763 |
| Structure | Rib 2 (Left) | 0.00155 | 69.9 | -8.4 | 0.6 | 0.110 | 0.0391 | 0.149 | -0.0763 |
| Structure | Rib 3 (Right) | 0.00559 | 78.0 | 13.5 | 0.3 | 1.02 | 0.962 | 1.98 | -1.38 |
| Structure | Rib 3 (Left) | 0.00559 | 78.0 | -13.5 | 0.3 | 1.02 | 0.962 | 1.98 | -1.38 |
| Structure | Rib 4 (Right) | 0.00559 | 79.0 | 14.5 | 0.3 | 1.17 | 1.11 | 2.29 | -1.60 |
| Structure | Rib 4 (Left) | 0.00559 | 79.0 | -14.5 | 0.3 | 1.17 | 1.11 | 2.29 | -1.60 |
| Structure | Rib 5 (Right) | 0.0000621 | 84.1 | 25.7 | 1.0 | 0.0410 | 0.0229 | 0.0640 | -0.0383 |
| Structure | Rib 5 (Left) | 0.0000621 | 84.1 | -25.7 | 1.0 | 0.0410 | 0.0229 | 0.0640 | -0.0383 |
| Structure | Floor | 0.0151 | 55.7 | 0 | 1.14 | 0 | 1.27 | 1.27 | 1.27 |
| Structure | Aileron (Right) | 0.0025 | 84.0 | 19.3 | 0.21 | 0.931 | 0.914 | 1.84 | -1.30 |
| Structure | Aileron (Left) | 0.0025 | 84.0 | -19.3 | 0.21 | 0.931 | 0.914 | 1.84 | -1.30 |
| Structure | Flap (Right) | 0.00274 | 86.0 | 9.82 | 0.21 | 0.264 | 1.22 | 1.49 | -1.35 |
| Structure | Flap (Left) | 0.00274 | 86.0 | -9.82 | 0.21 | 0.264 | 1.22 | 1.49 | -1.35 |

**Table 8.3.9: Moments of Inertia of R-UAV Components: Propulsion**

| **Category** | **Component** | **mass** (in) | **x position** (slugs) | **y position** (in) | **z position** (in) | $I_{xx}$ (slugs-$in^2$) | $I_{yy}$ (slugs-$in^2$) | $I_{zz}$ (slugs-$in^2$) | $I_{xz}$ (slugs-$in^2$) |
|---|---|---|---|---|---|---|---|---|---|
| Propulsion | EDF (Right) | 0.0477 | 83.3 | 3.6 | -2.4 | 0.618 | 16.2 | 16.8 | -16.5 |
| Propulsion | EDF (Left) | 0.0477 | 83.3 | -3.6 | -2.4 | 0.618 | 16.2 | 16.8 | -16.5 |
| Propulsion | ESC (Forward) | 0.0165 | 85.9 | 0 | 1.9 | 0 | 7.30 | 7.30 | -7.30 |
| Propulsion | ESC (Aft) | 0.0165 | 92.0 | 0 | 1.9 | 0 | 12.2 | 12.2 | -12.2 |
| Propulsion | Nacelle (Right) | 0.0344 | 74.2 | 3.6 | -2.0 | 0.447 | 2.99 | 3.44 | -3.21 |
| Propulsion | Nacelle (Left) | 0.0344 | 74.2 | -3.6 | -2.0 | 0.447 | 2.99 | 3.44 | -3.21 |
| Propulsion | Battery # 1 | 0.0571 | 46.0 | 1.0 | 2.2 | 0.0571 | 20.4 | 20.4 | 20.4 |
| Propulsion | Battery # 2 | 0.0571 | 46.0 | -1.0 | 2.2 | 0.0571 | 20.4 | 20.4 | 20.4 |
| Propulsion | Battery # 3 | 0.0571 | 64.0 | 1.0 | 2.2 | 0.0571 | 0.0443 | 0.101 | 0.0670 |
| Propulsion | Battery # 3 | 0.0571 | 64.0 | -1.0 | 2.2 | 0.0571 | 0.0443 | 0.101 | 0.0670 |
| Propulsion | Battery/ESC Connector #1 | 0.0134 | 56.56 | 0 | 1.28 | 0 | 0.942 | 0.942 | 0.942 |
| Propulsion | Battery/ESC Connector #2 | 0.0127 | 66.0 | 0 | 1.28 | 0 | 0.0159 | 0.0159 | 0.0159 |
| Propulsion | ESC/EDF Connector #1 | 0.00233 | 80.6 | 1.78 | 1.28 | 0.00733 | 0.575 | 0.583 | -0.579 |
| Propulsion | ESC/EDF Connector #2 | 0.00233 | 80.6 | 1.78 | 1.28 | 0.00733 | 0.575 | 0.583 | -0.579 |
| Propulsion | ESC/EDF Connector #3 | 0.00233 | 80.6 | 1.78 | 1.28 | 0.00733 | 0.575 | 0.583 | -0.579 |
| Propulsion | ESC/EDF Connector #4 | 0.00233 | 83.7 | -1.78 | 1.28 | 0.00733 | 0.844 | 0.852 | -0.848 |
| Propulsion | ESC/EDF Connector #5 | 0.00233 | 83.7 | -1.78 | 1.28 | 0.00733 | 0.844 | 0.852 | -0.848 |
| Propulsion | ESC/EDF Connector #6 | 0.00233 | 83.7 | -1.78 | 1.28 | 0.00733 | 0.844 | 0.852 | -0.848 |

**Table 8.3.10: Moments of Inertia of R-UAV Components: Systems**

| **Category** | **Component** | **mass** (in) | **x position** (slugs) | **y position** (in) | **z position** (in) | $I_{xx}$ (slugs-$in^2$) | $I_{yy}$ (slugs-$in^2$) | $I_{zz}$ (slugs-$in^2$) | $I_{xz}$ (slugs-$in^2$) |
|---|---|---|---|---|---|---|---|---|---|
| Avionics | Alpha-Beta Sensor | 0.00385 | 5 | 0 | 0 | 0 | 13.8 | 13.8 | 13.8 |
| Avionics | PixHawk | 0.00578 | 67.6 | 0.2 | 1.2 | 0.000231 | 0.0427 | 0.0430 | -0.0429 |
| Avionics | Current Measuring Device | 0.00199 | 67.6 | 0.2 | 1.2 | 0.0000794 | 0.0147 | 0.0147 | -0.0147 |
| Avionics | GPS | 0.00185 | 67.6 | 0.2 | 1.2 | 0.0000739 | 0.0137 | 0.0137 | -0.0137 |
| Avionics | Telemetry Radio | 0.00348 | 67.6 | 0.2 | 1.2 | 0.000139 | 0.0257 | 0.0259 | -0.0258 |
| Avionics | Buzzer | 0.000274 | 67.6 | 0.2 | 1.2 | 0.0000110 | 0.00203 | 0.00203 | -0.00203 |
| Avionics | Switch/Push Button | 0.000137 | 67.6 | 0.2 | 1.2 | 0.00000548 | 0.00101 | 0.00102 | -0.00102 |
| Avionics | RC Encoder | 0.000435 | 67.6 | 0.2 | 1.2 | 0.0000174 | 0.00322 | 0.00323 | -0.00323 |
| Avionics | Arduino Mega Pro | 0.00272 | 38 | 0 | 1.28 | 0 | 1.96 | 1.96 | 1.96 |
| Avionics | 1S LiPo Battery | 0.00335 | 40 | 0 | 1.28 | 0 | 2.08 | 2.08 | 2.08 |
| Avionics | Breakout Board | 0.000205 | 42 | 0 | 1.28 | 0 | 0.108 | 0.108 | 0.108 |
| Receiver | RX | 0.00155 | 42 | 0 | 1.28 | 0 | 0.813 | 0.813 | 0.813 |
| Receiver | Battery | 0.0113 | 43 | 0 | 1.28 | 0 | 5.39 | 5.39 | 5.39 |
| Receiver | Antenna | 0.00656 | 44 | 0 | 1.28 | 0 | 2.86 | 2.86 | 2.86 |
| Servos | Stabilator | 0.00528 | 88.4 | -0.6 | 2.8 | 0.0019 | 2.92 | 2.92 | -2.92 |
| Servos | Canards | 0.00377 | 29.1 | 0 | 2.51 | 0 | 4.82 | 4.82 | 4.82 |
| Servos | Vectored Thrust (Right) | 0.00149 | 83 | 1.0 | -0.5 | 0.00149 | 0.489 | 0.490 | -0.490 |
| Servos | Vectored Thrust (Left) | 0.00149 | 83 | -1.0 | -0.5 | 0.00149 | 0.489 | 0.490 | -0.490 |
| Servos | Aileron (Right) | 0.00149 | 83 | 18 | 0.859 | 0.483 | 0.341 | 0.824 | -0.530 |
| Servos | Aileron (Left) | 0.00149 | 83 | -18 | 0.859 | 0.483 | 0.341 | 0.824 | -0.530 |
| Servos | Flaps (Right) | 0.00404 | 79 | 10.5 | 0.859 | 0.445 | 0.805 | 1.25 | -1.00 |
| Servos | Flaps (Left) | 0.00404 | 79 | -10.5 | 0.859 | 0.445 | 0.805 | 1.25 | -1.00 |

**Table 8.3.11: Moments of Inertia of R-UAV Components: Landing Gear**

| **Category** | **Component** | **mass** (in) | **x position** (slugs) | **y position** (in) | **z position** (in) | $I_{xx}$ (slugs-$in^2$) | $I_{yy}$ (slugs-$in^2$) | $I_{zz}$ (slugs-$in^2$) | $I_{xz}$ (slugs-$in^2$) |
|---|---|---|---|---|---|---|---|---|---|
| Landing Gear | Nose Gear | 0.0206 | 31.6 | 0 | -6.5 | 0 | 22.8 | 22.8 | 22.8 |
| Landing Gear | Main Gear (Right) | 0.0130 | 68.5 | 7.7 | -8.0 | 0.773 | 0.171 | 0.944 | -0.402 |
| Landing Gear | Main Gear (Left) | 0.0130 | 68.5 | -7.7 | -8.0 | 0.773 | 0.171 | 0.944 | -0.402 |
| Landing Gear | Main Gear Mount (Right) | 0.00435 | 68.5 | 7.7 | 1.14 | 0.258 | 0.0570 | 0.315 | -0.134 |
| Landing Gear | Main Gear Mount (Left) | 0.00435 | 68.5 | -7.7 | 1.14 | 0.258 | 0.0570 | 0.315 | -0.134 |
| Landing Gear | Magnetic Brake (Right) | 0.00124 | 68.5 | 7.7 | 1.14 | 0.0737 | 0.0163 | 0.0899 | -0.0383 |
| Landing Gear | Magnetic Brake (Left) | 0.00124 | 68.5 | -7.7 | 1.14 | 0.0737 | 0.0163 | 0.0899 | -0.0383 |
| Landing Gear | Magnetic Brakes Power Modeul | 0.00137 | 68.5 | 0 | 1.28 | 0 | 0.0179 | 0.0179 | -0.0179 |

**Table 8.3.12: Comparison of Initial Estimated Weight to Measured Weight**

| Component | Initial Estimated Weight (lbf) | Measured Weight w/ 10% CF | Measured Weight (lbf) | % Difference |
|---|---|---|---|---|
| Fuselage (skin + support) | 6.526 | 3.072 | 2.839 | -109.0 |
| Wings (skin + support) | 7.704 | 4.138 | 4.552 | -69.24 |
| Canards | 0.976 | 0.1036 | 0.1140 | -756.5 |
| Vertical Tail | 0.353 | 0.048 | 0.0528 | -569.1 |
| Stabilator | 0.561 | 0.5200 | 0.5720 | 1.976 |

**Table 8.3.13: Comparison of Material Estimated Weight to Measured Weight**

| Component | Material Estimated Weight (lbf) | Measured Weight (lbf) | Measured Weight w/ 10% CF (lbf) | % Difference |
|---|---|---|---|---|
| Fuselage | 3.072 | 2.839 | 3.123 | 1.630 |
| Wings | 4.705 | 4.138 | 4.552 | -3.365 |
| Canards | 0.08015 | 0.1036 | 0.1140 | 29.68 |
| Vertical Tail | 0.03973 | 0.048 | 0.0528 | 24.75 |
| Stabilator | 0.4080 | 0.5200 | 0.5720 | 28.36 |